Propagation of Cosmic Rays in the Galaxy and their measurements at very high energies with LORA

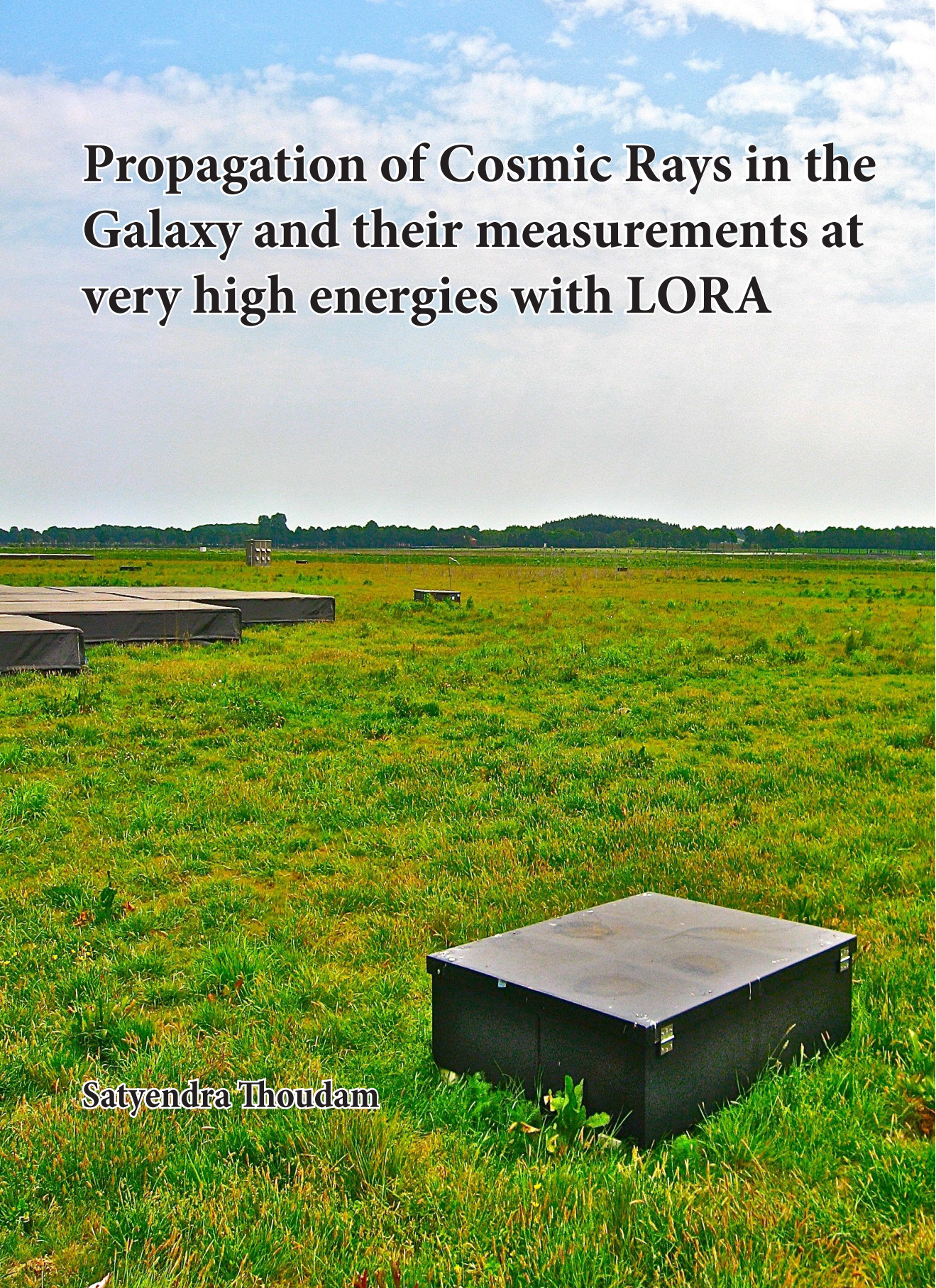

Satyendra Thoudam

Propagation of Cosmic Rays in the Galaxy and their measurements at very high energies with LORA

Satyendra Thoudam

Cover photo: A sectional view of the LORA detector array located in the core of LOFAR at Exloo in the Netherlands. The black boxes contained the LORA detectors and the wide tiles are the LOFAR high band antennas.

This thesis was typeset in LaTeX by the author and printed by Ipskamp Drukkers, Enschede (www.ipskampdrukkers.nl).

ISBN 978-90-819014-0-6

Propagation of Cosmic Rays in the Galaxy and their measurements at very high energies with LORA

Proefschrift

ter verkrijging van de graad van doctor
aan de Radboud Universiteit Nijmegen
op gezag van de rector magnificus prof. mr. S.C.J.J. Kortmann,
volgens besluit van het college van decanen
in het openbaar te verdedigen op dinsdag 12 juni 2012
om 10:30 uur precies

door

Satyendra Thoudam

geboren op 1 maart 1976
te Manipur, India

Promotor:	Prof. dr. Heino Falcke
Copromotor:	Dr. habil. Jörg R. Hörandel
Manuscriptcommissie :	Prof. dr. R. Kleiss (chair)
	Dr. A. W. Strong *Max-Planck-Institut für extraterrestrische Physik Garching, Germany*
	Prof. dr. R. A. M. J. Wijers *Universiteit van Amsterdam*
	Prof. dr. P. J. Groot
	Prof. dr. A. Achterberg

Propagation of Cosmic Rays in the Galaxy and their measurements at very high energies with LORA

Doctoral thesis

to obtain the degree of doctor
from Radboud University Nijmegen
on the authority of the Rector Magnificus, prof. dr. S.C.J.J. Kortmann,
according to the decision of the Council of Deans
to be defended in public on Tuesday, 12 June, 2012
at 10:30 hours

by

Satyendra Thoudam

born on 1 March 1976
in Manipur, India

Supervisor:	Prof. Dr. Heino Falcke
Co-supervisor:	Dr. habil. Jörg R. Hörandel
Reading Committee:	Prof. Dr. R. Kleiss (chair)
	Dr. A. W. Strong *Max-Planck-Institut für extraterrestrische Physik* *Garching, Germany*
	Prof. Dr. R. A. M. J. Wijers *University of Amsterdam*
	Prof. Dr. P. J. Groot
	Prof. Dr. A. Achterberg

Contents

Introduction

Cosmic rays

Cosmic rays are high-energy charged particles coming from outer space. They are most likely produced by very energetic astrophysical processes in the Universe. Observations of diffuse radiation from galaxies including our own Milky Way have revealed that cosmic rays are present throughout the galaxies [6, 133]. Measurements at the Earth show that they are mainly composed of atomic nuclei of almost all the elements present in the periodic table. Their elemental composition is dominated by protons which constitute $\sim 88\%$, followed by helium with $\sim 10\%$. The heavier nuclei and the leptonic components (mostly electrons) constitute $\sim 1\%$ each.

The elemental abundances of cosmic rays are shown in Figure 1 along with the abundances in the Solar system. The two distributions look similar for most of the elements. However, a few elements such as Li, Be, and B, which are generally not produced during stellar evolution, are found to be more abundant in the cosmic rays than in the Solar system. They are most likely produced by the interactions of primary cosmic-ray species such as C, N, and O with the interstellar matter during the propagation in the Galaxy.

Cosmic rays were first discovered by Victor Hess in 1912 using simple measuring instruments on manned balloon flights [110]. Since then, several independent measurements with more sophisticated detectors have been performed. Cosmic rays are now measured up to energies exceeding 10^{20} eV which is ~ 10 million times the maximum energy ever attained by man-made accelerators. In general, the spectrum of cosmic rays follows a power-law behavior of the form $E^{-\Gamma}$ over several decades in energy (Figure 2). A prominent feature in the spectrum is the presence of a kink at $\sim 3 \times 10^{15}$ eV which is commonly known as the "knee". Up to the knee, the spectral index is $\Gamma \sim 2.75$ and steepens to ~ 3.1 above the knee. Other important features in the spectrum include a further slight steepening which occurs at $\sim 3 \times 10^{17}$ eV called the "second knee", a hardening at $\sim 4 \times 10^{18}$ eV called the "ankle" and a steep decline in the flux at $\sim 3 \times 10^{19}$ eV called the "Greisen-Zatsepin-Kuzmin (GZK) cut-off".

Sources of cosmic rays

Even 100 years after their discovery, the origin of cosmic rays still remains a mystery. Present understandings on the possible acceleration mechanism of cosmic-rays and the nature of their confinement in our Galaxy seem to suggest a possible classification of cosmic rays based on their origin. Cosmic rays up to around the second knee are considered to be of

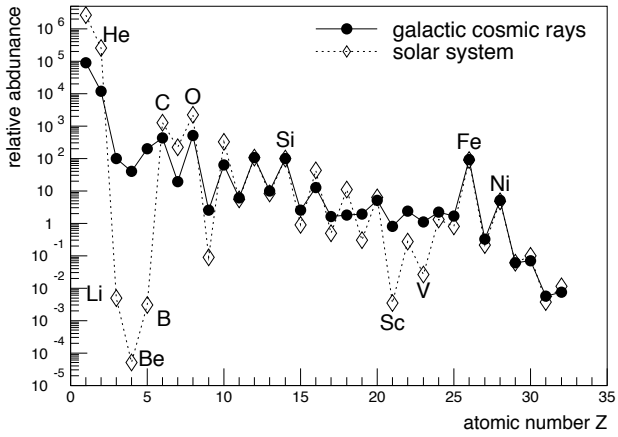

Figure 1: Relative abundance of cosmic-ray elements normalized to Si$=100$. Also shown for comparison are the solar system abundances [197].

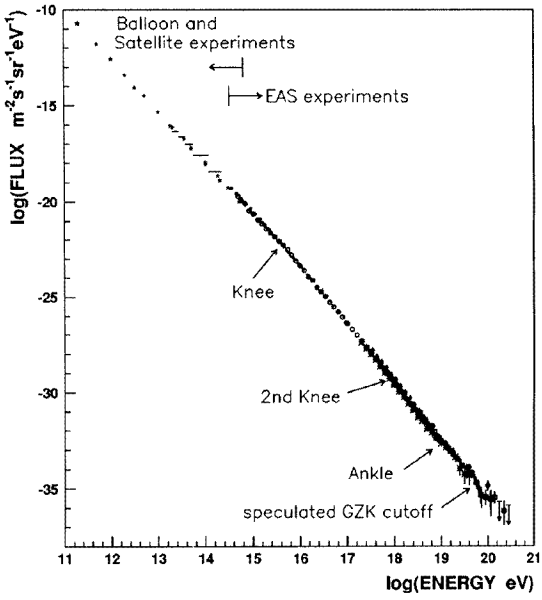

Figure 2: All particle cosmic-ray energy spectrum adapted from [148].

Galactic origin and hence, are commonly referred to as Galactic cosmic rays, while above that, they are considered to be of extra-galactic origin. Though the origin of the knee is not perfectly understood, it is now best explained as due to the cut-off of the proton spectrum, the most abundant cosmic-ray species (see e.g [113] and references therein). The cut-off can be either due to the maximum energy up to which the particles can be accelerated or due to the limited containment volume of our Galaxy (see [114] for details). Both scenarios suggest a charge dependent cut-off with cut-off energies proportional to the charge Z. Thus, the second knee might be a cut-off signature of the heavy elements such as iron $(Z = 26)$.

This thesis will concentrate primarily on Galactic cosmic rays. Several properties of Galactic cosmic rays such as their elemental composition, individual spectra, anisotropy, abundance ratios, and their associated diffuse high-energy gamma radiation in the Galaxy have been measured quite extensively (see [117, 182] for overviews). However, despite numerous measurements, the exact nature of their sources is still not clearly understood although supernova remnants are the most favorable candidates [99]. A supernova remnant is an object that results from a supernova explosion, an event mostly caused by the collapse of a massive star. It is characterized by high velocity stellar material ejected from the explosion and expanding outwards with speeds greater than the speed of sound in the interstellar medium, thereby producing shock waves. Supernova remnants are known to occur in our Galaxy at the rate of $\sim 1/30$ to $1/50$ yr^{-1} with each explosion releasing a total kinetic energy of $\sim 10^{51}$ ergs. This corresponds to a total power of $\sim 10^{42}$ ergs s^{-1} released by the supernova remnants in the Galaxy. If approximately 10% of the supernova kinetic energy is converted into cosmic rays, then the total power released is sufficient to maintain the cosmic-ray energy density in our Galaxy which is measured to be ~ 1 eV cm^{-3}. This measured energy density corresponds to a total cosmic-ray luminosity of $\sim 10^{41}$ ergs s^{-1}. Other potential sources of cosmic rays include neutron stars and stellar winds of O/B stars, both of which are known to produce a luminosity of $\sim 10^{41}$ ergs s^{-1} in the Galaxy.

In 1949, Enrico Fermi showed that charged particles can be accelerated under multiple reflections by randomly moving magnetic clouds present in the interstellar medium [93]. He showed that in such a process, the particles on average gain energy at a rate proportional to the square of the velocity of the moving clouds. Then later, it became known that a much more efficient way of acceleration can be produced with astrophysical shock waves in which the energy gain of the particles scales linearly with the shock velocity [45, 55]. This latter type of acceleration mechanism is known as the first-order Fermi acceleration, and the one originally proposed by Fermi is now known as the second-order Fermi acceleration.

The mechanism of particle acceleration by astrophysical shock waves via first-order Fermi acceleration is now commonly referred to as diffusive shock acceleration. Under diffusive shock acceleration theory, suprathermal particles in the tail of the Maxwell-Boltzmann distribution present in the interstellar medium are injected into the shock front. The particles are then reflected back and forth several times across the shock by the magnetic turbulence generated on either side of the shock and in each cycle of crossing, the particles gain energy by first-order Fermi acceleration [45, 55]. It is now theoretically established that under such acceleration mechanism, supernova remnants can accelerate particles up to energies

close to the knee [47]. In a simple planar shock model with a test-particle approach, such a mechanism naturally produces a power-law spectrum of the form $E^{-\Gamma}$ with the exponent $\Gamma = 2$ for strong shocks. The predicted value of the spectral index is in very good agreement with estimates from the radio observations of supernova remnants [104]. Later, several theorists then realized that because of the large amount of energy transferred into the particles, the effect of the back-reaction of the accelerated particles on the accelerator might not be negligible. Such sophisticated models which are known as non-linear diffusive shock acceleration models take into account the dynamical reaction of the accelerated particles on the shock structure and the magnetic field around the shock region (see [142] for a review). Under such models, higher energy particles are more efficiently accelerated than the lower energy ones, thereby leading to a particle spectrum which is harder than the predictions of standard diffusive shock acceleration theory [64, 163].

Observational evidence for the presence of high-energy particles inside supernova remnants (at least up to a few TeVs) is provided by the detection of non-thermal X-rays [43, 157] and high-energy TeV γ-rays from several remnants [20, 22, 23, 25, 30]. The non-thermal X-rays are most likely synchrotron emission produced by high-energy electrons in the presence of magnetic fields, but the origin of the TeV γ-rays is still under debate between the leptonic and the hadronic scenarios. TeV γ-rays can be produced either by high-energy electrons through inverse Compton interactions with low energy photons or by the decay of π^0 mesons which are produced by the interactions of high-energy hadrons (mostly protons) with the ambient matter. But, irrespective of the nature of production, the detection of TeV γ-rays suggests the presence of charged particles with energies larger than a few TeVs inside supernova remnants.

Cosmic-ray propagation in the Galaxy

The simplest model of cosmic-ray propagation is the leaky box model (see [70] for a review). Under this model, our Galaxy is considered as a closed-box with semi-reflecting walls which confine cosmic rays for some time before they escape into intergalactic space. The spatial distribution of cosmic rays and their sources are all assumed to be uniform in this model. Under stationary condition, the equilibrium density of cosmic rays in this model is given by the following balance equation,

$$\frac{N_p}{T_e} + \frac{N_p}{T_p} = Q \tag{1}$$

where N_p represents the cosmic-ray density, T_e is the escape (also confinement) time from the Galaxy, T_p is the spallation timescale and Q is the source injection rate. In cosmic-ray physics, nuclei such as H, He, C, O, and Fe which are formed during stellar evolution are referred to as primary cosmic rays. Primaries can undergo inelastic collisions (spallation) with the interstellar matter present in the Galaxy and produce lighter nuclear species which are generally referred to as the secondary cosmic rays. Some well-known secondaries are Li, Be, B, $\bar{p}$, and sub-Fe species such as Sc, Ti, and V. For the secondaries, the source term

in Eq. (1) can be written as $Q = nc\sigma N_p$, where n is the average matter density in the Galaxy, c is the velocity of light and N_p is given by Eq. (1). The equilibrium density for the secondaries N_s is given by,

$$\frac{N_s}{T_e} + \frac{N_s}{T_s} = nc\sigma N_p \tag{2}$$

where T_s is the spallation timescale. From Eq. (2), we can write,

$$\frac{N_s}{N_p} \approx nc\sigma T_e \tag{3}$$

Eq. (3) is referred to as the secondary-to-primary ratio and it is a quantity that can be measured at the Earth. Eq. (3) is important because by measuring the secondary-to-primary ratio, it is possible to determine the total amount of matter traversed by cosmic rays in the Galaxy which is given by $X = nmcT_e$, where m is the mass of a proton. X is measured to be ~ 5 g/cm^2 at ~ 1 GeV/n. Thus, if the confinement time of cosmic rays T_e is known, the averaged density of matter n traversed by cosmic rays in the Galaxy can be determined.

Measurements of abundance ratios of radioactive secondaries to the stable secondaries give an estimate of the confinement time of cosmic rays in the Galaxy to be $T_e \sim 1.7 \times 10^7$ yrs. This, along with the measured value of X, gives the averaged density of matter as $n \sim 0.2$ cm^{-3} [97]. This value of n is much less than the density of matter in the Galactic disk which is measured to be ~ 1 cm^{-3}. This suggests that cosmic rays spend most of their lifetime in the Galactic halo where the matter density is as small as ~ 0.01 cm^{-3}. In addition, if cosmic rays travel in straight paths with the speed of light, they would travel a distance of $\sim 5 \times 10^3$ kpc. To be compared, the vertical boundary of our Galaxy is only a few kpc say ~ 5 kpc and the radial boundary is $\sim (15 - 20)$ kpc. This suggests that cosmic rays do not travel in straight lines, they must undergo some sort of random motions in the Galaxy.

It is now well understood that cosmic rays, being charged particles, can be deflected or scattered by the magnetic fields present in our Galaxy. Our Galactic magnetic field consists of both, a regular component and a random component. The random component can cause pitch angle scattering leading to diffusive motion of cosmic rays. The nature of the scattering is that of wave-particle resonant interactions [98]. A cosmic-ray particle interacts with magnetic inhomogeneities of wave number $k = 1/r_l$, where r_l is the Larmor radius of the particle. The random magnetic field consists of a wide spectrum of inhomogeneities $W(k)$ with scale lengths $l = 2\pi/k$ appropriate to produce resonant scattering of cosmic rays with energies up to $\sim 10^{17}$ eV which corresponds to a scale length of ~ 100 pc. The spectrum peaks at large scale lengths and decreases at smaller lengths, which as a function of k can be represented as $W(k) \propto k^{-2+a}$ where a is a positive constant. The cosmic-ray diffusion coefficient D is related to the wave spectrum as $D \propto b(E/Z)^a$, where b is a constant which depends on the level of inhomogeneity. For a Kolmogorov-type of wave spectrum, $a = 1/3$ and for a Kraichnan-type wave spectrum, $a = 1/2$.

In the diffusion model, Eq. (1) can be written as,

$$-\nabla \cdot (D\nabla N_p) + \frac{N_p}{T_p} = Q \tag{4}$$

where the escape term in Eq. (1) is replaced by the diffusion term. The cosmic-ray escape time from the Galaxy in the diffusion model is given by $T_e \sim H^2/D$, where H denotes the size of the Galactic halo. Similarly, Eq. (2) which represents the equilibrium spectrum for the secondaries can be written as,

$$-\nabla \cdot (D\nabla N_s) + \frac{N_s}{T_s} = nc\sigma N_p \tag{5}$$

From Eq. (5), it can be checked that the secondary-to-primary ratio under the diffusion model is given by (see next Chapter),

$$\frac{N_s}{N_p} \propto \frac{1}{D} \tag{6}$$

Thus, measurements of secondary-to-primary ratios can give an estimate of the values of the diffusion coefficient. Compared to the Leaky box model, the diffusion model seems to be more realistic because it can describe a non-uniform distribution of cosmic rays in the Galaxy. In fact, observations of diffuse emissions from radio to gamma-rays from different regions of our Galaxy suggest that the cosmic-ray distribution is not uniform in the Galaxy.

There also exist other models of cosmic-ray propagation such as the diffusion-convection and the re-acceleration models. The diffusion-convection model also takes into account, in addition to the diffusive motion, the effect of cosmic-ray convection due to the Galactic wind generated by the outward flow of interstellar gas from the Galactic disk [58, 125]. The main difference in the results is that the fixed halo boundary H in the diffusion model is replaced by a convective boundary z_c in the diffusion-convection model. Basically, z_c is the characteristic distance from the Galactic plane for which the diffusive time of cosmic rays equals the convective time. Unlike H, z_c is energy dependent as $z_c \propto \sqrt{D/V}$ where V denotes the convection velocity [58, 139]. On the other hand, the re-acceleration model takes into account the possible re-acceleration of cosmic rays in the interstellar medium after they have left their sources [166]. The re-acceleration can be produced via second-order Fermi acceleration by the same magnetic inhomogeneities which are responsible for the spatial diffusion of cosmic rays in the Galaxy. In this thesis, we neglect the effects of both convection and re-acceleration which are relevant mostly at energies below a few GeVs, and consider the pure diffusion model in all our calculations.

Theoretical understandings and measurements

Because cosmic rays undergo diffusive motions in the Galaxy, their arrival directions at the Earth do not represent the direction of their sources. This makes it extremely difficult to

extract informations on the individual sources from the measurements. The measured data can only provide knowledge about the global averaged properties of the sources such as the averaged cosmic-ray source spectrum in the Galaxy. Even then, source information is entangled with those of the propagation, which is another process still not clearly understood. Thus, the determination of the source and the propagation information from the data are inter-dependent on each other and cannot be completely separated. However, as mentioned in the previous section, the secondary-to-primary ratios are largely sourced independent and their measurements can give a good estimate of cosmic-ray propagation parameters in the Galaxy.

For a power-law source spectrum $Q \propto E^{-\gamma}$ and the diffusion coefficient $D \propto E^{a}$, the equilibrium spectrum of cosmic rays in the Galaxy (solution of Eq. 4) follows a power-law form as $N_p \propto E^{-(\gamma+a)}$. Several independent measurements show that the cosmic-ray spectrum follows a power-law with index ~ -2.75 below the knee. Comparing theory and observation, we have $(\gamma + a) = 2.75$. Both γ and a cannot be measured directly. For the diffusion index a, an indirect estimate can be obtained from the measurements of secondary-to-primary ratios as indicated by Eq. (6). Measurements show that the ratio decreases as $\sim E^{-0.6}$ up to ~ 100 GeV and becomes flatter at higher energies. This seems to suggest a larger value of diffusion index at lower energies than at higher energies. In general, depending on the choice of the propagation model, the value of the diffusion index varies in the range of $a = (0.3 - 0.6)$. It may be recalled that the Kolmogorov-type of turbulence wave spectrum predicts $a = 0.33$ while the Kraichnan-type of spectrum predicts $a = 0.5$. The measured value of $a = (0.3 - 0.6)$ shows that the cosmic-ray source index may lie in the range of $\gamma = (2.05 - 2.45)$. Re-acceleration models suggest smaller values of the diffusion index $a \sim 0.33$ [175], whereas pure diffusion models favor $a \sim 0.6$ [186], which imply a source index of $\gamma \sim 2.4$ and 2.15, respectively. Both these estimated indices are softer than $\gamma = 2$, the value predicted by diffusive shock acceleration theory. The discrepancy becomes even more severe if we compare with the results of non-linear diffusive shock acceleration theory which predicts a spectrum harder than $\gamma = 2$ ([64] and references therein). But, compared to the re-acceleration model, the pure diffusion model seems closer to the theoretical predictions.

Independent constraints on the diffusion coefficient are provided by the measurement of cosmic-ray anisotropy. The diffusive motion of cosmic rays in the Galaxy provides a high level of isotropy in their distribution. But, at the same time, the global leakage of cosmic rays from the Galaxy can give rise to a small level of anisotropy. The anisotropy δ can be calculated using [51],

$$\delta = \frac{3D}{c} \frac{|\nabla N_p|}{N_p} \tag{7}$$

where N_p is given by solution of Eq. (4). Eq. (7) shows that the anisotropy $\delta \propto D \propto E^{a}$, i.e., increases with energy with a slope given by the diffusion index a. On the other hand, measurements have shown a very weak energy dependence of cosmic-ray anisotropy at the amplitude level of $(10^{-4} - 10^{-3})$ above ~ 100 GeV [33]. Though the measured data is not satisfactorily explained by the theoretical predictions, data seem to indicate a weaker

energy dependence of the diffusion coefficient (small a), thus supporting the re-acceleration model. It is worth noting that the observed anisotropy may also be related to other effects such as the non-uniform source distribution and the presence of nearby sources. Detailed studies on the topic are given in [162].

In short, it can be stated that both the propagation models can successfully explain the observed cosmic-ray data with different values of model parameters. But, the steep source index of $\gamma \sim 2.4$ required in the re-acceleration model is hard to agree with theoretical predictions. On the other hand, the diffusion model which requires a more reasonable value of the source index of $\gamma \sim 2.15$ suffers when confronted with the anisotropy data.

An independent measure of the source spectrum (independent of the propagation effects) could be obtained from the high-energy gamma-ray observations of their sources. Recent observations of several supernova remnants by the FERMI experiment seem to suggest that the high-energy gamma-rays detected from these sources could be of hadronic origin [5, 8, 9, 10]. If this is true, then the gamma-ray spectrum represents a direct measure of the primary particle spectrum. Recent TeV gamma-ray measurements made by the new generation Cherenkov telescopes such as H.E.S.S, MAGIC, and VERITAS have found that many supernova remnants show spectral indices in the range of $\gamma \sim (2.3 - 2.7)$ (see [96] and references therein). These values are much larger than the prediction of diffusive shock acceleration theory. But, it should be understood that even if the TeV gamma-rays are of hadronic origin, the observed gamma-ray spectrum may not necessarily represent the cosmic-ray source spectrum in the Galaxy. It only represents the spectrum of particles which are present inside the remnant at a certain stage of the supernova remnant evolution, while the source cosmic rays in the Galaxy is related to the integrated spectrum of particles which have escaped the remnant during the evolution. Moreover, the overall source cosmic rays injected into the Galaxy is given by the sum of the contributions from several individual remnants.

Cosmic rays measured at Earth may not carry information from all positions in the Galaxy. This is because the majority of cosmic rays reaching the Earth is produced by sources located within a distance which is comparable to the size of the Galactic halo [186]. The exact value of the halo boundary is not known. Different cosmic-ray propagation models adopt different values which fall in the range of $\sim (2 - 12)$ kpc [141, 172, 196]. The properties of cosmic rays at far away locations in the Galaxy can be provided by observations of diffuse radiation such as the radio emission, X-rays and high-energy gamma-rays. Recent measurements by the FERMI satellite show that the diffuse gamma-ray spectrum measured from different regions in the Galaxy can be explained with models which are consistent with the measured cosmic-ray spectra at Earth [4, 7]. However, there are some issues related to the distribution of cosmic rays in the Galaxy. The cosmic-ray density gradient determined from the observed gamma-ray emissivities in different regions of the Galaxy is found to be inconsistent with the theoretical predictions assuming supernova remnants or pulsars as cosmic-ray sources [7]. The discrepancy may be either due to incorrect values of halo boundaries adopted in theoretical models or due to the uncertainties associated with the source distributions which are related to poor statistics and large detection biases.

In recent years, results reported by new generation cosmic-ray and gamma-ray experiments have questioned some of the general understandings of cosmic rays. Some of the them are listed below:

(1) Balloon-borne experiments such as ATIC, CREAM, and TRACER have confirmed that the secondary-to-primary ratios becomes harder at energies above ~ 100 GeV/n [27, 149, 155]. Earlier experiments such as CRN had also indicated such a trend [178]. This is difficult to explain in the framework of conventional diffusion models assuming a single diffusion index at all energies. The data seem to indicate a change in the diffusion index at energies above ~ 100 GeV/n, but theoretically it is not clear why such a change should exist.

(2) The ATIC, CREAM, and TRACER experiments also reported that the spectra of all individual elements seem to become harder at TeV energies [40, 156, 198]. This indication is different from the general notion that the cosmic-ray spectrum follows a single power-law up to the knee. The spectral change is difficult to explain under the standard model of cosmic-ray acceleration and propagation in the Galaxy. As mentioned before, under diffusive shock acceleration theory, cosmic rays are accelerated with a single power-law at all energies.

(3) Recent measurements performed by the PAMELA satellite have found that the positron fraction increases with energy above ~ 10 GeV [15]. This result has also been confirmed by FERMI measurements [14]. The positron fraction f_{e+} is defined as the fraction of positrons (e^+) in the total leptonic component $(e^+ + e^-)$ of cosmic rays. Under standard models, positrons are assumed to be produced only as secondary products of cosmic-ray nuclear interactions in the Galaxy. Thus, the positron source spectrum follows the spectrum of their primaries as, $Q_{e^+} \propto E^{-(\gamma+a)}$. If cosmic-ray sources produce primary electrons with the same source spectrum as the primary nuclear species, we can write $Q_{e^-} \propto E^{-\gamma}$. Then, the positron fraction in the Galaxy is expected to decrease with energy as $f_{e^+} \propto E^{-a}$. This is in contradiction to the recent measurements above ~ 10 GeV.

(4) In addition, the PAMELA and the FERMI experiments along with the ground-based experiments H.E.S.S and MAGIC have measured the electron spectrum between 1 GeV and 5 TeV with much improved sensitivities over previous measurements [13, 16, 24, 26]. The spectrum above 10 GeV can be represented by a broken power-law with index $\Gamma_e \sim -3$ up to ~ 1 TeV and $\Gamma_e \sim -4$ above 1 TeV. The origin of the break or the cut-off is not clearly understood. It may be due to a cut-off in the intrinsic source spectrum or due to propagation effect.

(5) Several independent ground-based experiments such as MILAGRO, ICECUBE, TIBET III, and ARGO-YBJ have recently reported observations of localized cosmic-ray excess in certain regions of the sky [1, 2, 34, 80]. The excess is observed at energies of a few TeVs. The origin of the excess is not known. It may be due to the presence of nearby sources

or the effect of the unknown Galactic magnetic field structure focussing cosmic rays from those regions [83].

Aim and plan of the thesis

1 Cosmic-ray propagation

In the first part of this thesis, I investigate our current theoretical understandings on the origin and the propagation of cosmic rays in the light of new data provided by the new generation cosmic-ray and gamma-ray experiments. Some of the issues listed in the previous section are discussed in detail. This part is covered in Chapters $(1-4)$.

In Chapter 1, the effect of the presence of nearby supernova remnants on the observed cosmic-ray spectra is discussed, considering heavier nuclei such as boron, carbon, and oxygen. The subsequent effect on the secondary-to-primary ratio is also discussed.

In Chapter 2, a possible correlation between the observed break in the high-energy electron spectrum at $\sim$ 1 TeV and the flattening of the boron-to-carbon ratio above $\sim$ 100 GeV/n is discussed.

The study presented in Chapter 1 assumes that supernova remnants are point sources injecting cosmic rays independent of energy. Chapter 3 discusses the validity of such a widely adopted approximation for nearby cosmic-ray sources. It is expected that for very nearby sources the point source approximation may break down. Moreover, the particle escape from supernova remnants is expected to be energy dependent with the higher energy particles escaping at early stages of the supernova lifetime followed later by the lower energy ones.

Chapter 4 discusses the cosmic-ray spectral changes at TeV energies recently reported by the new generation balloon-borne experiments. It considers the effect of the nearby supernova remnants as a possible explanation for the apparent spectral changes.

2 Cosmic-ray measurements with LORA

Astrophysical models predict that if the "knee" in the cosmic-ray spectrum at $\sim 3\times10^{15}$ eV is due to the fall-off of the Galactic proton component, then a similar structure is expected at around 10^{17} eV which is due to the fall-off of the Galactic heavy components like iron. This predicted energy is very close to the energy where the "second knee" is observed which is at $\sim 3\times10^{17}$ eV. Although it is hard to define where exactly the Galactic component would end, the transition from the Galactic to extra-galactic cosmic rays is expected to occur at energies between around 10^{16} and 10^{18} eV [59, 116]. This is also the energy region we plan to measure with LORA.

Some of the cosmic rays, during their propagation through the Galaxy, may hit the Earth. Such cosmic rays can be measured either by using space-based (which include both, the satellite and the balloon experiments) or ground-based experiments. Ground-based experiments use the Earth's atmosphere as a detector medium. When high-energy cosmic

rays undergo collisions with the atoms of the atmosphere, a cascade of secondary particles comprised mostly of electrons, muons, hadrons, and photons are produced. This cascade of particles, which is generally referred to as extensive air showers, can be measured using array of detectors placed on the ground (Figure 3).

LORA (the LOfar Radboud air shower Array) is a ground-based experiment that measures cosmic rays at energies above $\sim 10^{16}$ eV. The array has been built as a part of the LOFAR "cosmic ray" key-science project and consists of 20 particle detectors distributed in the center of LOFAR (Figure 4). During the last 3 years, I have been extensively involved in building the LORA array, and in the development of the software required for the data acquisition and the data analysis of the experiment. The details about the experimental set-up and its performance are presented in the second part of this thesis which is given in Chapter 5.

The main role of LORA is to trigger LOFAR with cosmic-ray events. In addition, LORA will provide basic air shower parameters such as the position of the shower axis, the arrival direction, and the energy of the primary cosmic ray, to be used for analysis of the radio data measured with LOFAR. LOFAR, the LOw Frequency ARray, is a new kind of radio telescope that has been built in the Netherlands and its neighboring countries for astronomical observations in the low frequency range of $10 - 240$ MHz [123]. Unlike traditional radio telescopes, which consist of steerable big parabolic dishes, LOFAR uses simple dipole antennas which remain static on the ground. Being a fully digital telescope, LOFAR uses digital signal processing to point towards different directions in the sky. This unique property makes LOFAR suitable for the measurement of cosmic rays whose arrival directions are random in nature.

LOFAR is expected to measure cosmic rays with energies above $\sim 10^{16}$ eV. In the presence of the Earth's magnetic field, the charged particles contained in the air showers, especially the electrons, produce radio synchrotron emission which peaks in the frequency range sensitive to LOFAR. The radio detection technique, although started in 1965 by Jelly and his group [124], has not yet successfully emerged as an independent method of cosmic-ray detection, largely due to experimental limitations. The main objective of LOFAR is to push the technique to achieve this goal. With its significantly larger number of antennas distributed in a dense core and high sensitivity, together with its advanced digital signal processing system, LOFAR is expected to provide a better understanding of the emission mechanisms and the lateral density distribution of radio signals produced by air showers.

What LORA detects are the charged particles contained in the air showers. These are the same particles which produce the radio emissions detectable by LOFAR. The basic detection technique adopted by LORA is well established and better understood, so it can be used to test and confirm cosmic-ray measurements with LOFAR.

LORA started its first operation in February 2011 with 4 detectors. Later in June 2011, the full set-up was completed and LORA became fully operational with all its 20 detectors. During the same time, its primary aim of triggering LOFAR was implemented and it had already contributed to the first detection of cosmic rays with LOFAR in June 2011 [74]. LORA has now collected around 162 days of clean data which amounts to over 2 million

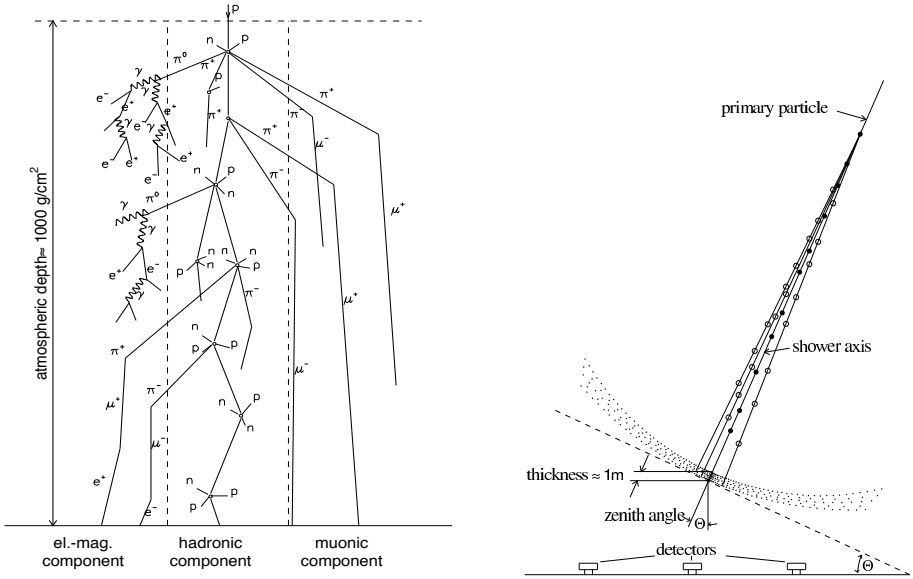

Figure 3: A schematic view illustrating the development of extensive air shower [32].

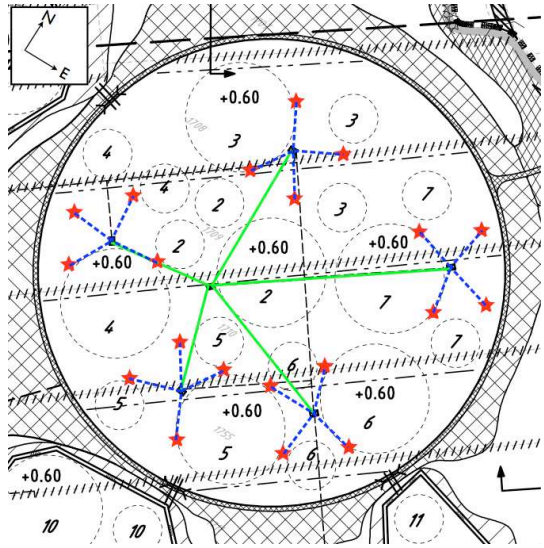

Figure 4: A schematic picture of the LORA array in the core of LOFAR. The stars represent the detector positions and the circles indicate the LOFAR antenna fields.

cosmic-ray events. In Chapter 5, we also present the first science results obtained with LORA. The main results include measurements of lateral density distribution of air showers, measurements of atmospheric attenuation coefficients, and the all-particle cosmic-ray energy spectrum.

Chapter 1

On the contribution of nearby sources to the observed cosmic-ray nuclei

Satyendra Thoudam

2008, MNRAS, 388, 335

Abstract The presence of nearby discrete cosmic-ray sources can lead to many interesting effects on the observed properties of cosmic rays. In this Chapter, we study the possible effects on the cosmic-ray primary and secondary spectra and also the subsequent effects on the secondary-to-primary ratios. For the study, we assume that cosmic rays undergo diffusive propagation in the Galaxy and we neglect the effect of convection, energy losses and reacceleration. In our model, we assume that there exists a uniform and continuous distribution of sources in the Galaxy generating a stationary cosmic-ray background at the Earth. In addition, we also consider the existence of some nearby sources which inject cosmic rays in a discrete space-time model. Assuming a constant cosmic-ray source power throughout the Galaxy, our study has found that the presence of nearby supernova remnants produces noticeable variations in the primary fluxes mainly above ~ 100 GeV/n, if cosmic rays are assumed to be released instantaneously after the supernova explosion. The variation reaches a value of $\sim 45\%$ at around 10^5 GeV/n. With respect to earlier studies, the variation in the case of the secondaries is found to be almost negligible. We also discuss the possible effects of the different particle release times from the remnants. For the particle release time of $\sim 10^5$ yr, predicted by the diffusive shock acceleration theories in supernova remnants, we have found that the presence of the nearby remnants hardly produces any significant effects on the cosmic rays at the Earth.

1.1 Introduction

Cosmic rays (CRs) below the knee region ($\sim 3 \times 10^{15}$ eV) are generally considered to be of Galactic origin. Though the nature of their sources are not exactly known, it is widely believed that the majority of them are accelerated in supernova remnant (SNR) shock waves. Such a hypothesis is mainly based on the similarity of the power supplied by a supernova explosion to the power required to maintain the CR energy density in the Galaxy ($\sim 10^{41}$ erg s^{-1}). In addition, studies using nonlinear effects produced by accelerated CRs have shown that the maximum energy of CRs that can be accelerated in SNRs is $\sim Z \times 10^{15}$ eV (where Z is the total charge of the particle) which is close to the knee [47].

It is quite expected that the presence of one or more nearby discrete sources can result in various significant effects on the observed properties of CRs. Studies concerning their contributions to the total CR electron flux can be found in earlier studies in the framework of an energy independent CR diffusive propagation model [75, 144] and also, assuming a more realistic energy dependent diffusion coefficient in the Galaxy [39, 134]. For CR nuclei, Lingenfelter (1969) studied the density variations at the Earth due to the local sources using a simple particle escape model [140] and later, Erlykin & Wolfendale (2001) carried out Monte Carlo calculations assuming SNRs to be distributed stochastically throughout the nearby Galaxy [87]. Strong & Moskalenko (2001) studied the influence of the discrete nature of SNRs on the CR proton densities in the Galaxy using their GALPROP CR propagation code [173]. In addition, some recent studies tried to stretch the importance of local sources to explain some strongly observed features of CRs like the knee and the anisotropy. For instance, Erlykin & Wolfendale (2000) claimed that the knee in the CR spectrum can be attributed to the presence of a single recent supernova (as yet unidentified) in the local region [86]. Erlykin & Wolfendale (2006) further tried to explain the rise in the anisotropy amplitude as well as the change in its phase near the knee using a single source exploded in the direction from the Sun downward of the main CR flux, which comes predominantly from the inner Galaxy [88]. Moreover, using a convection-diffusion CR propagation model, Thoudam (2006) tried to emphasize the necessity for the presence of at least one old nearby source in order to explain the observed proton flux below ~ 100 GeV/n [183]. In another recent study, Thoudam (2007) studied the effect of the nearby known SNRs on the observed CR anisotropy below the knee [184] and later on, suggested the possibility of explaining the data above 100 GeV/n by a single dominant source with properly chosen source parameters and claimed that the source may be an *undetected* old SNR with a characteristic age of $\sim 1.5 \times 10^5$ yr located at a distance of ~ 0.57 kpc from the Earth [185].

Taillet & Maurin (2003) pointed out that the majority of the CRs reaching the Earth are possibly emitted by sources located within few kpc and hence, the propagation parameters that we usually derived from the observed secondary/primary (s/p) may only give local information which may be different from other parts of the Galaxy [179]. In another work, Büsching et al. (2005) showed that even if the CR propagation parameters are assumed to be constant throughout the Galaxy, the discrete nature of the CR sources can produce much larger fluctuations of the CR primary densities than that of the secondaries, implying a

significant fluctuation in the s/p ratio [62]. In this Chapter, we shall also study the expected fluctuations on the CR primary and secondary spectra at the Earth, but by incorporating the nearby known CR sources (considered here as SNRs). Such an approach is expected to give a more detailed understanding of the CR density fluctuations and its implications as far as the position of the Earth is concerned.

We plan the Chapter as follows. In section 1.2, we give a brief description of our model. In section 1.3, we calculate the CR primary and secondary spectra from a discrete point-like source and in section 1.4, we calculate for the CRs from a continuous and stationary source distribution. In section 1.5, we study the CR density variations at the Earth due to a single nearby source and in section 1.6, we give an application to the nearby SNRs and present a comparison of the calculated CR spectra with the observed data. Finally in section 1.7, we give a brief discussion of our results and their implications.

1.2 Model description

Our model assumes that a major fraction of the CRs detected at the Earth are liberated from sources which are distributed uniformly and continuously (both in space and time) in the Galaxy. We refer to these sources as the background sources and the CRs they emit as the background CRs. In addition, we also assume that there exist some nearby discrete sources which inject CRs in a discrete space-time model and whose contributions to the total CRs are yet to be investigated. The contributions of the discrete and the background sources will be treated separately. CRs from the discrete sources will be discussed in the framework of a time dependent diffusive propagation model while those from the background sources will be treated in a steady state model.

For the background CRs, the flattened shape of our Galaxy allows us to assume their diffusion region as a cylindrical disk of infinite radius with finite half-thickness H. Such an assumption of infinite radius is valid at least for CR studies at the position of the Earth, which is at a distance of ~ 8.5 kpc from the Galactic Centre, where the effect of the Galactic radial boundary (assumed to be $\gtrsim 20$ kpc) on the CR flux is expected to be negligible. This is because a substantial fraction of the CRs reaching the Earth are liberated from sources located within an approximate distance which is of the order of H [179]. The actual value of H is not exactly known. The values estimated using different CR propagation models fall in the wide range of $(2 - 12)$ kpc [141, 172, 196]. For our calculations, we choose a value of $H = 5$ kpc. Note that choosing other reasonable values of H will not significantly change our results. We further assume that the background sources as well as the interstellar matter are distributed in a thin disk of radius R and half-thickness h. Here again, the effect of R on the CR flux is negligible as long as $R > H$. Observations have found that both the distributions of the SNRs, and those of the atomic and the molecular hydrogen extend approximately up to a radial distance of $R \sim 16$ kpc [69, 107]. Regarding the vertical distributions, detailed studies have found that most of the SNRs and the molecular hydrogen are confined within the region $\sim \pm 200$ pc from the Galactic plane [61, 176]. The distribution of atomic hydrogen also follow a similar structure but with a thin long tail extending as far

Table 1.1: Parameters of known SNRs located within a distance of 1.5 kpc from the Earth (See the references given in [184]).

SNR	Distance (kpc)	Age (yr)
G65.3+5.7	1.0	14000
G73.9+0.9	1.3	10000
Cygnus Loop	0.4	14000
HB21	0.8	19000
G114.3+0.3	0.7	41000
CTA1	1.4	24500
HB9	1.0	7700
S147	0.8	4600
Vela	0.3	11000
G299.2-2.9	0.5	5000
SN185	0.95	1800
Monogem	0.3	86000
Geminga	0.15	340000

as $\sim$ 700 pc from the plane [81]. Therefore, in our calculations we consider an infinitely thin disk approximation for both the background sources and the matter distributions. Such an approximation can also be found in some earlier works [166, 195].

For the nearby discrete sources, we consider only known SNRs located within a distance of 1.5 kpc from the Earth. They are listed in Table 1 along with their estimated distances and ages. They are the sources which are expected to produce significant temporal fluctuations in the CR densities at the Earth [183]. The diffusion region for CRs from these sources is assumed to be of infinite dimensions. This assumption is based on the fact that CRs from nearby sources are not much affected by the presence of the Galactic boundaries (both in the radial and the vertical directions) due to their much shorter propagation time to the Earth compared to the escape timescales from the Galaxy [185].

One more assumption that we make in our model is that since the Earth is reported to be only $\sim$ 15 pc away from the Galactic median plane [73], we will simply consider that the Earth is located on the median plane itself in all our calculations.

1.3 CRs from a discrete point source

1.3.1 CR primaries

In the diffusion model, neglecting convection, energy losses and particle re-acceleration processes, the propagation of CR primaries in the Galaxy can be represented by the equa-

tion,

$$\nabla \cdot (D_p \nabla N_p) - 2hnv_p\sigma_p\delta(z)N_p + \mathbb{Q}_p = \frac{\partial N_p}{\partial t} \tag{1.1}$$

where the subscript p denotes the primary nuclei, $N_p(\mathbf{r}, E, t)$ is the differential number density at a distance $\mathbf{r}$ at time t, E is the kinetic energy per nucleon of the nuclei, $D_p(E)$ is the diffusion coefficient and n is the target density both of which are assumed to be constant in the Galaxy, σ_p is the primary spallation cross-section assumed to be independent of energy, v_p is the primary velocity and $\mathbb{Q}_p(\mathbf{r}, E, t) = Q_p(E)\delta(\mathbf{r})\delta(t - t_0)$ is the particle production rate from the source. In Eq. (1.1), we neglect the yield of the primaries from the fragmentation of heavier nuclei.

We are also interested in the study of the secondary nuclei which are produced by the nuclear interactions of the primaries with the interstellar medium (ISM). Since the energy per nucleon is an almost conserved quantity in the fragmentation process, we will be dealing with the energy per nucleon in all our relations rather than the total kinetic energy of the nuclei. Using Green's function technique and performing proper Fourier and Laplace transforms, the exact unbounded solution of Eq. (1.1) for a source having particle release time t_0 is obtained as (see Appendix 1.A),

$$N_p(\mathbf{r}, E, t) = \frac{Q_p(E)e^{-\left[\frac{r^2}{4D_p(t-t_0)}\right]}}{8\pi D_p^{3/2}(t - t_0)} \left\{ \frac{e^{-q^2/[4(t-t_0)]}}{\sqrt{\pi(t - t_0}} - be^{bq+b^2(t-t_0)} \times \mathrm{erfc}\left(b\sqrt{t - t_0} + \frac{q}{2\sqrt{t - t_0}}\right) \right\} \tag{1.2}$$

where $q = |z|/\sqrt{D_p}$, $b = 2hnc\sigma_p/2\sqrt{D_p}$ and we have taken $v_p \approx c$, the velocity of light since we are dealing with high energy particles. The particle flux can then be calculated using $I_p(\mathbf{r}, E, t) \approx (c/4\pi)N_p(\mathbf{r}, E, t)$. It should be noted that we assume the source spectrum to be $Q_p(E) = A_p q_p(T)$ with $q_p(T)$ given by

$$q_p(T) = k(T^2 + 2Tm_p)^{-(\Gamma+1)/2}(T + m_p) \tag{1.3}$$

where $T = A_p E$ represents the total kinetic energy of the nuclei, A_p is the mass number, m_p is the mass energy, Γ is the spectral index and k is the normalization constant.

1.3.2 CR secondaries

The transport of CR secondaries in the Galaxy also follow an equation similar to that of the primaries given above as,

$$\nabla \cdot (D_s \nabla N_s) - 2hnv_s\sigma_s\delta(z)N_s + \mathbb{Q}_s = \frac{\partial N_s}{\partial t} \tag{1.4}$$

where the subscript s represents the secondary nuclei and all the quantities have the similar definitions as in Eq. (1.1). In our model, we assume that the secondaries are the results

of fragmentation of one or more heavier primaries and we neglect the production of secondaries at the source. For secondaries originating from a single type of primary, we can write the source term in Eq. (1.4) as,

$$\mathbb{Q}_s(\mathbf{r}, E, t) = 2hnc\delta(z)\int_E^\infty \frac{d}{dE'}\sigma_{ps}(E, E')N_p(\mathbf{r}, E', t)dE' \tag{1.5}$$

We can approximate the differential production cross-section $d\sigma_{ps}(E, E')/dE'$ of an s-type nuclei of energy per nucleon E by the fragmentation of a p-type nuclei of energy per nucleon E' by a delta function as,

$$\frac{d}{dE'}\sigma_{ps}(E, E') = \sigma_{ps}\delta(E' - E) \tag{1.6}$$

where σ_{ps} denotes the total fragmentation cross-section of p to s. This simplifies Eq. (1.5) as,

$$\mathbb{Q}_s(\mathbf{r}, E, t) = 2hnc\sigma_{ps}\delta(z)N_p(\mathbf{r}, E, t) \tag{1.7}$$

Note that here $N_p(\mathbf{r}, E, t)$ is given by Eq. (1.2). For a secondary source term given by Eq. (1.7) we can easily obtain the solution of Eq. (1.4) at the spatial location $\mathbf{r} = 0$ as,

$$\begin{aligned} N_s(E, t) = 2hnc\sigma_{ps}\int_0^t dt_0 \int dV \exp\left[-\frac{(\mathbf{r} - \mathbf{r}')^2}{4D_s(t - t_0)}\right] \exp\left[\frac{4h^2n^2c^2\sigma_s^2(t - t_0)}{4D_s}\right] \\ \times \left[\frac{1}{8\pi^{3/2}\left[D_s(t - t_0)\right]^{3/2}} - \frac{2hnc\sigma_s}{16D_s^2(t - t_0)}\right] \mathrm{erfc}\left[\frac{2hnc\sigma_s\sqrt{t - t_0}}{2\sqrt{D_s}}\right] \\ \times N_p(\mathbf{r}', E, t)\delta(z') \end{aligned} \tag{1.8}$$

where $\mathbf{r}'$ denotes the position of the primaries with respect to the point source which in cylindrical coordinates yield an integral over the volume element as,

$$\int dV = \int_0^\infty r'dr' \int_0^{2\pi} d\phi' \int_{-\infty}^\infty dz' \tag{1.9}$$

Eq. (1.8) gives the CR secondary density at $\mathbf{r} = 0$, which is considered here as the position of the observer, due to a single type of primary emitted from a point source located at a distance $\mathbf{r}$ from the observer. If a particular secondary species is produced as the result of fragmentations of more than one type of heavier primaries, the total number of secondaries produced is obtained by simply adding the contributions from the different primary species as,

$$N_s^{Tot} = \sum_j N_s^j \tag{1.10}$$

where j denotes the primary species.

1.4 CRs generated by the background sources

1.4.1 CR primaries

CRs from the background sources are assumed to follow a steady state propagation equation in the Galaxy as given below,

$$\nabla \cdot (D_p \nabla N_p) - 2hnv_p\sigma_p\delta(z)N_p = -S_p \tag{1.11}$$

where $S_p(\mathbf{r}, E)$ represents the source term. For the presence of a Galactic vertical boundary at $z = \pm H$, the solution of Eq. (1.11) for a uniform source distribution $S_p(\mathbf{r}, E) = \Re Q_p(E)\delta(z)$ extended up to a radial distance R in the Galactic plane is given by (see Appendix 1.B),

$$N_p(z, E) = \frac{R\Re Q_p(E)}{2D_p} \int_0^\infty \frac{\sinh[K(H-z)]}{\sinh(KH)\left[K\coth(KH) + \frac{2hnc\sigma_p}{2D_p}\right]} \times \mathrm{J}_1(KR)dK \tag{1.12}$$

where J_1 is the Bessel function of order 1 and $\Re = 25$ Myr^{-1} kpc^{-2} denotes the supernova explosion rate in the Galaxy [106]. As already mentioned in section 1.2, a major fraction of the CRs reaching the Earth are liberated by sources located within a distance which is of the order of the vertical height $H = 5$ kpc (see [179]). Therefore, considering the fact that the Earth is located at a distance of ~ 8.5 kpc away from the center of the Galaxy and that the sources are distributed up to a radial distance of $R \sim 16$ kpc, Eq. (1.12) can be used to obtain the CR density at the Earth by setting $z = 0$.

1.4.2 CR secondaries

The density of CR secondaries which are produced by the fragmentation of the heavier primaries originated from a stationary source distribution can be obtained similar to that of the primaries as,

$$N_s(z, E) = 2hnc\sigma_{ps}N_p(z, E)\frac{R}{2D_s} \int_0^\infty \frac{\sinh[K(H-z)]}{\sinh(KH)\left[K\coth(KH) + \frac{2hnc\sigma_s}{2D_s}\right]} \times \mathrm{J}_1(KR)dK \tag{1.13}$$

where we have taken the secondary source term as $S_s(\mathbf{r}, E) = 2hnc\sigma_{ps}\delta(z)N_p(\mathbf{r}, E)$. Taking $z = 0$, Eq. (1.13) gives the secondary densities at the Earth. Eq. (1.13) shows that for very large D_s, the secondary to primary ratio for a stationary source distribution follows,

$$\frac{N_s}{N_p} \propto \frac{1}{D_s} \tag{1.14}$$

The above relation shows that if CRs are liberated by stationary sources which are distributed uniformly, the s/p can be used to estimate the CR diffusion coefficient in the

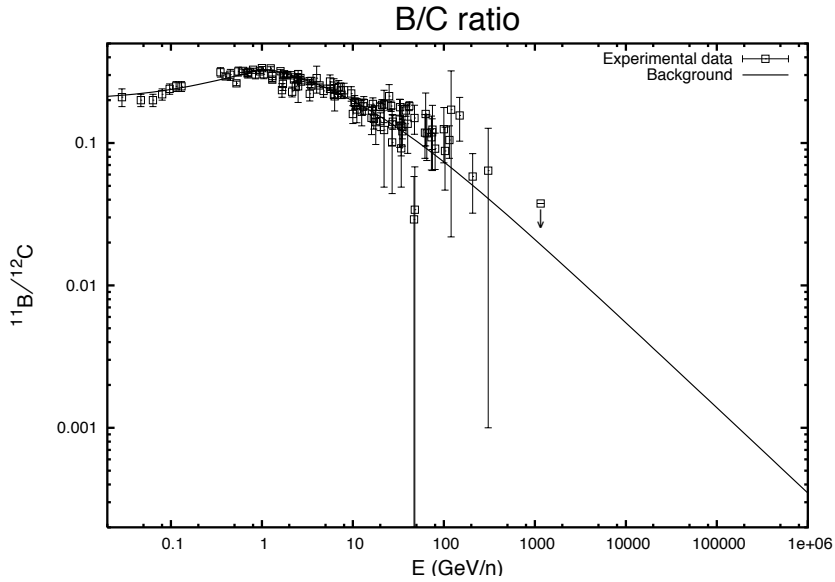

Figure 1.1: B/C ratio at the Earth due to the background CRs (solid line). Model parameters: Oxygen/carbon source abundance ratio $\mathrm{O/C} = 1.4$ and $\Phi = 500$ MV. Experimental data are taken from [155, 178] and the compilations of different experiments given in [169].

Galaxy. However, this approach may fail in cases where the influence of nearby discrete sources is significant. It is because the presence of strong nearby sources can significantly affect the CR fluxes (mainly the primaries) which can subsequently affect the s/p ratio [62]. How far the measured ratio will deviate from Eq. (1.14) actually depends on the ages and distances of the nearby sources. In the next section, we will investigate the variations that one can expect in the CR densities due to the presence of a single nearby source.

1.5 CR density variations due to a single nearby source

One very important parameter in the study of CR propagation in the Galaxy is the CR diffusion coefficient D. The diffusion of CRs is generally considered to be due to scattering either by magnetic field irregularities or by self excited Alfvén and hydromagnetic waves. Because of the possible spatial variations in the scattering processes, the value of D may be different at different locations in the Galaxy. However, in the present work we make a simple approximation that D remains constant throughout the Galaxy. As already discussed in the last section, the diffusion coefficient can be determined using the s/p ratio under the steady state model. Though the value thus obtained may not represent the true value because

of the presence of nearby discrete sources, to begin with, we assume that

$$\begin{aligned} D_i(E_i) &= D_0 \left(\frac{E_0}{E_i}\right)^{0.6} \quad ; \quad (E_i < E_0) \\ &= D_0 \left(\frac{E_i}{E_0}\right)^{0.6} \quad ; \quad (E_i > E_0) \end{aligned} \tag{1.15}$$

where E_i denotes the kinetic energy per nucleon of a particular nuclear species denoted by the subscript i and the values of D_0 and E_0 are chosen so that Eq. (1.15) fits the observed boron/carbon (B/C) ratio at 1 GeV/n (see Figure 1.1). We obtain $D_0 = 2.9 \times 10^{28}$ cm^{2}s^{-1} and the particle rigidity (corresponding to energy E_0) with charge Z_i and mass number A_i as $\rho_0 = A_i E_0/Z_i = 3$ GV. We assume that the boron secondaries (^{11}B) are produced by the nuclear interactions of the ^{12}C and ^{16}O progenitors with the ISM. The values for the nuclear fragmentation cross-sections ($\sigma_p, \sigma_s, \sigma_{ps}$) used in the present work are taken from [194, 195] and are listed in Table 1.2. We assume the ISM target density which consists mainly of hydrogen atoms to be $n = 1$ cm^{-3}, and we take into account the solar modulation effect using the force field approximation with modulation parameter $\Phi = 500$ MV [101]. Note that the necessity for the break in the diffusion coefficient at E_0 to reproduce the peak in the observed data somewhere around 1 GeV/n is consistent with the earlier studies based on the diffusive and leaky box propagation models. It is also worth mentioning that in the case of re-acceleration models, the peak can be explained using a single power-law diffusion coefficient without assuming any break in energy (see e.g., [166] and references therein). However, the observed decrease of the secondary abundances with energy above about 1 GeV/n suggests that re-acceleration in the ISM cannot be regarded as the dominant process for particles with energies $\gtrsim 1$ GeV/n [109]. Therefore, by neglecting particle re-acceleration as well as other possible low energy effects like convection and energy losses, we assume that Eq. (1.1) properly describes the propagation of CRs in the Galaxy at least for energies greater than ~ 1 GeV/n.

Figure 1.2 (top) shows the expected variations of ^{12}C densities at the Earth due to the presence of a nearby discrete source. We choose the distance to the source as 0.2 kpc and the source spectral index as $\Gamma = 2.25$. The density variations are obtained from the ratio N^{ds}/N^{bg} where N^{ds} and N^{bg} denote the densities due to the discrete (given by Eq. 1.2) and the background (Eq. 1.12) sources respectively. In Figure 1.2 (top), the curves from right to left represent for energies $(10 - 10^5)$ GeV/n. We can see that higher energy particles can produce variations of much larger amplitudes than the lower energy ones. This can be understood from Figure 1.2 (bottom) where we have plotted only the maximum density variations (represented by the solid squares) at different energies, i.e. the peak values for each of the curves shown in Figure 1.2 (top). Neglecting particle losses due to nuclear fragmentations, the maximum density of particles of energy E due to a point source located at a distance r can be found at an age $t_{max}(E) = r^2/6D_p(E)$ and is given by $N^{ds(max)}(E) \propto Q_p(E)$. The background CRs as given by Eq. (1.12) follows $N^{bg}(E) \propto Q_p(E)/D_p(E)$. Therefore, the maximum deviation that a discrete source can produce can

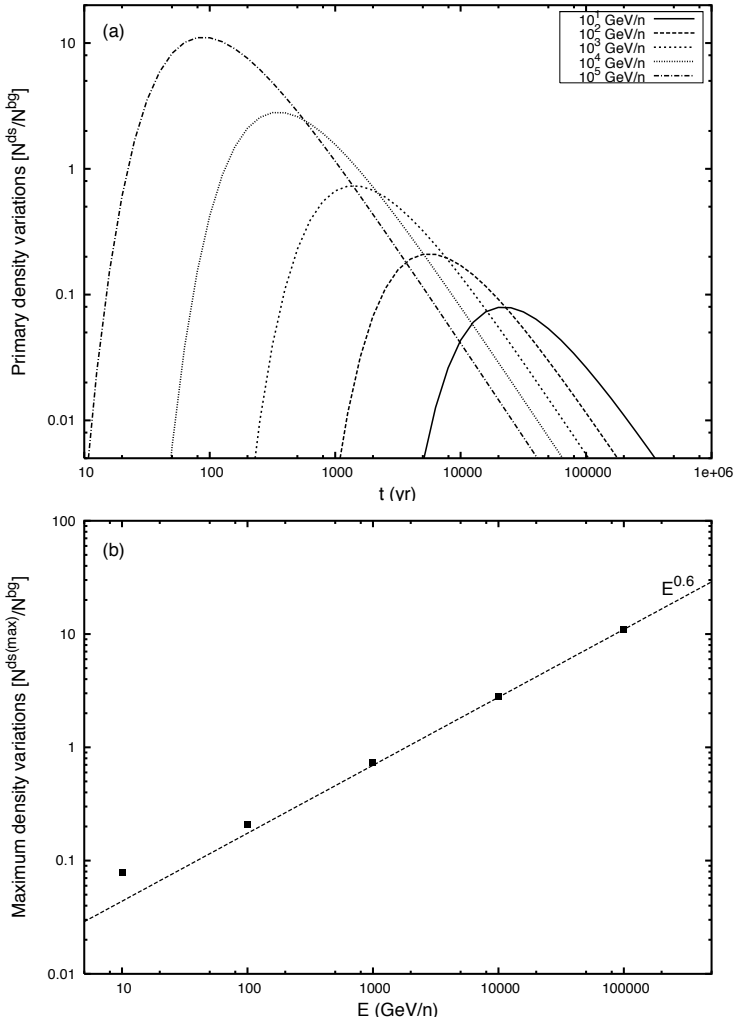

Figure 1.2: Top panel: ^{12}C temporal density variations expected at the Earth for energies $(10 - 10^5)$ GeV/n due to the presence of a nearby discrete source. For the calculation, we assume the source distance $r = 0.2$ kpc, $t_0 = 0$, $\Gamma = 2.25$, $\Re = 25$ Myr^{-1} kpc^{-2} and $\Phi = 500$ MV. The variations are calculated from the ratio N^{ds}/N^{bg}, where N^{ds} and N^{bg} denote the CR densities due to the discrete and the background sources respectively. Bottom panel: Maximum density variations (solid squares) expected at different energies, i.e. the peak values for the curves shown in the left panel. The dashed straight line in the figure corresponds to $E^{0.6}$ which shows that the maximum density variation increases with energy with a slope close to the diffusion coefficient index. $N^{ds(max)}$ denotes the maximum density the source can produce at the Earth (see text for details).

Table 1.2: Fragmentation cross-sections used in our calculations (taken from [194, 195]). The subscripts C, O & B denote the ^{12}C, ^{16}O & ^{11}B nuclei respectively and CB & OB represent the ^{12}C$\rightarrow^{11}$B & ^{16}O$\rightarrow^{11}$B processes respectively.

Cross-section	Value (mbarn)
σ_C	250
σ_O	308
σ_B	232
σ_{CB}	76.8
σ_{OB}	38.5

be obtained as,

$$\frac{N^{ds(max)}}{N^{bg}} \propto D_p(E) \tag{1.16}$$

For reference, we have also drawn a straight line ($\propto E^{0.6}$) in Figure 1.2 (bottom) which shows that the maximum density variation increases with energy with a slope equal to the index of the CR diffusion coefficient. The deviation from the straight line at lower energies is due to the increasing importance of the nuclear fragmentations compared to the diffusion processes at these energies. Therefore, if a nearby source is present in the local ISM, we should expect larger density variations for particles which diffuse faster in the Galaxy. However in actual practice, since the observations are made at a particular time and location, the actual variation at an energy E depends on the age(s) and distance(s) of the nearby source(s).

1.6 Application to the nearby SNRs

In this section, we will investigate the possible effects of the presence of nearby SNRs on the observed primary and secondary spectra and also, the subsequent effects on the s/p ratios. For the s/p ratio study, we choose the B/C ratio as an example since it is found to be the most well-measured ratio among all the available s/p ratios.

In our study, we consider only the ^{12}C and ^{16}O primaries since boron secondaries are found to be predominantly produced by the nuclear interactions of these two species with the ISM. They contribute roughly 50% and 25% respectively to the overall boron produced [194]. The calculated spectra (total as well as background) for the CR primaries and secondaries are shown in Figures 1.3 & 1.4 respectively along with the experimental data. The total spectra represented by the solid lines in the figures correspond to the total CR densities which are given by,

$$N_C = N_C^{bg} + \sum_i N_C^{ds_i} \tag{1.17}$$

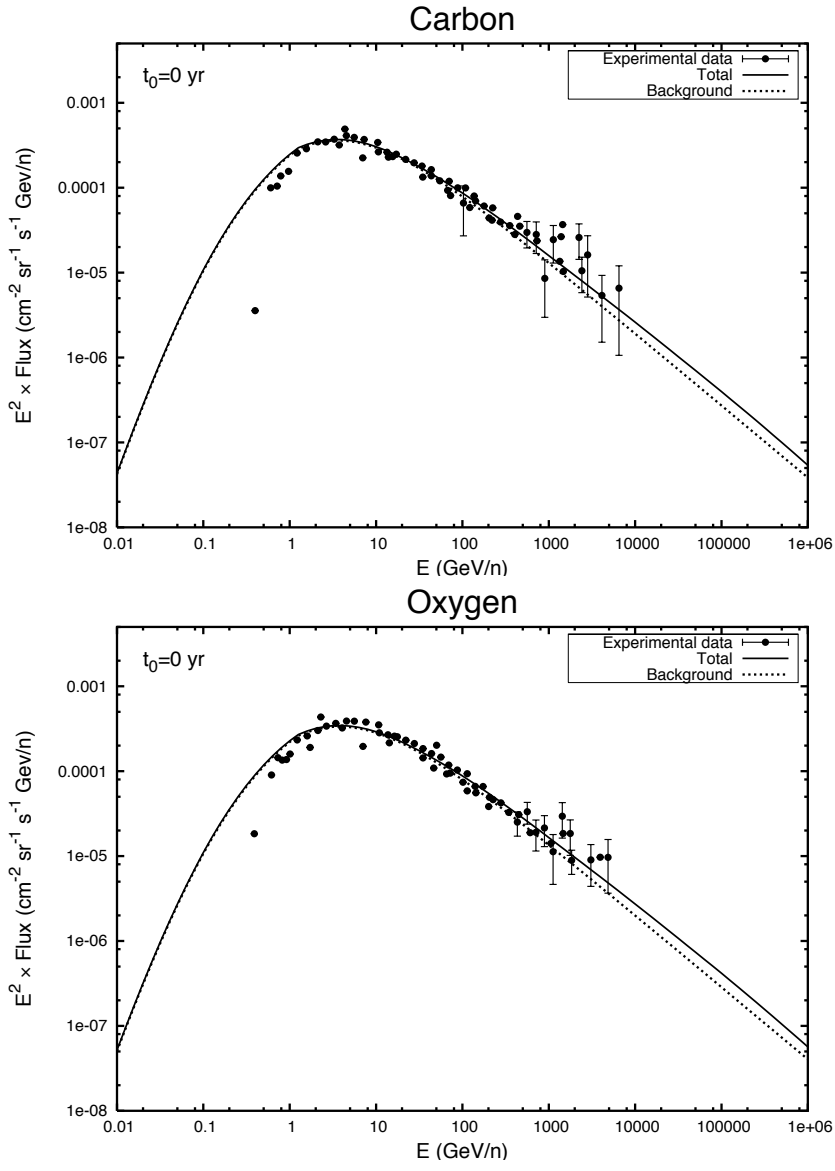

Figure 1.3: Top: Calculated ^{12}C spectra normalized to the observed data at 10 GeV/n. Bottom: ^{16}O spectra calculated for the O/C source abundance ratio of 1.4. Other model parameters: $t_0 = 0, \Gamma = 2.25, \Re = 25$ Myr^{-1} kpc^{-2}, $\Phi = 500$ MV. The dotted lines represent the background CRs and the solid lines the total flux which also include the contributions of the nearby SNRs listed in Table 1.1. Data points are taken from the results of different experiments given in [200].

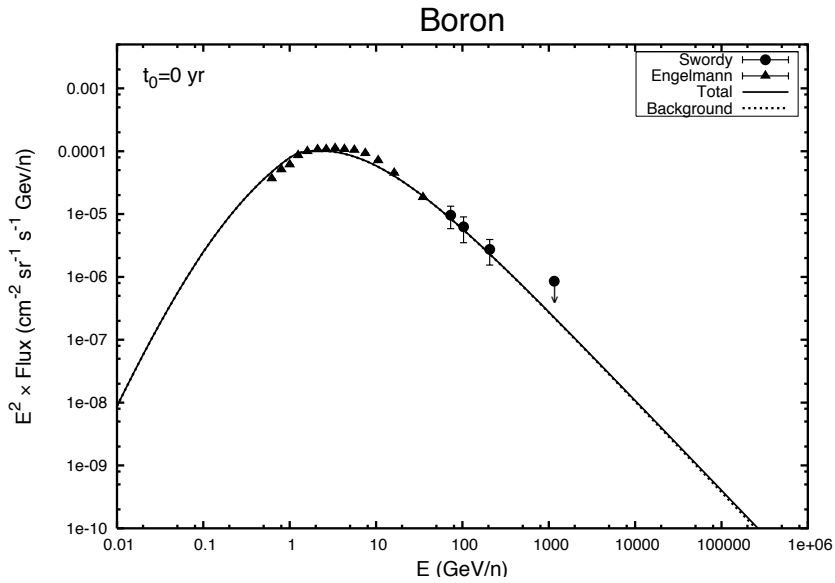

Figure 1.4: ^{11}B secondary spectra at the Earth calculated using the ^{12}C and ^{16}O spectra shown in Figure 3. The background flux (dotted line) almost overlap with the total flux (solid line) since the total contribution of the nearby SNRs is almost neglible. Solar modulation parameter $\Phi = 500$ MV. The data are taken from [85, 178].

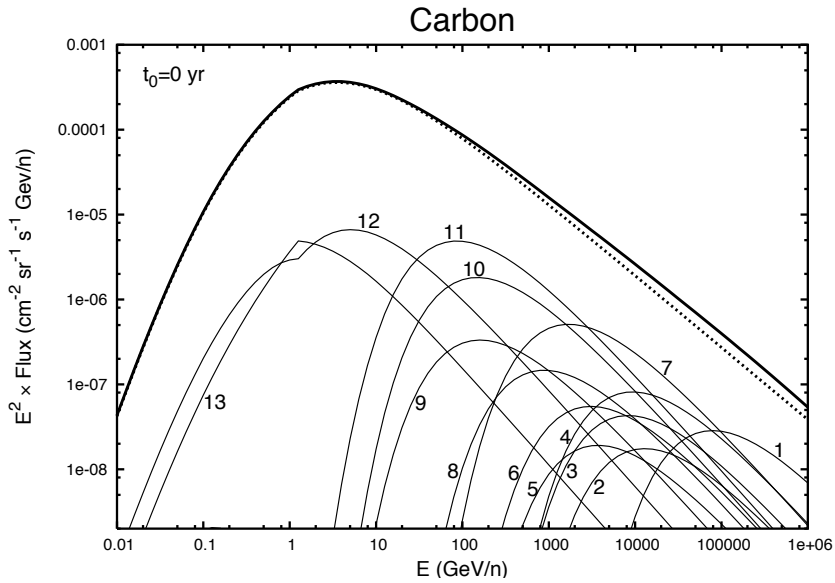

Figure 1.5: Same as the ^{12}C spectra shown in Figure 1.3 (top), but now showing the contributions from the individual SNRs. Dotted line: Background spectra. Thick solid line: Total spectra. The thin solid lines labelled as $(1-13)$ represent the contributions from the individual SNRs listed in Table 1: $1-$ SN185, $2-$ G73.9+0.9, $3-$ HB9, $4-$ S147, $5-$ CTA1, $6-$ G65.3+5.7, $7-$ G299.2-2.9, $8-$ HB21, $9-$ G114.3+0.3, $10-$ Cygnus Loop, $11-$ Vela, $12-$ Monogem and $13-$ Geminga.

$$N_O = N_O^{bg} + \sum_i N_O^{ds_i} \tag{1.18}$$

$$N_B = N_{CB}^{bg} + N_{OB}^{bg} + \sum_i N_{CB}^{ds_i} + \sum_i N_{OB}^{ds_i} \tag{1.19}$$

where the subscripts C, O and B denote the ^{12}C, ^{16}O and ^{11}B nuclei respectively, the superscripts bg and ds denote the background (represented by the dotted lines in the figures) and the discrete components respectively, and the summations are over the discrete sources i listed in Table 1.1. The subscripts CB and OB represent the ^{12}C$\rightarrow^{11}$B and ^{16}O$\rightarrow^{11}$B processes respectively. We adopt a particle release time of $t_0 = 0$ for the discrete sources. The source spectral index is taken as $\Gamma = 2.25$ and the value of the source normalization constant k is chosen such that the resulting total ^{12}C spectrum is normalized to the observed spectrum at 10 GeV/n for the supernova explosion rate of $\Re = 25$ Myr^{-1} kpc^{-2} in the Galaxy. This is shown in Figure 1.3 (top). The ^{16}O spectra calculated using the source abundance ratio of O/C $= 1.4$ is shown in Figure 1.3 (bottom). Note that Engelmann et al. 1990 had used a source abundance ratio of 1.24 to reproduce the observed C and O abundances using the simple leaky box CR propagation model [85]. The experimental data in Figure 1.3 are taken from the compilation of different experiments given in [200]. The secondary boron spectrum, calculated using the ^{12}C and ^{16}O primary spectra shown in Figure 1.3, is found to explain the observed boron data quite well. This is shown in Figure 1.4 where the experimental data are taken from [85, 178].

For the primaries, one can notice from Figure 1.3 that the inclusion of the nearby SNRs in the study produces noticeable deviations from the background flux for energies above ~ 100 GeV/n. For instance, the deviation in the case of ^{12}C reaches a value of $\sim 45\%$ at energies around 10^5 GeV/n. But, from Figure 4 we can see that the deviation in the case of ^{11}B which is considered here as a purely secondary particle is almost negligible. The results for the secondaries obtained in this work agree quite well with the earlier findings given in [62], but some major differences can be seen in the case of the primaries. They found a typical primary amplitude variations of $\sim 20\%$ at almost all the energies whereas we find almost no variations up to ~ 100 GeV/n and beyond that we see a slow increase reaching a value of $\sim 45\%$ at $\sim 10^5$ GeV/n. This can be clearly understood if one examines Figure 1.5 in detail where we have plotted the individual components of the overall ^{12}C spectrum previously shown in Figure 1.3 (top). The contributions from the individual SNRs are labelled as $1-13$ (see the figure caption for details). It can be seen that among the SNRs, only Monogem and Geminga give the highest contribution below ~ 100 GeV/n while the rest of the SNRs contribute mostly above $\gtrsim 100$ GeV/n. Since the CR flux from a point source depends strongly on the age and distance of the source, the low energy CRs from the nearby SNRs have not yet reached us effectively except those coming from the Monogem and Geminga SNRs. But still, the maximum contributions of Monogem and Geminga below ~ 100 GeV/n are found to be approximately two orders of magnitude less than the overall flux. Above $\gtrsim 100$ GeV/n, the major contributors are Vela, G299.2-2.9 and SN185, each one of them contributing around 10% of the total flux at different energy regions. Adding the contributions of the other SNRs also, the total contribution from the nearby known SNRs

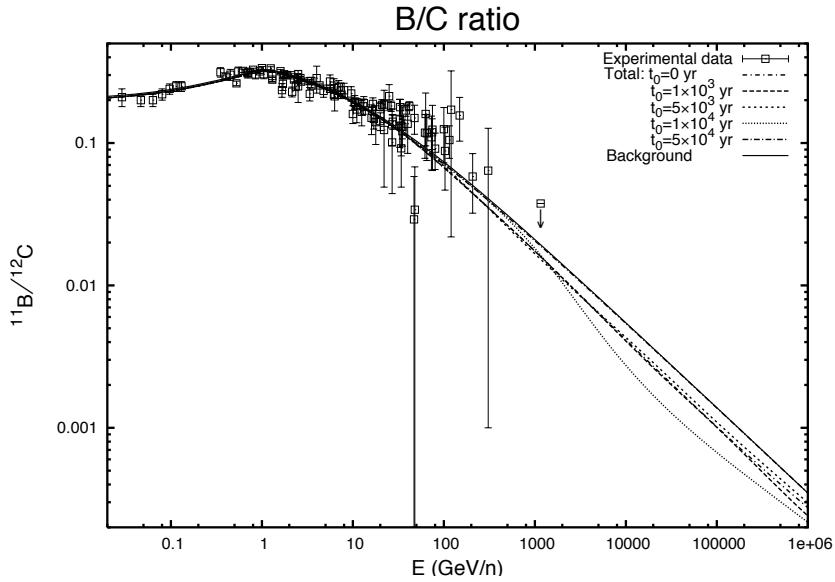

Figure 1.6: Expected B/C ratios at the Earth in the presence of the nearby SNRs listed in Table 1, calculated for different particle injection times $t_0 = (0 - 5 \times 10^4)$ yr as indicated in the key box. Experimental data are the same as in Figure 1. For reference, we have also shown the B/C ratio arising purely from the CR background (solid line). Model parameters: O/C $= 1.4, \Gamma = 2.25, \Re = 25$ Myr^{-1} kpc^{-2} and $\Phi = 500$ MV.

comes to $\sim 31\%$ of the overall CR flux which corresponds to $\sim 45\%$ deviation from the background level at energies $\sim (10^4 - 10^6)$ GeV/n.

The deviation in the ^{12}C primary spectra is expected to give a direct implication on the total B/C ratio. This is shown in Figure 1.6 where we have plotted the ratios (N_B/N_C) expected in the presence of the nearby SNRs. For reference, we have also plotted the ratio expected purely from the CR background (solid line). The experimental data are taken from [155, 178] and the compilations of different experiments given in [169]. Strictly speaking, it is not the age t alone which determines the contribution of a discrete source but the propagation time $\Delta_t = t - t_0$ of the particles after they are released from the source. But, the value of t_0 is not exactly known. It may be even different for different sources though we assume the same value for all the sources in the present work. So, in Figure 1.6 we have considered various particle release times i.e. $t_0 = (0, 10^3, 5\times10^3, 10^4$ & $5\times10^4)$ yr. Below ~ 100 GeV, it can be seen that at all the t_0's the ratios show almost zero deviations from the background ratio. Any deviation, if existent, are seen at energies $\gtrsim 100$ GeV. At $t_0 < 10^4$ yr, we see deviations of magnitude $\sim (16 - 26)\%$ in the energy range of $\sim (10^3 - 10^6)$ GeV/n. At $t_0 = 10^4$ yr, the ratio shows the maximum deviation reaching a value of $\sim 52\%$ at $\sim 6 \times 10^4$ GeV/n and for $t_0 > 10^4$ yr, say at $t_0 = 5 \times 10^4$ yr, the effect of the nearby

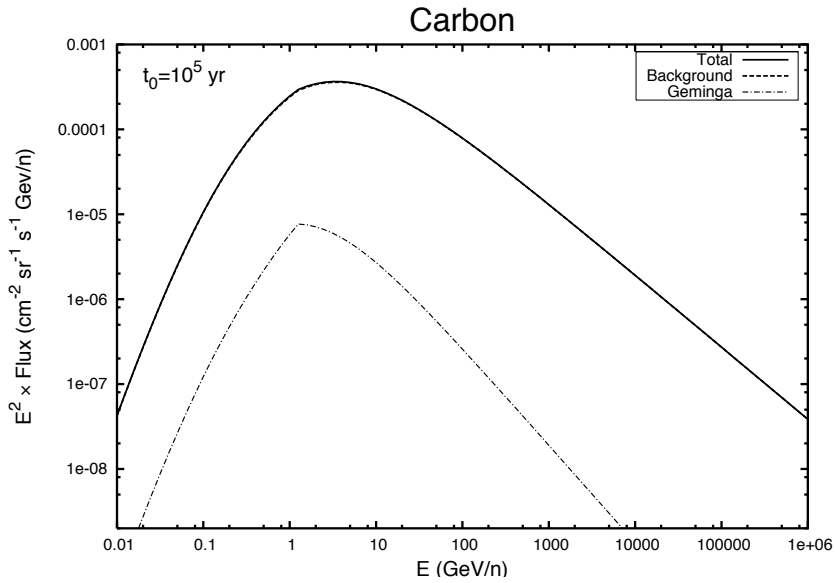

Figure 1.7: Same as Figure 1.5, but calculated for $t_0 = 10^5$ yr. Among all the SNRs listed in Table 1.1, only Geminga with an estimated age of $\sim 3.4 \times 10^5$ yr have released CRs in the ISM. Dot-dashed line: Geminga. Solid line: Total flux. Thick-dashed line: Background flux (not clearly visible because it almost overlap with the total flux).

SNRs becomes negligible producing almost zero deviation from the background ratio. It is worth mentioning at this point that detailed studies based on the diffusive shock acceleration in SNRs suggest that the highest energy particles start leaving the source region already at the beginning of the Sedov phase [47], but the major fraction of the accelerated CRs remain confined for almost around 10^5 yr for a typical interstellar hydrogen atom density of $n = 1$ cm^{-3}. We will come to this point later again in the next section while discussing about the implications of the results obtained in this work. Just for the sake of completeness, we have plotted the ^{12}C spectrum for $t_0 = 10^5$ yr in Figure 1.7. Here, except Geminga (being an old SNR with age $\sim 3.4 \times 10^5$ yr), all the other nearby SNRs have not yet released CRs into the local ISM, thereby, leading to a negligible effect at the Earth.

1.7 Discussions and conclusions

We have studied the effect of the presence of nearby SNRs on the CR primary and secondary spectra at the Earth. We see strong variations in the primary spectra and almost no variation in the case of the secondaries. The results for the primaries obtained here are quite different from those obtained from the simulation studies given in [62, 87]. We see variations mostly above ~ 100 GeV/n whereas they showed significant fluctuations at all the energies. In fact, their results represent the density fluctuations that one can expect at any arbitrary location in the Galaxy due to the random nature of supernova explosions both in space and time. But, as far as the position of the Earth is concerned, the actual variations can be determined only when one incorporates the nearby sources in the study. We, therefore, include the nearby known SNRs in our analysis and found that the primary variations obtained at the Earth show considerable differences from those predicted using the Monte Carlo simulations.

Below $\sim$ 100 GeV/n, we have found that the effect of the nearby SNRs on the B/C ratio is negligible (see Figure 1.6). This implies that we can safely rely on the observed ratio to determine the CR diffusion coefficient in the Galaxy particularly below $\sim$ 100 GeV/n. Above this energy the observed data will not give a reliable information about the propagation parameter because of the significant contaminations of the background CRs by those coming from the nearby SNRs. One should note that the primary CRs observed at the Earth are liberated from sources located within a short distance which is of the order of the vertical halo height H [179]. This can also be understood from Fig. 1.8 where we have plotted the fraction of ^{12}C primaries at the Earth originated within a radial distance r for energies $(10 - 10^4)$ GeV/n. The calculations are performed for $H = 5$ kpc. We can see from the figure that for energies less than 100 GeV/n, 50% (70%) of the total CRs are emitted within a distance of $\sim$ 3 kpc (5 kpc). This shows that even though the B/C ratio below ~ 100 GeV/n can give reliable information about the diffusion coefficient, the small Galactic region scanned by the CRs reaching the Earth allows them to carry information only for a small fraction of the whole Galaxy (see also [179]).

We have also studied the effect of different particle release times ($t_0 = 0 - 10^5$ yr) from the SNRs on the B/C ratio. At $t_0 < 10^4$ yr, we have found a deviation of $\sim (16 - 26)\%$ from the background ratio for energies $\sim (10^3 - 10^6)$ GeV/n and at $t_0 = 10^4$ yr

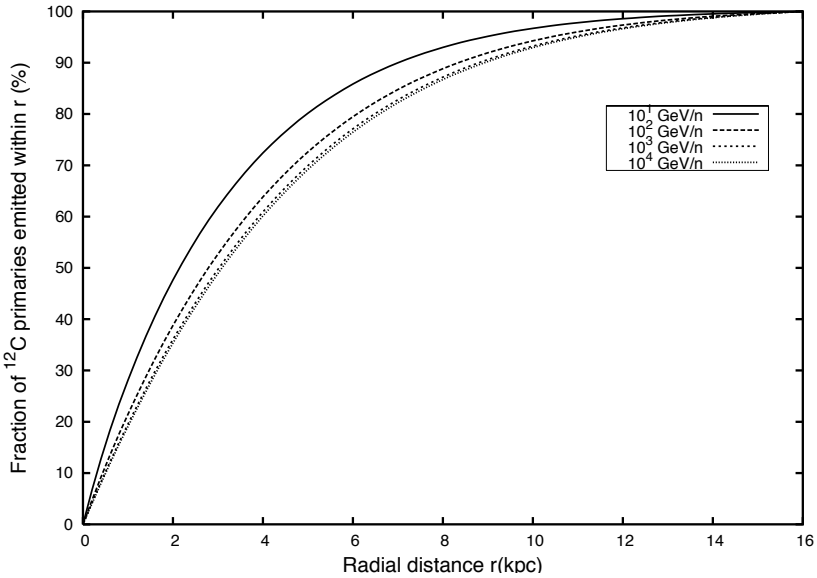

Figure 1.8: Fraction of ^{12}C primaries emitted within the radial distance r from the Earth for various energies $(10 - 10^4)$ GeV/n. We assume the vertical halo height $H = 5$ kpc.

we see the maximum deviation reaching a value of $\sim 52\%$ at around 6×10^4 GeV/n. For $t_0 > 10^4$ yr, say at $t_0 = 5 \times 10^4$ yr, the effect of the nearby SNRs becomes almost negligible, thereby, making the observed B/C data a reliable quantity for determining the CR propagation parameters at all energies. This conclusion is, in fact, supported by the predictions of the diffusive shock acceleration theories in SNRs which show that a major fraction of the accelerated CRs remain confined in SNRs for almost around 10^5 yr [47]. For such a confinement time, we see that except Geminga all the other local SNRs listed in Table 1.1 look quite young and might not have liberated CR particles in the local ISM. This can be understood from Figure 1.7 where we have plotted the ^{12}C spectra for $t_0 = 10^5$ yr.

Therefore, we can conclude that if one accepts the theoretical view of CRs confinement in SNRs for up to $\sim 10^5$ yr, the effect of the nearby SNRs on the observed CRs is expected to be quite negligible. Then, one can expect the observed s/p ratio to give a good estimation of the CR diffusion coefficient at all energies, but only for the small Galactic region traversed by them before reaching the Earth.

Appendix 1.A: Solution of the time dependent diffusion equation without boundaries

In rectangular coordinates, the Green's function $G(\mathbf{r}, \mathbf{r}', t, t')$ of Eq. (1.1) satisfies

$$D_p\left(\frac{\partial^2 G}{\partial x^2}+\frac{\partial^2 G}{\partial y^2}+\frac{\partial^2 G}{\partial z^2}\right)-2hnc\sigma_p\delta(z)G-\frac{\partial G}{\partial t}=-\delta(x-x')\delta(y-y')\delta(z-z')\delta(t-t') \tag{1.20}$$

Since the particles are assumed to be liberated at time $t = t'$, Eq. (1.20) for $t > t'$ becomes simply

$$D_p\left(\frac{\partial^2 G}{\partial x^2}+\frac{\partial^2 G}{\partial y^2}+\frac{\partial^2 G}{\partial z^2}\right)-2hnc\sigma_p\delta(z)G-\frac{\partial G}{\partial t}=0 \tag{1.21}$$

Taking Fourier transform of Eq. (1.21) with respect to x and y, we obtain

$$-D_pK^2\bar{G}+D_p\frac{\partial^2\bar{G}}{\partial z^2}-2hnc\sigma_p\delta(z)\bar{G}-\frac{\partial\bar{G}}{\partial t}=0 \tag{1.22}$$

where $K^2 = k_x^2 + k_y^2$ and

$$\bar{G}(k_x, x', k_y, y', z, z', t, t') = \int_{-\infty}^{\infty} dx \int_{-\infty}^{\infty} dy G(x, x', y, y', z, z', t, t') e^{ik_x x + ik_y y} \tag{1.23}$$

Now, taking Laplace transform of Eq. (1.22) with respect to t, we have

$$D_p\frac{\partial^2\bar{\bar{G}}}{\partial z^2}-\left[D_pK^2+2hnc\sigma_p\delta(z)\right]\bar{\bar{G}}+\delta(z)e^{ik_x x'+ik_y y'}e^{-st'}-s\bar{\bar{G}}=0 \tag{1.24}$$

where $\bar{\bar{G}}(k_x, x', k_y, y', z, z', s, t') = \int_0^\infty \bar{G}e^{-st}dt$ and we have used the condition that at $t = t'$, $G(x, x', y, y', z, z', t, t') = \delta(x - x')\delta(y - y')\delta(z - z')$. Note that in Eq. (1.24), we have set the value of z' equal to 0 since we will be assuming that the CR sources are located on the Galactic plane itself. Solving Eq. (1.24) for the regions above and below the $z = 0$ plane by using the proper boundary conditions at $z = \pm\infty$, we get

$$\bar{\bar{G}}(z, s, t') = \bar{\bar{G}}_0(0, s, t')e^{-|z|\sqrt{K^2+s/D_p}} \tag{1.25}$$

The continuity equation at $z = 0$ can be obtained by integrating Eq. (1.24) over z around 0 as

$$D_p\left[\frac{\partial\bar{\bar{G}}}{\partial z}\right]_{-0}^{+0}-2hnc\sigma_p\bar{\bar{G}}_0+e^{ik_x x'+ik_y y'}e^{-st'}=0 \tag{1.26}$$

Solving for $\bar{\bar{G}}_0$ from Eqs. (1.25 & 1.26), we get

$$\bar{\bar{G}}_0(0, s, t') = \frac{e^{ik_x x'+ik_y y'}e^{-st'}}{\left[2D_p\sqrt{K^2+s/D_p}+2hnc\sigma_p\right]} \tag{1.27}$$

and substituting it back to Eq. (1.25), we get

$$\bar{\bar{G}}(z,s,t') = \frac{e^{-|z|\sqrt{K^2+s/D_p}} \times e^{ik_x x'+ik_y y'} e^{-st'}}{\left[2D_p\sqrt{K^2+s/D_p}+2hnc\sigma_p\right]} \tag{1.28}$$

Taking an inverse Laplace transform of Eq. (1.28), we get (see Abramovitz & Stegun 1964)

$$\bar{G}(k_x,x',k_y,y',z,z',t,t') = \frac{e^{ik_x x'+ik_y y'} e^{-D_p K^2(t-t')}}{2\sqrt{D_p}} \left\{ \frac{e^{-q^2/\left[4(t-t')\right]}}{\sqrt{\pi(t-t')}} - be^{bq+b^2(t-t')} \times \mathrm{erfc}\left(b\sqrt{t-t'}+\frac{q}{2\sqrt{t-t'}}\right)\right\} \tag{1.29}$$

where $q = |z|/\sqrt{D_p}$ and $b = 2hnc\sigma_p/2\sqrt{D_p}$. Further taking an inverse Fourier transform of Eq. (1.29) gives

$$G(x,x',y,y',z,z',t,t') = \frac{e^{-\left[\frac{(x'-x)^2+(y'-y)^2}{4D_p(t-t')}\right]}}{8\pi D_p^{3/2}(t-t')} \left\{ \frac{e^{-q^2/\left[4(t-t')\right]}}{\sqrt{\pi(t-t')}} - be^{bq+b^2(t-t')} \times \mathrm{erfc}\left(b\sqrt{t-t'}+\frac{q}{2\sqrt{t-t'}}\right)\right\} \tag{1.30}$$

Using the Green's function given by Eq. (1.30), we can easily obtain the CR density due to an arbitrary source $\mathbb{Q}_p(\mathbf{r},E,t)$ as,

$$N_p(\mathbf{r},E,t) = \int_{-\infty}^{\infty} d\mathbf{r}' \int_{-\infty}^{t} dt' G(\mathbf{r},\mathbf{r}',t,t')\mathbb{Q}_p(\mathbf{r}',,t') \tag{1.31}$$

For a point source of the form $\mathbb{Q}_p(\mathbf{r}',E,t') = Q_p(E)\delta(\mathbf{r}')\delta(t'-t_0)$, we obtain a solution given by

$$N_p(\mathbf{r},E,t) = \frac{Q_p(E)e^{-\left[\frac{x^2+y^2}{4D_p(t-t_0)}\right]}}{8\pi D_p^{3/2}(t-t_0)} \left\{ \frac{e^{-q^2/[4(t-t_0)]}}{\sqrt{\pi(t-t_0}} - be^{bq+b^2(t-t_0)} \times \mathrm{erfc}\left(b\sqrt{t-t_0}+\frac{q}{2\sqrt{t-t_0}}\right)\right\} \tag{1.32}$$

where in cylindrical coordinates, we can write $x^2+y^2 = r^2$.

Appendix 1.B: Solution of the steady state diffusion equation with vertical Galactic boundaries

The Green's function of the steady state diffusion equation [Eq. (1.11)] in rectangular coordinates satisfies

$$D_p\left(\frac{\partial^2 G}{\partial x^2}+\frac{\partial^2 G}{\partial y^2}+\frac{\partial^2 G}{\partial z^2}\right)-2hnc\sigma_p\delta(z)G=-\delta(x-x')\delta(y-y')\delta(z-z') \quad (1.33)$$

Taking Fourier transform with respect to x and y, we get

$$-D_pK^2\bar{G}+D_p\frac{\partial^2\bar{G}}{\partial z^2}-2hnc\sigma_p\delta(z)\bar{G}=-e^{ik_xx'+ik_yy'}\delta(z) \quad (1.34)$$

where $K^2=k_x^2+k_y^2$ and

$$\bar{G}(k_x,x',k_y,y',z,z')=\int_{-\infty}^{\infty}dx\int_{-\infty}^{\infty}dyG(x,x',y,y',z,z')e^{ik_xx+ik_yy} \quad (1.35)$$

Also note that we have assigned $z'=0$ in Eq. (1.34). Solving Eq. (1.34) for the regions $z>0$ and $z<0$ by using the boundary conditions at $z=\pm H$, we get

$$\bar{G}(k_x,x',k_y,y',z)=\bar{G}_0(k_x,x',k_y,y',0)\frac{\sinh\left[K(H-|z|)\right]}{\sinh(KH)} \quad (1.36)$$

The continuity equation at $z=0$ is obtained by integrating Eq. (1.34) over z around 0 as

$$D_p\left[\frac{\partial\bar{G}}{\partial z}\right]_{-0}^{+0}-2hnc\sigma_p\bar{G}_0+e^{ik_xx'+ik_yy'}=0 \quad (1.37)$$

Solving for $\bar{G}_0$ from Eqs. (1.36 & 1.37), we get

$$\bar{G}_0(k_x,x',k_y,y',0)=\frac{e^{ik_xx'+ik_yy'}}{\left[2D_pK\coth(KH)+2hnc\sigma_p\right]} \quad (1.38)$$

and substituting it back to Eq. (1.36), we obtain

$$\bar{G}(k_x,x',k_y,y',z)=\frac{e^{ik_xx'+ik_yy'}}{\left[2D_pK\coth(KH)+2hnc\sigma_p\right]}\times\frac{\sinh\left[K(H-|z|)\right]}{\sinh(KH)} \quad (1.39)$$

Taking an inverse Fourier transform of Eq. (1.39) gives,

$$G(x,x',y,y',z)=\frac{1}{4\pi^2}\int_{-\infty}^{\infty}dk_x\int_{-\infty}^{\infty}dk_y\frac{e^{-ik_x(x-x')-ik_y(y-y')}}{\left[2D_pK\coth(KH)+2hnc\sigma_p\right]}\times\frac{\sinh\left[K(H-|z|)\right]}{\sinh(KH)} \quad (1.40)$$

Eq. (1.40) is a two dimensional Fourier transform which can be easily simplified in the form of Hankel transform by changing the variables as

$$k_x = K\cos\phi\ ; \quad k_y = K\sin\phi\ ; \quad x - x' = (r - r')\cos\theta\ ; \quad y - y' = (r - r')\sin\theta \tag{1.41}$$

Then,

$$G(r, r', z) = \frac{1}{4\pi D_p} \int_0^\infty \frac{\sinh[K(H - |z|)]}{\sinh(KH)\left[K\coth(KH) + \frac{2hnc\sigma_p}{2D_p}\right]} \times \mathrm{J}_0\left[K(r - r')\right] K dK \tag{1.42}$$

where J_0 is the Bessel function of order 0. Having calculated the Green's function, the CR density at $r = 0$ due to a uniform source distribution $S_p(\mathbf{r}', E) = \Re Q_p(E)\delta(z')$ in the Galactic plane with radial distances between r_1 and r_2 from the Galactic center is given by

$$N_p(z, E) = 2\pi\Re \int_{r_1}^{r_2} r' dr' G(r = 0, r', z) Q_p(E) \tag{1.43}$$

This gives,

$$N_p(z, E) = \frac{\Re Q_p(E)}{2D_p} \int_0^\infty \frac{\sinh\left[K(H - |z|)\right]}{\sinh(KH)\left[K\coth(KH) + \frac{2hnc\sigma_p}{2D_p}\right]} \times \left[r_2 \mathrm{J}_1(Kr_2) - r_1 \mathrm{J}_1(Kr_1)\right] dK \tag{1.44}$$

where J_1 represents the Bessel function of order 1 and we have used the standard relation

$$\int_{r_1}^{r_2} r' \mathrm{J}_0(Kr') dr' = \frac{1}{K}\left[r_2 \mathrm{J}_1(Kr_2) - r_1 \mathrm{J}_1(Kr_1)\right] \tag{1.45}$$

By setting $r_1 = 0$ and $r_2 = R$, Eq. (1.44) can be used to find the CR primary density due to all the sources extended up to a radial distance R from the Earth.

Chapter 2

A possible correlation between the high energy electron spectrum and the cosmic-ray secondary-to-primary ratios

Satyendra Thoudam and Jörg R. Hörandel

2011, MNRAS, 414, 1432

Abstract Recent observations of high energy cosmic-ray electrons by the Fermi-LAT and the H.E.S.S experiments between 20 GeV and 5 TeV have found that the energy spectrum closely follows a broken power-law with a break at around 1 TeV. On the other hand, measurements of cosmic-ray secondary-to-primary ratios like the boron-to-carbon ratio seem to indicate a possible change in the slope at energies around 100 GeV/n. In this Chapter, we discuss one possible explanation for the observed break in the electron spectrum and its possible correlation with the flattening in the secondary-to-primary ratios at higher energies. In our model, we assume that cosmic rays, after acceleration by supernova remnant shock waves, escape downstream of the shock and remain confined within the remnant until the shock slows down. During this time, the high-energy electrons suffer from radiative energy losses and the cosmic-ray nuclei undergo nuclear fragmentations due to their interactions with the matter. Once the cosmic rays are released from the supernova remnants, they follow diffusive propagation in the Galaxy where they further suffer from radiative or fragmentation losses.

2.1 Introduction

A few years ago, measurements of high energy cosmic-ray (CR) electrons above 10 GeV were performed mainly by balloon-borne experiments ([134] and references therein). Their measurements showed that the electron spectrum follows a power-law behavior of the form $E^{-\Gamma}$ with the index $\Gamma \approx 3.2$ without any significant features up to energies around 2 TeV. However, recent measurements made by the ATIC balloon experiment has found a sharp peak at $E \approx 600$GeV [71]. But, this feature was later not detected by two experiments, the spaced-borne Fermi-LAT and the ground-based H.E.S.S experiments [3, 24, 26] that measured the energy spectrum in the range of $20\mathrm{GeV}-5\mathrm{TeV}$. Their combined spectrum can be closely represented by a broken power-law with spectral indices $\Gamma_1 \approx 3$ and $\Gamma_2 \approx 4$ for energies below and above 1 TeV respectively. In standard CR propagation studies assuming a homogeneous source distribution, one way to explain such a spectral behavior is to assume that the electron source spectrum follows a power-law behavior with an exponential cut-off of the form $\exp(-E/E_c)$ with $E_c \approx 1$TeV. Radio and X-ray observations do support such a form of electron spectrum inside supernova remnants (SNRs), but with cut-off energies as high as $E_c \approx 80$ TeV as suggested by the study of Reynolds & Keohane (1999) considering magnetic field strengths of 10μG inside the remnants [164]. However, for young SNRs where magnetic field amplification seems to occur, the field strengths can reach values even more than 100μG and the maximum energies for the electrons can be strongly limited by radiative losses to values less than ~ 10 TeV [192].

The observed break can also be an effect of an inhomogeneous distribution of CR sources contributing to the electrons at higher energies [39, 56, 134]. This is because high energy electrons cannot travel far distances in the Galaxy due to their faster radiative cooling. Therefore, it is possible that most of the TeV electrons that we measure in the Solar System are produced by a few young nearby sources. Then, the general assumption of a continuous source distribution may break down and a more reasonable treatment would be to take into account a discrete source distribution. A common method to do this is to use the idea of separation of distant and nearby sources, i.e., assuming a continuous distribution for the distant sources and considering known SNRs or pulsars as the nearby discrete sources. One of the main uncertainties involved in such studies can be the effect of missing sources due to detection biases. Moreover, even for the known sources, the lack of precise information about the source parameters such as the distance, age and the spectral information can lead to strong uncertainties in the high energy electron spectrum. Recently, Delahaye et al. 2010 presented a detailed study using this method where they included all the known SNRs and pulsars located within 2 kpc from the Earth and they found that the total high energy spectrum from the nearby sources strongly depends on several source parameters including the assumed cut-off energy [78]. They also showed that the cut-off energy should be somewhere around a few TeV in order to explain the break in the observed data. An alternative explanation for the break, as will be shown in this work, is that after acceleration the high energy electrons might have suffered significant losses within the sources themselves before they are released into the Galaxy.

On the other hand, measurements of CR secondary-to-primary (s/p) ratios like the boron-to-carbon (B/C) up to $E \approx 100$ GeV/n by several independent experiments (see the experiments listed in [169]) show that above 1 GeV/n, the ratio decreases with energy as $\sim E^{-\delta}$ with the index $\delta \approx 0.6$ implying an energy dependent CR propagation path length in the Galaxy. However, these measurements seem to indicate a possible hardening at higher energies [178]. Recent data from the CREAM balloon-borne experiment also show flattening at energies around 1 TeV/n [27]. One way to explain this is to assume that CRs traverse some minimum amount of matter of approximately 0.3 g cm^{-2} in the Galaxy [41]. This implies an energy dependent escape path length of CRs up to some certain energy and beyond that energy, the path length becomes constant in energy. This view is, in fact, supported by the observed CR anisotropy which remain almost constant above around 100 GeV energies. But such a model needs to assume a break in the source spectrum in order to explain the observed CR spectrum which closely follows a pure power-law without any break up to the knee. Another possible explanation is that some amount of secondaries might be produced inside the sources due to the nuclear interaction of the primaries with the matter [48]. Under such models, the CR anisotropy is expected to increase with energy as E^{δ} which does not agree well with the observed data. However, it is quite possible that at higher energies the anisotropy might not be determined by the global diffusion leakage of CRs from the Galaxy. Rather, it might be the effects of high energy CRs coming from nearby sources because of their faster diffusion in the Galaxy [161, 185]. One more possible explanation which we will not discuss here is the possible reacceleration of some fraction of the background CRs by strong SNR shocks while propagating in the Galaxy [48, 193].

In this Chapter, we present one possible explanation for the observed break in the electron spectrum at around 1 TeV and its possible correlation with the flattening in the B/C ratio at energies above around 100 GeV/n. In our model, we assume that CRs are accelerated by SNR shock waves by diffusive shock acceleration (DSA) mechanism [45, 55]. Under DSA theory, suprathermal particles in the tail of the Maxwell-Boltzmann distribution present in the interstellar medium (ISM) are injected into the supernova shock front. They are then reflected back and forth several times across the shock by the magnetic turbulence generated on either side of the shock and in each cycle of crossing, the particles gain energy by first order Fermi acceleration. In a simple planar shock model, such a mechanism naturally leads to a power-law spectrum of the form $E^{-\Gamma}$ with $\Gamma = 2$ for strong shocks which is in good agreement with radio observations of several SNRs [104].

One important consideration of the standard DSA theory is that most of the particles do not escape upstream of the shock, they can only escape downstream mainly due to advection by the bulk flow and remain confined within the remnant due to the strong magnetic turbulence generated by the CRs themselves. Though it is still not fully understood, it is generally considered that the particles remain inside the remnant for as long as the shock remains strong. During the confinement period, the high energy electrons may suffer from radiative energy losses while the nuclear components suffer from nuclear fragmentations. At later stages when the shock slows down and does not efficiently accelerate the CRs, the magnetic turbulence level goes down and the particles can no longer be confined effectively

within the remnant. At such a stage, all the particles present inside the remnant escape and they are injected into the ISM. For a typical ISM density of 1 H cm^{-3}, this happens at around 10^5 yr after the supernova explosion [49]. The scenario described above might be true mostly for the lower energy particles because it is quite possible that some of the highest energy particles may escape the remnant already at the start of the Sedov phase itself due to their faster diffusion. Such an energy dependent escape of particles has been discussed in the literature [94, 163]. Recent high energy γ-ray observations of SNRs associated with molecular clouds also suggest that some of the high energy particles might have already escaped the remnant at much earlier times [21, 23]. But, as mentioned above, it is still not clear how and when exactly the particles escape the remnant. For simplicity, we consider an energy independent scenario for our present work and assume that all the particles are released into the ISM at some characteristic time after the supernova explosion.

Once the CRs are released into the ISM, we assume that they undergo diffusive propagation in the Galaxy where the electrons again suffer from radiative losses and the nuclei from nuclear spallation with the interstellar matter. Therefore, in our model the CR spectra that we finally observe in the Solar System are modified from their original source spectrum (the one generated by the SNR shocks) due to the various interactions or energy loss processes occurring not only during their propagation in the Galaxy, but also within the SNRs itself.

This Chapter is planned as follows. In section 2.2, we present our calculations for the CR spectra inside the SNRs and in section 2.3, we calculate the spectra in the Galaxy. Then, in section 2.4, we compare our results with the observed data and also give a short discussions about our results. Finally, in section 2.5, we give a brief conclusion of our study.

2.2 CR spectra within the SNRs

We assume that CR acceleration by SNR shock waves begins at the time of the supernova explosion itself and the CRs then escape downstream of the shock and remain confined within the remnant. We further assume that at some later stage of the SNR evolution characterize by age $t = T$ when the shock slows down, particle acceleration stops and also all the CRs present inside the remnant are released into the ISM. In our study, we do not consider the effect of expansion of the remnant such as the adiabatic energy losses and other related effects. A detailed study including the evolution of the remnant, the weakening of the shock with time and the possible energy dependent escape of CRs will be presented elsewhere.

2.2.1 High energy electrons

Under the assumption that the acceleration time of CRs is much less than their confinement time within the SNR, the CR electron spectrum inside a SNR can be described by the following equation,

$$\frac{\partial N_e}{\partial t} - \frac{\partial}{\partial E}\{b(E)N_e\} = q_e \tag{2.1}$$

where $N_e(E,t)$ is the total number of electrons of kinetic energy E present within the SNR at time t, $b(E) = -dE/dt$ is the energy loss rate and $q_e(E)$ is the source term which, in our case, is the rate at which CR electrons are injected downstream of the shock. We believe that Eq. (2.1) represents a valid approximation at least for energies up to around 10 TeV for which the typical acceleration timescale is less than ~ 100 yr [177]. In Eq. (2.1), we consider the energy loss of the electrons to be due to synchrotron and inverse Compton interactions which is true for energies $E \gtrsim 10$ GeV. Therefore, we take in the Thompson regime

$$b(E) = aE^2 \tag{2.2}$$

with $a = 1.01 \times 10^{-16}(w_{ph} + w_B)$ GeV^{-1} s^{-1}, where w_{ph} and w_B are the energy densities of the radiation fields and the magnetic field respectively in eV cm^{-3}. With this, we define the radiative energy loss timescale for the electrons as $t_{loss}(E) = 1/(aE)$. Now, for the source spectrum taken as a power-law of the form,

$$q_e(E) = k_e E^{-\Gamma} \tag{2.3}$$

the solution of Eq. (2.1) at time t can be written as [103, 129],

$$\begin{aligned} N_e(E,t) &= \frac{k_e E^{-(\Gamma+1)}}{(\Gamma-1)a}\left[1-(1-aEt)^{\Gamma-1}\right], \text{ for } E < E_0 \\ &= \frac{k_e E^{-(\Gamma+1)}}{(\Gamma-1)a}, \qquad\qquad\qquad\qquad \text{for } E \geq E_0 \end{aligned} \tag{2.4}$$

where $E_0 = 1/(at)$ is the energy at which the energy loss time t_{loss} becomes equal to time t. Eq. (2.4) shows that for energies $E \ll E_0$, the electron spectrum still reflects the source spectrum because of their large t_{loss}, i.e. $N_e(E) \propto E^{-\Gamma}$. However, for electrons with energies $E \gg E_0$, their spectrum is quite steep due to their faster energy loss rate and follows $N_e(E) \propto E^{-(\Gamma+1)}$.

2.2.2 CR nuclei

For the CR primary nuclei, the spectrum inside the SNR can be described by

$$\frac{\partial N_p}{\partial t} + \eta' c \sigma_p N_p = q_p \tag{2.5}$$

where $N_p(E,t)$ is the total number of particles of kinetic energy per nucleon E at time t, η' is the matter density in the SNR, c is the velocity of light and σ_p is the spallation cross-section of the primary nuclei assumed to be independent of energy. In Eq. (2.5), we assume that the source term $q_p(E) = k_p E^{-\Gamma}$ has the same index as those of the electrons.

The solution of Eq. (2.5) can be obtained as,

$$N_p(E,t) = \frac{q_p(E)}{\eta' c \sigma_p}\left[1 - e^{-\eta' c \sigma_p t}\right] \tag{2.6}$$

For time much less than the nuclear spallation time, i.e. $t \ll 1/(\eta' c\sigma_p)$, Eq. (2.6) becomes $N_p(E,t) \approx q_p(E)t$.

During the time when primary CRs are confined within the SNRs, they interact with matter and produce secondary nuclei of almost the same kinetic energy per nucleon as their primaries. These secondaries can also be described by an equation similar to Eq. (2.5) by replacing the source term by $\eta' c\sigma_{ps} N_p(E,t)$ where σ_{ps} is the total fragmentation cross-section of primary to secondary. The solution for these secondaries is then obtained as,

$$N_s(E,t) = \frac{\sigma_{ps}}{\sigma_p} \frac{q_p(E)}{\eta' c\sigma_s} \left[1 - e^{-\eta' c\sigma_s t} + F\right] \tag{2.7}$$

where,

$$F = \frac{\sigma_s}{(\sigma_s - \sigma_p)} \left(e^{-\eta' c\sigma_s t} - e^{-\eta' c\sigma_p t}\right)$$

In Eq. (2.7), σ_s represents the spallation cross-section of the secondary nuclei. Now, taking $t = T$ which is the CR confinement time inside the SNR, we can use Eqs. (2.4), (2.6) & (2.7) to calculate the spectrum of CR electrons and the spectra of primary and secondary CR nuclei finally injected into the ISM from a single SNR. Then, knowing the rate of supernova explosions per unit volume in the Galaxy, we can calculate the rate at which CRs are injected per unit volume in the Galaxy.

2.3 CR spectra in the Galaxy

After escaping from the SNRs, CRs undergo diffusive propagation in the Galaxy due to scattering either by magnetic field irregularities or by self-excited Alfvén and hydromagnetic waves. For the present work, we assume the diffusion region as a cylindrical disk of infinite radius with finite half-thickness H and that the sources as well as the matter are distributed uniformly and continuously in the Galactic disk with half-thickness h and radius R, where $R \gg H \gg h$. The details of the geometry are described in [186]. During the propagation, high energy electrons interact with the background radiation and the magnetic fields and lose their energies. On the other hand, CR nuclei undergo nuclear spallation interactions with the interstellar matter and produce lighter nuclear species.

As already mentioned in section 2.1, the assumption of a continuous source distribution may not be fully appropriate for high energy electrons particularly those in the TeV region because of their faster energy loss rate. Electrons with energies greater than 1 TeV cannot travel distances more than ~ 1 kpc in the Galaxy through diffusive propagation before they lost all their energies. Therefore, high energy electrons from distant and old sources may not reach the Earth effectively and TeV electrons that we observe can be mostly dominated by those produced by a few young local sources. The effect of this can be that the spectrum at high energies can be quite complex because of its strong dependence on the local source parameters [78]. Moreover, it may even show up features related to the stochastic nature of the local sources in space and time (see e.g., [159]).

In our study, our focus is to explore the possibility of explaining the break in the electron spectrum as an effect of CR confinement in the downstream region of SNRs and at the same time, following the standard model of CR propagation in the Galaxy. Such an effect of confinement within the sources is generally not considered in CR propagation studies and we believe that they may exist if SNRs are the main sources of galactic CRs. Therefore, we do not intend to focus on a detailed source distribution and in what follows, we adopt the continuous and stationary source distribution for calculating the CR spectrum in the Galaxy.

2.3.1 High energy electrons

Under the diffusion model, the propagation of high energy electrons in the Galaxy can be described by

$$\nabla \cdot (D\nabla n_e) + \frac{\partial}{\partial E}\{b(E)n_e\} = -Q_e \tag{2.8}$$

where $n_e(\mathbf{r}, E)$ is the electron number density in the Galaxy, $D(E)$ is the diffusion coefficient which is assumed to be constant throughout the Galaxy and $Q_e(\mathbf{r}, E)$ is the source term given by $Q_e(\mathbf{r}, E) = \Re N_e(E, T)\delta(z)$. Here, $N_e(E, T)$ is given by Eq. (2.4) which represents the total amount of CR electrons liberated by a SNR and $\Re$ denotes the rate of supernova explosion per unit surface area on the Galactic disk. As already mentioned, high energy electrons cannot travel large distances because of their large energy loss rate. Therefore, their equilibrium spectrum is not much affected by the presence of the halo boundary H and we solve Eq. (2.8) without imposing the finite boundary conditions for our study. The solution at the position of the Earth ($z = 0$) is then obtained as,

$$n_e(E) = \frac{\Re}{2\sqrt{\pi}b(E)} \int_E^\infty dE' N_e(E', T) \left[\int_E^{E'} \frac{D(u)}{b(u)} du\right]^{-1/2} \tag{2.9}$$

For the diffusion coefficient $D(E) \propto E^\delta$, Eq. (2.9) shows that

$$n_e(E) \propto \frac{1}{b(E)} \int_E^\infty dE' \frac{N_e(E', T)}{\sqrt{E^{\delta-1} - E'^{\delta-1}}} \tag{2.10}$$

From Eq. (2.10), we see that for a power-law source spectrum such as $N_e(E) \propto E^{-\gamma_e}$, we get $n_e(E) \propto E^{-\gamma_e-1+\beta}$ where $\beta = (1 - \delta)/2$. Thus, the equilibrium electron spectrum in the Galaxy is modified mainly by the radiative energy losses with a small correction β arising due to the diffusive propagation effect.

2.3.2 CR nuclei

The steady state transport equation for primary CR nuclear species in the Galaxy, neglecting the effect of energy losses due to ionization, is given by

$$\nabla \cdot (D\nabla n_p) - 2h\eta c\sigma_p \delta(z) n_p = -Q_p \tag{2.11}$$

where $n_p(\mathbf{r}, E)$ is the density of primary CRs of energy per nucleon E, η is the matter density in the ISM and $Q_p(\mathbf{r}, E) = \Re N_p(E,T)\delta(z)$ is the source term where $N_p(E,T)$ is given by Eq. (2.6). Eq. (2.11) is solved by imposing proper boundary conditions as described in detail in [186] and the solution at $z = 0$ is given by,

$$n_p(E) = \frac{R\Re N_p(E,T)}{2D} \int_0^\infty \frac{J_1(KR)dK}{\left[K\coth(KH) + \frac{2h\eta c\sigma_p}{2D}\right]} \tag{2.12}$$

where J_1 is the Bessel function of order 1.

Primary nuclei during their propagation in the Galaxy interact with matter in the Galaxy and produce secondary nuclei. The equilibrium spectrum for these secondaries $n_s(\mathbf{r}, E)$ in the Galaxy can be described by,

$$\nabla \cdot (D\nabla n_s) - 2h\eta c\sigma_s\delta(z)n_s = -Q_s \tag{2.13}$$

where the source term $Q_s(\mathbf{r}, E) = 2h\eta c\sigma_{ps}n_p(\mathbf{r}, E)\delta(z)$. There is also an additional component of the secondaries in the Galaxy due to their production inside the SNRs as discussed in section 2.2.2. The equilibrium spectrum n'_s for this additional component can also be described by an equation similar to Eq. (2.13) with the source term replaced by $Q'_s(\mathbf{r}, E) = \Re N_s(E,T)\delta(z)$, where $N_s(E,T)$ is given by Eq. (2.7). The spectra of these two secondary components at the position of the Earth can be obtained respectively as,

$$n_s(E) = 2h\eta c\sigma_{ps}n_p(E)\frac{R}{2D} \int_0^\infty \frac{J_1(KR)dK}{\left[K\coth(KH) + \frac{2h\eta c\sigma_s}{2D}\right]} \tag{2.14}$$

and

$$n'_s(E) = \frac{R\Re N_s(E,T)}{2D} \int_0^\infty \frac{J_1(KR)dK}{\left[K\coth(KH) + \frac{2h\eta c\sigma_s}{2D}\right]} \tag{2.15}$$

Having calculated the spectra for the primaries and the secondaries in the Galaxy, the overall s/p ratio can be obtained by simply taking the ratio $(n_s + n'_s)/n_p$. Note that in the standard model of CR propagation in the Galaxy where secondary nuclei are assumed to be produced only in the ISM, the ratio is given by n_s/n_p.

2.4 Results and discussions

For our calculations, we choose $R = 16$ kpc, $H = 5$ kpc, $h = 200$ pc and the rate of supernova explosion as $\Re = 25$ Myr^{-1} kpc^{-2} [106]. This corresponds to a total supernova explosion rate of $\sim 1/50$ yr^{-1} in our Galaxy. The total energy density of the radiation field is taken as $w_{ph} = w_{MBR} + w_{op} + w_{FIR}$ where w_{MBR}, w_{op} and w_{FIR} are the energy densities of the microwave background, the NIR-optical and the FIR radiation fields respectively. We take $w_{MBR} = 0.25$ eV cm^{-3}, $w_{op} = 0.5$ eV cm^{-3} [143], $w_{FIR} = 0.2$

eV cm^{-3} [72] and the magnetic field value as $B = 6\mu$G [44]. We assume these values to be the same for both the Galaxy and the SNRs. We take the ISM density as $\eta = 1$ cm^{-3} typical for our Galaxy [61, 107] and the CR diffusion coefficient in the Galaxy as [186]

$$\begin{aligned} D(E) &= D_0 \left(\frac{\xi}{E}\right)^{\delta}, \qquad \text{for } E < \xi \\ &= D_0 \left(\frac{E}{\xi}\right)^{\delta}, \qquad \text{for } E > \xi \end{aligned} \tag{2.16}$$

where $D_0 = 2.9 \times 10^{28}$ cm^{2}s^{-1} and $\delta = 0.6$. For CR nuclear species, E represents energy per nucleon and the particle rigidity ρ (corresponding to ξ) for charge Z and mass number A is taken as $\rho = A\xi/Z = 3$ GV. For electrons, E in Eq. (2.16) represents the kinetic energy and ξ is directly taken as 3 GeV.

Finally, we take the source spectral index $\Gamma = 2.2$ and the CR confinement time within the SNRs as $T = 1.2 \times 10^5$ yrs. Then, using the solutions for the CR spectra derived in section 2.3, we calculate the CR electron spectrum and the B/C ratio in the Galaxy and compare them with the observed data. In Figure 2.1, we plot our calculated electron spectrum normalized to the data reported by the Fermi and the H.E.S.S experiments at 50 GeV. This corresponds to approximately 0.3% of the total kinetic energy of the supernova explosion, taken as $E_{SN} = 10^{51}$ ergs, converting into the CR electrons above 1 GeV. In Figure 2.2, we plot the B/C ratio in the Galaxy where the solid line represents the ratio expected under the standard model which assumes boron production entirely only in the ISM, the dotted and the dot-dashed lines represent the results of our model which also include additional boron production inside the SNRs for $\eta' = 1$ cm^{-3} and 2 cm^{-3} respectively. In our calculation, we consider that boron nuclei are produced due to the spallation of carbon and oxygen nuclei and we take the oxygen to carbon (O/C) source abundance ratio as 1.4. The data in Figure 2.2 includes the compilation given in [169] and also the recent data from the CREAM experiment [27]. From the figures, we see that our model explains quite well the observed break in the electron spectrum at $E \sim 1$ TeV without invoking any exponential cut-off in the source spectrum and also it explains the observed flattening in the B/C ratio above ~ 100 GeV/n.

Our results can be understood as follows. We see from section 2.3.1 that the spectrum of high energy electrons in the Galaxy follow $n_e(E) \propto E^{-\gamma_e - 1 + \beta}$, where γ_e is the index of electron injection spectrum into the Galaxy and $\beta = (1-\delta)/2$ is a small correction due to propagation. For the diffusion index $\delta = 0.6$, we get $\beta = 0.2$. In our model, γ_e is the spectrum of CR electrons produced by the SNRs (see section 2.2.1) and is given by $\gamma_e = \Gamma$ for energies $E \ll E_0$ and $\gamma_e = \Gamma + 1$ for $E \gg E_0$. Therefore, for $\Gamma = 2.2$ we get,

$$\begin{aligned} \gamma_e &= 2.2, \qquad \text{for } E \ll E_0 \\ &= 3.2, \qquad \text{for } E \gg E_0 \end{aligned} \tag{2.17}$$

which gives the corresponding high energy electron spectrum in the Galaxy as $n_e(E) \propto E^{-3}$ and E^{-4} respectively. The energy at which the spectral break occurs depends both on

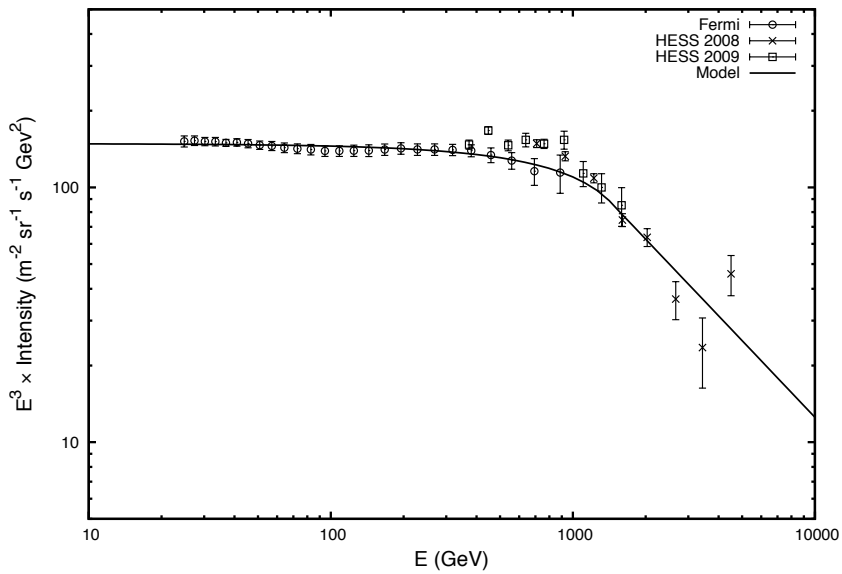

Figure 2.1: CR electron spectrum at the position of the Earth. The solid line is the result of our calculation using Eq. (2.9) normalized to the data at 50 GeV. The data are taken from the Fermi [3] and the H.E.S.S [24, 26] experiments. This normalisation corresponds to $\sim 3 \times 10^{48}$ ergs of the supernova explosion energy converting into CR electrons above 1 GeV. Our model parameters: $T = 1.2 \times 10^5$ yrs, $\Gamma = 2.2$, $\delta = 0.6$, $\Re = 25$ Myr^{-1} kpc^{-2} and $E_{SN} = 10^{51}$ ergs. Other model parameters: $w_{MBR} = 0.25$ eV cm^{-3}, $w_{ph} = 0.5$ eV cm^{-3}, $w_{FIR} = 0.2$ eV cm^{-3} and $B = 6\mu$G, which are taken to be same both in the Galaxy and in the SNRs.

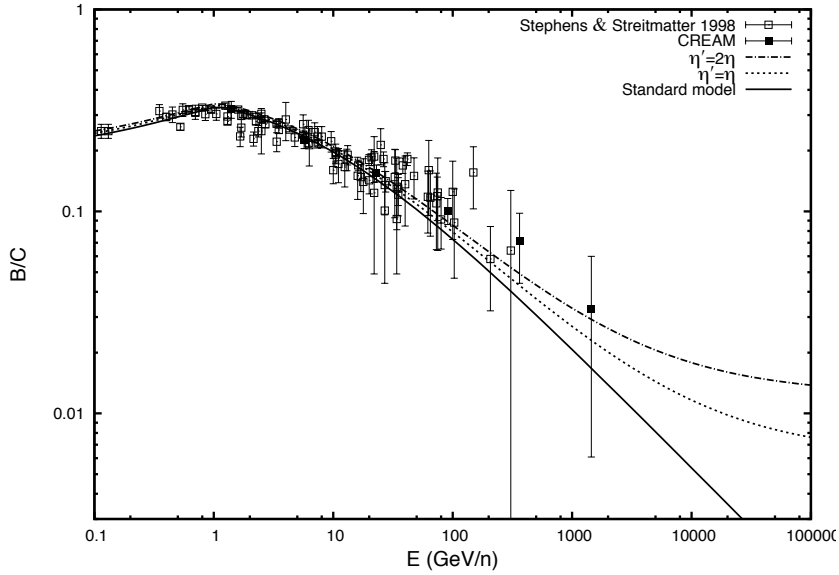

Figure 2.2: B/C ratio at the position of the Earth. The solid line is the ratio under the standard model where boron is assumed to be produced only in the ISM. The results of the present model, where boron production inside the sources are included, are shown for two values of matter density inside the remnants $\eta' = 1$ cm^{-3} (dotted line) and 2 cm^{-3} (dot-dashed line) respectively. The ISM density is taken as $\eta = 1$ cm^{-3}. The model parameters used are the same as in Figure 2.1.

the CR confinement time within the remnants and also on the total energy density w_{ph} of the radiation and the magnetic fields present in the SNRs as $E_0 = 1/(aT)$. For the values of T, w_{ph} and w_B adopted in the present work, we obtain $E_0 = 1.4$ TeV.

The spectra of high energy primary nuclei in the Galaxy follow $n_p(E) \propto E^{-\gamma_p-\delta}$, where γ_p is the primary injection spectrum in the Galaxy. The secondary nuclei, for those which are produced in the ISM, follow a spectrum given by $n_s(E) \propto E^{-\gamma_p-2\delta}$ in the Galaxy whereas, those produced due to the interaction of the primaries within the remnants follow $n'_s(E) \propto E^{-\gamma_s-\delta}$, where γ_s is the secondary injection spectrum in the Galaxy. We see from section 2.2.2 that both the primary and the secondary injection spectra in the ISM have the same index as the intrinsic source spectrum, i.e. $\gamma_p = \gamma_s = \Gamma$. Thus, n_s is steeper than n'_s by $E^{-\delta}$. Therefore, the overall s/p ratio follows,

$$\begin{aligned} \frac{(n_s + n'_s)}{n_p} &\propto \frac{n_s}{n_p} \propto E^{-\delta}, && \text{for } E \ll E_a \\ &\propto \frac{n'_s}{n_p} = \text{constant}, && \text{for } E \gg E_a \end{aligned} \tag{2.18}$$

where E_a is the energy at which the amount of secondaries produced in the ISM equals those produced within the SNRs, i.e. at $n_s = n'_s$. For our results shown in Figure (2.2), we get $E_a = 7.5$ TeV/n and 2.5 TeV/n for $\eta' = 1$ cm^{-3} and 2 cm^{-3} respectively.

To better understand the relative production of CR secondaries inside the SNRs and in the Galaxy, it is good to compare the amount of matter traversed by the CRs during their confinement within the remnants to the amount traversed during their propagation in the Galaxy. For this, we calculate the path length X as a function of s/p as,

$$X = \frac{m}{(\sigma_p - \sigma_s)} \ln \left[1 - R_{sp} \frac{(\sigma_s - \sigma_p)}{\sigma_{ps}} \right] \tag{2.19}$$

where m denotes the mass of hydrogen atom and R_{sp} represents the s/p ratio. Using Eq. (2.19), we can calculate the CR path length for a given R_{sp}. For the path length calculation within the SNRs, R_{sp} is given by the ratio N_s/N_p taken at time $t = T$ (see section 2.2.2) and for the path length in the Galaxy, $R_{sp} = n_s/n_p$ from section 2.3.2. Their comparison corresponding to the B/C ratio shown in Figure 2.2 is plotted in Figure 2.3 where the dot-dashed line represents the path-length inside the SNRs X_s and the dotted line that in the Galaxy X_g. Also shown in the figure by the solid line is the total path length $(X_s + X_g)$ traversed by the CRs during their whole lifetime in the Galaxy. The average path length within the SNRs is found to be $X_s \approx 0.09$ gm cm^{-2} for $\eta' = 1$ cm^{-3} independent of energy whereas the path length in the Galaxy has a maximum value of $X_g \approx 5$ gm cm^{-2} at around 1 GeV/n which then decreases with energy as $X_g \propto E^{-\delta}$ because of the energy dependent escape of CRs from the Galaxy. From Figure 2.3, we can also see that CRs with energies greater than around 7 TeV/n traversed most of the matter within the source itself and its effect is seen in the B/C ratio in Figure 2.2 already at energies around 1 TeV/n.

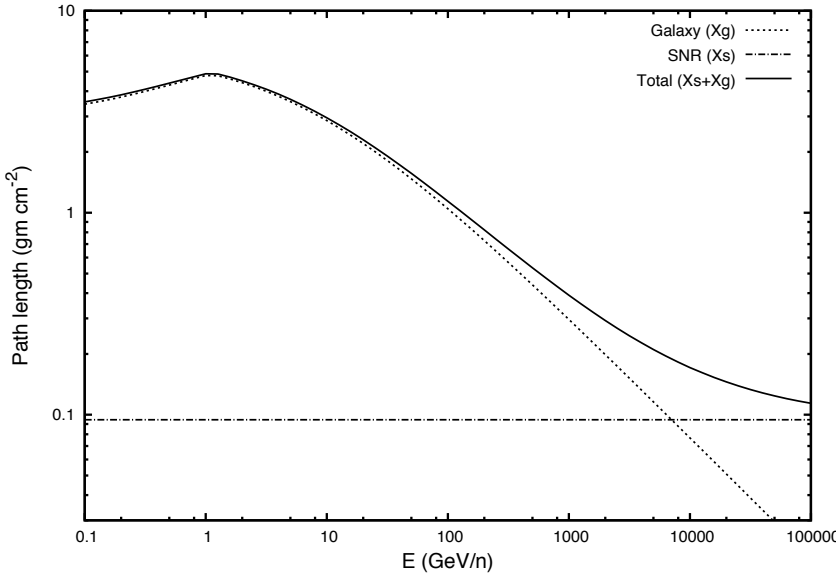

Figure 2.3: CR path length corresponding to the B/C ratio shown in Figure 2.2. The dotted line represents the path length in the Galaxy X_g and the dot-dashed line represents the path length within the SNRs X_s. The solid line represents the total path length ($X_s + X_g$) traversed during their total lifetime in the Galaxy. Model parameters: $T = 1.2 \times 10^5$, $\eta = 1$ cm^{-3}, $\eta' = 1$ cm^{-3} and $\delta = 0.6$.

2.5 Conclusions

We present a simple model based on the considerations of DSA theory which can explain both the observed electron spectrum and the s/p ratios for a conservative set of model parameters. In our model, we assume that CRs, after acceleration by SNR shock waves, escape downstream of the shock and remain confined within the remnant for some time before they are released into the ISM. During this time, CR electrons suffer from radiative energy losses while the nuclear species undergo nuclear fragmentations. For a magnetic field strength of 6μG inside the SNRs and assuming a uniform and continuous distribution of SNRs in our Galaxy, we find that a CR confinement time of 1.2×10^5 yr can produce the observed break in the electron spectrum at $\sim$ 1 TeV. Moreover, the hardening in the available B/C data above ~ 100 GeV/n can also be explained if we assume the averaged matter density inside the SNRs to be ~ 2 cm $^{-3}$. Our results on the B/C ratio which are based on a simple model are very similar to those obtained in [48] for the case of secondary production inside SNRs calculated for the normal ISM density of 1 cm^{-3} and the CR confinement time of 10^5 yr. Their results were calculated using a detailed self consistent model of CR production inside SNRs.

Our model, in its present form, looks similar to nested leaky box model proposed by Cowsik & Wilson 1973, 1975 [76, 77]. However, there are major differences in the basic assumptions between the two models. They assumed that CRs after acceleration spend some time in a cocoon-like region surrounding the sources where the primaries interact with the matter and produce secondaries. The residence time of CRs inside the cocoon was assumed to be energy *dependent* and after they are released from the source region, they undergo an energy *independent* propagation in the Galaxy. In their model, secondary production inside the cocoon dominates at lower energies and at higher energies, it is dominated by the production in the ISM. On the other hand, the basic idea of our model comes from our understanding of DSA theory inside SNRs. In our model, the CR confinement region as well as the confinement time are strongly related to the acceleration mechanism itself. Moreover, secondary production inside the remnant dominates only at higher energies while at lower energies, they are dominated mostly by those produced in the Galaxy. A more proper treatment of our model would be to perform a self consistent calculation of primary CR acceleration and their confinement, both of which are strongly related to the efficiency of CR scattering around the shocks by magnetic turbulence. Also, we should include the secondaries produced during the acceleration process along with those produced during the confinement period and if there, also their acceleration by the same shock waves which accelerate their primaries. Such a scenario of secondary acceleration has been considered to explain the rise in the positron fraction reported by the PAMELA experiment [56]. Though it is beyond the scope of this work to discuss this issue, it is worthwhile to mention in relation to our present model, that the relative contribution of the accelerated and the non-accelerated secondaries to their total spectrum strongly depends on the relative time their primaries spend in the acceleration region and in the downstream region (see e.g. [127]).

We emphasize that under our present model, both the high energy electron spectrum and

the s/p ratio depend strongly on the CR confinement time inside the SNRs. Therefore, their data can be used to put constraints on the average confinement time provided that detailed informations about the magnetic field strengths and the matter densities inside the remnants are taken into account. Note that the value of the magnetic field strength of 6μG and also that of the matter density $\eta' = (1-2)$ cm^{-3} adopted in our present work can be different from those expected in SNRs. For SNRs expanding in an environment consisting of monoatomic ideal gas, their values are expected to be equal to the ISM values scaled by some constant factor which in the case of strong shocks is approximately equal to 4. Moreover, these values can also be different for different SNRs and their true values can only be inferred from observations of radio or X-ray synchrotron emissions and thermal X-rays from SNRs [42, 190]. In future, we will include such details in our calculation and also try to extend our work to other secondary species like the CR anti-protons and the positrons. In addition, we will also include some important aspects which we have neglected in our present study like the evolution of the remnant, the weakening of the shocks and the energy dependent escape of CRs from the SNRs. Adding such aspects, particularly the energy dependent escape, can strongly affect our results. For instance, assuming an escape model which follows the same energy dependence as in the Galaxy can lead to disappearance of the flattening in the s/p ratio at higher energies.

Chapter 3

On the point source approximation of nearby cosmic-ray sources

Satyendra Thoudam and Jörg R. Hörandel
2012, MNRAS, 419, 624

Abstract In this Chapter, we check in detail the validity of the widely adopted point source approximation for nearby cosmic-ray sources. Under an energy independent escape model for cosmic rays from the sources, we show that for young nearby sources, the point source approximation breaks down at lower energies and the cosmic-ray spectrum depends on the size and the morphology of the source. When applied to the nearby supernova remnants, we find that the approximation breaks down for some of the individual remnants such as the Vela, but interestingly it still holds good for their combined total spectrum at the Earth. Moreover, we also find that the results obtained under this simple approximation are quite different from those calculated under an energy dependent escape model which is favored by diffusive shock acceleration models inside supernova remnants. Our study suggests that if supernova remnants are the main sources of cosmic rays in our Galaxy, then the commonly adopted point source model (with an energy independent escape scenario) appears flawed for cosmic-ray studies from the nearby remnants.

3.1 Introduction

Cosmic rays (CRs) with energies below the knee region ($\sim 3 \times 10^{15}$ eV) are considered to be of galactic origin. Although the exact nature of their sources is not known, the most favorable candidates are supernova remnants (SNRs). They are known to occur in our Galaxy at the rate of $\sim 1/30$ to $1/50$ yr^{-1} with each explosion releasing a total kinetic energy of $\sim 10^{51}$ ergs. If approximately 10% of this energy is converted into CRs, then the total power release is sufficient to maintain the CR energy density in our Galaxy which is measured to be around 1 eV cm^{-3}.

It is also now theoretically established that SNR shock waves can accelerate CRs up to energies close to the knee by the diffusive shock acceleration (DSA) mechanism [45, 55]. In a simple planar shock model, such a mechanism naturally leads to a power-law spectrum of the form $E^{-\Gamma}$ with the exponent $\Gamma = 2$ for strong shocks. This value is found to be in good agreement with the radio observations of SNRs [104]. In addition, direct evidence for the presence of high energy particles up to few TeVs (1 TeV= 10^{12} eV) inside SNRs comes from the detection of non-thermal X-rays [43, 157] and high energy TeV γ-rays from several SNRs [20, 22, 23, 25, 30]. The non-thermal X-rays are best explained as synchrotron emission from high energy electrons while the origin of the TeV γ-rays is still not certain between the leptonic (via inverse Compton process) and the hadronic scenarios (via π^0 decays). If the high energy γ-rays are of hadronic origin as indicated by the recent observations of several SNRs by the FERMI experiment [5, 8, 9, 10], then the measured γ-rays can provide direct informations about the spectral shape of the primary particles. But, TeV measurements made by the new generation Cherenkov telescopes like the H.E.S.S, MAGIC and VERITAS have found that many SNRs show $\Gamma \sim (2.3 - 2.7)$ which is steeper than the expectations from DSA theory. The discrepancy becomes even more severe if we compare with the results of non-linear DSA theory which predicts a spectrum flatter than $\Gamma = 2$ ([64] and references therein). Although this discrepancy is still not yet fully understood, for our study we will assume that SNRs are the main sources of CRs in our Galaxy.

Quite often, theoretical studies on the propagation of CRs assume the sources to be stationary and continuously distributed in the Galaxy. This simple assumption seems reasonable for calculating the Galactic average CR properties and for understanding the diffuse radiation produced by the interaction of CRs in the interstellar medium (ISM). But, for CR studies in the vicinity of the sources where the influence of the source is expected to dominate over the background produced by the distant sources, the discrete nature of the sources (both in space and time) may become important. For instance, in the study of gamma-ray emission from the environment of the sources or from molecular clouds associated with them, the emission can be strongly dependent on the age and the distance of the source as discussed in [19, 68, 94].

Similarly, for the study of CRs observed at the Earth, the uniform source distribution looks proper only for the distant sources but for the nearby sources, a more reasonable treatment would be to consider the discrete nature of the sources. For CR electrons at few TeV

energies, such treatment seems even more important because of their fast energy loss rate. Electrons with energies greater than ~ 1 TeV cannot travel distances more than ~ 1 kpc in the Galaxy through diffusive propagation before they have lost all their energy. Therefore, high energy electrons from distant and old sources may not reach the Earth effectively and it is possible that most of the TeV electrons that we observed are mostly produced by a few young nearby sources [39, 78, 134, 167]. Also for the CR protons and other nuclear species which do not suffer significant losses (the typical nuclear fragmentation loss time scale in our Galaxy $\sim 10^7$ yr) and for which we expect a strong background from the distant sources, the discrete treatment of the nearby sources can still be important especially at higher energies (see e.g. [62, 88, 173] and references therein). This is because high energy CRs diffuse relatively faster compared to the lower energy ones and hence, they are expected to produce stronger fluctuations on their observable properties such as the spectrum and the anisotropy in the arrival direction [186]. Moreover, at these energies, the contribution from the recent sources may dominate and the effect of discreteness in time may also become important [180].

In most of the studies mentioned above, the discrete sources are assumed to be point-like, thereby neglecting their finite size and the morphology. At first sight, the point source approximation seems reasonable for sources whose size $s \ll r$, the distance from the Earth. But, for those whose size is comparable to the distance, the point source approximation may break down and it looks more appropriate to take their size and morphology into account. Under the standard DSA theory, CRs are confined within the SNRs due to the strong magnetic turbulence generated by the CRs themselves and therefore, it is reasonable to assume that CRs remain confined as long as the shocks remain strong enough to act as an efficient accelerator. For a typical interstellar matter density of 1 H cm^{-3}, the confinement last until the SNR age $\sim 10^5$ yr [49]. In reality, an energy dependent confinement/escape scenario is expected [65, 163]. Using the Sedov relation between the SNR age and the shock radius, if we assume an initial shock velocity of 10^9 cm s^{-1}, we can roughly estimate that at the age of 10^5 yr the remnant expands to a size of radius around 100 pc. Such a size is comparable to the distance of some of the nearest SNRs like Geminga and Loop1. The distance to Geminga is estimated to be ~ 157 pc [66] and that to Loop1 as ~ 170 pc [84].

The argument just mentioned is purely based on the geometrical consideration, i.e., the source size compared to its distance and we have not considered any possible effects due to the propagation of CRs in the Galaxy. It is now well accepted that CRs undergo diffusive motion due to scattering by the magnetic field irregularities and the self excited hydromagnetic waves in the ISM. Measurements of secondary-to-primary (s/p) ratios like boron-to-carbon indicate that the diffusion is energy dependent with the diffusion coefficient increasing with energy [169]. If we also take into account such an energy dependent diffusion, the validity of the point source approximation may become somewhat relaxed for high energy particles, i.e, it may still represent a good approximation even for the nearby sources at higher energies. We will discuss this in detail later in the Chapter.

Recently, Ohira et al. 2011 highlighted the importance of the finite source size in the study of gamma-ray emission from SNRs interacting with molecular clouds [153]. They

claimed that the observations of different gamma-ray spectra from four SNRs (W51C, W28, W44 and IC 443) by the FERMI experiment could be an effect of finite size of the SNRs. In this work, we will investigate the importance of the source size for the nearby SNRs considering the CR spectrum expected at the Earth. Although SNRs can have complex morphologies, that are also different from each other, for simplicity we will consider a spherical geometry for our study. In one part, we will consider an energy *independent* escape of CRs from the SNRs. This is discussed in sections 3.2 and 3.3. In another part of our study, we will investigate the energy *dependent* escape model under which CRs of different energies are assumed to escape at different times. This study is given in section 3.4. Then in section 3.5, we apply our study to the nearby known SNRs and compare the results obtained under the different source models. Finally in section 3.6, we present an overview of our results and discuss their implications.

3.2 CR proton spectrum from an SNR

In the diffusion model, neglecting losses due to interactions in the ISM, the propagation of CR protons in the Galaxy can be described by ([95] and references therein),

$$\nabla \cdot (D \nabla N_p) + Q_p = \frac{\partial N_p}{\partial t} \tag{3.1}$$

where $N_p(\mathbf{r}, E, t)$ is the differential proton density, E is the kinetic energy, $D(E)$ is the diffusion coefficient and $Q_p(\mathbf{r}, E, t)$ is the source term, i.e. the proton production rate from the SNR. In Eq. (3.1), we also neglect other effects which are relevant mostly below a few GeVs like convection due to the Galactic wind and re-acceleration by the interstellar turbulence. We assume the diffusion coefficient to be spatially constant throughout the Galaxy and take $D(E) = D_0(E/E_0)^\delta$ for $E > E_0$, where $D_0 = 2.9 \times 10^{28}$ cm^2 s^{-1}, $E_0 = 3$ GeV and $\delta = 0.6$ [186]. These values are different from those given by models based on diffusive re-acceleration. For instance, Trotta et al. 2011 give a value of $D_0 \sim 8.3 \times 10^{28}$ cm^2 s^{-1} and $\delta \sim 0.3$ [189].

For sources within a distance of ~ 1 kpc from the Earth which are also our main interest here, Thoudam 2007 showed that the CR spectrum is not much affected by the presence of the Galactic boundaries [185] . In fact, D_0 does depend on the boundaries and is proportional to the size of our Galactic halo (e.g. [189]). For our present study, we neglect such dependencies and solve Eq. (1) without imposing any boundary conditions. We then obtain the well known Green function $G_p(\mathbf{r}, \mathbf{r}', t, t')$, i.e. the solution for a δ-function source term $Q_p(\mathbf{r}, E, t) = \delta(\mathbf{r} - \mathbf{r}')\delta(t - t')$ as given below,

$$G_p(\mathbf{r}, \mathbf{r}', t, t') = \frac{1}{8\left[\pi D(t - t')\right]^{3/2}} \exp\left[\frac{-(\mathbf{r}' - \mathbf{r})^2}{4D(t - t')}\right] \tag{3.2}$$

The general solution of Eq. (3.1) can be then obtained using,

$$N_p(\mathbf{r}, E, t) = \int_{-\infty}^{\infty} d\mathbf{r}' \int_{-\infty}^{t} dt' G_p(\mathbf{r}, \mathbf{r}', t, t') Q_p(\mathbf{r}', E, t') \tag{3.3}$$

The source term in Eq. (3.3) can be written as,

$$Q_p(\mathbf{r}', E, t') = q(\mathbf{r}')q(E)q(t') \tag{3.4}$$

where $q(E)$ is the source spectrum, i.e., $q(E)dE$ is the number of protons with energy between E and $E + dE$ produced by the SNR. For this part of our study, we assume an energy independent escape of CRs from the SNR. We will first consider the burst-like injection of particles followed later by the continuous injection case. Later on, in section 3.4 we will discuss the energy dependent escape model.

If we assume that the burst-like emission of particles happen at time t_0, we can write the temporal source term as $q(t') = \delta(t' - t_0)$. Then, using Eqs. (3.2) & (3.4) in Eq. (3.3), we get,

$$N_p(\mathbf{r}, E, t) = \frac{q(E)}{8\left[\pi D(t - t_0)\right]^{3/2}} \int_{-\infty}^{\infty} d\mathbf{r}' \exp\left[\frac{-(\mathbf{r}' - \mathbf{r})^2}{4D(t - t_0)}\right] q(\mathbf{r}') \tag{3.5}$$

The proton intensity can be then calculated using the relation $I_p(E, t) \approx (c/4\pi)N_p(E, t)$, where c is the velocity of light. To make our calculations simpler, hereafter we take $\mathbf{r} = 0$, i.e., we set the origin of the coordinate system at the position of the Earth.

3.2.1 Point source approximation

If we assume the SNR to be a point source located at a distance $\mathbf{r}_s$ from the Earth, we can write

$$q(\mathbf{r}') = \delta(\mathbf{r}' - \mathbf{r}_s) \tag{3.6}$$

Then, the proton density is obtained from Eq. (3.5) as,

$$N_p(E, t) = \frac{q_p(E)}{8\left[\pi D(t - t_0)\right]^{3/2}} \exp\left[\frac{-r_s^2}{4D(t - t_0)}\right] \tag{3.7}$$

Eq. (3.7) represents the most commonly adopted solution for a CR spectrum from a nearby single source. For high energy particles for which the diffusion radius defined as $r_{diff} = \sqrt{4D(t - t_0)}$ is much larger than the distance to the SNR r_s, the exponential term in Eq. (3.7) tends to 1 which implies,

$$N_p(E, t) \rightarrow \frac{q_p(E)}{8\left[\pi D(t - t_0)\right]^{3/2}} \tag{3.8}$$

For a power-law source spectrum given by $q_p(E) = k_p E^{-\Gamma}$ and for $D(E) \propto E^{\delta}$, Eq. (3.8) shows that the spectrum of high energy protons reaching us follows $N_p(E) \propto E^{-\left(\Gamma + \frac{3}{2}\delta\right)}$. Particles with $r_{diff} > r_s$ are those which have already passed the Earth. Those with $r_{diff} < r_s$ are the ones which have not yet reached us effectively due to their slower diffusion and therefore, their intensity is comparatively much suppressed.

3.2.2 Spherical solid source

Most of the SNRs are observed to roughly follow a spherical geometry and they come under three main categories: shell-type, plerion-type and composite-type. Shell-type SNRs show bright shell structure which expands into the ISM with velocities of $\sim (3-10) \times 10^8$ cm s^{-1} (e.g. Cassiopeia A). Plerions also known as pulsar wind nebulae have filled centers where normally a pulsar powers high energy particles into the ISM (e.g. Crab Nebula). They do not show any shell-like features. Composite SNRs have both shell structure and a filled center (e.g. IC443). The surface brightness of shell-type SNRs in radio as well as in X-rays are observed to peak near the surface whereas in plerions, it tends to increase towards the center. We can expect that the high energy particles responsible for radio and X-ray emission also follow a similar distribution within the remnant.

Let us now consider a spherical solid source with uniform density. We believe that this source model roughly represents the plerions and the composite type SNRs. For this model, if $\mathbf{r}_s$ denotes the position of the center of the SNR from the Earth and $\mathbf{r}_0$ represents the position of the source CRs with respect to the SNR center, we can write $\mathbf{r}'$ in Eq. (3.5) as $\mathbf{r}' = \mathbf{r}_s + \mathbf{r}_0$ and then rewrite Eq. (3.5) as,

$$N_p(E,t) = \frac{q(E)}{8\left[\pi D(t-t_0)\right]^{3/2}} \int d\mathbf{r}_0 \exp\left[\frac{-(\mathbf{r}_s+\mathbf{r}_0)^2}{4D(t-t_0)}\right] q(\mathbf{r}_0) \tag{3.9}$$

In Eq. (3.9), the integral over the volume element in spherical geometry is given by,

$$\int d\mathbf{r}_0 = \int_0^R r_0^2\, dr_0 \int_0^\pi \sin\theta_0\, d\theta_0 \int_0^{2\pi} d\phi_0$$

where R denotes the radius of the SNR. We take the source spectrum in this case as $q(E) = q_p(E)/V$ where $q_p(E)$ is the source spectrum we took in the case of the point source approximation (section 2.1) and $V = \frac{4}{3}\pi R^3$ represents the total SNR volume. We assume that CRs are uniformly distributed throughout the SNR volume before releasing into the ISM and take the spatial source term as,

$$q(r_0) = \begin{cases} 1, & \text{for } r_0 \le R \\ 0, & \text{otherwise} \end{cases} \tag{3.10}$$

Integrating Eq. (3.9) over θ_0 and ϕ_0, we get

$$\begin{aligned} N_p(E,t) = {} & \frac{q_p(E)}{r_s V\sqrt{\pi D(t-t_0)}} \exp\left[\frac{-r_s^2}{4D(t-t_0)}\right] \\ & \times \int_0^R r_0 \exp\left[\frac{-r_0^2}{4D(t-t_0)}\right] \sinh\left(\frac{r_s r_0}{2D(t-t_0)}\right) dr_0 \end{aligned} \tag{3.11}$$

Using the properties $\sinh(x) \approx x$ and $e^x \to 1$ for very small x, it is easy to check that for very small R, Eq. (3.11) reduces to the point source solution (Eq. 3.7) at all energies.

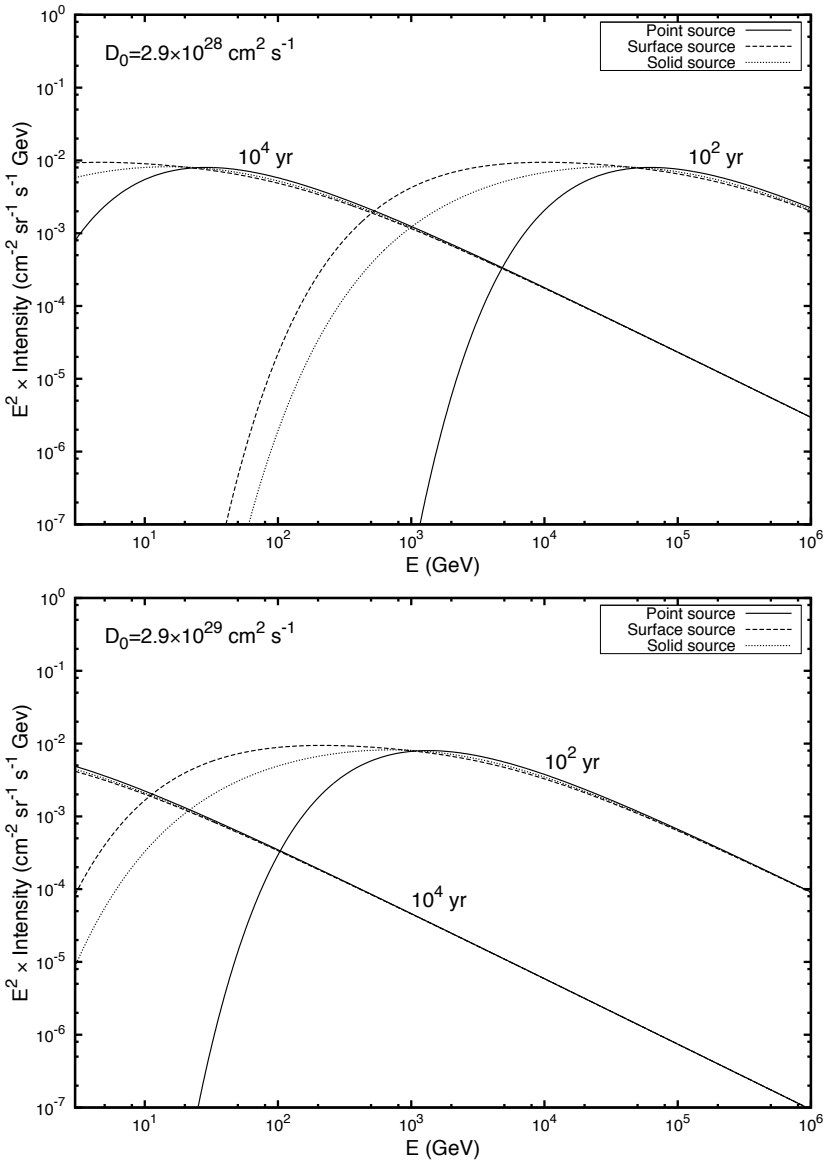

Figure 3.1: CR proton spectra from an SNR with distance $r_s = 0.15$ kpc at different times $t = 10^2$ yr and 10^4 yr for different source models: point source (solid line), surface source (dashed line), solid source (dotted line). We consider an energy independent burst-like injection of CRs at $t_0 = 0$ and we take $\Gamma = 2.0$, $\delta = 0.6$ and $E_0 = 3$ GeV. Top: $D_0 = 2.9 \times 10^{28}$ cm^2 s^{-1}. Bottom: $D_0 = 2.9 \times 10^{29}$ cm^2 s^{-1}.

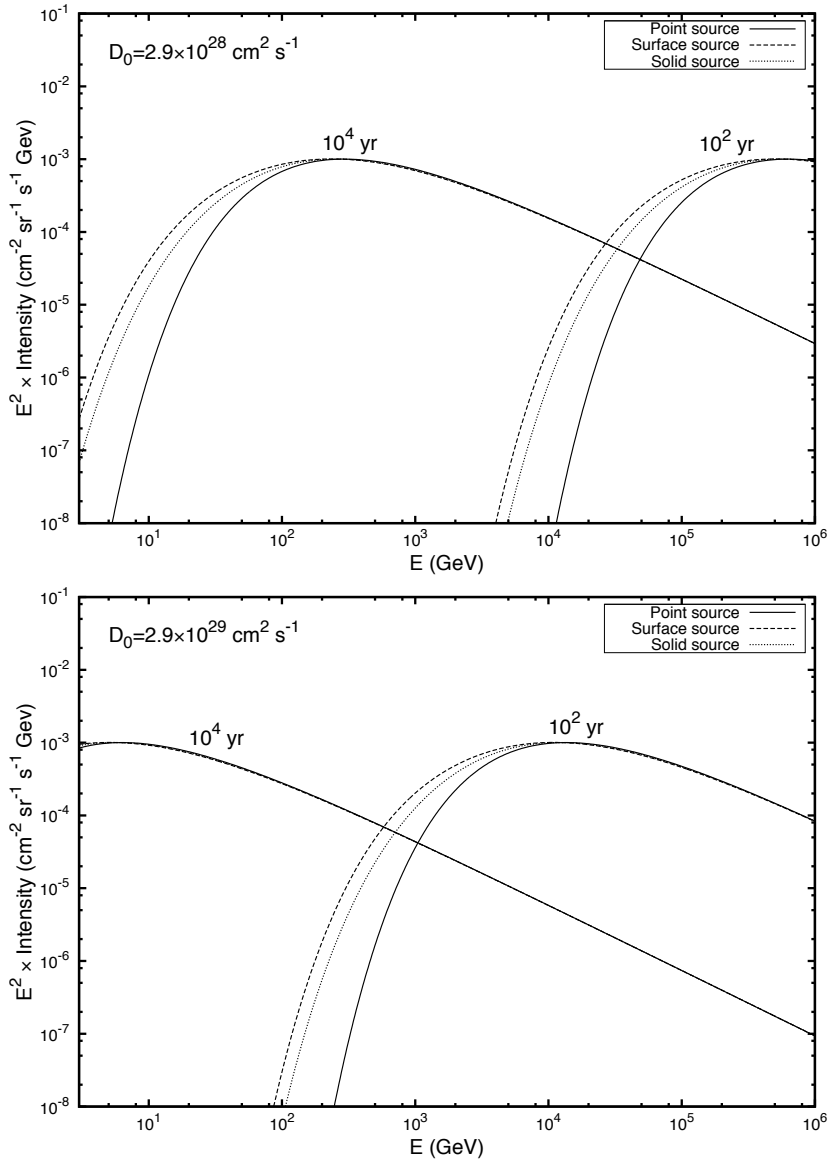

Figure 3.2: Same as in Figure 3.1 but for $r_s = 0.3$ kpc.

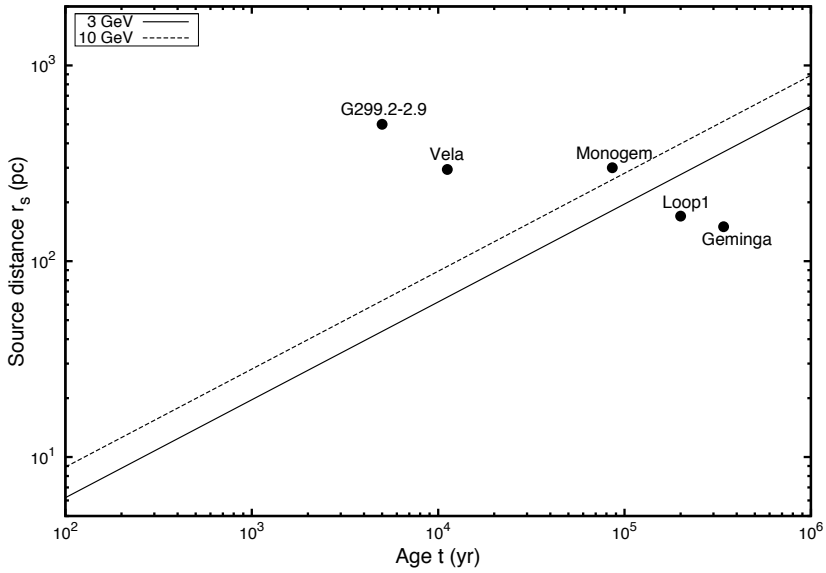

Figure 3.3: Source age t versus distance r_s plot for $E_{pt} = 3$ GeV and 10 GeV energies. The area below each line represents the (r_s, t) parameters space where the point source represents a good approximation for energies $E > E_{pt}$. We assume $D_0 = 2.9 \times 10^{28}$ cm ^{2} s^{-1}, $\delta = 0.6$, $E_0 = 3$ GeV and $t_0 = 0$ for our calculation. The black dots represent the nearby known SNRs with distances ≤ 500 pc (see Table 3.1).

3.2.3 Spherical surface source

If we assume that the CRs are distributed uniformly only on the surface of the SNR before they are released, the spatial source term in Eq. (3.9) can be written as,

$$q(r_0) = \delta(r_0 - R) \tag{3.12}$$

and the source spectrum as $q(E) = q_p(E)/A$, where $A = 4\pi R^2$ denotes the total surface area of the SNR. The CR density in this case is then obtained as,

$$N_p(E,t) = \frac{q_p(E)\,R}{r_s A\sqrt{\pi D(t-t_0)}} \exp\left[-\frac{\left(R^2+r_s^2\right)}{4D(t-t_0)}\right] \sinh\left(\frac{r_s R}{2D(t-t_0)}\right) \tag{3.13}$$

Here again, we can notice that Eq. (3.13) tends towards the point source solution for very small values of R. The spherical surface source model considered here closely represents the shell-type SNRs and it is probably more relevant than the uniform solid source model for CR studies in our Galaxy. According to the recent catalogue of Galactic SNRs, 78% of the total known SNRs are of shell-type while the remaining 12% and 4% are of composite and plerion types respectively [104].

In Figure 3.1 top panel, we compare the spectra obtained under the different source models for $t = 10^2$ yr and 10^4 yr. The calculation assumes $t_0 = 0$, the SNR distance as $r_s = 0.15$ kpc and the diffusion constant as $D_0 = 2.9 \times 10^{28}$ cm^2 s^{-1}. For our present illustration, we take the source spectral index as $\Gamma = 2$ which is the value predicted by DSA theories inside SNRs. Later on, in section 3.5 when we apply our study to the nearby known SNRs, we will use values which are determined based on the observed CR data. In Figure 3.1 top panel, we can see that for a given value of t, the point source solution (solid line) above some energy E_{pt} agrees well with the results of the surface source (dashed line) and the uniform solid source (dotted line) models, while below E_{pt} the results are quite different. E_{pt} is roughly the energy at which $r_{diff} = r_s$. We can check that for $E > E_{pt}$ for which $r_{diff} > r_s$, Eqs. (3.11) & (3.13) tend towards Eq. (3.8) which is the asymptotic solution of the point source approximation at high energies. The bottom panel shows the results for larger values of the diffusion constant $D_0 = 2.9 \times 10^{29}$ cm^2 s^{-1}. The only difference between the two sets of results is that E_{pt} is shifted towards lower values as D_0 increases. This shows that the point source becomes valid over a broader energy range as D_0 takes larger values. In order to understand the effect of the source distance, we show in Figure 3.2 the results obtained for $r_s = 0.3$ kpc by keeping all other parameters the same as in Figure 3.1. In comparing the results in Figure 3.2 to those in Figure 3.1, we can see that apart from the scaling down of the flux and the right shifting of E_{pt} due to the increased source distance, the differences between the different source models also become smaller. This is simply the geometrical effect mentioned in section 3.1, i.e. as the source distance increases, the point source approximation becomes more valid.

These results can be understood as follows. The diffusion radius $r_{diff} = \sqrt{D(t-t_0)}$, which is the effective distance from the SNR travelled by CRs due to diffusive propagation, is a strong function of D_0 and t. For a given energy, the larger the values of D_0 and/or

t, the larger is r_{diff}. This implies a decrease in the value of E_{pt} which satisfies the condition $r_{diff} = r_s$. Similarly, for larger source distances r_s, we can understand that E_{pt} shifts towards higher values. These results show that the point source can remain a valid approximation even for the nearby sources as long as the particles satisfy the condition $r_{diff} \gg (R, r_s)$. For $r_s = 0.15$ kpc, $D_0 = 2.9 \times 10^{28}$ cm^2 s^{-1} and $t_0 = 0$ (Figure 3.1 top panel), we obtain $E_{pt} = 1.2 \times 10^5$ GeV and 57 GeV for $t = 10^2$ yr and 10^4 yr respectively. The corresponding values for $r_s = 0.3$ kpc (Figure 3.2 top panel) are found to be 1.2×10^6 GeV and 575 GeV respectively. For a given age or distance, the closer or the older the source is, the lower is the E_{pt}. This is shown in Figure 3.3 for $E_{pt} = 3$ GeV (solid line) and 10 GeV (dashed line). The area below each line represents the parameter space in (r_s, t) where the point source approximation works as a good approximation for all energies above the given E_{pt}. In the same figure, the black dots represent the nearby known SNRs with distances ≤ 500 pc (see Table 3.1). We can see that only the Loop1 and the Geminga remnants lie below both lines while Monogem lies just above the 10 GeV line. The other two SNRs, Vela and G299.9-2.9 are located well above the lines. It is worth mentioning that the CR spectrum below $\sim (1-10)$ GeV is very likely to be modified by the solar modulation and hence, only those above this energy region are reliable for estimates of Galactic CR properties. Therefore, as far as the CRs of our interests are concerned, the point source approximation looks valid only for the Loop1, Geminga and the Monogem among the nearest SNRs, while for the others it appears important to take their sizes into account in the calculations. It should be noted that for distant SNRs like SN185 for which the distances $r_s \gg R$, the point source will always remain a good approximation independent of their ages. We will show this in detail in section 3.5.

The results shown in Figures 3.1 and 3.2 are obtained for the burst-like injection of particles. Let us now investigate the case of continuous injection of particles. For continuous injection for a finite time interval from 0 to T with the injection rate $q_c(E)$, the solution of Eq. (3.1) can be obtained by integrating Eq. (3.5) over the injection time as,

$$N_p(E,t) = \int_0^{t_f} dt' \int_{-\infty}^{\infty} d\mathbf{r}' \frac{q_c(E)}{8\left[\pi D(t-t')\right]^{3/2}} \exp\left[\frac{-\mathbf{r}'^2}{4D(t-t')}\right] q(\mathbf{r}') \tag{3.14}$$

where $t_f = \min[t, T]$ and $q_c(E) = q(E)/T$, $q(E)$ representing the source spectrum in the burst-like injection case which for a point source is given by $q(E) = q_p(E)$. For a point source positioned at $\mathbf{r}_s$, Eq. (3.14) becomes,

$$N_p(E,t) = \frac{q_p(E)}{4\pi r_s DT}\{\mathrm{erf}\,(\sqrt{x_2}) - \mathrm{erf}\,(\sqrt{x_1})\} \tag{3.15}$$

where,

$$x_2 = \frac{r_s^2}{4D(t-t_f)} \quad \text{and} \quad x_1 = \frac{r_s^2}{4Dt}$$

For $t < T$, $t_f = t$ which implies $x_2 = \infty$. Then, using the property of the error

function, $\mathrm{erf}(\sqrt{x_2}) = 1$ for $x_2 = \infty$, Eq. (3.15) in this case becomes,

$$N_p(E,t) = \frac{q_p(E)}{4\pi r_s DT}\{1 - \mathrm{erf}\,(\sqrt{x_1})\} \tag{3.16}$$

For high-energy particles for which the diffusion radius $r_{diff} \gg r_s$, $x_1 \to 0$, and because $\mathrm{erf}(\sqrt{x_1}) \to 0$ for $x_1 \to 0$, the spectrum given by Eq. (3.16) follows a power law of the form $N_p(E) \propto E^{-(\Gamma+\delta)}$ which is flatter than the spectrum we obtain in the burst-like injection model. A detailed discussion on this topic can also be found in Aharonian & Atoyan (1996) [19] in the study of CR spectrum in the vicinity of the sources.

For $t > T$, $t_f = T$ and $x_2 = r_s^2/4D(t-T)$. For particles with large r_{diff} for which $x_1 \to 0$, we can safely write $x_2 \ll 1$ as $(t-T) < t$. Then, using the property $\mathrm{erf}(\sqrt{x_2}) \approx 2\sqrt{x_2/\pi}$ for $\sqrt{x_2} \ll 1$, the particle spectrum (Eq. 3.15) in this case reduces to

$$N_p(E,t) \approx \frac{q_p(E)}{4(\pi D)^{3/2}T\sqrt{t-T}} \tag{3.17}$$

The spectral shape of Eq. (3.17) follows $N_p(E) \propto E^{-\left(\Gamma+\frac{3}{2}\delta\right)}$ which is the same as in the case of the burst-like injection of particles discussed earlier (Eq. 3.8).

Similarly, using Eq. (3.14) we also obtain our results for the case of the solid and the surface source models by taking into account their proper source terms given by Eqs. (3.10) and (3.12) respectively. The results are plotted in Figure 3.4 (bottom panel) for $t = (10^2, 10^4, 10^6)$ yr along with the results obtained under the burst-like injection model (top panel) for comparison. The calculations in Fig. 4 assume $r_s = 0.2$ kpc, $D_0 = 2.9 \times 10^{28}$ cm^{2}s^{-1}, $\Gamma = 2.0$ and $T = 10^5$ yr. We can see that at all t's, the effect of assuming different source models are similar in both types of injection. As discussed above, we can also see that for $t < T$ the spectra in the case of continuous injection are flatter than those in the burst-like injection case while at $t \gg T$, they exactly follow the same behavior as shown by the results at 10^6 yr.

A short conclusion that we can draw at this stage of our study is that for very old sources ($t \gg T$), the effect of choosing different source geometry or different particle injection model is negligible on the CR spectrum. Therefore, the widely adopted burst-like point source approximation remains a good approximation for very old nearby sources at all the energies. However, for young nearby sources, the spectrum at high energies strongly depends on type of the particle injection model and at lower energies, it starts to depend on the physical size and the geometry of the source irrespective of the type of the injection model unless the source is really closed to the Earth i.e., only a few pc away as shown in Figure 3.3.

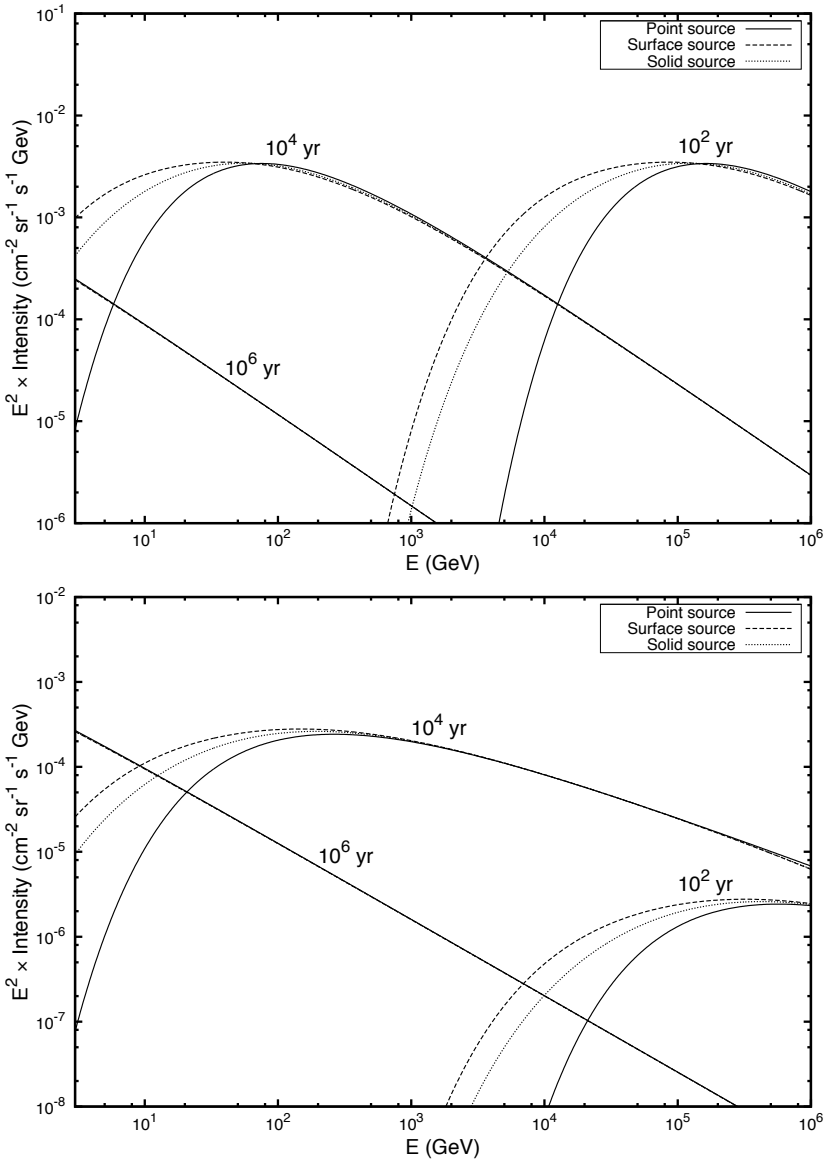

Figure 3.4: CR proton spectra for different source models from an SNR at $r = 0.2$ kpc at different times $t = (10^2, 10^4, 10^6)$ yr. Top: Burst-like injection. Bottom: Continuous injection with $T = 10^5$ yr. Other model parameters are the same as in Figure 3.1 top panel.

3.3 High energy electron spectrum from an SNR

The diffusive propagation of high energy electrons in the Galaxy can be described by the following transport equation,

$$\nabla \cdot (D\nabla N_e) + \frac{\partial}{\partial E}\{b(E)N_e\} + Q_e = \frac{\partial N_e}{\partial t} \tag{3.18}$$

where $N_e(E,t)$ is the density of electrons with kinetic energy E, $b(E) = -dE/dt$ is the energy loss rate and $Q_e(\mathbf{r}, E, t)$ denotes the electron injection rate into the ISM. The Green function of Eq. (3.18) can be obtained as given below [99, 103],

$$G_e(\mathbf{r}, \mathbf{r}', E, E', t, t') = \frac{1}{8\left[\pi f(E,E')\right]^{3/2} b(E)} \exp\left[\frac{-(\mathbf{r}'-\mathbf{r})^2}{4f(E,E')}\right] \delta\left[t' - t + g(E,E')\right] \tag{3.19}$$

where,

$$f(E,E') = \int_E^{E'} \frac{D(u)}{b(u)} du \quad \text{and} \quad g(E,E') = \int_E^{E'} \frac{1}{b(u)} du$$

For our present study, we assume that the energy loss of the electrons are due to synchrotron and inverse Compton interactions which are true mostly for energies $E \gtrsim 10$ GeV. We take,

$$b(E) = aE^2 \tag{3.20}$$

where $a = 1.01 \times 10^{-16}(w_{ph} + w_B)$ GeV s^{-1} and, w_{ph} and w_B represent the energy densities in eV cm^{-3} for the background photons and the magnetic field respectively. Eq. (3.20) assumes that the inverse Compton scattering of the background photons occurs in the Thompson regime.

The general solution of Eq. (3.18) is given by,

$$N_e(\mathbf{r}, E, t) = \int_{-\infty}^{\infty} d\mathbf{r}' \int_E^{\infty} dE' \int_{-\infty}^{t} dt' G_e(\mathbf{r}, \mathbf{r}', E, E', t, t')\, Q_e(\mathbf{r}', E, t') \tag{3.21}$$

For an energy independent burst-like injection of electrons at time t_0, we take the source term as $Q_e(\mathbf{r}', E', t') = q(\mathbf{r}')q(E')\delta(t' - t_0)$ where $q(E') \propto E'^{-\Gamma}$ denotes the source spectrum. Now, setting $\mathbf{r} = 0$ as we did for the protons in section 3.2 and performing the integrals over E' and t', Eq. (3.21) becomes,

$$N_e(E,t) = \frac{q(E)}{8(\pi C)^{3/2}} \left(1 - \frac{E}{E_t}\right)^{\Gamma-2} \int_{\infty}^{-\infty} d\mathbf{r}' \exp\left(\frac{-\mathbf{r}'^2}{4C}\right) q(\mathbf{r}') \tag{3.22}$$

where $E_t = 1/(a(t - t_0))$ is the energy at which the energy loss time is equal to $(t - t_0)$,

$$C = \frac{D(E)}{a(1-\delta)E}\left[1 - \left(1 - \frac{E}{E_t}\right)^{1-\delta}\right] \tag{3.23}$$

and δ is the index of the diffusion coefficient. Eq. (3.22) is valid for electrons with energies $E < E_t$. For $E > E_t$, $N_e = 0$.

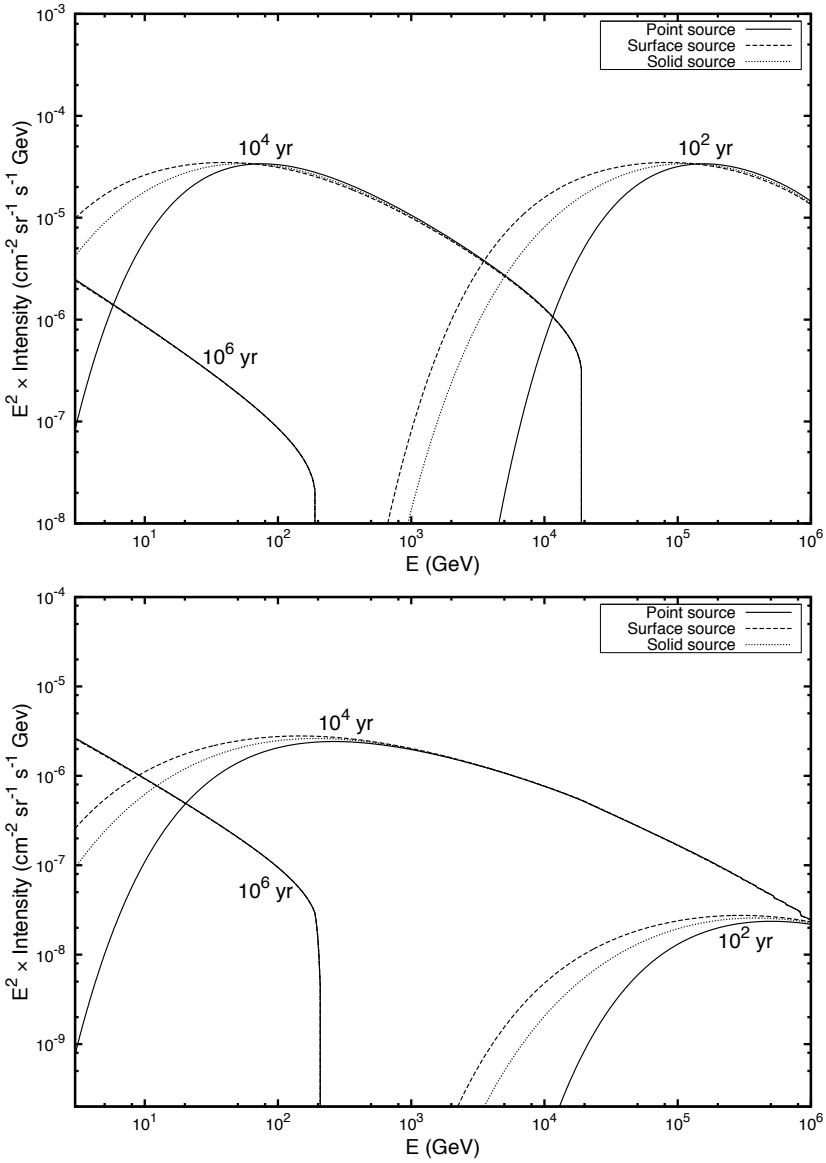

Figure 3.5: CR electron spectra for different source models from an SNR at $r_s = 0.2$ kpc. We assume $w_{MBR} = 0.25$ eV cm^{-3}, $w_{op} = 0.5$ eV cm^{-3} and the ISM magnetic field as 6μG. All other model parameters are the same as in Figure 3.4. Top: Burst-like injection. Bottom: Continuous injection.

3.3.1 Point source approximation

For a point source described by Eq. (3.6) located at a distance $\mathbf{r}_s$, the electron spectrum at time t can be obtained from Eq. (3.22) as given below,

$$N_e(E,t) = \frac{q_e(E)}{8(\pi C)^{3/2}} \left(1 - \frac{E}{E_t}\right)^{\Gamma-2} \exp\left(\frac{-\mathbf{r}_s{}^2}{4C}\right) \tag{3.24}$$

where $q_e(E) = k_e E^{-\Gamma}$ is the source spectrum for the point source. From Eq. (3.23), we can see that in the energy region $E \ll E_t$ where the effect of the energy loss is less important, $C \rightarrow D(t - t_0)$ and Eq. (24) tends towards the point source solution for CR protons (Eq. 3.7). Therefore, high energy electrons whose $r_{diff} \gg r_s$ and $E \ll E_t$ have spectrum which follows $N_e(E) \propto E^{-\left(\Gamma + \frac{3}{2}\delta\right)}$ which is similar to the asymptotic solution of high energy protons (Eq. 3.8).

3.3.2 Spherical solid source

Following exactly the same procedure as for the protons described in the previous section, the electron spectrum for the case of the uniform spherical solid source is obtained as,

$$N_e(E,t) = \frac{q_e(E)}{r_s V\sqrt{\pi C}} \left(1 - \frac{E}{E_t}\right)^{\Gamma-2} \exp\left(\frac{-r_s^2}{4C}\right) \int_0^R r_0 \exp\left(\frac{-r_0^2}{4C}\right) \sinh\left(\frac{r_s r_0}{2C}\right) dr_0 \tag{3.25}$$

3.3.3 Spherical surface source

The solution for the spherical surface source is given below,

$$N_e(E,t) = \frac{q_e(E)\, R}{r_s A\sqrt{\pi C}} \left(1 - \frac{E}{E_t}\right)^{\Gamma-2} \exp\left[-\frac{\left(R^2 + r_s^2\right)}{4C}\right] \sinh\left(\frac{r_s R}{2C}\right) \tag{3.26}$$

It is easy to check that for very small values of R, the solutions for the solid source (Eq. 3.25) and the surface source (Eq. 3.26) models reduce to the point source solution (Eq. 3.24).

The solutions we have obtained above are based on burst-like injection of electrons from the SNR. For the case of continuous injection, the solutions are given by,

$$N_e(E,t) = \int_0^{t_f} dt' \frac{q_c(E)}{8(\pi C)^{3/2}} \left(1 - \frac{E}{E'_t}\right)^{\Gamma-2} \int_\infty^{-\infty} d\mathbf{r}' \exp\left(\frac{-\mathbf{r}'^2}{4C}\right) q(\mathbf{r}') \tag{3.27}$$

where t_f and $q_c(E)$, they bear the same definitions as defined in the case of protons and $E'_t = 1/(a(t - t'))$. For a point source at $\mathbf{r}_s$, Eq. (3.27) becomes,

$$N_e(E,t) = \int_0^{t_f} dt' \frac{q_e(E)}{8(\pi C)^{3/2} T} \left(1 - \frac{E}{E'_t}\right)^{\Gamma-2} \exp\left(\frac{-\mathbf{r}_s{}^2}{4C}\right) \tag{3.28}$$

where $q_e(E)$ is the source spectrum we assumed in the case of burst-like injection (section 3.3.1). In Eqs. (3.27) and (3.28), C is given by Eq. (3.23) but with E_t replaced by E_t' in this case. Here again, we can check that for energies $E \ll E_t'$, $C \rightarrow D(t-t')$ and Eq. (3.28) reduces to a solution similar to that of the CR protons (Eq. 3.15). Therefore, the same discussions we presented in the previous section for the protons under the continuous injection model also apply to the electrons. At time $t < T$, the spectrum of high energy electrons with $E \ll E_t'$ and whose diffusion radii $r_{diff} \gg r_s$ follow $N_e(E) \propto E^{-(\Gamma+\delta)}$ and at $t > T$, they follow $N_e(E) \propto E^{-\left(\Gamma+\frac{3}{2}\delta\right)}$ which is similar to the result obtained in the burst-like injection model (section 3.3.1). More discussions on the different types of electron spectra generated by a CR source under different particle injection models can also be found in [39].

Using Eq. (3.27), we also calculate the spectra for the solid and the surface sources under the continuous injection model. The results are plotted in Figure 3.5 (bottom panel) for $t = (10^2, 10^4, 10^6)$ yr. The top panel shows the results for the case of burst-like injection. The calculations assume $\Gamma = 2.0$, $\delta = 0.6$, $D_0 = 2.9 \times 10^{28}$ cm^2 s^{-1}, $r_s = 0.2$ kpc, $T = 10^5$ yr and $t_0 = 0$. The magnetic field in the ISM is taken as 6μG (Beck 2001). The total energy density of the background photon field is assumed to be $w_{ph} = w_{MBR} + w_{op}$, where $w_{MBR} = 0.25$ eV cm^{-3} is the energy density of the microwave background and $w_{op} = 0.6$ eV cm^{-3} that of the ultraviolet-NIR-optical radiation field. The latter is taken from the estimates given in [168] for the galactocentric distance of 8.5 kpc which they obtain using the data provided by GALPROP [160]. On comparing Figure 3.5 top and bottom panels, we can notice that at $t < T$ apart from the difference in the slope of the spectra, there are sharp spectral breaks present in the case of burst-like injection. These are due to the effect of fast energy loss rate for high energy electrons. Electrons with energy $E > E_t$ are lost before reaching the Earth. We also notice that the differences between the different source models below E_{pt} are similar in both the types of injection model. At very late times $t \gg T$, the spectra become independent of the injection model or of the source model and they exhibit the same shape with breaks at $E = E_t$.

On comparing the results of electrons (Figure 3.5) to those of the protons (Figure 3.4), we can see that except for the presence of spectral breaks in the case of electrons, the results are quite similar in all other respects. Even the differences between the results obtained for different source models are similar. Therefore, the overall conclusions on the validity of the point source approximation that we had drawn earlier for the protons also apply to the electrons.

3.4 Energy dependent CR escape from SNRs

So far, we have only considered a simple model of CR escape from the SNRs where CRs of all energies are assumed to escape at the same time independent of energy. However, detailed theoretical studies suggest that their escape mechanism can be more complex which may be strongly related with the acceleration process itself and depends on the shock dynamics as well as on the particle energies and their back reaction on the shocks [142, 163].

As already mentioned in section 3.1, under DSA theory CRs are assumed to be confined by the magnetic turbulence generated by the CRs themselves. They cannot escape the remnant as long as their upstream diffusion length normally defined as $l_{diff} = D_s(E)/u_s$ is less than the escape length from the shock front which is usually taken as $l_{esc} = \xi R_s$, where u_s and R_s denote the shock velocity and the shock radius respectively and the constant $\xi \sim (0.01 - 0.1)$ (see [163] and references therein). In the Bohm diffusion limit where the maximum confinement is achievable, the upstream diffusion coefficient depends on the particle energy and the upstream magnetic field B_s as $D_s(E) \propto E/B_s$. Under this condition, the escape energy E_{esc} follows,

$$E_{esc} \propto B_s R_s u_s \tag{3.29}$$

There are strong theoretical arguments which suggest that CRs might amplify the magnetic fields near the shock surface [65]. This idea is also supported experimentally by the recent observations of thin X-ray filaments inside several SNRs, which are most likely synchrotron emissions of high energy electrons in the presence of strong magnetic fields of the order of $\sim (100 - 1000)\mu$G [192]. Taking such possible amplification into account, we can assume that the magnetic field scales with the shock velocity as $B_s \propto u_s^d$, with the index d representing the degree of amplification. Some studies suggest that d can reach values as high as 1.5 [46].

One reasonable assumption of DSA theory is that CRs do not escape during the free expansion phase of the SNR evolution. It is because shock waves traveling at some constant velocity can always overtake particles undergoing diffusive motion [82]. However, during the Sedov phase when the shock velocity decreases with the age t as $u_s \propto t^{-0.6}$ and the shock radius increases as $R_s \propto t^{0.4}$, some of the high energy CRs can start escaping because of their relatively larger diffusion length ($l_{diff} > l_{esc}$). Therefore, under the Sedov scaling, the escape energy at any stage during the evolution can be obtained using Eq. (3.29) as,

$$E_{esc} \propto t^{-(0.2+0.6d)} \tag{3.30}$$

This gives,

$$E_{esc} \propto \begin{cases} t^{-0.2}, & \text{for } d = 0 \\ t^{-1.1}, & \text{for } d = 1.5 \end{cases} \tag{3.31}$$

In deriving Eq. (3.31), we assume that $D_s(E)$ scales linearly with E. But, the exact dependence is still not well understood and depends on some poorly known yet important quantities like the spectral distribution of the self-excited turbulence waves, their dissipation rate and their CR scattering efficiencies. Moreover, magnetic field amplification and the dynamical reaction of the accelerated particles on the shock structure are also not fully understood. Due to these uncertainties, a simple but reasonable approach which is commonly followed is to parameterize the escape energy as given below [94, 153],

$$E_{esc} = E_{max} \left(\frac{t}{t_{sed}} \right)^{-\alpha} \tag{3.32}$$

where E_{max} is the maximum CR energy and t_{sed} denotes the start of the Sedov phase. We assume $E_{max} = 10^6$ GeV ($= 1$ PeV) and $t_{sed} = 500$ yr for our study. Eq. (3.32) assumes that the escape of the highest energy particles start at the onset of the Sedov phase itself. For detailed studies of particle escape from SNRs, see e.g. [64, 65, 163]. Using Eq. (3.32), we can calculate the escape time t_{esc} as a function of energy as,

$$t_{esc}(E) = t_{sed} \left(\frac{E}{E_{max}} \right)^{-1/\alpha} \tag{3.33}$$

At some later stage of the SNR evolution when the shock slows down and does not efficiently accelerate the CRs, the turbulence level in the vicinity of the shock goes down and no particles can remain confined effectively within the remnant. At this stage, we can assume that all the CRs escape into the ISM. As previously mentioned, for an ISM density of 1 H cm^{-3}, this happens at around 10^5 yr after the supernova explosion [49]. Taking this into account, the CR escape time for our study is taken as,

$$T_{esc}(E) = \min \left[t_{esc}(E), 10^5 \mathrm{yr} \right] \tag{3.34}$$

Using the Sedov relation between the shock radius and the SNR age, we can also calculate the escape radius R_{esc} which we define as the radius of the SNR at the time when CRs of energy E escape as follows,

$$R_{esc}(E) = 2.5 v_0 \, t_{sed} \left[\left(\frac{T_{esc}}{t_{sed}} \right)^{0.4} - 0.6 \right] \tag{3.35}$$

In Eq. (3.35), v_0 represents the initial shock velocity, i.e the velocity at $t = t_{sed}$ which we take as 10^9 cm/s for our study.

Eq. (3.34) is plotted in Figure 3.6 (top panel) where different lines correspond to different values of α: solid (0.2), dashed (1.1) and dotted (2.0). The plots show that even for the fixed values of E_{max} and t_{sed}, the energy dependence of $T_{esc}(E)$ strongly depends on the value of α. For $\alpha = 0.2$, except for particles with energies greater than 3.5×10^5 GeV all the particles remain confined till the end of the SNR evolution. As the value of α increases, lower energy particles start escaping at relatively early stages. For $\alpha = 1.1$ and 2.0, only particles with energies up to 3×10^3 GeV and 25 GeV respectively are confined till the end of the evolution. The bottom panel shows the corresponding values of $R_{esc}(E)$ calculated using Eq. (3.35). For the assumed value of v_0, CRs escape starts when the remnant expands to a radius of ~ 5 pc and continues until it expands up to ~ 100 pc. The latter value denotes the maximum CR confinement radius in our study.

For our calculations in the following, we will assume that at the time of escape from the SNRs, CRs are distributed uniformly at the shock surface. This assumption is similar to that of the spherical surface source discussed in sections 3.2 and 3.3.

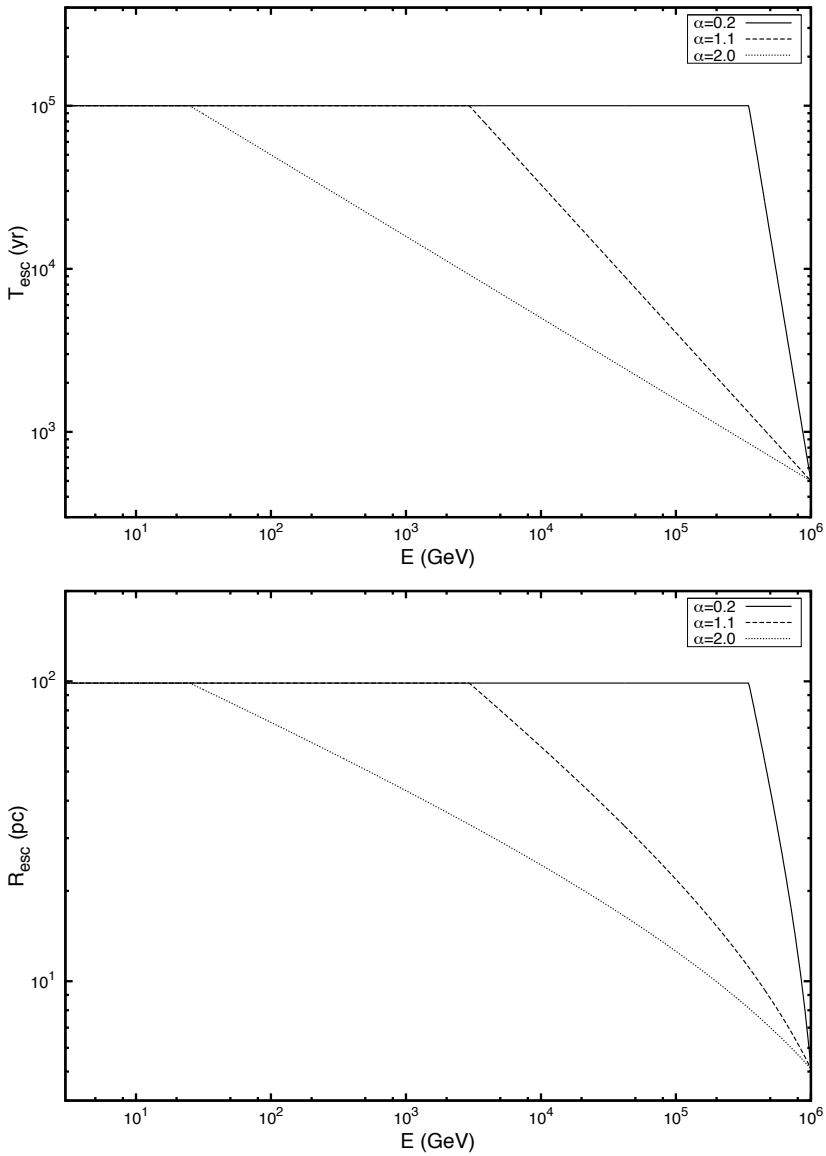

Figure 3.6: CR escape time (top) and escape radius (bottom) for an SNR under the energy dependent escape model for different values of α: 0.2 (solid line), 1.1 (dashed line), 2.0 (dotted line). We assume $E_{max} = 10^6$ GeV and $t_{sed} = 500$ yr.

3.4.1 CR proton spectrum from an SNR

For CR protons, the source term components in the energy dependent escape model can be written as,

$$\begin{aligned} q(r_0) &= \delta(r_0 - R_{esc}) \\ q(E) &= \frac{q_p(E)}{A_{esc}} \\ q(t') &= \delta(t' - T_{esc}) \end{aligned} \tag{3.36}$$

where $q_p(E)$ is the point source spectrum given in section 2.1, T_{esc} and R_{esc} are given by Eq. (3.34) and Eq. (3.35) respectively and $A_{esc} = 4\pi R_{esc}^2$. Now, the proton spectrum in this case is obtained using Eq. (3.13) by substituting the above source parameters as,

$$N_p(E,t) = \frac{q_p(E)\, R_{esc}}{r_s A_{esc}\sqrt{\pi D(t - T_{esc})}} \exp\left[-\frac{\left(R_{esc}^2 + r_s^2\right)}{4D(t - T_{esc})}\right] \sinh\left(\frac{r_s R_{esc}}{2D(t - T_{esc})}\right) \tag{3.37}$$

In Figure 3.7, we show the proton spectra calculated using Eq. (3.37) for a source at $r_s = 0.2$ kpc at different times $t = (10^3, 10^4, 10^5, 10^6)$ yr. The dashed lines correspond to $\alpha = 1.1$ and the solid lines to $\alpha = 2.0$. The sharp breaks in the spectra are due to the effect of the energy dependent escape time of the particles. Particles with energies below the breaks have not yet been escaped from the SNR or even if they do, they have not yet reached the Earth at the given time t. The effect of choosing different values of α is clearly visible. For $\alpha = 1.1$, the spectra at all times except for $t \gg 10^5$ yr peak at relatively higher energies compared to those for $\alpha = 2$. This is because particles at all energies except for those which remain till the end of the evolution are confined for relatively longer period in the case of $\alpha = 1.1$ (see Figure 3.6 top panel). Looking into the individual spectrum, we can also see that at high energies it follows a power-law spectrum as $N_p(E) \propto E^{-\left(\Gamma + \frac{3}{2}\delta\right)}$. This can be understood from Eq. (3.37) which shows that for particles with large diffusion radius $r_{diff} \propto \sqrt{D(t - T_{esc})}$, the solution reduces to that of the point source approximation at high energies (Eq. 3.8). An additional effect of large r_{diff} is that the spectra at the highest energies for the two different α's are very similar. These high energy particles are those which escaped the remnant long ago and their $r_{diff} \gg (R_{esc}, r_s)$ so that they have already passed the Earth at the given time. For these particles, the expected spectrum is almost independent of the chosen values of α, T_{esc} and R_{esc}. This is more clearly visible in the results obtained for $t = 10^6$ yr where the two spectra are almost identical to each other over the energy range considered here.

Although taking different values of α result into different types of spectrum especially at the lower energies at a given time, hereafter we will adopt $\alpha = 2.0$ for our study. The effects of choosing other values of α on our results will be discussed later in section 3.6.

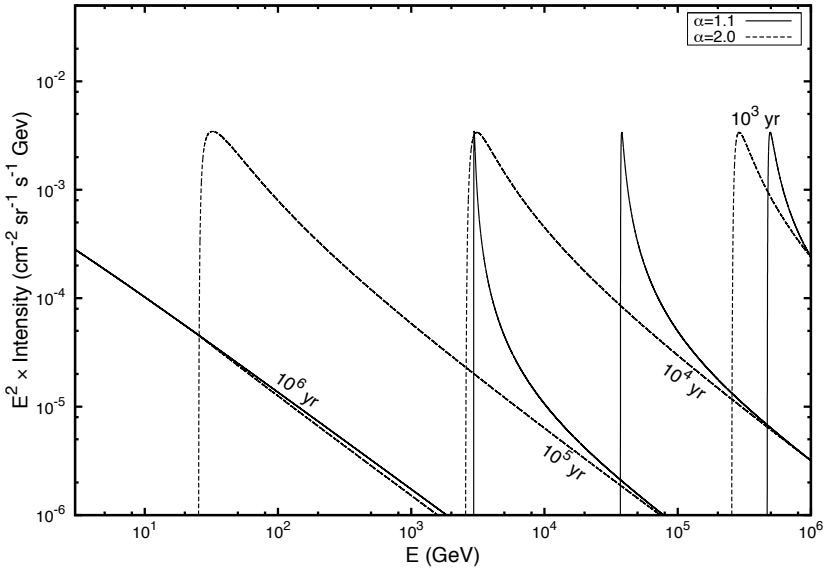

Figure 3.7: CR proton spectra at different times $t = (10^3, 10^4, 10^5, 10^6)$ yr under the energy dependent escape model for $\alpha = 1.1$ (solid line) and 2.0 (dashed line). We assume $r_s = 0.2$ kpc, $\Gamma = 2.0$, $D_0 = 2.9 \times 10^{28}$ cm^2 s^{-1}, $\delta = 0.6$, $E_0 = 3$ GeV, $E_{max} = 10^6$ GeV and $t_{sed} = 500$ yr.

3.4.2 High energy electron spectrum from an SNR

To proceed, we recall Eq. (3.26) which represents the electron spectrum $N_e(E)$ for the spherical surface source obtained under the energy independent escape model. In that equation, electrons of energy E observe at time t had an initial energy E' at the time of their escape given by,

$$E' = \frac{E}{1 - aE(t - t_0)} \tag{3.38}$$

where t_0 denotes the escape time from the SNR. We can reverse the situation and calculate the energy of an electron after time t for a given initial energy E' as,

$$E = \frac{E'}{1 + aE'(t - t_0)} \tag{3.39}$$

For an energy dependent escape, we can now substitute t_0 by $T_{esc}(E')$ and rewrite Eq. (3.39) as follows,

$$E = \frac{E'}{1 + aE'\left[t - T_{esc}(E')\right]} \tag{3.40}$$

If $q_e(E')$ represents the source spectrum of electrons with initial energy E' which escape the remnant at time $T_{esc}(E')$, their energy E at time t is given by Eq. (3.40) and their number density is obtained using Eq. (3.26) as given below,

$$N_e(E,t) = \frac{q_e(E')\, R'_{esc}}{r_s A'_{esc}\sqrt{\pi C'}} \left[1 + aE'(t - T'_{esc})\right]^2 \exp\left[-\frac{\left(R'^2_{esc} + r_s^2\right)}{4C'}\right] \times \sinh\left(\frac{r_s R'_{esc}}{2C'}\right) \tag{3.41}$$

where C' is given by,

$$C' = \frac{D(E')}{a(1-\delta)E'}\left\{1 - \left[1 + aE'(t - T'_{esc})\right]^{\delta - 1}\right\} \tag{3.42}$$

and $R'_{esc} \equiv R_{esc}(E')$, $T'_{esc} \equiv T_{esc}(E')$ and $A'_{esc} \equiv A_{esc}(E')$.

Using Eq. (3.41), we calculate the electron spectra at different t's for a source distance $r_s = 0.2$ kpc. The results are shown in Figure 3.8. On comparing with the results obtained for the protons shown in Figure 3.7 ($\alpha = 2.0$), one can notice that the major difference is the presence of additional breaks at higher energies which are due to the effect of radiative energy losses. The breaks at the lower energies which are due to the effect of T_{esc} are seen at the same energies for both the type of particles. The electron spectrum between the breaks follow an exponent $\Gamma + \frac{3}{2}\delta$ similar to the proton spectrum and at very late times (say at $t = 10^6$ yr), it also tends towards the point source solution. These results show that also in the case of energy dependent escape scenario, for very old sources ($t \gg 10^5$ yr) the spectrum at all energies can be well approximated by the simple point source solution.

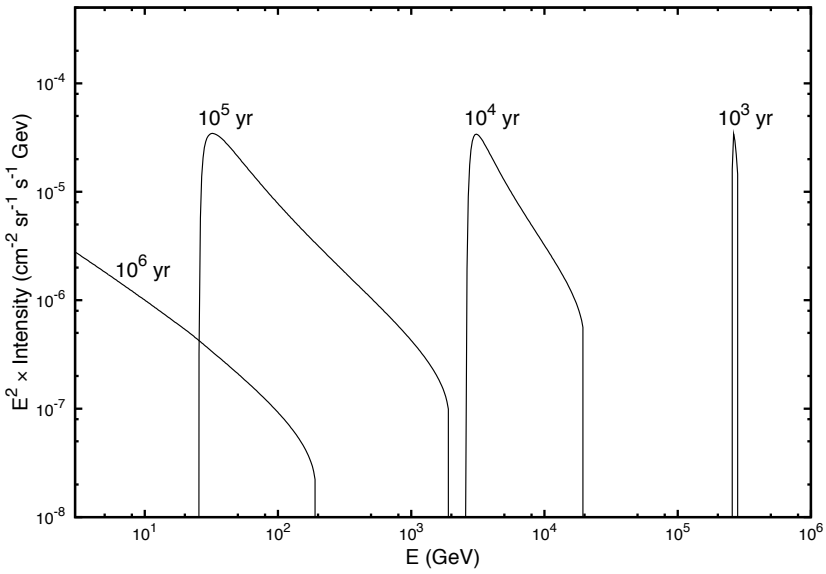

Figure 3.8: CR electron spectra at different times under energy dependent escape model for $\alpha = 2.0$. Other model parameters are same as in Figure 3.7.

3.5 Application to the nearby SNRs

In this section, we shall apply our study to the nearby known SNRs listed in Table 3.1 with distances < 1 kpc from the Earth. It should be mentioned that some of the age and the distance parameters listed in Table 1 carry large uncertainties. For instance, the distance to Geminga was measured to be 157 pc using Hubble Space Telescope (HST) observations [66] but recently, again using HST measurements, Faherty et al. 2007 reported the distance of Geminga to be 250 pc [92]. For Cygnus Loop, Minkowski 1958 reported a distance of 770 pc [146] whereas measurements based on HST observations claimed a distance of 440 pc [54]. Recent measurements further claimed the distance to be 540 pc [53] (Blair et al. 2005). For HB21, Tatematsu et al. 1990 measured a distance of 800 pc [181] and Leahy & Aschenbach 1996 estimated an age of 1.9×10^4 yr [137] while later, Byun et al. 2006 suggested a distance of 1.7 kpc [63] and Lazendic & Slane 2006 estimated an age of 5.6×10^3 yr [135]. Leahy & Aschenbach 1995 estimated the distance and age of HB9 as 1 kpc and 7.7×10^3 yr respectively [136], and Leahy & Tian 2007 suggested a distance of 800 pc with sedov age of 6.6×10^3 yr and age of $(4 - 7) \times 10^3$ yr based on evaporation cloud model [138]. The lack of precise informations on these parameters can affect our results because of the strong dependence of the CR spectrum on these parameters.

For our study, we will assume that the proton source index $\Gamma = 2.13$ so that for $\delta = 0.6$, we get $\Gamma + \delta = 2.73$ the observed proton spectral index at the Earth [108]. It should

Table 3.1: Parameters of known SNRs with distances < 1 kpc from the Earth. *For the age we take the mean of 2700 yr and 4300 yr reported in the literature.

SNR	Distance (kpc)	Age (yr)	References
Cygnus Loop	0.540	1.0×10^4	[53]
HB21	0.800	1.9×10^4	[137, 181]
HB9	0.800	6.6×10^3	[138]
S147	0.800	4.6×10^3	[60]
Vela	0.294	1.12×10^4	[67, 145]
G299.2-2.9	0.500	5.0×10^3	[126]
SN185	0.950	1.8×10^3	[170]
Monogem	0.300	8.6×10^4	[158]
Geminga	0.157	3.4×10^5	[66]
Loop1	0.170	2.0×10^5	[84]
G114.3+0.3	0.700	4.1×10^4	[126]
Vela Junior	0.750	3.5×10^3	[130]*

be noted that the value of the source index can depend on the choice of the propagation model and different propagation models may take different values. For instance, models based on diffusive re-acceleration in the Galaxy favors a diffusion index of $\delta \sim 0.3$ which corresponds to a source index of $\Gamma \sim 2.4$ [189]. This is steeper than the value adopted in our present work which is based on a purely diffusive model of CR propagation. For the CR electrons, to get the source index, we first determine the background spectrum. This is done by fitting the observed data between $(10 - 200)$ GeV provided by the FERMI and the PAMELA experiments [13, 16]. We assume that this is the energy region where the contamination due to the local sources as well as the effect of the solar modulation are minimum. From the fit, the background spectral index is found to be 3.10 ± 0.01. Under diffusive propagation model, CR electrons produced by a uniform and stationary source distribution, and subject to radiative losses during their propagation in the Galaxy results into an equilibrium spectrum given by $E^{-(\Gamma+1-\beta)}$ where $\beta = (1-\delta)/2$ (see e.g. [187]). Using the value of the background index obtained from the fit, we get the electron source index as $\Gamma = 2.3$. This is the value we will adopt for the rest of our calculations for the electrons. Furthermore, in the following we will assume that 10% of the supernova explosion energy of 10^{51} ergs converts into CR protons and 0.1% into the electrons. All these parameters are assumed to be the same for all the SNRs.

3.5.1 CR protons

First, we compare the results of the point source approximation with those of the spherical solid and the surface source models which are all based on the energy independent escape model. These are shown in Figure 3.9 where different lines represent different source model:

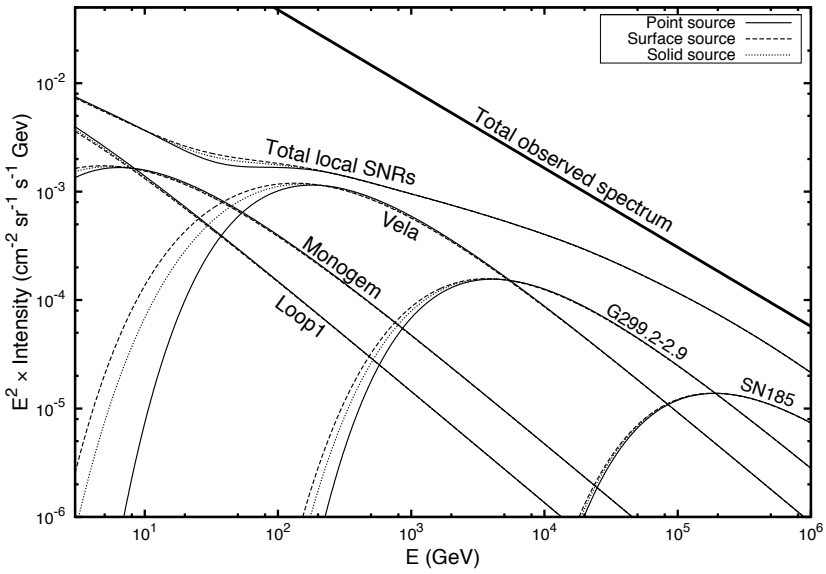

Figure 3.9: CR proton spectra from nearby SNRs listed in Table 3.1 for the three different source models: point source (solid line), surface source (dashed line) and solid source (dotted line). The contributions from the individual SNRs are labelled by their names and their total contributions as "Total local SNRs". The thick solid line represents the fitted total observed spectrum, $1.37 \times (E/\mathrm{GeV})^{-2.73}$ cm^{-2} s^{-1} sr^{-1} GeV^{-1} taken from [108]. Our calculation assumes an energy independent burst-like injection of particles at $t_0 = 0$ and that each SNR produces 10^{50} ergs of CR protons. Other model parameters: $\Gamma = 2.13$, $D_0 = 2.9 \times 10^{28}$ cm^2 s^{-1}, $\delta = 0.6$ and $E_0 = 3$ GeV.

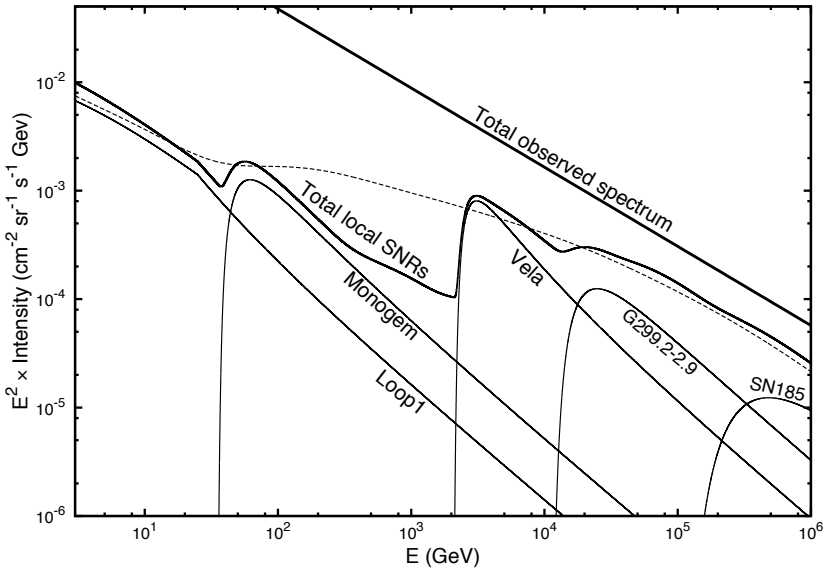

Figure 3.10: Same as in Figure 3.9 but for an energy dependent escape model. We assume $\alpha = 2.0$, $E_{max} = 10^6$ GeV and $t_{sed} = 500$ yr. The dashed line represents the "Total local SNRs" we obtained in the case of the point source approximation shown in Figure 3.9.

thin solid (point), dashed (surface) and dotted (solid). The thick solid line represents the fitted observed proton spectrum given in [108]. The calculation assumes a burst-like injection of CRs at time $t_0 = 0$. The contributions from the dominant SNRs in different energy intervals are indicated by their names. Although some of the individual SNRs like the Vela and the G299.2-2.9 show different spectra at low energies under the different source models, the differences are not significant in the total combined spectrum from the nearby SNRs. It is because at low energies below ~ 60 GeV, the dominant contributions are from Monogem and Loop1 whose spectra do not show any differences between the models because of their old ages. Although different SNRs dominate at different energy intervals, their total spectrum looks smooth except for a slight dent somewhere between $\sim (10 - 100)$ GeV.

We have also checked the results for other values of $t_0 \leq 10^5$ yr. Except for the signatures of the absence of young sources as t_0 takes larger values, we have found that their total spectra does not show any significant differences between the different source models at all values of t_0.

When we apply the energy dependent escape model, we find that the results are significantly different from those of the energy independent models. This is shown in Figure 3.10. The dashed line represents the total spectrum we obtain for the point source approximation shown in Figure 3.9. We can see that the total spectrum in the energy dependent case show irregular structures which are due to the low energy spectral breaks of the individual SNRs. However, such features can remain embedded in the dominant CR background and may not be distinctly visible in the observed spectrum.

3.5.2 Electrons

The electron spectra for the point, solid and the surface source models are shown in Figure 3.11. In the figure the data are from the FERMI [13], PAMELA [16] and the H.E.S.S [24, 26] experiments. As in the case of protons, the total electron spectra also do not show any differences between the different models. However, unlike in the case of the protons, the total electron spectra show some irregular features near the highest energies which are due to the effects of sharp cut-offs in the individual spectra due to radiative energy losses. For instance, the strong peak at $E \sim 10^5$ yr is due to the effect of SN185. From the figure, we can notice that at energies greater than few TeVs our results which are based on a pure power-law source spectrum significantly over predicts the data. Taking larger values of t_0 can suppress the contributions of Vela, G299.2-2.9 and SN185 which are the dominant contributors at high energies. For $t_0 = 2 \times 10^4$ yr, their contributions will be completely removed. This points towards the importance of source modeling in order to understand the contribution of local sources in the high energy electron spectrum. One common way to handle this problem is to assume an exponential cut-off $\exp(-E/E_c)$ in the source spectrum at a few TeVs [78]. Another possibility is that the high energy electrons might have suffered significant energy losses within the SNR itself before they are released into the ISM [187]. Therefore, electrons at higher energies might be released with a spectrum steeper than the lower energy ones. For the present study, we adopt the much simpler exponential cut-off

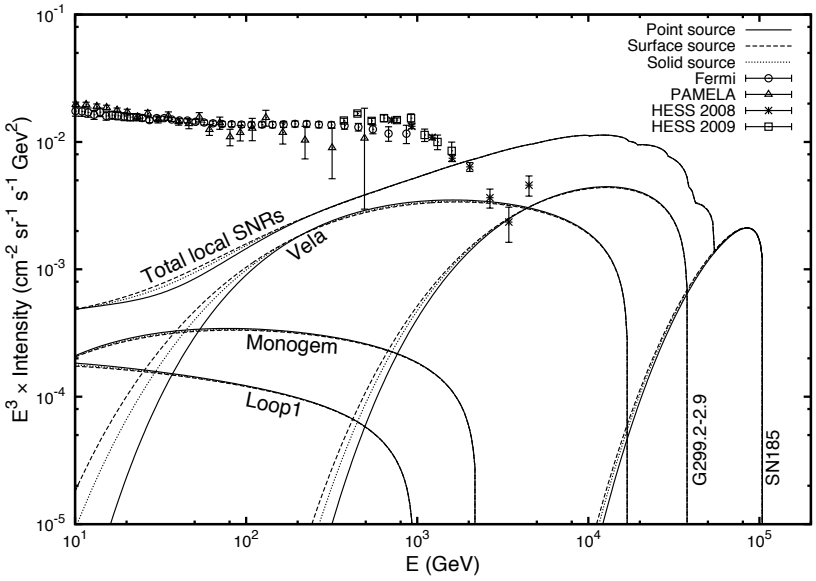

Figure 3.11: Electron spectrum from the nearby SNRs listed in Table 3.1 for the three different source models: point source (solid line), surface source (dashed line) and solid source (dotted line). We assume a burst-like injection of particles and a pure power-law source spectrum of index $\Gamma = 2.3$ with each SNR producing 10^{48} ergs of CR electrons. All other model parameters remain the same as in Figure 3.9. The data are taken from the FERMI, PAMELA and H.E.S.S experiments.

and in Figure 3.12, we show the results obtained for $E_c = 2$ TeV. We can see that the shape of the total local spectrum in the TeV region is now determined mostly by the exponential cut-off and the irregular structures present near the highest energies in Figure 3.11 no longer exist. In Figure 3.12, the thick dashed line represents the background spectrum (which we obtain as mentioned before) with an index 3.1 and an exponential cut-off at 2 TeV. The thick solid line represents the total background plus the nearby SNRs contribution obtained in the point source approximation. Detailed calculations of the background spectrum taking into account the various source models discussed here will be presented elsewhere.

For the energy dependent escape model, the results are shown in Figure 3.13 for a pure power-law source spectrum. In the figure, we also show for comparison the total local spectra obtained in the case of the point source approximation (dashed line in Figure 3.11). The total spectrum show several irregular features and spikes. These features are stronger than those present in the proton spectrum which is due to the presence of additional breaks in the individual electron spectra at high energies. The position of these spikes not only depends on the age and distance of the individual SNRs but also on the assume energy dependent escape model (i.e., on the parameters α, t_{sed} and E_{max}).

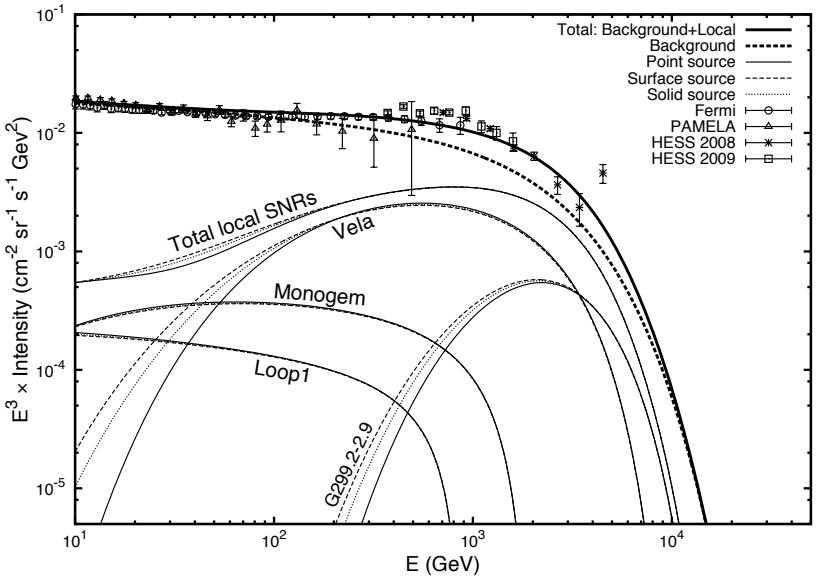

Figure 3.12: Same as in Figure 3.11 but for a source spectrum with an exponential cut-off at $E_c = 2$ TeV. The thick dashed line represents the background spectrum (see text for details) and the thick solid line represents the total background plus nearby SNRs in the point source approximation. The data are the same as in Figure 3.11.

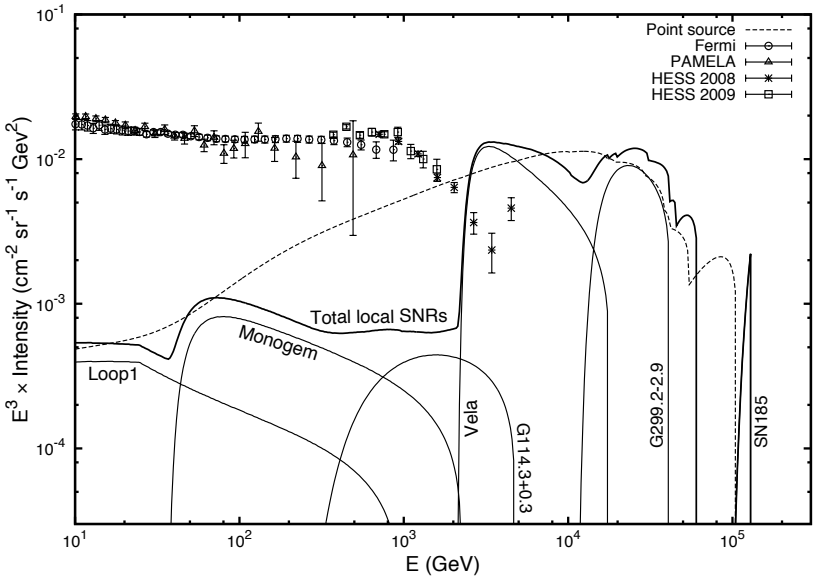

Figure 3.13: Electron spectrum from nearby SNRs for the energy dependent injection model and a pure power-law source spectrum. The dashed line represents the "Total local SNRs" obtained under the point source approximation shown in Figure 3.11. We assume $\alpha = 2.0$, $E_{max} = 10^6$ GeV and $t_{sed} = 500$ yr. The data and all other model parameters remain the same as in Figure 3.11.

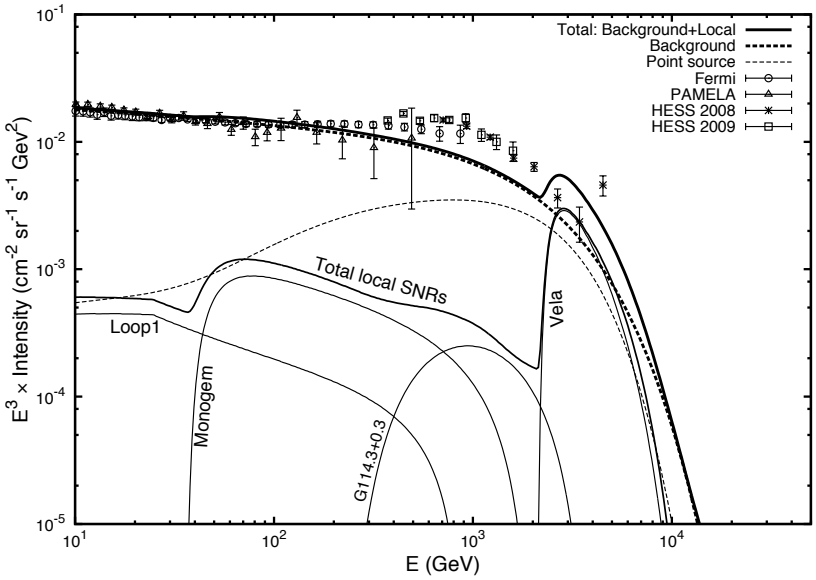

Figure 3.14: Same as in Figure 3.13 but for a source spectrum with an exponential cut-off at $E_c = 2$ TeV. The thick dashed line represents the background spectrum and the thin dashed line represents the "Total local SNRs" for the point source approximation shown in Figure 3.12. The data are the same as given in Figure 3.11.

In Figure 3.14, we show the electron spectra obtained using the same model as in Figure 3.13 but with an exponential cut-off in the source spectrum at $E_c = 2$ TeV. In the figure, the thin and the thick dashed lines represent the local SNRs contribution in the case of the point source approximation and the background spectrum respectively as shown in Figure 3.12. The thick solid line denotes the total background plus local spectrum for this case. We can notice that even after imposing the cut-off some prominent features still remain at few TeVs in the overall total spectrum unlike in the point source approximation where the cut-off almost smoothens the total spectrum.

3.6 Overall results and discussions

We have shown that the commonly adopted point source approximation does not always remain a good approximation as far as nearby CR sources are concerned. For a typical source distance of $r_s \sim (100 - 300)$ pc, we have shown that at low energies, the point source results for young sources (typically $t \lesssim 10^5$ yr) differ significantly from those calculated using a finite source size. At high energies the point source still remains a good approximation. Under the energy *independent* particle escape model, we found that the effects of the finite source size are similar in both the types of particle injection model considered in our study: the burst-like and the continuous injection. For very old nearby sources ($t \gtrsim 10^5$ yr), we have found that the results are independent of both the source size and the particle injection model and hence, the burst-like point source model represents a good approximation at all energies. We have also shown in Figure 3.3 that for a given value of the CR diffusion coefficient, there is a certain parameter space in (r_s, t) under which the point source approximation remains valid for CRs of our interest, i.e., with energies $E > (3 - 10)$ GeV. When applied to the nearby known SNRs within 1 kpc, interestingly we have found that their total spectrum almost remain the same in the three different source models although some of the individual SNRs like Vela show differences between the models (Figures 3.9 & 3.11). We found that it is because at low energies where the point source approximation is most likely to break down, the local spectrum is dominated by Monogem and Loop1. These SNRs are quite old with Monogem age $\sim 8.6 \times 10^4$ yr and Loop1 $\sim 2.0 \times 10^5$ yr due to which their CR spectra at the Earth are independent of their sizes and are well represented by the point source solutions.

We have also studied an energy *dependent* escape scenario where CRs of different energies are assumed to escape at different times during the SNR evolution. We assumed that the escape time follows, $t_{esc} \propto E^{-1/\alpha}$ with α chosen to be equal to 2.0. Under this model, we assumed that the highest energy particles escape the remnant at the start of the Sedov phase followed by the lower energy ones at later times. For $E_{max} = 1$ PeV, $t_{sed} = 500$ yr and the maximum CR confinement time of 10^5 yr adopted for our study, we found $t_{esc} = (500 - 10^5)$ yr and the escape radius $R_{esc} = (5 - 100)$ pc for energies $E = (1\mathrm{PeV} - 25\mathrm{GeV})$. For young sources, the spectrum obtained under this model show breaks at lower energies which are due to the longer confinement times at those energies. At high energies, the results are very similar to those of the point source approximation.

This is not just because of the small values of R_{esc} at high energies but also due to their large values of $D(E)$ at these energies. In fact, we have shown in section 3.2 that even for a large escape radius of 100 pc, the point source still represents a good approximation at high energies (see e.g., Figure 3.1 surface source). Therefore, it should be understood that it is not the small R_{esc}, but actually the large $D(E)$ which is responsible for the point source validity at high energies under the energy dependent escape model. When applied to the nearby known SNRs, we have found that the results obtained under this model are significantly different from those obtained under the point source approximation. The total local spectrum show more irregular structures as compared to the point source results. Also, we have noticed that there is a big dip between around $(10^2 - 3 \times 10^3)$ GeV which is mainly due to the low energy cut-off in the Vela spectrum (Figs. 10 & 13). These results seem to suggest that if SNRs are the main sources of CRs in our Galaxy, then the widely adopted point source approximation with an energy independent escape scenario appears flawed for CR studies from the nearby SNRs.

For the protons, the irregular spectral features that we have found in the energy dependent escape model may be suppressed by the dominant background produced by distant sources and hence, may not show up distinctly in the total observed spectrum. But, for the electrons they can show up to detectable levels especially at TeV energies where the background level is expected to be significantly less. Recently, Kawanaka et al. 2011 proposed that such spectral features can be used to estimate the CR confinement time inside SNRs [131]. Their study assumed a single nearby source having characteristics similar to that of the Vela remnant. It should be noted that the position and the strength of such features strongly depend on the CR escape model especially on the α parameter and also on E_c (if there is an exponential cut-off in the source spectrum). For instance, assuming $E_c > 2$ TeV would produce stronger features and vice versa compared to our results shown in Figure 3.14. Similarly, assuming $\alpha < 2.0$ would produce stronger peaks at comparatively higher energies as low energy CRs would be confined for relatively longer times as indicated by Figures 3.6 & 3.7, and taking $\alpha > 2.0$ would smoothen the peaks as low energy CRs would also start escaping at early times. For $\alpha \gg 2.0$, the energy dependent results will tend towards the point source results obtained for $t_0 = t_{sed}$. These can be understood from Figure 3.15 where in the top panel we have shown the electron spectrum for the case of pure power-law source spectrum (which corresponds to $E_c = \infty$) for different values of α: 1.8 (solid line), 2.0 (dashed line), 2.5 (dotted line). We can clearly see the left shifting of the peak between $(1 - 10)$ TeV as α increases from 1.8 to 2.5. In the bottom panel, we have shown the spectra calculated for the case of $\alpha = 1.8$ for source spectra with exponential cut-offs at $E_c = 10$ TeV (solid line), 2 TeV (dashed line) and 1 TeV (dotted line). Here again, we can notice that the peak at around 5 TeV grows stronger as E_c takes larger values.

If we look into the H.E.S.S electron data, there is an indication of an abrupt rise at the highest measured energy. If future better sensitive experiments like the CTA and the CALET provide good quality data at these energies, that would indeed provide useful informations to understand CR escapes from some of our nearby SNRs. However, the large uncertainties involved in the age and the distance estimates of some of these SNRs may be an issue

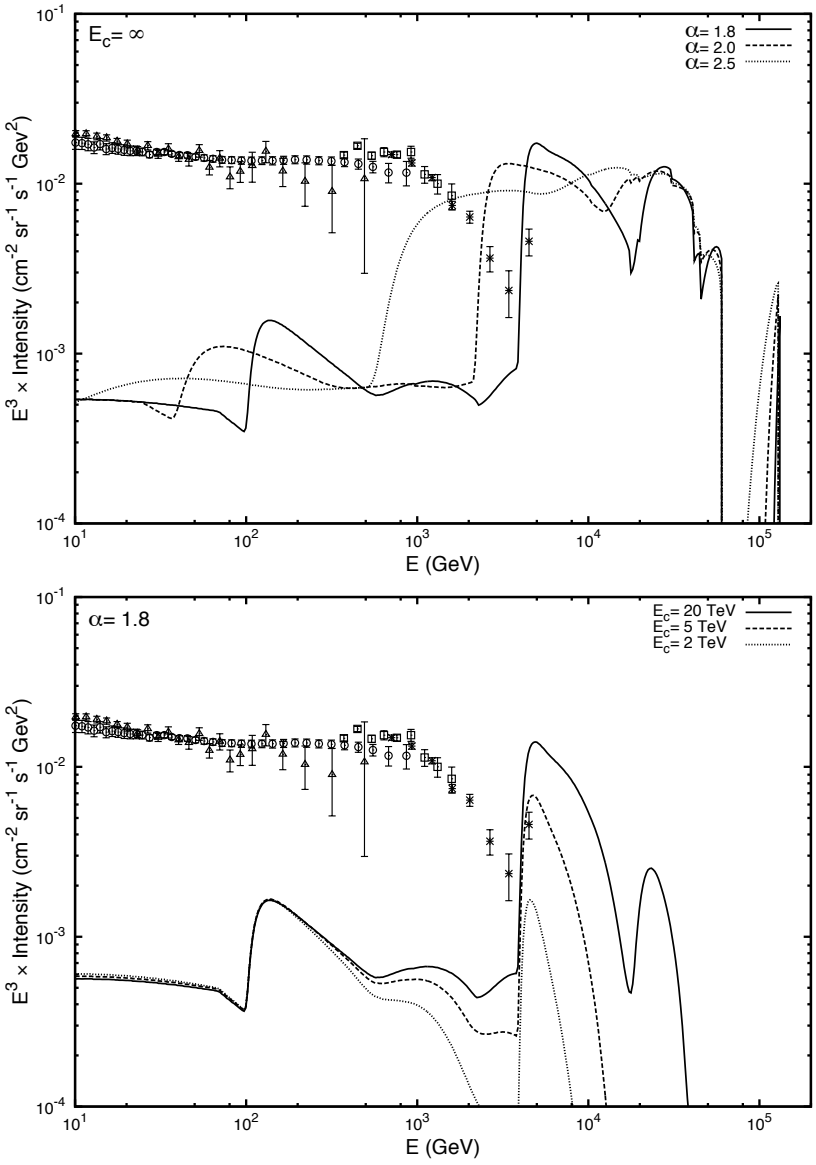

Figure 3.15: Top: Total electron spectrum from nearby SNRs assuming a pure power-law source spectrum ($E_c = \infty$) for different values of α: 1.8 (solid line), 2.0 (dashed line), 2.5 (dotted line). Bottom: For $\alpha = 1.8$ with exponential cut-off in the source spectrum at $E_c = 10$ TeV (solid line), 2 TeV (dashed line) and 1 TeV (dotted line). The data and other model parameters remain the same as in Figure 3.11.

because of the strong dependence of the CR spectrum on these parameters. Regarding this, measurements of electron anisotropy both amplitude and its direction at these energies might also be important in order to identify the dominant source.

Recently, Di Bernardo et al. 2011 studied the contributions of the nearby pulsars and the SNRs to the high energy electron spectrum [79]. One of their conclusions is that a strong contribution from the nearby SNRs is not supported by the recent upper limits on the electron anisotropies provided by the FERMI Large Area Telescope observations [12]. But, it should be noted that their calculations assumed the sources to be burst-like point sources emitting CR particles independent of energy. In Figure 3.14, we show that between $\sim (100\mathrm{GeV} - 2\mathrm{TeV})$, the contribution from the nearby SNRs is significantly larger in the point source approximation than in the energy dependent model. We believe that a more realistic treatment of particle escape model from the SNRs may change their conclusion. Other class of sources which might also produce significant contributions to the high energy leptonic (electron plus positron) spectrum are pulsars and dark matter. Models based on these sources are motivated mostly by the detection of the rise in the positron fraction above $\sim$ 10 GeV by the PAMELA experiment [15]. If we assume that positrons are produced only during the interaction of the primary CRs with the interstellar gas, the positron fraction is expected to decrease with energy which is in contrast to the observations. A possible solution to this problem among others may be the presence of one or more nearby positron sources like pulsars or dark matter (e.g. [102] and references therein). Future measurements of electron anisotropies with better sensitivities and also the absolute positron spectrum at high energies can provide better understanding of the nature and the type of the dominant source(s).

Moreover, a good understanding of the background contribution would also be crucial. In an earlier work, we had presented calculations of the averaged background based on a simple energy *independent* model of CR confinement within the SNRs [187]. In future, we will present background estimates for both the protons and the electrons taking into account the energy *dependent* confinement/escape of particles. The calculation will include the various energy loss and the interaction processes taking place during the time particles are confined within the sources. In addition, we will also present the possible effects on other observed CR properties like the Galactic diffuse γ-ray emission, s/p ratios and the anisotropies.

Chapter 4

Nearby supernova remnants and the cosmic-ray spectral hardening at high energies

Satyendra Thoudam and Jörg R. Hörandel

2012, MNRAS, 421, 1209
2012, ApJ, in preparation

Abstract Recent measurements of cosmic-ray spectra of several individual nuclear species by the CREAM, TRACER, and ATIC experiments indicate a change in the spectral index of the power laws at TeV energies. Possible explanations among others include non linear diffusive shock acceleration of cosmic rays, different cosmic-ray propagation properties at higher and lower energies in the Galaxy and the presence of nearby sources. In this Chapter, we show that if supernova remnants are the main sources of cosmic rays in our Galaxy, the effect of the nearby remnants can be responsible for the observed spectral changes. Using a rigidity dependent escape of cosmic rays from the supernova remnants, we explain the apparent observed property that the hardening of the helium spectrum occurs at relatively lower energies as compared to the protons and also that the spectral hardening does not persist beyond $\sim (20-30)$ TeV energies. Future sensitive measurements of heavier cosmic-ray species and of the Galactic diffuse γ-ray emission at TeV energies can provide an important check of our model.

4.1 Introduction

Recently, cosmic-ray (CR) measurements by the new-generation balloon-borne experiments such as the ATIC [156], CREAM [198], and TRACER [40] seem to indicate that the CR spectrum deviates from a single power law. The spectra of all individual elements seem to be harder at TeV energies than at lower energies. Such a hardening is not easy to explain under the standard models of CR acceleration and their propagation in the Galaxy. Under the standard theory, CRs below the knee ($\sim$ 3 PeV) are considered to be produced by supernova remnant (SNR) shock waves by diffusive shock acceleration (DSA) mechanism [45, 55]. Such a mechanism naturally predicts a power law spectrum of $E^{-\gamma}$ with the index $\gamma = 2$ for strong shocks. On the other hand, CR propagation in the Galaxy is considered to be of diffusive nature which is due to scattering by magnetic field irregularities and the CR self excited Alfvén and hydromagnetic waves present in the Galaxy. Measurements of CR secondary-to-primary ratios indicate that the diffusion is energy dependent with the diffusion coefficient $D(E) \propto E^{\delta}$ with $\delta \approx (0.3 - 0.7)$. Under these considerations, the CR spectrum in the Galaxy is expected to follow a single power law with index $(\gamma + \delta)$ up to the knee, which do not seem to agree quite easily with the observed hardening at TeV energies.

The observed data can be explained if either the source spectrum or the diffusion index flattens at higher energies. Non linear DSA theories where CRs modify the shock structure predict concave spectra (flatter at higher energies) at the shocks. But, the total spectrum injected into the interstellar medium (ISM) which is the sum of the instantaneous spectra over the SNR lifetime is very close to a pure power-law [64]. The concave signature can be even more diluted when summed over an ensemble of SNRs [163]. From the propagation point of view, there are models which assume a harder or constant CR diffusion coefficient at higher energies in the Galaxy [41]. Such models are motivated not only by the apparent flattening of the observed boron to carbon ratio above ~ 100 GeV energies, but also by the observed CR anisotropy which is almost independent of energy. Recently, it has also been proposed that dispersion in the spectral indices of CR source spectrum from many sources can also be responsible for the observed spectral hardening [199].

Another possible explanation, as also pointed out in [29], is the presence of nearby sources. Erlykin & Wolfendale (2011) suggested that an extra component of CRs with a steep spectrum could be contributing below ~ 200 GeV/n while above that, the spectrum is entirely determined by a harder CR background [89]. They proposed that the sources of the extra component could be in OB associations in the Local Bubble. Recently, Ohira & Ioka (2011) proposed that the hardening could be due to decreasing Mach number in hot superbubbles with multiple supernovae [151]. In another recent work, Vladimirov et al. 2011 investigated several possible interpretations (including local source effect) for the observed spectral features at low and high energies using the GALPROP propagation code [191]. They also presented the possible effects on other observed properties such as CR anisotropy, isotopic ratios and the Galactic diffuse γ-ray emissions.

In our present study, we investigate whether the spectral hardening observed at TeV energies could be an effect of the nearby SNRs. Although there has not been any direct

detection of CRs from any sources, SNRs remain the most favorable candidates both theoretically and observationally. At least the presence of high energy particles up to few TeVs inside SNRs have been confirmed by the detections of non-thermal X-rays [157] and TeV γ-rays from several SNRs [20, 22]. Moreover, the detection of TeV electrons by the H.E.S.S experiment [24] indicates the presence of one or more CR sources within a distance of ~ 1 kpc from us. If these sources produce both electrons and nuclei, we expect to see some effects on the spectra of CR nuclei observed at the Earth.

4.2 Model

The diffusive propagation of CRs in the Galaxy neglecting the effects due to nuclear spallation can be described by the following equation,

$$\nabla \cdot (D \nabla N) + Q = \frac{\partial N}{\partial t} \tag{4.1}$$

where $N(\mathbf{r}, E, t)$ is the differential number density at a distance $\mathbf{r}$ from the source at time t, E is the kinetic energy/nucleon and $Q(\mathbf{r}, E, t)$ is the source term. The diffusion coefficient is taken as $D(\Re) = D_0(\Re/\Re_0)^\delta$ for $\Re > \Re_0$, where $\Re$ denotes the particle rigidity which is given by $\Re = AE/Z$ for charge Z and mass number A. For our study, we consider two sets of values for $(D_0, \Re_0, \delta)$: one based on purely diffusion model (hereafter Model A) and the other based on models including CR re-acceleration due to interstellar turbulence (hereafter Model B). We choose $(D_0, \Re_0, \delta) = (2.9, 3, 0.6)$ for Model A [186] and $(5.8, 4, 0.33)$ for Model B [175], where D_0 is in units of 10^{28} cm^2 s^{-1} and $\Re_0$ is in GV.

Under DSA theory, CRs are confined within the remnant due to the magnetic turbulence generated by the CRs themselves. They can escape when their upstream diffusion length defined as $l_{diff} = D_s(E)/u_s$ is greater than the escape length from the shock front which is usually taken as $l_{esc} \approx 0.1 R_s$, where u_s and R_s denote the shock velocity and the shock radius respectively. In the Bohm diffusion limit, the upstream diffusion coefficient scales linearly with energy as $D_s(E) \propto E$ which implies that higher energy particles can escape the remnant at early times followed later by the lower energy ones. But, the exact energy dependence of D_s is still not well understood and depends on some poorly known quantities which include the spectral distribution of the CR self-excited turbulence waves, the level of magnetic field amplification by the CRs and the dynamical reaction of CRs on the shock structure. Therefore, we follow a simple but reasonable parameterization for the CR escape time similar to that adopted by Gabici et al. 2009 [94] as given below,

$$t_{esc}(\Re) = t_{sed} \left(\frac{\Re}{\Re_{max}} \right)^{-1/\alpha} \tag{4.2}$$

where t_{sed} denotes the start of the Sedov phase, $\Re_{max}$ denotes the maximum CR rigidity and α is a positive constant. We assume that the maximum CR energy accelerate by an SNR scales with the charge number Z as ZU_{max}, where U_{max} denotes the maximum kinetic

energy of the protons which is taken as 1 PeV for our study [47]. This scaling gives $\Re_{max} = 1$ PV. In units of energy/nucleon, the maximum energy for helium is $E_{max} = 0.5$ PeV/n.

Eq. (4.2) assumes that the highest energy CRs of all the species start escaping at the onset of the Sedov phase itself. Writing Eq. (4.2) in terms of total kinetic energy, it is easy to check that for the same kinetic energy, the escape time of CRs scales with the charge number as $Z^{1/\alpha}$, i.e, higher charged particles escape at relatively later stages of the SNR evolution. Thus, our escape model takes into account the general understanding of DSA theory that higher charged particles can be confined for relatively longer duration within the remnant. In terms of energy/nucleon, we can write Eq. (4.2) as

$$t_{esc}(E) = t_{sed}\left(\frac{AE}{Z\Re_{max}}\right)^{-1/\alpha} \tag{4.3}$$

Eq. (4.3) shows that for the same energy/nucleon, all nuclei with charge $Z > 1$ escape earlier than the protons by a factor of $(A/Z)^{-1/\alpha}$. We further assume that no particles remain confined after the shock completely dies out which we assume to occur when the SNR age 10^5 yr. Taking this into account, the CR escape time for our study is taken as $T_{esc}(E) = \min\left[t_{esc}(E), 10^5\text{yr}\right]$. For detailed studies on particle escape from SNRs, see e.g., [65, 152, 163].

The corresponding escape radius of CRs is calculated using the age-radius Sedov relation for SNRs as given below,

$$R_{esc}(E) = 2.5u_0\, t_{sed}\left[\left(\frac{T_{esc}}{t_{sed}}\right)^{0.4} - 0.6\right] \tag{4.4}$$

where u_0 represents the initial shock velocity, i.e the velocity at $t = t_{sed}$.

The source term in Eq. (4.1) is taken as,

$$Q(\mathbf{r}, E, t) = \frac{q(E)}{A_{esc}}\delta(t - T_{esc})\delta(r - R_{esc}) \tag{4.5}$$

where $A_{esc} = 4\pi R_{esc}^2$ denote the surface area of the SNR at the time when CRs of energy E escape the remnant. It should be noted that our consideration of the rigidity dependent escape time and the finite source size are different from the commonly adopted burst-like point source approximation where CRs of all rigidities are assumed to escape at the same time from a point source. For CR study near the sources, the point source approximation can break down and it looks more realistic to take their sizes into account [188]. Recently, such importance has also been highlighted in [153] in the study of γ-ray emission from SNRs interacting with molecular clouds.

The source spectrum in Eq. (4.5) is taken as $q(E) = Aq(U)$ with $q(U)$ given by,

$$q(U) = k(U^2 + 2Um)^{-(\gamma+1)/2}(U + m) \tag{4.6}$$

where $U = AE$ represents the particle total kinetic energy, m is the rest mass energy and k is the normalization constant which is related to the CR injection efficiency.

Solving Eq. (4.1), the spectrum at a distance r_s from the SNR follows,

$$N(r_s, E, t) = \frac{q(E)\, R_{esc}}{r_s A_{esc} \sqrt{\pi D(t - T_{esc})}} \exp\left[-\frac{(R_{esc}^2 + r_s^2)}{4D(t - T_{esc})}\right] \sinh\left(\frac{r_s R_{esc}}{2D(t - T_{esc})}\right) \tag{4.7}$$

For high energy particles for which the diffusion radius defined as $r_{diff} = \sqrt{D(t - T_{esc})}$ is much larger than (r_s, R_{esc}), Eq. (4.7) follows a power-law of the form $N(E) \propto E^{-(\Gamma + \frac{3}{2}\delta)}$.

Eq. (4.7) can be used to calculate the CR spectra from the nearby SNRs. We choose the proton and the helium for our study and consider only those SNRs with distances $<$ 1 kpc from the Earth and ages $< 2 \times 10^5$ yr. From the available literature, we found 10 SNRs listed as follows with their distances (kpc) and ages (yr) respectively given in parentheses: Cygnus Loop $(0.54, 10^4)$, HB21 $(0.8, 1.9 \times 10^4)$, HB9 $(0.8, 6.6 \times 10^3)$, S147 $(0.8, 4.6 \times 10^3)$, Vela $(0.3, 1.1 \times 10^4)$, G299.2-2.9 $(0.5, 5 \times 10^3)$, SN185 $(0.95, 1.8 \times 10^3)$, Monogem $(0.3, 1.1 \times 10^5)$, G114.3+0.3 $(0.7, 4.1 \times 10^4)$ and Vela Junior $(0.75, 3.5 \times 10^3)$.

In addition to the contributions from the nearby SNRs, we assume that there exists a steady CR background in the Galaxy which dominates the overall CR spectrum. For the CRs observed at the Earth, we assume that this background component consists of contributions from distant SNRs plus any other possible sources in the Galaxy. For our study, we obtain the background by fitting the observed CR spectrum between $(20 - 200)$ GeV/n. This is the energy region where the contamination from the nearby sources is expected to be less and at the same time, not much affected by the Solar modulation. In fact, it has been shown in [186] that the presence of nearby sources can produce stronger density fluctuations at higher energies than at lower energies because of the energy dependent nature of CR diffusion. Therefore, we believe that it is reasonable to assume that the low energy CRs that we observe at the Earth are not much affected by the presence of nearby SNRs and they largely represent the averaged background spectrum in the Galaxy. We will show in the following that this is indeed the most likely case.

4.3 Results

From the fit, the spectral indices of the background CRs are found to be 2.75 ± 0.01 for the protons and 2.68 ± 0.02 for the helium. The reason for the flatter helium spectrum is not properly understood. Recently, Blasi & Amato (2011) showed that the flatter helium spectrum with respect to the protons above 1 TeV could be due to spallation effects [57]. Later, Vladimirov et al. 2011 showed that such effects can lead to boron-to-carbon ratios and the anti-proton fluxes which are inconsistent with the observed data [191]. Another possibility for the different spectral indices could be that the intrinsic source spectra itself are different. It could be due to different acceleration sites of protons and helium [52] or inhomogeneous abundance of elements in superbubbles [151]. For our present study, we assume that CRs are injected into the Galaxy with different source indices. The index γ

for an individual species is chosen such that $(\gamma + \delta)$ is equal to the spectral index of the background obtain from the fit.

Before illustrating our results, we briefly discuss the choice of other model parameters involved in our calculations. Typically, t_{sed} has values between $\sim (100 - 10^3)$ yr depending on the gas density of the ISM, mass of the ejecta and the energy output of the supernova explosion. For our study, we take $t_{sed} = 500$ yr. We assume the initial shock velocity u_0 to be 10^9 cm/s. This gives CR escape times from the SNRs in the range of $t_{esc} = (500 - 10^5)$ yr and the corresponding escape radii as $R_{esc} \sim (5 - 100)$ pc. Finally, we treat the escape parameter α and the injection efficiency of the protons (helium) hereafter denoted by $\epsilon_{p(he)}$ as free parameters. For our calculations, we will assume that all the parameters mentioned above are same for all the SNRs.

Because of lack of precise informations on the values of α and $\epsilon_{p(he)}$, we perform calculations for several of their randomly chosen combinations. We choose the escape parameter in the range of $\alpha = (1 - 3)$. This range approximately covers the α values given in some available literatures. Studies based on non-linear DSA theories which takes into account the modification of the shock structure by the CRs give $\alpha \sim 0.8$ (e.g., [163]). Blasi & Amato (2011) adopted $\alpha \sim 3.2$ in their study of the effect of random nature of SNRs on the CR spectrum [57]. Investigations of γ-ray emissions from molecular clouds interacting with nearby SNRs adopt values in the range of $\alpha = (2.4 - 2.6)$ [94, 153]. We consider the CR injection efficiencies in the range of $\epsilon_p = (5 - 25)\%$ for protons and $\epsilon_{he} = (1 - 5)\%$ for helium, where the values are in units of 10^{51} ergs. The averaged proton to helium injection ratio of 5 which we consider here is less than the observed proton to helium flux ratio of $\sim (20 - 13)$ in the energy range of $\sim (20 - 200)$ GeV/n [198]. But, our wide range of efficiencies for both the species well cover the observed flux ratios. It should be understood that the observed flux ratios may not necessarily represent the injection efficiency ratios from the source. Effects during the propagation in the Galaxy such as due to spallation (which are different for different nuclear species depending on their interaction cross-sections) may change the composition ratios produced by the source. In addition, propagation of CRs is charged dependent. Those which undergo faster diffusion will escape more easily from the Galaxy and eventually lead to less flux observed at the Earth.

Figure 4.1 shows our calculated proton spectra $\left(\times E^{2.75}\right)$ for Models A (top panel) and B (bottom panel). In each panel, the thin grey lines represent an example of 30 different random spectra we have calculated. Each random spectrum corresponds to a set of $\{\alpha, \epsilon_{p(he)}\}$ which is assumed to be the same for all the SNRs. Each spectrum is the sum of the background CRs (shown as the black dotted line) and the total contribution from all the nearby SNRs we have considered. The thick black line represents the averaged spectrum of a total of 200 such random spectra. The data are taken from CREAM [198], ATIC[1] [156], AMS [18, 31], BESS [108], and PAMELA[1] [17] experiments. One common result that we can notice between the two models is that the contribution of the nearby SNRs show up mostly above $\sim (0.5 - 1)$ TeV. However, there are some general differences between the two results. The results for Model A not only show larger variations between individual spectra

[1]Data taken from the database compiled by Andrew W. Strong [174]

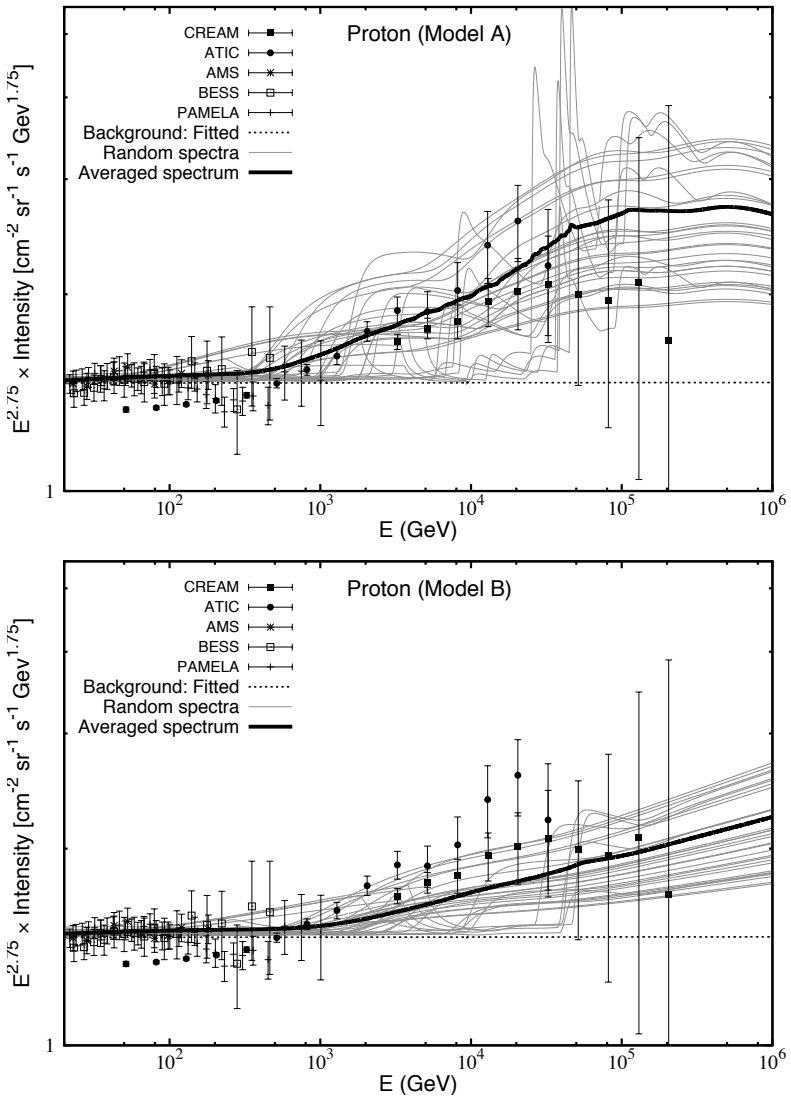

Figure 4.1: Proton spectra ($\times E^{2.75}$) for Model A (top panel) and Model B (bottom panel). The black dotted line represents the background spectrum. The thin grey lines represent an example of 30 random spectra calculated with proton escape parameters and the injection efficiencies in the range of $\alpha = (1-3)$ and $\epsilon_p = (5-25) \times 10^{49}$ ergs respectively. Each spectrum is the sum of the background and the contribution from the nearby SNRs. The thick black line represents the averaged of 200 random spectra. See text for data references and other details.

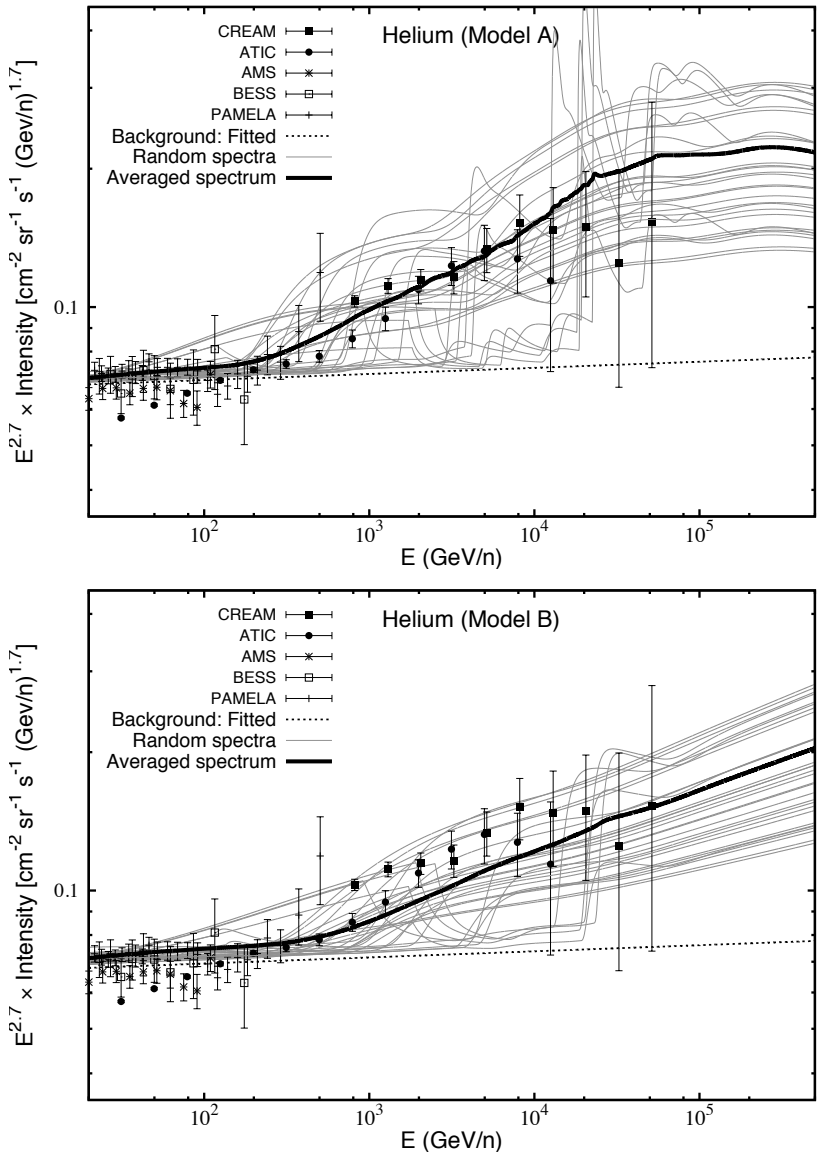

Figure 4.2: Helium spectra ($\times E^{2.7}$) for Model A (top panel) and Model B (bottom panel). The calculation assumes injection efficiencies in the range of $\epsilon_{he} = (1-5) \times 10^{49}$ ergs. All other model parameters, results representation and the data references remain the same as in Figure 4.1.

Table 4.1: Background spectral indices Γ and the range of CR injection efficiency ϵ considered in our study for different CR species: protons (P), helium (He), carbon (C), oxygen (O) and iron (Fe). The background is obtained by fitting the low energy CRs in the range of $(20 - 200)$ GeV/n as described in the text.

Element	Γ	ϵ ($\times 10^{49}$ ergs)
P	2.75 ± 0.01	$(5 - 25)$
He	2.68 ± 0.02	$(1 - 5)$
C	2.59 ± 0.037	$(2 - 10) \times 10^{-2}$
O	2.61 ± 0.05	$(1.6 - 8.3) \times 10^{-2}$
Fe	2.69 ± 0.037	$(0.8 - 4.2) \times 10^{-2}$

but also stronger irregular features and spikes. Also, in general Model A produces larger contribution from the nearby SNRs as compared to Model B. This is largely due to the comparatively harder source spectrum of CRs required in Model A. For the reasonable range of injection efficiencies considered in our study, the results of Model A seem to be in better agreement with the data both in terms of the size and the shape of the spectra. On comparing the averaged spectra (thick black lines) above $\sim (0.5 - 1)$ TeV, the result of Model A is comparatively harder up to ~ 100 TeV which then becomes steeper at higher energies. This spectral behavior of Model A is in good agreement with the recent data which also seem to indicate that the spectral hardening for protons does not persist beyond $\sim (20 - 30)$ TeV. On the other hand, the averaged spectrum in Model B show less hardening above ~ 1 TeV and it continues without any turn over or steepening up to the maximum energy considered here.

The corresponding results for helium are shown in Figure 4.2: Model A (top panel) and Model B (bottom panel). Our results for helium look similar to those obtained for protons. One general difference we notice is the shifting of the helium results towards lower energies with respect to the proton results. Though not very significant, a similar trend is also present in the observed data. For instance, the spectral hardening in the helium data occurs at ~ 0.5 TeV/n whereas for the protons it occurs at $\sim$ 1 TeV. Moreover, the spectral turnover at higher energies seems to occur at $\sim$ 10 TeV/n for helium while for protons it seems to occur at $\sim (20 - 30)$ TeV.

The results for the heavier elements are shown in Figure 4.3 for carbon (top), oxygen (middle) and iron (bottom). The calculation is based on Model A. The values of the background spectral indices and the range of the CR injection efficiencies used in the calculation are given in Table 4.1 along with those for the lighter species (protons and helium). The range of the escape parameter α remain the same as in the case of the lighter nuclei. The data are taken from CREAM [28], ATIC[1] [156], CRN [178], HEAO[1] [85] and TRACER [150] experiments. Compared to the lighter species, the data for the heavier nuclei are less significant, but they also show an indication of hardening at energies above a few hundred GeVs/n. Our results are in general good agreement with the measurements as shown by the

Table 4.2: Best fit values of the injection efficiency ϵ under Models A and B for different CR species: protons (P), helium (He), carbon (C), oxygen (O) and iron (Fe). The corresponding escape energies E_{esc} for the escape times $t_{esc} = (500 - 10^5)$ yr are also given.

Element	ϵ ($\times 10^{49}$ ergs) Model A	ϵ ($\times 10^{49}$ ergs) Model B	E_{esc} (PeV/n$-$GeV/n) Model A	E_{esc} (PeV/n$-$GeV/n) Model B
P	9	20	$(1.0 - 8.6)$	$(1.0 - 3.0)$
He	2	3.7	$(0.5 - 4.3)$	$(0.5 - 1.5)$
C	3.7×10^{-2}	5×10^{-2}	$(0.5 - 4.3)$	$(0.5 - 1.5)$
O	3×10^{-2}	4×10^{-2}	$(0.5 - 4.3)$	$(0.5 - 1.5)$
Fe	2×10^{-2}	3.5×10^{-2}	$(0.46 - 4.02)$	$(0.46 - 1.39)$

averaged spectra (thick black lines). Under our model, the spectral hardening for the heavier nuclei is expected to occur at almost the same energy (slightly less for iron) as that of the helium. Moreover, the spectral turnover at even higher energies is also expected to be at the same energy as the helium, i.e, at ~ 10 TeV/n. The results for Model B are not shown here. They follow a similar trend as for the protons and the helium shown in Figures. 4.1 & 4.2.

In Figure 4.4, we present our best fit results for the lighter species: protons ($\times E^{2.75}$, top panel) and helium ($\times E^{2.7}$, bottom panel). They are obtained by choosing $(\alpha, \epsilon_p, \epsilon_{he}) = (2.2, 9\%, 2\%)$ for Model A and $(2.4, 20\%, 3.7\%)$ for Model B. Our model parameters give escape times of $t_{esc} = (500 - 10^5)$ yr for protons of energies (1 PeV$-$8.6 GeV) and for helium of (0.5 PeV/n$-$4.3 GeV/n) in Model A. In model B, the corresponding values are (1 PeV$-$3 GeV) and (0.5 PeV/n$-$1.5 GeV/n) respectively. The data in Figure 4.4 top and bottom panels are the same as in Figures 4.1 & 4.2 respectively. The black dotted line represents the background CR spectrum. The solid lines correspond to Model A and the double dotted lines to Model B in which the thin and the thick lines represent the total contributions from the nearby local SNRs and the total background plus nearby contributions respectively. In Model A, the dominant nearby contributors are the Vela, G299.2-2.9 and SN185 remnants. They are shown by the thin dashed lines in the figures. Vela dominates in the range of $\sim (0.7 - 10)$ TeV/n while above that, the spectrum is mostly dominated by G299.2-2.9 and SN185. In Model B, Vela dominates over a wide range up to ~ 300 TeV/n and beyond that, it is dominated by G299.2-2.9 (not shown in the figure).

The steep low energy cut-offs in the individual SNR contributions in our model are largely due to the energy dependent escape of CRs. CRs below the cut-offs are mostly those which are still confined within the SNRs and are not yet released into the ISM. Our best fit result for Model A show a rise in the total spectrum at $\sim (0.5 - 1)$ TeV/n which remain constant up to $\sim (5 - 10)$ TeV/n. This is due to the effect of the low energy cut-off of the Vela remnant. To be specific, the rise in the proton spectrum occurs at ~ 1.2 TeV while that of the helium at ~ 0.6 TeV/n. This difference is largely due to the effect of early escape of helium compared to the protons for the same energy/nucleon. There is also some

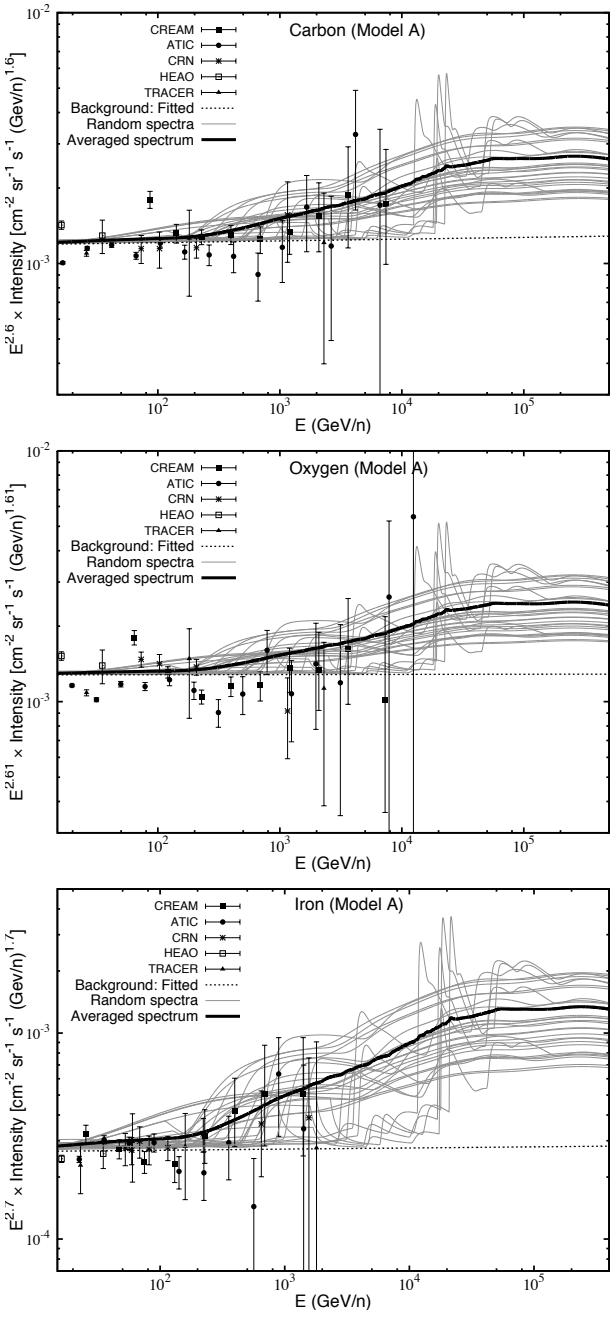

Figure 4.3: *Top:* Carbon spectra $(\times E^{2.6})$, *Middle:* Oxygen spectra $(\times E^{2.61})$ and *Bottom:* Iron spectra $(\times E^{2.7})$. The results are for Model A. See text for the data and for the details about the range of model parameters used in the calculation.

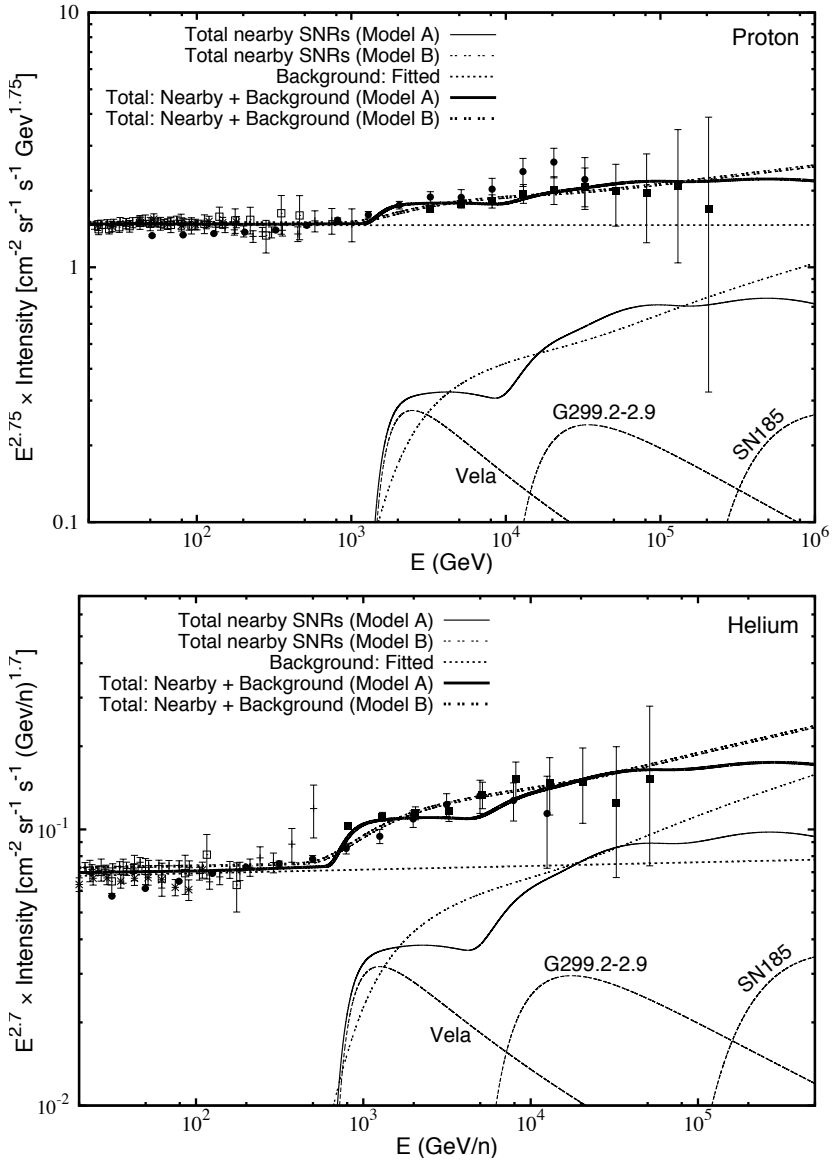

Figure 4.4: Best fit results for proton ($\times E^{2.75}$, top panel) and helium ($\times E^{2.7}$, bottom panel). The data are the same as given in Figures 1&2 respectively. The black dotted line represents the background spectrum. Solid lines correspond to Model A and double dotted lines to Model B of which the thin line represents the total contributions from the nearby SNRs and the thick line represents the total background plus nearby contributions. The thin dashed lines represent the dominant nearby contributors in Model A.

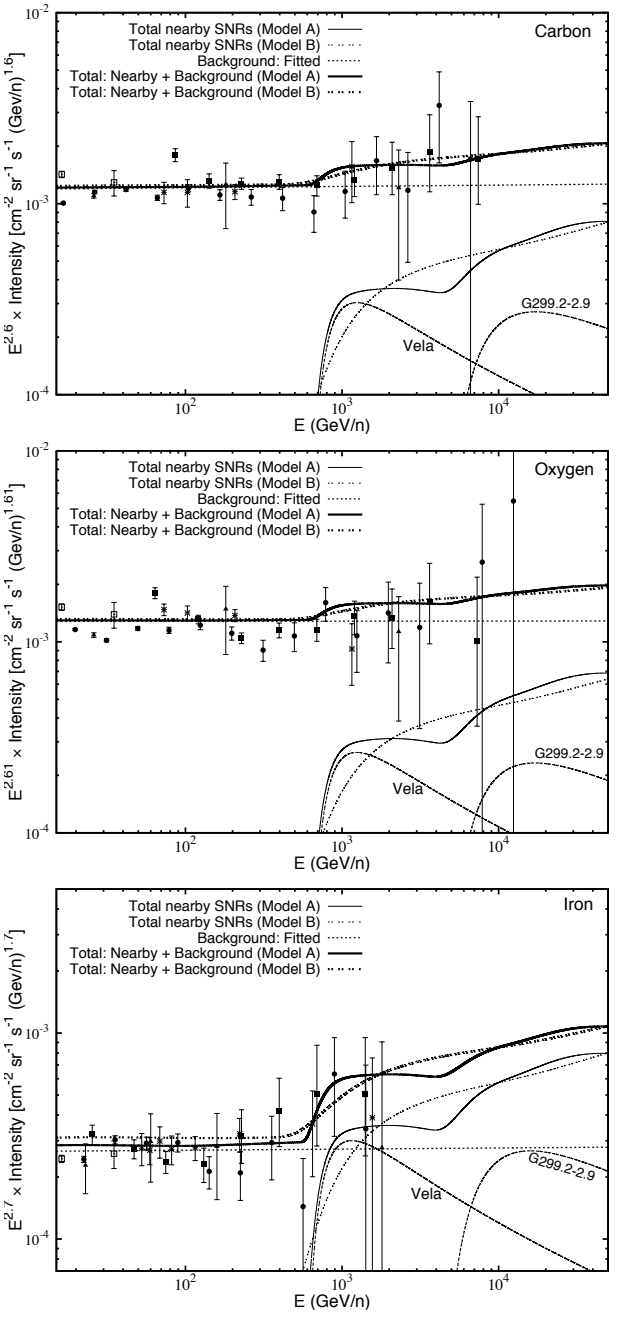

Figure 4.5: Best fit results for carbon ($\times E^{2.6}$, *top*), oxygen ($\times E^{2.61}$, *bottom*) and iron ($\times E^{2.7}$, *bottom*). The data are the same as in Figure 4.3.

effect due to the faster diffusion of helium than the protons for the same energy/nucleon. As mentioned above, it is interesting to see that the recent data also seem to indicate that the helium spectrum starts hardening at comparatively lower energies than the protons. Our best fit results then show a slow increase above $\sim (5-10)$ TeV/n which again becomes almost constant above $\sim (40-60)$ TeV/n. This is due to the combined effect of other SNRs mainly G299.2-2.9 and SN185. These spectral features are found to be more pronounced for helium. In Model B, these features are smeared out and we get a smooth spectrum with a slow increase above a few TeVs. This is due to the comparatively slower diffusion of CRs in this model and the dominance by a single source (Vela) over a wide range of energy spectrum.

The best fit results for the heavier nuclei are shown in Figure 4.5: carbon (top), oxygen (middle) and iron (bottom). The values of the best fit model parameters are listed in Table 4.2 along with those of the lighter species. The general explanations given above for the protons and the helium also apply for the heavier nuclei. The abrupt rise in the carbon and oxygen spectra due to the Vela remnant is expected at the same energy as in the helium spectrum because of the same value of (A/Z). However for iron, it is expected at slightly lower energy because of its slightly larger (A/Z) value.

The total CR anisotropy Δ expected under our model can be calculated using the following equation [184],

$$\Delta = \frac{\sum_i I_i \delta_i \hat{r}_i . \hat{r}_m}{I_T} \tag{4.8}$$

where the summation is over the nearby SNRs, $\hat{r}_i$ denotes the direction of the i^{th} SNR giving an intensity I_i at the Earth, $\hat{r}_m$ denotes the direction of maximum intensity, I_T represents the total observed CR intensity and δ_i denotes the anisotropy amplitude due to a single SNR. δ_i under the diffusion approximation is given by [144],

$$\delta_i = \frac{3D}{c} \frac{|\nabla N_i|}{N_i} \tag{4.9}$$

where N_i (given by Eq. 4.7) denotes the CR density from an SNR with distance r_i and age t_i. For our best fit proton results, we get $\Delta \approx (1.7 \times 10^{-2} - 0.12)$ and $(1-4) \times 10^{-2}$ for Model A and B respectively in the energy range of $(1-100)$ TeV. Our estimates are larger than the measured anisotropies of $\sim (0.5-1) \times 10^{-3}$ in the same energy range. But, compared to Model A, Model B looks closer to the measured values (see also [162]).

4.4 Discussions

We show that for both Models A and B, the nearby SNRs contribute mostly above $\sim (0.5-1)$ TeV/n and they may account for the observed spectral hardening at high energies. We show this for a wide range of CR injection efficiencies and CR escape parameters from the SNRs. Looking into the averaged spectra in Figures 4.1 & 4.2, we find that both the

models predict that the hardening of the helium spectrum should occur at lower energies as compared to the protons. We also find that the averaged result of Model A seems to explain the overall data better than that of Model B.

However, the wide range of parameters values considered in our study allow both the propagation models to successfully explain the observed data with a careful choice of model parameters. We show this with our best fit results in Fig. 3. But, the high CR injection efficiency of $\epsilon_p = 20\%$ required in Model B is around a factor of 2 larger than the normally considered value of $\sim 10\%$ for CR studies in the Galaxy. Moreover, the steep source index of $\gamma \sim 2.4$ required in this model is also hard to reconcile with the results of diffusive shock acceleration theory which predict an index of $\gamma = 2$. Model A, on the other hand, looks favorable considering its relatively more reasonable values of the source index ($\gamma = 2.15$) and the proton injection efficiency ($\epsilon_p = 9\%$) required to explain the observed hardening. In addition, Model A also better explain the apparent observed property that the spectral hardening does not persist above a few TeVs. However, the measured anisotropy seem to favor Model B which assumes a weaker energy dependence of CR diffusion in the Galaxy.

Our results look different from the predictions of other models. Models based on constant diffusion coefficient at high energies or spectral dispersion in the source spectrum are expected to produce a high energy spectrum which remains hard up to the maximum energy [41]. But, the data indicates that the spectral hardening happens only up to $\sim (20-30)$ TeV for protons and ~ 10 TeV/n for helium which in general agrees well with our predictions (especially with Model A). Future measurements of heavier CR species at higher energies would be important to check the presence of any spectral turnover at ~ 10 TeV/n which is a unique prediction of our model. It should be mentioned that our results may not be significantly different from others if the CR spectrum has a break or a cut-off (normally assumed to be exponential) at energies $\lesssim 0.1$ PeV. In such a case, the spectrum will start rolling over before it starts showing noticeable differences. But, note that a cut-off somewhere between $\sim (3-5)$ PeV is preferred, irrespective of the nature and the origin of the cut-off, in order to explain the observed CR knee [113].

The secondary CR spectrum under our model can be even more different from other models. Secondaries are those which are considered to be produced by the spallation of the primaries only during the propagation in the Galaxy. Their spectrum N_s in the Galaxy is related to their primary spectrum N_p as $N_s(E) \propto N_p(E)/D(E)$. Thus, for $N_p(E) \propto E^{-\Gamma}$, the secondary spectrum follows $N_s(E) \propto E^{-(\Gamma+\delta)}$ which is steeper than their primaries by the diffusion index δ. Therefore, once $D(E)$ is fixed, the shape of the secondary spectrum depends on the shape of their primary spectrum. This means that models which assume the same $D(E)$ but different $N_p(E)$ will produce different $N_s(E)$. Under our model, if we neglect the production of secondaries inside the SNRs, we can assume that all the secondaries are produced by the background CRs. As our background primary spectrum is steeper than the spectrum used in other models to explain the spectral hardening, e.g. [199], we expect a steeper secondary spectrum in our case. This difference would be even more significant when compared to propagation models which assume a constant CR escape time from the Galaxy at higher energies (Ave et al. 2009). Under such models, $N_s(E) \propto E^{-\Gamma}$ at higher

energies while at lower energies $N_s(E) \propto E^{-(\Gamma+\delta)}$. The differences we just mentioned are expected in all kinds of secondary nuclear species like boron, sub-Fe, and anti-protons. At present, data on secondary spectra are available at most only up to ~ 100 GeV/n. Future high energy measurements would be crucial to test our model.

In addition, the diffuse γ-ray emission of our Galaxy can also provide an important check of our model. If the diffuse emission is dominated by the π^0-decay γ-rays, then their intensity would largely follow the proton spectrum at high energies. Therefore, under our model we expect a diffuse spectrum which is steeper than the predictions from other models. In fact, it has already been shown in [199] that under their model, the γ-ray spectrum would become harder above ~ 50 GeV. Preliminary results from the FERMI measurements up to ~ 100 GeV show that the spectrum is in good agreement with the conventional model assuming a single power-law CR spectrum above few GeVs [171]. The spectrum do show some excess above the model which could well be attributed to unresolved point sources like pulsars. Detailed investigation of the diffuse γ-ray spectrum and also future measurements at even higher energies would be important to check the validity of our model.

4.5 Conclusions

In short, we conclude that the apparent change in the spectral index of the CR energy spectra at TeV energies could be a local effect due to nearby SNRs. A detailed investigation of both the proton and the helium spectra seems to favor this model. Future high energy measurements of heavier CR species and the detection of any spectral turnover at ~ 10 TeV/n can provide an additional evidence in support of our model. Moreover, future measurements of secondary CR spectra and of the Galactic diffuse γ-ray emission at TeV energies would be important for deeper understanding of the problem.

Chapter 5

Measurement of cosmic rays at very high energies with LORA

S. Thoudam[1], M. van den Akker [1], L. Bähren[1,a], A. Corstanje[1], H. Falcke[1,2]
J. R. Hörandel[1], A. Horneffer[1,b], J. Kelley[1], M. Mevius[3], A. Nelles[1]
O. Scholten[3], S. ter Veen[1]

[1]Department of Astrophysics, IMAPP, Radboud University Nijmegen
P.O. Box 9010, 6500 GL Nijmegen, The Netherlands
[2]ASTRON, 7990 AA Dwingeloo, The Netherlands
[3]Kernfysisch Versneller Instituut, NL-9747 AA Groningen, The Netherlands
[a]now at: Sterrenkundig Instituut Anton Pannekoek, Universiteit van Amsterdam, The Netherlands
[b]now at: Max Planck Institut für Radioastronomy, Bonn, Germany

Section $5.1 - 5.5$: *2012, Nuclear Instruments and Methods A, to be submitted*
Section $5.6 - 5.9$: *2012, Astroparticle Physics, to be submitted*

Abstract An air shower array LORA (the LOfar Radboud air shower Array) has been installed in the core of the LOFAR radio telescope in the Netherlands. The objective is to contribute to the investigation of radio emission from extensive air showers with LOFAR. The main purpose of LORA is to trigger the read-out of the LOFAR radio antennas to register extensive air showers and to measure the properties of air showers.

In this Chapter, the details on the set-up of the experiment, its performance, and first science results are presented. Main results include the measurements of the charged particle lateral density distribution of air showers, measurements of atmospheric attenuation coefficients, and the all-particle cosmic-ray energy spectrum. The energy spectrum is presented in the range of $\sim (2 \times 10^{16} - 1.5 \times 10^{18})$ eV and is found to be in very good agreement with the measurements of other cosmic-ray experiments.

5.1 Introduction

The search for the origin of the highest energy particles in the Universe is a big challenge in astroparticle physics [59, 116, 148]. From the experimental point of view, a precise measurement of the elemental composition of cosmic rays at the highest energies is crucial. The present work is part of an endeavor to establish a new method to measure air showers at high energies and determine the mass composition of cosmic rays with nearly 100% duty cycle: the radio detection of air showers. To contribute to the measurement of radio signals from air showers with the LOFAR telescope, we have installed an air shower array in the LOFAR core. To demonstrate the performance of the array, we want to measure the all-particle energy spectrum of cosmic rays in the energy region from 10^{16} to 10^{18} eV.

High energy cosmic rays impinging onto the atmosphere of the Earth induce cascades of secondary particles. The bulk of charged particle are electrons and positrons. They are deflected by the magnetic field of the earth, while in addition, there is an excess of negative charge. Due to the variation of the number of charged particles, coherent radiation is emitted with frequencies of tens of MHz [90, 111, 112, 165].

The feasibility of quantitative radio measurements of air showers has been demonstrated with the LOPES experiment (LOFAR prototype station) [91, 118, 119]. It has been shown that radio emission can be detected using low-noise amplifiers and fast digitizers in combination with sufficient computing power to analyze the registered signals.

Radio emission from air showers is detected with the LOFAR radio telescope in the framework of the LOFAR key science project "cosmic rays" [118]. The LOw Frequency ARray (LOFAR) is a new digital observatory which has been inaugurated in June 2010 [123]. It is designed as multi-sensor network to assist scientists in the fields of astronomy, geophysics and agriculture. The main focus of the astronomy community is to observe the radio Universe in the frequency range of $(30 - 240)$ MHz.

More than 40 stations with fields of relatively simple antennas work together as a digital radio interferometer, i.e the measured signals are digitized with fast ADCs and interferences are formed in a central processing unit. The antenna fields are distributed over several countries in Europe with a dense core in the Netherlands. The latter consists of 24 stations on an area measuring roughly (2×3) km^2. Each station comprises 96 low-band antennas, simple inverted V-shaped dipoles, operating in the frequency range of $(30 - 80)$ MHz. Each antenna has a dipole oriented in the north-south and east-west direction, respectively. In addition, fields of high band antennas cover the frequency range of $(110 - 240)$ MHz. For air shower observations, the signals from the low band antennas are digitized and stored in a ring buffer (transient buffer board, TBB). For valid triggers, the data are sent to a central processing facility, based on an IBM Blue Gene supercomputer.

The ultimate goal is to independently detect radio emission from air showers with LOFAR. This requires a sophisticated trigger algorithm that analyses the digitized antenna signals in real time. To assist with the development of the trigger algorithm and to measure basic air shower parameters, a field of conventional particle detectors has been installed in the core of LOFAR.

The LOFAR Radboud Air Shower Array (LORA) is an array of scintillation counters located in the compact center of LOFAR, the "super-terp". It has been designed to register air showers initiated by primaries with energies exceeding 10^{16} eV. Strong radio signals are expected from air showers in this energy region. This energy regime is also of astrophysical interest, since a transition is expected from a Galactic to extra-galactic origin of cosmic rays at energies between 10^{17} and 10^{18} eV [59, 116].

In the following, we describe the set-up of LORA, its properties and first results. The experimental set-up is described in section 5.2 and the detector gain calibration in section 5.3. Section 5.4 describes the various steps involved in the reconstruction of air shower parameters and section 5.5 discusses about the reconstruction accuracies. The measured distribution of the air shower parameters are given in section 5.6. Section 5.7 presents an estimate of the atmospheric attenuation coefficient of air showers and 5.8 presents the zenith angle correction on the measured number of charged particles from air showers. Then, 5.9 presents the all-particle cosmic-ray energy spectrum measured with LORA.

5.2 Experimental set-up

LORA comprises 20 detector units, located on a circular area with almost ~ 300 m diameter. The positions of the detectors in the core of LOFAR are illustrated in Figure 5.1. The array is sub-divided into five electronic units, each comprising four detectors. The detectors are located on circles with a radius of about 40 m around a central electronic unit, respectively with a spacing of 50 to 100m between the detectors.

Each detector unit contain two scintillators (0.45 m^2, NE 114), read out via wavelength shifter bars (NE 174 A) through a photomultiplier tube (EMI 9902). A detector is sketched in Figure 5.2. The detectors are installed inside weatherproof shelters.

Four detectors form an electronic unit, comprising two digitizer units (with two electronic channels each) [122], controlled by a Linux-operated, single-board mini-PC. The PC also controls a four-channel high-voltage supply. Five such units are installed to read out the 20 detectors.

The two photomultipliers in one detector unit share a common high-voltage channel. To match the gain in the two tubes, we use a resistor network to adjust the voltage correspondingly. The signals of the two photomultiplier tubes in each detector are read out via RG223 coaxial cables into a single digitizer channel. 12-bit ADCs are used, which sample the incoming voltage with a time resolution of 2.5 ns. A field programmable gate array (FPGA) provides a trigger signal in real time. The digitizer unit contains a GPS receiver and a 200 MHz clock counter to assign a time stamp in nanoseconds accuracy to each triggered event.

For each event, traces are stored in a time window of 10μs. We have chosen to start the recorded data 2μs before the trigger, thus, we measure ADC traces from 2μs before to 8μs after the trigger for each event. A typical ADC trace is depicted in Figure 5.3.

The data from the five mini-PC are sent via Ethernet to a central, Linux-operated PC. Data are stored locally on this PC. In this PC, a high-level trigger is formed based on the

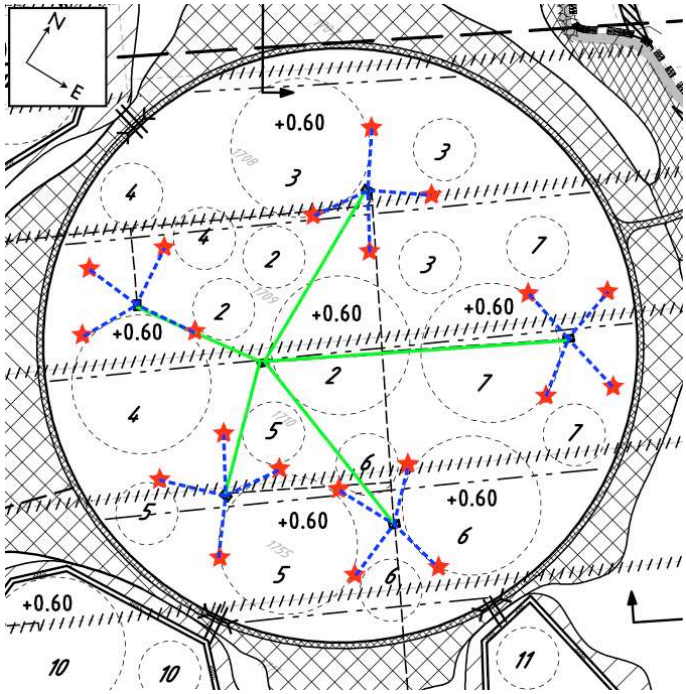

Figure 5.1: Layout of LORA. The stars represent the detector positions and the circles indicate the LOFAR antenna fields. The dashed lines show the cable connections between the detectors and the respective data acquisition systems. The solid lines represent the connections between the local DAQ computers and the central master computer. The geographical North (N) and the East (E) directions are also indicated.

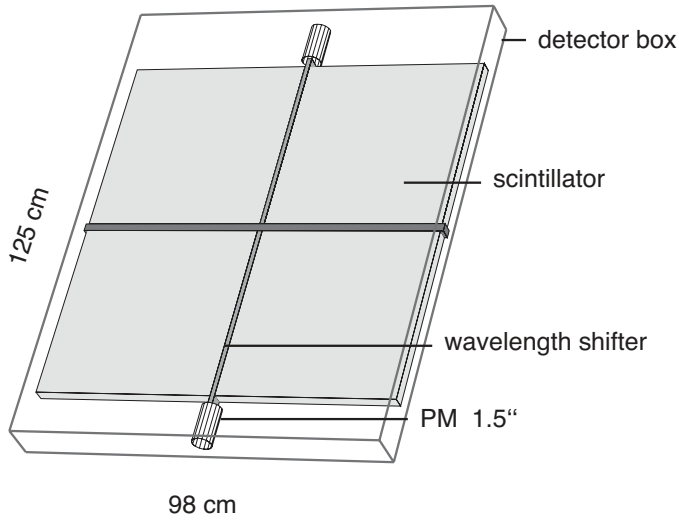

Figure 5.2: Schematic view of a scintillation detector.

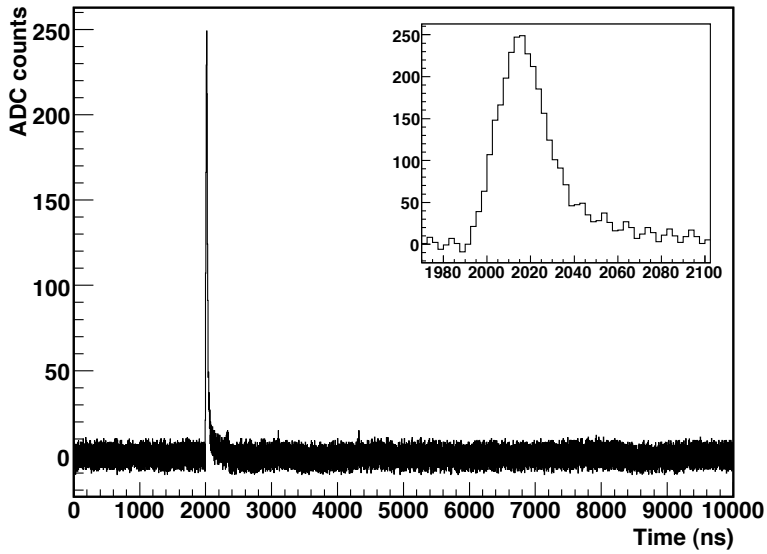

Figure 5.3: Example of a signal time trace produced by a charged particle passing though one of our detectors. Also shown is the closer view of the signal for the time window $(1970 - 2100)$ ns.

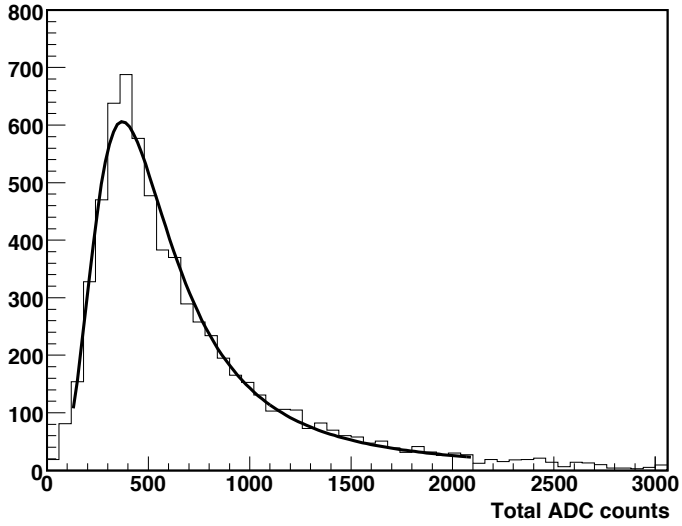

Figure 5.4: Distribution of total energy deposition by single charged particles on one of our detectors. The solid curve represents a fit with Landau distribution function. The most probable value (the single particle peak) given by the fit is (400.5 ± 3.5) ADC counts.

number of sub-arrays that have detected an air shower. This trigger is used to trigger LOFAR, i.e to read out the radio antennas.

The main data acquisition (DAQ) is run on the master computer. This program also controls the DAQ programs running on the local computers. All the input parameters including those required by the DAQ on the local computers are set on the master computer. The whole DAQ is controlled and monitored using an online monitoring panel displayed on the master computer which can be accessed remotely. The display panel provides continuous monitoring of the performances of the electronics and the detectors during operations. Details on the LORA DAQ are described in Appendix 5.A.

5.3 Detector calibration and data taking

To calculate the total signal produced by a charged particle (which corresponds to the total energy deposited by the particle) from the recorded time traces, the following procedure is applied: The average pedestal is calculated from the 2μs window before the trigger. This pedestal is subtracted from the ADC values and the signal trace is integrated over the time window of $(T_{peak} - 40\text{ns})$ to $(T_{peak} + 250\text{ns})$. T_{peak} is the time of the maximum ADC count in the trace.

The resulting measured energy deposition of singly charged particles on a detector is shown in Figure 5.4. A Landau function is fitted to the measured distribution. The most probable value (the single particle peak) corresponds to the energy deposition of the through-going charged particle. This value is taken for the energy calibration of each detector and calculated to amount to 6.4 MeV. The high voltage applied to each photomultiplier is adjusted such that the Landau distribution peaks at ~ 400 ADC counts.

During operation, the trigger threshold for each individual channel is set with respect to the corresponding ADC noise of the channel. The recorded noise level exhibits a dependence on the ambient (outside) temperature and in particular, shows day-night variations. Therefore, we apply a dynamic trigger threshold to the recorded data. Every hour the threshold is calculated on the noise level registered during the last hour. The threshold is set to a value of $(\bar{N} + 4\sigma)$ where $\bar{N}$ and σ denote the mean value and the fluctuation of the noise for the last hour respectively.

The photomultipliers, placed in weather-proof shelters are also exposed to the ambient (outside) temperature. It is well known that the gain of a photomultiplier changes as function of operating temperature. A stable gain is necessary for the good performance of the experiment. Details on the stability of the gain for all the detectors during approximately 6 months of operation are given in Appendix 5.C. The overall stability looks good with 18 out of the 20 detectors showing gain variations within $\pm 10\%$ for more than $\sim 93\%$ of the total operation time.

For the present operation, a coincidence trigger condition of 3 out of 4 detectors has been set for each station. An event is accepted by the master computer if at least one station has been triggered. These trigger settings generate a total event rate of ~ 0.14 Hz from the full LORA array. The total daily data output amounts to about 180 Mb. Details on the different types of the data recorded are given in Appendix 5.B.

Full operation of LORA started in June 2011. Since then, air showers are continuously recorded with the set-up. By the time of writing this thesis, around 162 days of clean data have been collected with the full array. This amounts to a total of $2,154,327$ air shower events. For the analysis presented here, only events which trigger a minimum of 5 detectors (so, at least 2 stations) are considered. In total, we have recorded $114,659$ such events.

5.4 Reconstruction of air shower parameters

For a registered air shower, the arrival time of the first particle and the energy deposition in each detector are measured. Air shower properties are derived from these quantities, in particular: the arrival time of the shower, the direction and the position of the shower axis, the lateral density distribution of the charged particle and the total number of charged particles contained in the shower. The latter is used to estimate the energy of the shower inducing primary particle.

An example of a measured air shower is given in Figure 5.5. The top panel represents the measured arrival times and the bottom panel represents the energy depositions in the detectors.

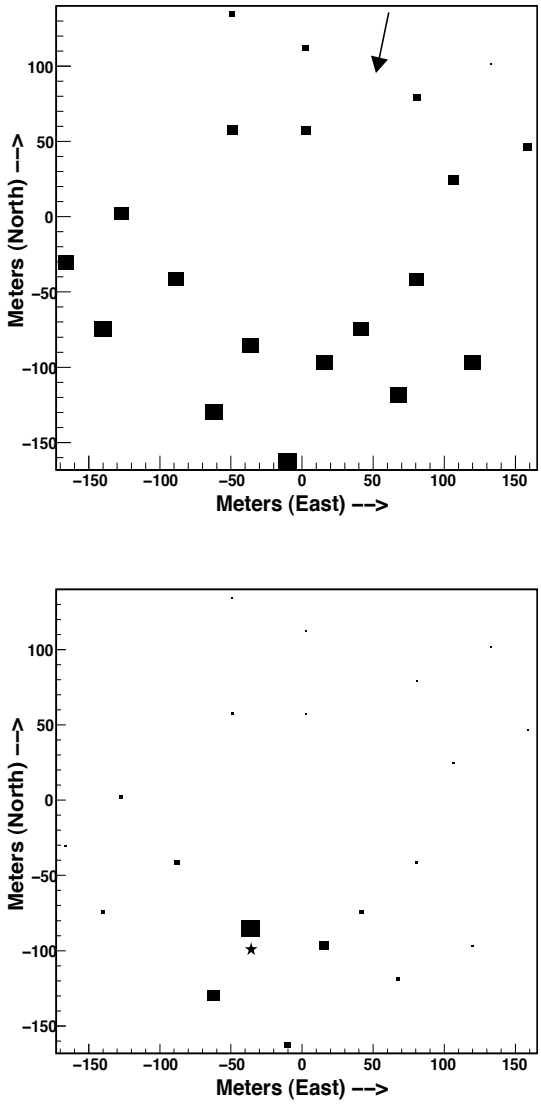

Figure 5.5: Display of a measured event. Top: Arrival times. Bottom: Energy depositions. The position of each box denotes the position of detector on the ground. The reconstructed direction is $(\theta, \phi) = (17.9°, 14.2°)$ and the reconstructed position of the shower axis is $(x_c, y_c) = (-35.7, -99.9)$ m. The arrow in the top panel indicates the azimuth angle ϕ of the arrival direction and the star in the bottom panel indicates the position of the shower axis.

5.4.1 Arrival direction

The arrival time of the particles in the detector is taken as the time at which the recorded signal crosses the threshold. The measured values are corrected for time offsets from different electron transit times in the photomultiplier tubes, different signal propagation speeds in different electronic channels and different signal cable lengths. The averaged offset is determined for each detector by a fit to the measured air shower data. In the LORA set-up, the main time offsets result from different cable lengths.

Using the relative signal arrival times between the detectors, the arrival direction of the primary cosmic ray can be reconstructed. For our reconstruction, we assume that the air shower particles move in a plane towards the ground and we neglect the small but finite curvature of the shower front [100]. We assume this plane moves with the speed of light c in the direction of its normal towards the ground. The normal to the shower plane is taken as the arrival direction of the primary cosmic ray (or the direction of the shower axis).

The direction of the shower axis is calculated by minimizing the function

$$\delta^2 = \sum_{i=1}^{k} [lx_i + my_i + nz_i + c(t_i - t_0)]^2 \tag{5.1}$$

The summation is over the total number of detectors k, (x_i, y_i, z_i) denote the position of the i^{th} detector on the ground, t_i the relative signal arrival time on that detector measured with respect to the first hit detector and t_0 denotes the time at which the shower plane passes through the origin of the coordinate system. The origin is taken as the center of the LORA detector array. And (l, m, n) denote the direction cosines of the normal to the plane and are related to the orientation of the shower axis.

Minimizing Eq. (5.1), we obtain the best fit values of (l, m, n, t_0). The zenith angle of the shower axis, measured from the vertical direction is obtained as,

$$\theta = \sin^{-1}\left(\sqrt{l^2 + m^2}\right) \tag{5.2}$$

and the azimuthal angle, measured clockwise from the North through East is obtained using

$$\phi = \cos^{-1}\left(\frac{m}{\sqrt{l^2 + m^2}}\right) \tag{5.3}$$

5.4.2 Position of shower axis and lateral density distribution

The position of the shower axis on the ground corresponds to the position where the primary cosmic ray would have hit, if it would not have interacted with the Earth's atmosphere. Diving the amount of energy deposition on each detector by the mean energy deposit per particle, the number of charged particles hitting the detector is obtained. Note that for our detectors, the mean energy deposition by one particle corresponds to ~ 400 ADC counts. The particle density n_i in each detector can be calculated by dividing the measured number

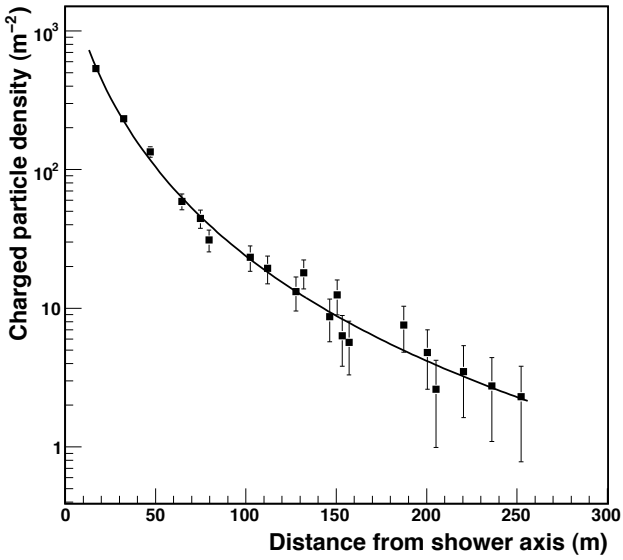

Figure 5.6: Lateral density distribution of an air shower event measured by LORA. The solid line is the fit using the NKG function (Eq. 1) to the measured data. The fit parameters obtained are $(N_{ch}, r_M) = (5.5 \times 10^6, 37.2\ \mathrm{m})$.

of particles by the effective detector area $A_d \cos\theta$. A_d denotes the actual geometrical area of the detector and the factor $\cos\theta$ takes into account the reduction in the effective area of the detector for inclined showers with zenith angle θ. However, the decrease in the detector effective area is compensated by an increase in the particle track length (and so, the amount of energy deposits) inside the detector which also scales as $\propto \cos\theta$. Plotting the measured particle density as function of the distance to the shower axis yields the lateral distribution. As an example, the lateral distribution of the event shown in Figure 5.5 is depicted in Figure 5.6.

The lateral density distribution can be described by a Nishimura-Kamata-Greisen function (NKG) [105, 128], given as

$$\rho(r) = N_{ch} C(s) \left(\frac{r}{r_M}\right)^{s-2} \left(1 + \frac{r}{r_M}\right)^{s-4.5} \tag{5.4}$$

where r denotes the radial distance from the position of the shower axis, N_{ch} is the total number of charged particles, r_M is the Molière radius (the shower scale length parameter), s is the lateral shape parameter (frequently referred to as the "shower age"). $C(s)$ is given

by,

$$C(s) = \frac{\Gamma(4.5-s)}{2\pi r_M^2 \Gamma(s)\Gamma(4.5-2s)} \tag{5.5}$$

Fitting a NKG function to the measured density distribution, the position of the shower axis and the total number of charged particles can be determined simultaneously along with the other two parameters r_M and s. As illustration, the curve in Figure 5.6 represents a fit of a NKG function to the data.

For the reconstruction of the shower parameters, it is convenient to transform the detector coordinates into the shower frame of reference. The origin of the shower frame is taken as the center of the detector array with the z-axis taken along the shower axis and the x-y plane containing the shower plane. This transformation makes the shower properties independent of the shower direction. The reconstruction is not straightforward and it needs to be done in several steps. First, proper starting values of the air shower parameters need to be provided to initiate the minimization procedure (see e.g., Ref. [132]). For the position of the shower axis (X_c, Y_c) in the shower frame, a good staring value can be obtained using the center of gravity of the energy depositions as given below,

$$X_c = \frac{\sum_{i=1}^{4} X_i n_i}{\sum_{i=1}^{4} n_i}\ ; \quad Y_c = \frac{\sum_{i=1}^{4} Y_i n_i}{\sum_{i=1}^{4} n_i} \tag{5.6}$$

where (X_i, Y_i) denote the coordinates of the detectors in the shower frame and the summation is over the 4 detectors which recorded the highest energy depositions.

Using Eq. (5.4), the measured lateral density at the position of the i^{th} detector (X_i, Y_i) in the shower frame can be written as,

$$n_i(X_i, Y_i) = N_{ch} F_i(X_i, Y_i) \tag{5.7}$$

$F_i(X_i, Y_i)$ represents the normalized lateral density distribution function given by,

$$F_i(X_i, Y_i) = C(s) \left(\frac{r_i}{r_M}\right)^{s-2} \left(1 + \frac{r_i}{r_M}\right)^{s-4.5} \tag{5.8}$$

where $r_i = \sqrt{(X_c - X_i)^2 + (Y_c - Y_i)^2}$ is the distance of (X_i, Y_i) from the position of the shower axis (X_c, Y_c) in the shower frame. Summing Eq. (5.7) over the number of detectors, we obtain

$$\sum_{i=1}^{k} n_i(X_i, Y_i) = N_{ch} \sum_{i=1}^{k} F_i(X_i, Y_i) \tag{5.9}$$

We determine the staring value of N_{ch} using Eq. (5.9). For r_M and s, we choose initial values based on averaged values of the measured showers, we take $r_M = 30$ m and $s = 1.7$ (see section 5.6). Throughout the minimization process, we keep s fixed. It is because fitting

r_M and s simultaneously is known to give poor results because of the strong correlation between them. Simulation studies with CORSIKA have shown that fixing s gives better results than fixing r_M (see also [35]). We have checked that choosing the starting value of r_M in the range of $(20 - 90)$ m produces almost the same final values of the fit parameters.

In the first minimization step, we fixed r_M and keep the others (X_c, Y_c, N_{ch}) as free parameters. In the second step, we take the results given by the first fit as the starting values. Then, we fixed (X_c, Y_c) and fit for (r_M, N_{ch}). These minimization steps are iterated a few times with the outputs of each iteration taken as the starting values for the next iteration. For the position of the shower axis, the result of the last iteration is taken as the final value. This value can be further transformed into the position of the shower axis on the ground (x_c, y_c) following a proper coordinate transformation. For N_{ch} and r_M, we follow one step further. After the last iteration run, we determine the lateral density distribution as a function of the radial distance from the position of the shower axis. Then, we fit the measured lateral distribution with Eq. (5.4) and determine the final values of N_{ch} and r_M.

The reconstructed quantities are shown in Figure 5.5 for illustration. The reconstructed azimuth angle ϕ is indicated by the arrow on the top panel. The star on the bottom panel represents the reconstructed position of the shower axis. For the shower depicted in Figure 5.6, the reconstructed number of charged particles and the Molière radius are found to be 5.5×10^6 and 37.2 m respectively.

5.5 Reconstruction accuracies

The accuracies in the reconstruction of air shower parameters are determined from the data itself using the divided array method. We divide the full array into two sub-arrays. For the accuracy in the position of the shower axis, we calculate the difference between the estimates of the two half sub-arrays as,

$$\Delta^{12}_{pos} = \sqrt{(x_1 - x_2)^2 + (y_1 - y_2)^2} \tag{5.10}$$

where (x_1, y_1) and (x_2, y_2) are the reconstructed positions of the shower axis on the ground with the two sub-arrays respectively. Then, the reconstruction accuracy for the full array σ_{pos} is calculated as,

$$\sigma_{pos} = \frac{\sigma^{12}_{pos}}{\sqrt{2}} \tag{5.11}$$

where σ^{12}_{pos} denote the spread of the distribution of Δ^{12}_{pos}.

For the arrival direction accuracy, we calculate the space angle difference between the estimates of the two sub-arrays as,

$$\Delta^{12}_{angle} = \cos^{-1}\left[\sin\theta_1 \sin\theta_2 \cos(\phi_1 - \phi_2) + \cos\theta_1 \cos\theta_2\right] \tag{5.12}$$

where (θ_1, ϕ_1) and (θ_2, ϕ_2) are the arrival directions reconstructed with the two sub-arrays. For accuracy in the number of charged particles, the difference between the two sub-arrays

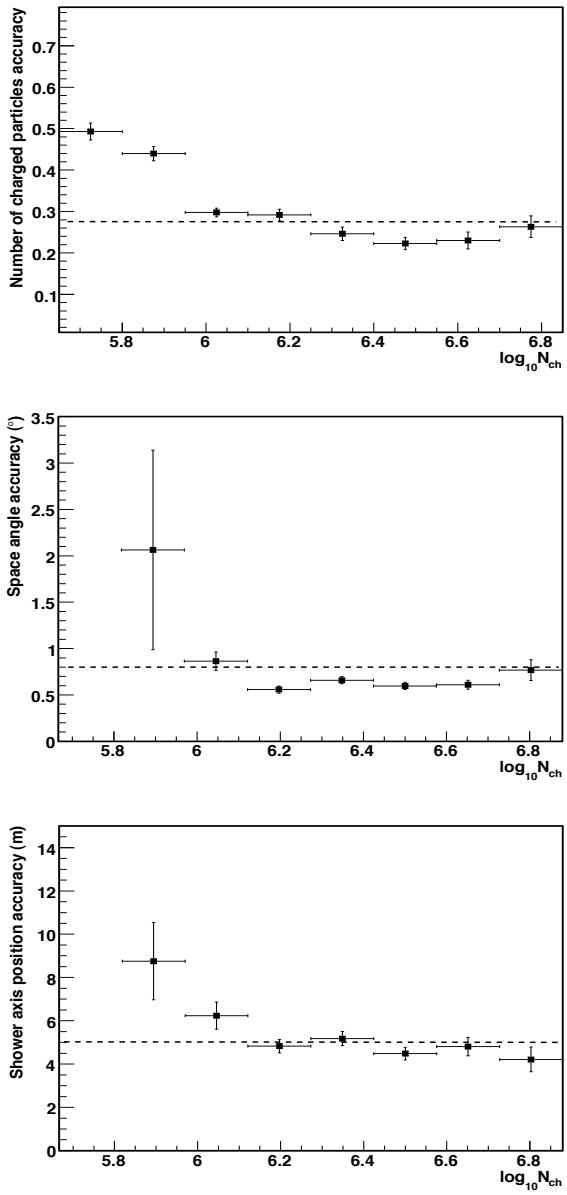

Figure 5.7: Reconstruction accuracies obtained from the data: number of charged particles N_{ch} (top), arrival direction (middle) and position of the shower axis (bottom). Only showers with zenith angles $< 18^\circ$ are considered. For showers with $\log_{10} N_{ch} \gtrsim 6.2$, the accuracies are $\lesssim 27\%$ for the number of particles, $\lesssim 0.8^\circ$ for the arrival direction and $\lesssim 5$ m for the position of the shower axis. These are shown by the dashed line in the figures.

is calculated relative to the number given by the full array as,

$$\Delta_{ch}^{12} = \left(\frac{N_{ch}^{1} - N_{ch}^{2}}{N_{ch}} \right) \tag{5.13}$$

where N_{ch}^{1}, N_{ch}^{2} are the number of particles given by the two sub-arrays and N_{ch} is the number given by the full array. The reconstruction accuracies for the arrival direction and the number of particles are then calculated using a similar relation as given by Eq. (5.11).

Figure 5.7 shows the reconstruction accuracies calculated from the data as a function of the number of particles determined from the full array. Only showers with zenith angle $\theta < 18^{\circ}$ are considered in the calculation. The top, middle and the bottom panels in the figure correspond to the number of particles, arrival direction and the position of the shower axis, respectively. The reconstruction accuracies for showers with number of particles $\log_{10} N_{ch} \gtrsim 6.2$ are within approximately 27% for the number of particles, 0.8° for the arrival angle and 5 m for the position of the shower axis. It will be shown later that only showers with total number of particles $\log_{10} N_{ch} > 6.25$ are reliable for the reconstruction of the all particle energy spectrum with LORA and also this number corresponds to the energy range which is sensitive to LOFAR.

5.6 Measured distribution of extensive air shower parameters

A good check and also a better understanding of the performance of our experiment can be provided by the nature of the distribution of several air shower parameters reconstructed from the measured data.

Figure 5.8 shows the distribution of the positions of the shower axis for air showers measured with LORA. For the distribution, we select only those events that trigger at least 5 detectors with a minimum particle density of 1 particle m^{-2} and which have Molière radii in the range of $(10 - 200)$ m. The black squares in the figure represent detector positions and the circle represents a fiducial volume of radius 150 m around the array center. For our analysis in the following, we only select those events with position of the shower axis falling within this fiducial volume. This volume is chosen such that we include in our analysis only those events with reliable estimates of the position of the shower axis and at the same time, retain as many events as possible.

Figure 5.9 shows the zenith angle (top panel) and the azimuthal angle (bottom) distribution of the measured air shower events. The distributions consider events with positions of the shower axis within the fiducial range and Molière radii within $(10 - 200)$ m. The zenith angle distribution is fitted in the range of $(4^{\circ} - 40^{\circ})$ with the following equation,

$$f(\theta) = a_1 \ \sin\theta \cos^{a_2}\theta \tag{5.14}$$

The fit parameters are found to be $a_1 = (1.073 \times 10^4 \pm 71)$ and $a_2 = (8.786 \pm 0.062)$. The thick curve in the figure represents the fit result. The peak of the distribution is found

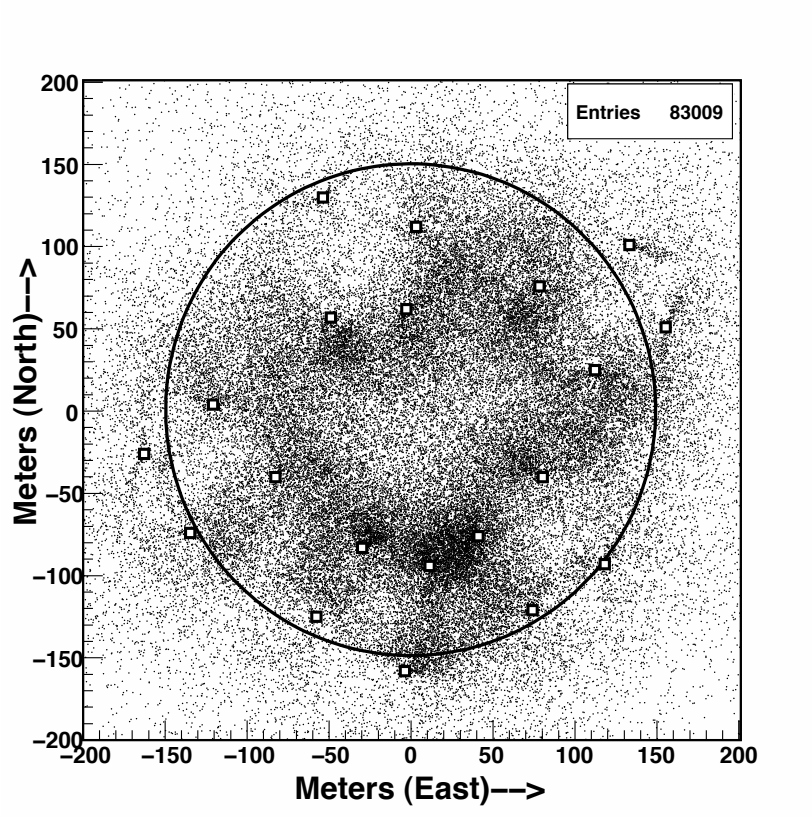

Figure 5.8: Distribution of the reconstructed position of the shower axis for measured events. Only showers with Molière radii in the range of $r_M = (10 - 200)$ m are included in the distribution. The open squares denote detector positions and the circle represents a fiducial volume of radius 150 m chosen for our analysis.

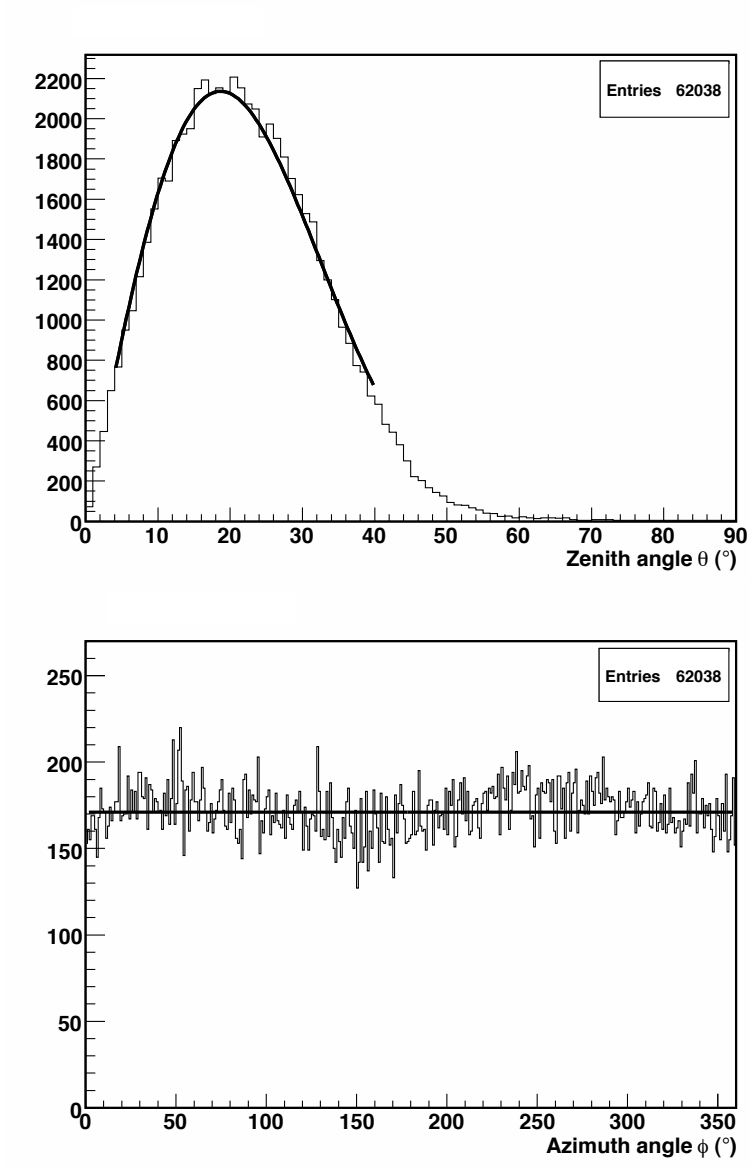

Figure 5.9: Arrival direction distribution for the measured showers with positions of the shower axis within the fiducial volume and Molière radii in the range of $(10\ \mathrm{m} < r_M < 200\ \mathrm{m})$. Top: Zenith angle distribution. The thick line is the fit using Eq. (14) in the range of $4^\circ \leq \theta \leq 40^\circ$. The fit parameters are found to be $a_1 = (1.073 \times 10^4 \pm 71)$ and $a_2 = (8.786 \pm 0.062)$. Bottom: Azimuth distribution. The azimuth is measured eastwards from the north. The horizontal line represents a straight line fit to the distribution.

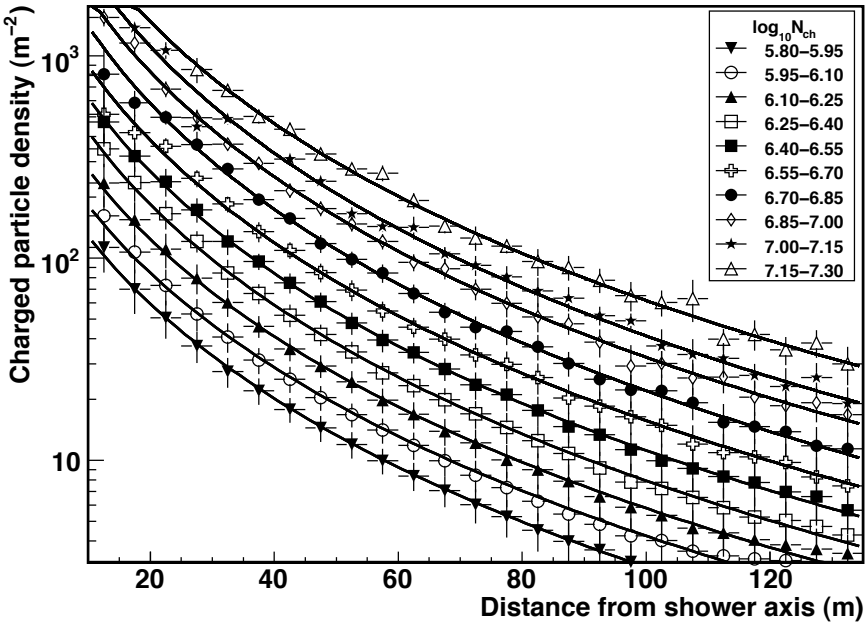

Figure 5.10: Measured averaged lateral density distribution for different showers with $\log_{10}N_{ch} = (5.8 - 7.3)$. Only showers with $\theta < 18^\circ$ and positions of the shower axis within the fiducial volume are considered. The lines represent the fits of a NKG function to the data for fixed age parameter at $s = 1.7$. The fits yield Molière radii in the range of $r_M \sim (26 - 35)$ m.

to be at $\theta \sim 19^\circ$. The steep rise in the distribution below the peak is due to the increase in the solid angle with the zenith angle. The steep fall above the peak is due the combined effect of the decrease in the effective collection area of the array and the increase in the shower attenuation at larger zenith angles. The effect of the attenuation is expected to be more significant for showers initiated by low energy primaries.

The azimuth distribution is almost uniform at all angles. This is expected because of the high level of isotropy in the arrival direction of cosmic rays which is related to their diffusive nature of propagation in the Galaxy. The horizontal line in Figure 5.9 (bottom panel) represents a straight line fit to the measured distribution.

Figure 5.10 shows the averaged lateral density distributions for showers with the number of charged particles in the range of $\log_{10} N_{ch} = (5.8 - 7.3)$. Only showers with zenith angles $\theta < 18^\circ$ and positions of the shower axis within the fiducial volume are considered for the distribution. The lines represent the fits of a NKG function (Eq. 5.4) to the distributions

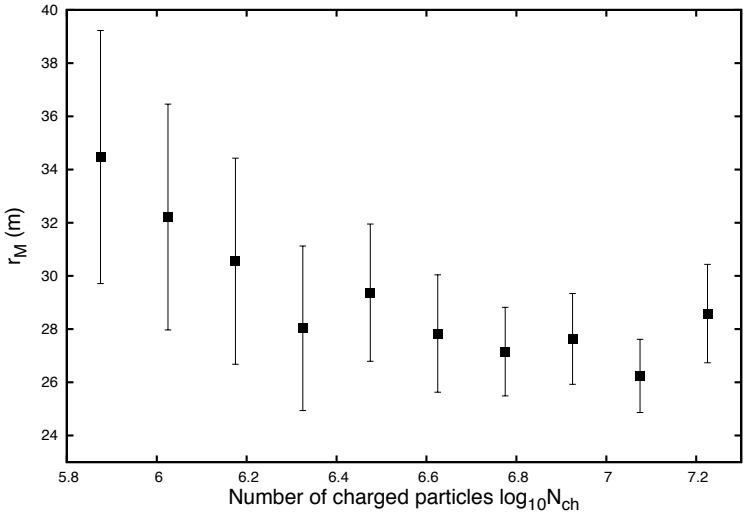

Figure 5.11: Molière radius r_M as a function of the number of charged particles N_{ch} for showers with zenith angle $\theta < 18.4°$. The r_M values are obtained from the NKG fits shown in Figure 5.10.

taking the age parameter fixed at $s = 1.7$. Taking $s = 1.7$ produces an overall best fit to the distributions than taking other values. Moreover, the mean value of s for the overall data is found to be ~ 1.7 and that of r_M as ~ 30 m when both s and r_M are fitted simultaneously during the minimization procedure described in section 5.2. Thus, we chose $s = 1.7$ and $r_M = 30$ m as the starting values in the determination of air shower parameters described in section 5.4.

The values of the Molière radii obtained from the NKG fits are shown in Figure 5.11. The values obtained are in the range of $(26 - 35)$ m. These values are smaller than the classical value for the electromagnetic shower component of ~ 80 m. The value of r_M is found to decrease with the number of charged particles up to $\log_{10} N_{ch} \sim 7.1$. This decrease in the r_M (scale length) is possibly due to the increase in the depth of the shower maximum as the primary energy increases. As the shower maximum gets closer to the ground, the particles suffer less scattering from the shower axis due to the smaller column density of air they need to traverse. For $\log_{10} N_{ch} \gtrsim 7.1$, our measurements seem to indicate an increase in r_M as N_{ch} increases. The reason for this behavior is not properly understood, though a change in the composition might be responsible for such an effect. More data in the future would be needed for a better understanding. Similar effects on the atmospheric attenuation coefficient that we have measured will be discussed in section 5.7.

5.7 Estimation of atmospheric attenuation

Extensive air showers suffer from attenuation in the atmosphere. The attenuation results into a decrease in the number of charged particle N_{ch} as the shower traverse through the atmosphere. The amount of attenuation, as a function of the atmospheric depth X, can be described by the attenuation length Λ given as [37],

$$N_{ch}(X) = N_0 \exp\left(-\frac{X}{\Lambda}\right) \tag{5.15}$$

N_0 denotes the true number of particles which corresponds to no attenuation. Since the atmospheric depth scales with the zenith angle θ as $X = X_0 \sec\theta$ where X_0 is the vertical atmospheric depth, the shower attenuation is expected to increase with the zenith angle.

There are different methods to determine the attenuation length [37]. One method is the method of constant intensity [147]. The constant intensity method is based on the assumption that the intensity of cosmic rays remains constant in all directions in the sky. This assumption is reasonable considering the observed isotropic flux of cosmic rays (see e.g. [154]). The method uses shower N_{ch} spectra of different zenith angles to determine the amount of atmospheric attenuation. Showers initiated by primaries of the same type and energy, but arriving at different zenith angles, will produce different number of charged particles on the ground due to different levels of attenuation in the atmosphere. Since each primary energy is assumed to correspond to a certain intensity, for a given intensity we expect to see shifts in N_{ch} with zenith angle. The amount of the shift can give a good estimate of the amount of attenuation in the atmosphere. In the following, we present our estimates of the attenuation length Λ from the LORA data using the constant intensity method.

Figure 5.12 (top panel) shows the integral N_{ch} distribution of the measured showers for 7 different zenith angle bins taken in the range of $(0^\circ - 34.9^\circ)$. The angular bins are chosen such that they cover the same solid angle in the sky. From the distribution, the integral N_{ch} spectrum can be constructed by folding in the total observation time and the total effective collection area of the array. The N_{ch} spectra thus obtained for the different angular bins are shown in Figure 5.12 (bottom panel) for the range $5.65 \leq \log_{10} N_{ch} \leq 7.6$. In the figure, the vertical dashed line represents the value of N_{ch} above which the detection efficiency is 100%. Details about the reconstruction of the N_{ch} spectrum and the calculations of detection efficiency and the effective area will be presented in section 5.9. For the calculation of the attenuation length, we consider only the spectra in the region of 100% detection efficiency. We select 11 intensity cuts within the range of $(1.90 \times 10^{-10} - 2.71 \times 10^{-9})$ m^{-2}sr^{-1}s^{-1}. In Figure 5.12 (bottom panel), the horizontal lines represent 2 such cuts, one at 3.80×10^{-10} m^{-2}sr^{-1}s^{-1} and the other at 1.95×10^{-9} m^{-2}sr^{-1}s^{-1}. It can be noticed that an intensity cut intersects the spectra at different values of N_{ch}. In calculating the intersection points, we consider an interpolated value between two points in the N_{ch} spectrum. The intersection points (N_{ch}) are plotted as function of θ in Figure 5.13 for the 11 intensity cuts. In the plots, the values of θ are taken as the zenith angles corresponding to half the solid angle for the different zenith angle bins. Figure 5.13 is commonly referred to as the attenuation curves.

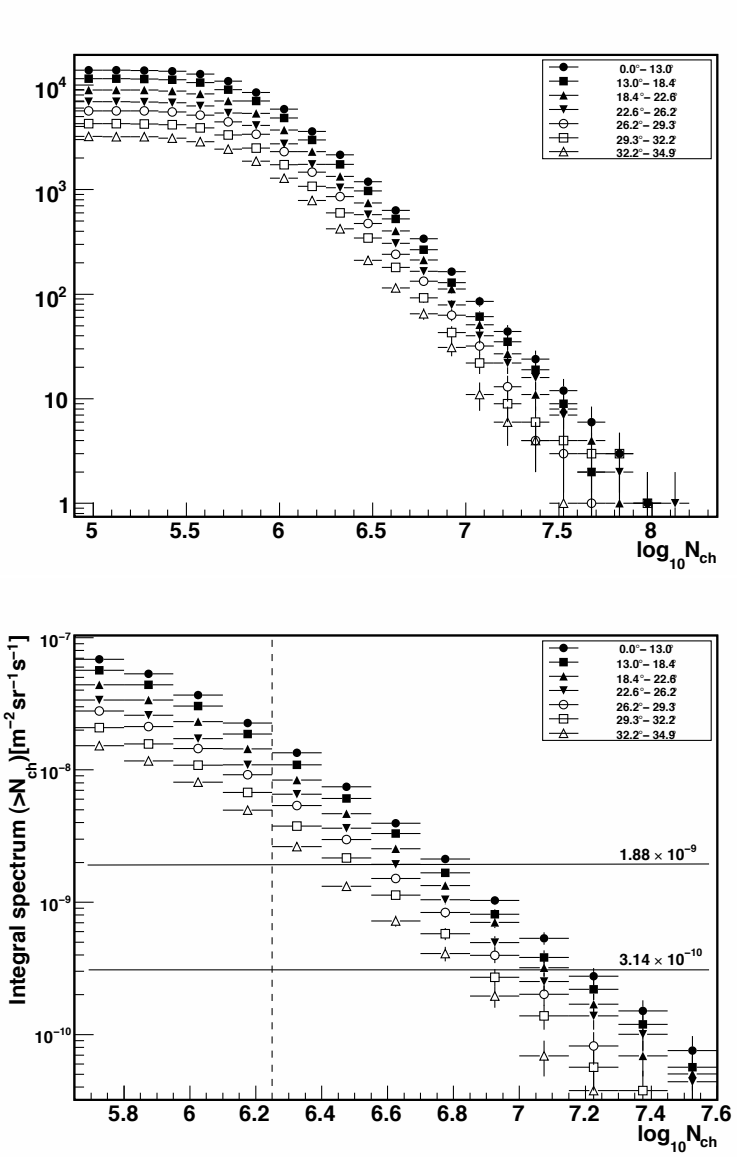

Figure 5.12: Top: Integral N_{ch} distributions of the measured showers for different zenith angle bins in the range of $(0^\circ - 34.9^\circ)$. Bottom: Integral N_{ch} spectra in the range $5.65 \leq \log_{10} N_{ch} \leq 7.6$ for the distributions shown in the top panel. The vertical dashed line represents the N_{ch} value above which the detection efficiency is 100%. The two horizontal lines represent the integral cuts applied at 3.80×10^{-10} m^{-2}sr^{-1}s^{-1} and 1.95×10^{-9} m^{-2}sr^{-1}s^{-1}.

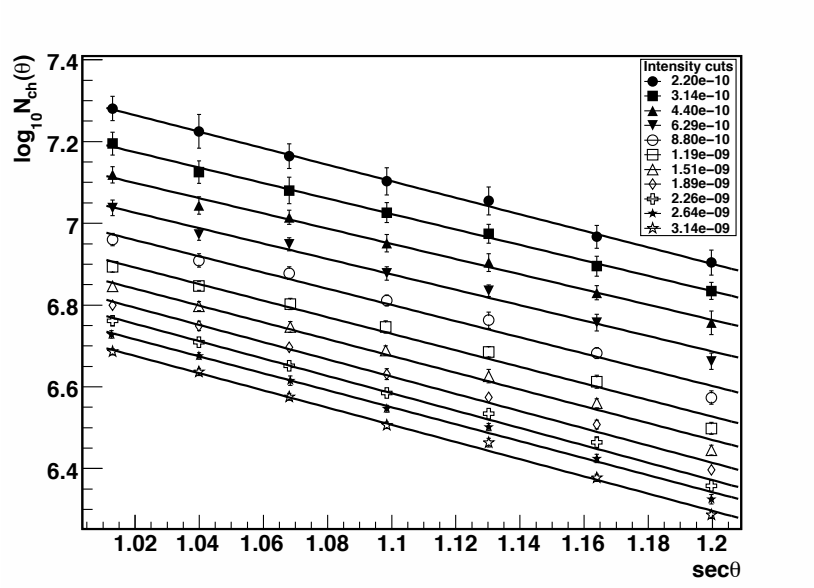

Figure 5.13: N_{ch} as a function of zenith angle (θ) for the 11 intensity cuts. The θ values are taken as the zenith angles which correspond to half the solid angle for the different zenith angle bins used in Figure 5.12. Different symbols corresponds to the different intensity cuts as indicated in the key box in units of $\mathrm{m}^{-2}\mathrm{sr}^{-1}\mathrm{s}^{-1}$ and the lines represent the fits using Eq. (5.18).

Eq. (5.15) can be written as a function of the zenith angle θ as follows,

$$N_{ch}(\theta) = N_0 \exp\left(-\frac{X_0 \sec\theta}{\Lambda}\right) \tag{5.16}$$

We now introduce a reference angle θ_r for which we can write an equation similar to Eq. (5.16) as,

$$N_{ch}(\theta_r) = N_0 \exp\left(-\frac{X_0 \sec\theta_r}{\Lambda}\right) \tag{5.17}$$

From Eqs. (5.16) and (5.17), we can now write $N_{ch}(\theta)$ in terms of θ_r as,

$$N_{ch}(\theta) = N_{ch}(\theta_r) \exp\left(-\frac{X_0}{\Lambda}(\sec\theta - \sec\theta_r)\right) \tag{5.18}$$

The significance of introducing the reference angle will be discussed later in the next section. For our calculation, we choose θ_r to be 21° as in [132] and $X_0 = 1024$ g cm^{-2} which is the vertical atmospheric thickness for the North-Western Europe. By fitting the attenuation curves in Figure 5.13 with Eq. (5.18), the attenuation length Λ can be determined along

Table 5.1: Values of the fit parameters obtained by fitting the attenuation curves in Figure 5.13 with Eq. (5.18).

Intensity cut ($m^{-2}sr^{-1}s^{-1}$)	Attenuation length Λ (g cm^{-2})	$\log_{10} N_{ch}(21^\circ)$
2.19×10^{-10}	220.00 ± 20.61	7.161 ± 0.014
3.14×10^{-10}	235.13 ± 18.67	7.077 ± 0.012
4.39×10^{-10}	238.83 ± 16.84	7.004 ± 0.008
6.28×10^{-10}	235.83 ± 14.01	6.930 ± 0.007
8.79×10^{-10}	224.20 ± 10.64	6.857 ± 0.006
1.19×10^{-09}	219.40 ± 9.01	6.788 ± 0.005
1.51×10^{-09}	216.42 ± 7.16	6.735 ± 0.005
1.88×10^{-09}	210.94 ± 5.95	6.686 ± 0.004
2.26×10^{-09}	209.31 ± 5.96	6.645 ± 0.004
2.64×10^{-09}	214.13 ± 6.18	6.610 ± 0.004
3.14×10^{-09}	211.23 ± 5.18	6.568 ± 0.003

with $N_{ch}(\theta_r)$ for the different intensity cuts. The fit results are represented by the different lines shown in Figure 5.13 and the values of the fit parameters are listed in Table 5.1.

In Figure 5.14, the attenuation lengths obtained from the fits are plotted as a function of intensity cuts (integral flux). It is found that the attenuation length first increases from $\Lambda \sim 211$ g cm^{-2} with decreasing integral flux till it reaches a maximum of $\Lambda \sim 245$ g cm^{-2} at a flux of $\sim 3.80 \times 10^{-10}$ $m^{-2}sr^{-1}s^{-1}$ and then, it starts decreases with decreasing value of the integral flux. In terms of energy, the result implies that Λ increases with the primary energy until it reaches a certain peak energy and beyond this energy, Λ starts decreasing as the energy increases. The initial increase in Λ with energy below the peak energy may be due to the increase in the depth of the shower maximum X_{max} as the primary energy increases. Showers with X_{max} closer to the ground are expected to suffer less attenuation due to the lesser amount of air mass they traverse on reaching the ground, thus producing larger values of Λ. On the other hand, the decrease in Λ above the peak energy might be related to the transition in the composition of cosmic rays from lighter to heavier elements. For the same total energy, a heavy cosmic-ray primary of mass number A produces an X_{max} value smaller than that of a proton as given by $X^A_{max} = X^p_{max} - \bar{X} \ln A$, where X^A_{max} and X^p_{max} denote the X_{max} for the heavy primary and the proton respectively and $\bar{X} = 36.66$ g cm^{-2} is the radiation length of electrons in air [115]. An air shower initiated by a heavy primary carrying a total energy E can be considered as equivalent to a sum of A number of individual showers initiated by protons each carrying an energy of E/A. Because the effective primary energy of the heavy nucleus initiating the shower is relatively less (by a factor of $1/A$) as compared to the proton, the X_{max} value in the case of heavy nuclei are comparatively smaller (shallower). This will lead to an increase in the amount of attenuation in the atmosphere at those energies producing an apparent lower values of Λ.

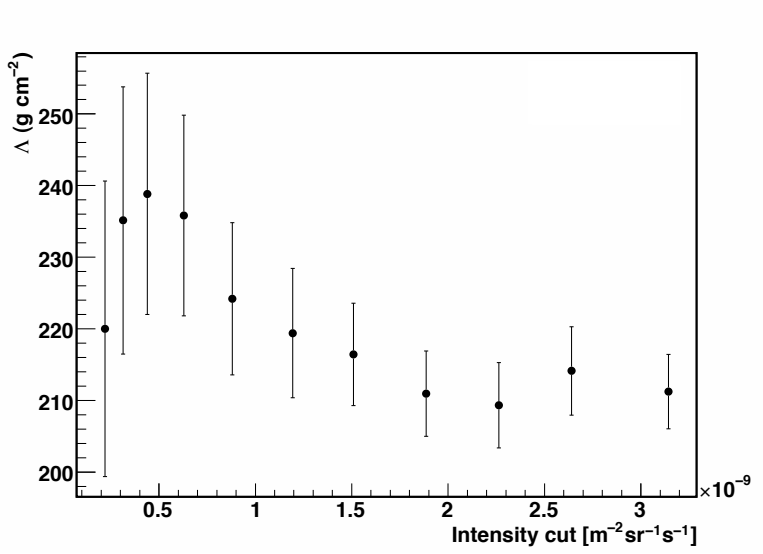

Figure 5.14: Attenuation lengths Λ for the different intensity cuts (integral flux) obtained by fitting the attenuation curves shown in Figure 5.13.

5.8 Zenith angle correction on the number of particles

In the previous section, we introduce the reference zenith angle θ_r for which the number of charged particles can be expressed using Eq. (5.18) as,

$$\ln N_{ch}(\theta_r) = \ln N_{ch}(\theta) + \frac{X_0}{\Lambda}(\sec\theta - \sec\theta_r) \tag{5.19}$$

For an air shower, $N_{ch}(\theta)$ and θ in Eq. (5.19) are obtained from the measurements, and Λ is obtained by fitting the attenuation curve as discussed in the previous section. Thus, for any measured shower, a reference number of charged particles $N_{ch}(\theta_r)$ can be determined using Eq. (5.19). The reference number is the number of particles that would have been measured if the shower had arrived at the reference angle θ_r instead of θ. Introducing the reference angle has an advantage in that it produces a zenith angle independence measure of N_{ch} thus getting rid of the effects of different levels of shower attenuation in the atmosphere and, ultimately, produces an N_{ch} spectrum which is independent of the zenith angle. Having calculated $N_{ch}(\theta_r = 21^\circ)$ for every shower measured with LORA, the resulting zenith angle corrected distribution of the number of particles is shown in Figure 5.15. The errors shown are only statistical and are calculated as the 1σ poissonian error on the number of events contained in each bin. The distribution in Figure 5.15 considers only events that trigger a minimum of 5 detectors. This minimum trigger condition along with other quality cuts applied in our analysis as listed in Table 5.2 result into a total of $54,172$ events left for

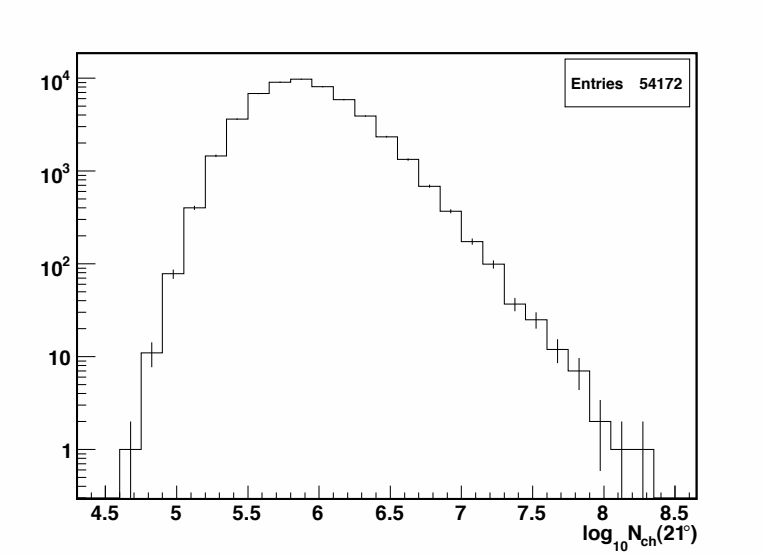

Figure 5.15: Zenith angle corrected distribution of the number of particles. The errors represent the 1σ poissonian error on the number of events. Only events that trigger a minimum of 5 detectors are considered. Other quality cuts applied in our analysis are listed in Table 5.2.

further analysis. This left over number is only $\sim 2.5\%$ of the total number of $2,154,327$ events we have recorded using a 3-fold detector coincidence trigger condition. The number of events that remain at different levels of applying the quality cuts are summarized in Table 5.3.

As mentioned earlier, the number of particles is a good measure of the primary energy. Thus, the peak of the N_{ch} distribution gives a good estimate of the energy threshold of the measured primary. The peak value depends strongly on the number of detectors triggered. Higher energy primary generate bigger showers and hence, can effectively trigger a wider area on the ground. This is shown explicitly in Figure 5.16 (top panel) where we have plotted the zenith angle corrected N_{ch} distributions as a function of the minimum number of detectors triggered $N_D = (5, 8, 11, 14, 17, 20)$ as indicated in the figure. We can notice that the distributions peak at relatively higher values of N_{ch} as N_D takes larger values. The corresponding event rates as a function of N_D are shown in the bottom panel of Figure 5.16. The rates are found to be in the range of $\sim (4 \times 10^{-3} - 1.5 \times 10^{-5})$ Hz for $N_D = (5 - 20)$. The numbers next to the data points denote the corresponding primary energy thresholds in PeV. They are calculated using the N_{ch}-energy relation given by Eq. (5.22) in the next section. The measured energy thresholds are in the range of $(5.1 - 48.9)$ PeV for $N_D = (5 - 20)$. Also shown in the bottom panel is the energy threshold for LOFAR to detect

Table 5.2: Quality cuts and shower parameter values adopted in our analysis. The first column gives the names of the parameters and the second column gives their values.

Parameter	Values
Detector trigger threshold	≥ 1 particle m^{-2}
Number of detectors triggered	≥ 5
Reference zenith angle	21°
Shower age parameter	1.7
Molière radius	$(10 - 200)$ m
Position of the shower axis	< 150 m
Zenith angle	$< 34.9^{\circ}$

Table 5.3: Number of events left at different levels after applying the quality cuts.

Selection/quality cuts	Number of events
Total recorded with 3-fold detector coincidence	$2,154,327$
Minimum 5 detectors trigger	$114,659$
Molière radius within $(10 - 200)$ m	$83,009$
Position of the shower axis < 150 m	$62,038$
Zenith angle $< 34.9^{\circ}$	$54,172$

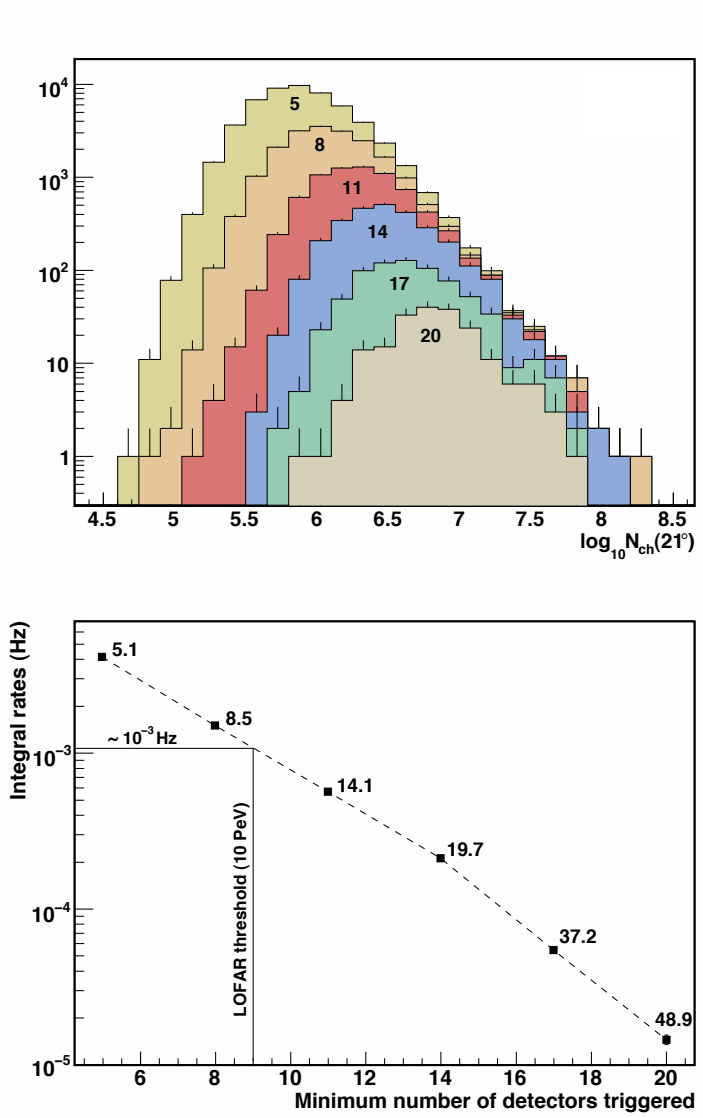

Figure 5.16: Top: Zenith angle corrected distributions of the number of charged particles for different minimum number of detectors triggered $N_D = (5, 8, 11, 14, 17, 20)$. The peak of each distribution corresponds to the energy threshold of the measured cosmic rays. Bottom: The corresponding integral event rates as a function of N_D. The numbers near the points represent the energy thresholds in PeV. The LOFAR energy threshold to detect air showers which is ~ 10 PeV is also indicated. It corresponds to $N_D = 9$ and an event rate of $\sim 10^{-3}$ Hz.

radio signals from air showers. The expected LOFAR energy threshold which is ~ 10 PeV corresponds to $N_D = 9$. This corresponds to an event rate of $\sim 10^{-3}$ Hz which is ~ 3.6 events per hour.

5.9 Energy reconstruction and the all-particle energy spectrum

5.9.1 Detection efficiency and effective collection area

To construct the all-particle energy spectrum, we first calculate the detection efficiency as a function of the position of the shower axis, zenith angle, and the number of charged particles. The detection efficiencies are calculated by simulating showers of different number of particles in the range of $4 \leq \log_{10} N_{ch}(21^\circ) \leq 9$ with randomly chosen positions of the shower axis within the fiducial volume. The arrival angles are chosen in the range of $0 < \theta < 35^\circ$ and the zenith angle dependence of the number of particles is taken into account using Eq. (5.18) with $X_0 = 1024$ g cm^{-2} and $\Lambda = 221.4$ g cm^{-2}. The latter value is the mean of the attenuation lengths obtained from the LORA data (see Table 5.1). The number of particles hitting each detector are calculated by assuming that the lateral densities follow Eq. (5.4) with $s = 1.7$ and $r_M = 30$ m. We assume a Gaussian fluctuation on the number of particles hitting each detector and apply a detector trigger threshold of 1 particle m^{-2}. Our simulation also takes into account the zenith angle reduction of the detector collection area. The positions of the shower axis are binned in rectangular cells each of size $(1\mathrm{m} \times 1\mathrm{m})$ and the zenith angles are binned in 1° bin size. For each position cell of the shower axis, the detection efficiency for each zenith angle bin is calculated. Then, the effective solid angle Ω_{eff} for a given position cell of the shower axis, hereafter, denoted by the indices (i, j) is calculated as,

$$\Omega_{eff}(i,j) = 2\pi \sum_{k=1}^{q} p(i,j,\theta_k)\,(\cos\theta_{k-1} - \cos\theta_k) \tag{5.20}$$

where the indices i and j runs along the X and Y axes of the detector array respectively, q denotes the number of zenith angle bins with $\theta_0 = 0^\circ$ and $\theta_q = 35^\circ$, and $p(i, j, \theta_k)$ denotes the detection efficiency for the k^{th} zenith angle bin. $p(i, j, \theta_k)$ is calculated as the ratio of the number of showers triggered to the total number of showers generated with position of the shower axis in the (i, j) cell and with zenith angles in the k^{th} bin. Eq. (5.20) assumes that the detection efficiency is independent of the azimuthal direction.

Figure 5.17 represents one of our simulation results. The figure shows the detection efficiencies at different positions of the shower axis for showers with $\log_{10} N_{ch}(21^\circ) = (5.5 - 5.65)$ and which trigger a minimum of 5 detectors. The detector positions are also superimposed in the figure, they are represented by the black and white squares. The grey scale represents different values of the detection efficiency with the black corresponding to

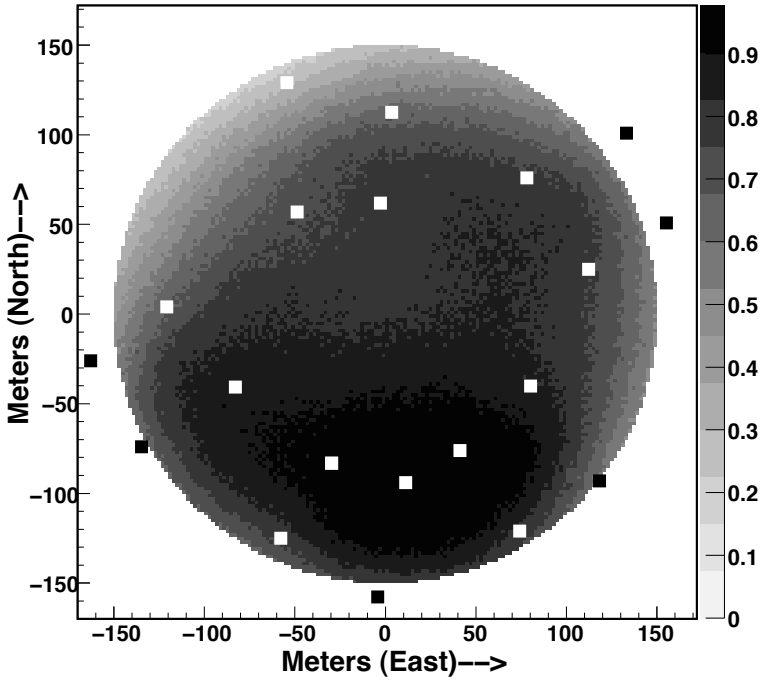

Figure 5.17: Simulated detection efficiencies at different positions of the shower axis for showers with $\log_{10} N_{ch}(21^\circ) = (5.5 - 5.65)$. The showers are simulated with positions within 150 m from the array center and with zenith angles $\leq 35^\circ$. The simulation assumes a detector trigger threshold of 1 particle m^{-2} and a minimum trigger condition of 5 LORA detectors to accept as an event. The black and white squares represent the detector positions.

100% efficiency. The higher detection efficiencies on the lower half of the figure is due to the slightly denser arrangement of detectors in the region.

Multiplying Eq. (5.20) by the area of a cell gives the effective area $a(i,j)$ of one cell. The total effective area A_{eff} for a shower with number of particles at the reference angle $N_{ch}(21^\circ)$ is then calculated by summing over all the cells as,

$$A_{eff} = \sum_i \sum_j a(i,j) \tag{5.21}$$

Figure 5.18 (bottom panel) shows the effective collection area of the LORA array as a function of $N_{ch}(21^\circ)$. Also shown in the figure (top panel) is the total detection efficiency for different values of $N_{ch}(21^\circ)$. The vertical dashed line shows the value of $N_{ch}(21^\circ)$ above which the detection efficiency is 100%.

5.9.2 Energy parameterization

To convert the measured number of particles into the primary energy, a proper conversion relation is required. For the present analysis, we use the relation given for the KASCADE-Grande experiment [132],

$$\log_{10} E = a + b \log_{10} N_{ch}(21^\circ) \tag{5.22}$$

where E represents the primary energy in GeV and (a,b) are constants. The values of a and b depend on the choice of the primary mass composition. For mixed composition, i.e., assuming equal fractions of protons, helium, carbon, silicon, and iron, the values of the constants are given as $a = 1.23$ and $b = 0.95$ [132]. The energy parameterization given by Eq. (5.22) is plotted in Figure 5.19 as function of the number of charged particles.

In Eq. (5.22), $N_{ch}(21^\circ)$ represents the number of particles calculated at the reference angle $\theta_r = 21^\circ$ as discussed earlier. In [132], θ_r is chosen to be 21° which is the peak angle of the zenith angle distribution for the KASCADE-Grande experiment. For LORA, the measured zenith angle distribution peaks at $\theta \sim 19^\circ$ which is quite closed to the KASCADE-Grande value. It should be noted that the zenith angle correction on the number of particles can be performed by taking any value of the reference angle θ_r. Taking different reference angles will produce different $N_{ch}(\theta_r)$ spectra, but the resulting energy spectra will remain the same and is independent of the choice of the reference angle.

5.9.3 N_{ch} spectrum and the all-particle energy spectrum

For the reconstruction of the N_{ch} spectrum, we use the $N_{ch}(21^\circ)$ distribution obtained with the minimum number of triggered detectors taken as $N_D = 5$ (shown in Figure 5.15). From the distribution, the differential spectrum is obtained by folding in the total effective collection area and the total observation time as follows,

$$\left(\frac{dI}{dN_{ch}}\right)_i = \left(\frac{\Delta n}{\Delta N_{ch}}\right)_i \times \frac{1}{A_{eff} T_{obs}} \tag{5.23}$$

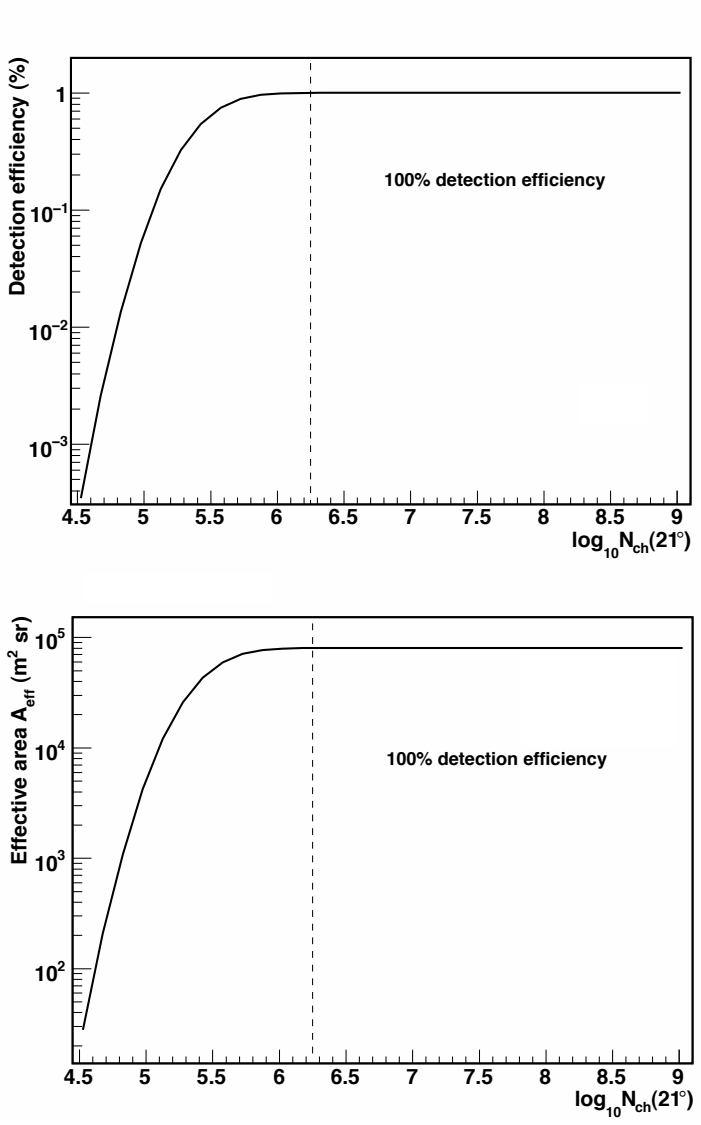

Figure 5.18: Detection efficiency (top panel) and effective collection area (bottom panel) as function of the number of particles at the reference angle $N_{ch}(21^\circ)$. The vertical dashed line represents the value of $N_{ch}(21^\circ)$ above which the detection efficiency is 100%.

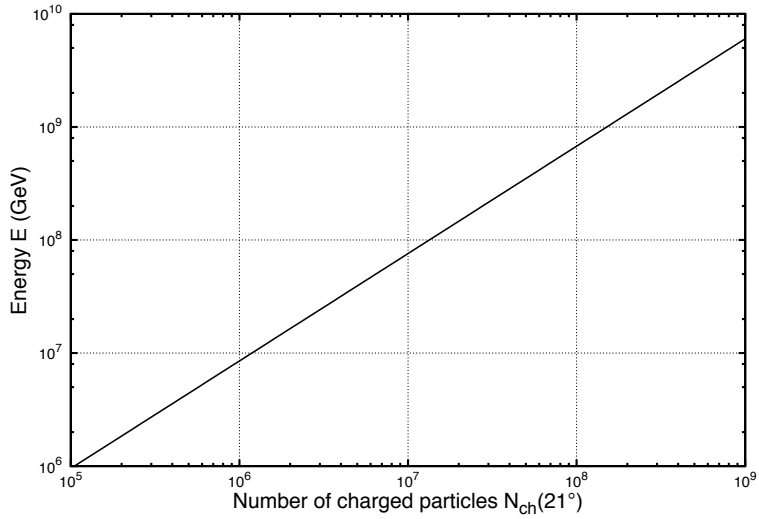

Figure 5.19: Energy parameterization as a function of the number of charged particles $N_{ch}(21^{\circ})$ given by Eq. (5.22).

where Δn is the number of events in the i^{th} bin of the number of particles with bin width ΔN_{ch}, A_{eff} is the effective area which also depends on the number of particles as shown in Figure 5.18 (bottom panel) and T_{obs} is the total observation time which is ~ 162 days. Note that in Eq. (5.23), $N_{ch} \equiv N_{ch}(21^{\circ})$. The resulting spectrum is shown in Figure 5.20 (top panel). The bottom panel in the figure shows the spectrum multiplied by N_{ch}^{3}. The dashed line indicates the value of $N_{ch}(21^{\circ})$ above which the detection efficiency is 100%. The errors shown in Figure 5.20 represent only the statistical uncertainties propagated from the $N_{ch}(21^{\circ})$ distribution. Detailed evaluation on the systematic uncertainties are in progress.

Using the energy parameterization relation given by Eq. (5.22), the all-particle differential energy spectrum (dI/dE) is constructed from the $N_{ch}(21^{\circ})$ spectrum. This is shown in Figure 5.21 (top panel) where the energy is given in GeV. The peak value of the spectrum which is at $\sim 5 \times 10^{6}$ GeV gives the energy threshold. The bottom panel in Figure 5.21 shows the energy spectrum multiplied by E^{3}. The dashed line shows that the detection efficiency above 2×10^{7} GeV is 100%. In Figure 5.22, we compare our measured spectrum with that obtained by the KASCADE-Grande experiment [132]. Only spectrum in the region of 100% detection efficiency is plotted for the comparison. It can be noticed that our result is in good agreement with that measured by KASCADE-Grande. Our measured data are listed in Table 5.4. Finally, Figure 5.23 shows a comparison with the world data reported by several independent cosmic-ray experiments [117]. The LORA data is represented by the big black circle. The solid line represents the contribution of the Galactic cosmic rays [113] and the dashed line represents the extra-galactic component. The good agreement of our

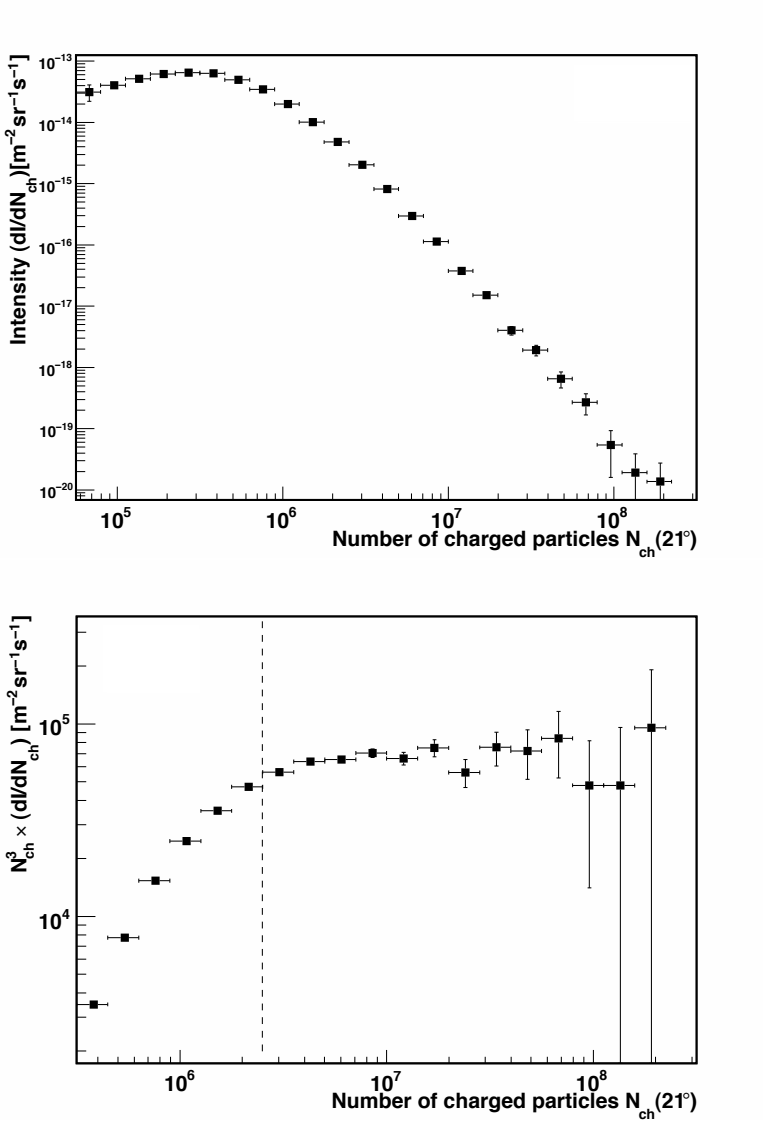

Figure 5.20: Top: Measured N_{ch} spectrum obtained by taking $\theta_r = 21°$. Bottom: Spectrum multiplied by N_{ch}^3. The dashed line represents the $N_{ch}(21°)$ value above which the air shower detection efficiency is 100%. Only statistical errors are shown in the plots.

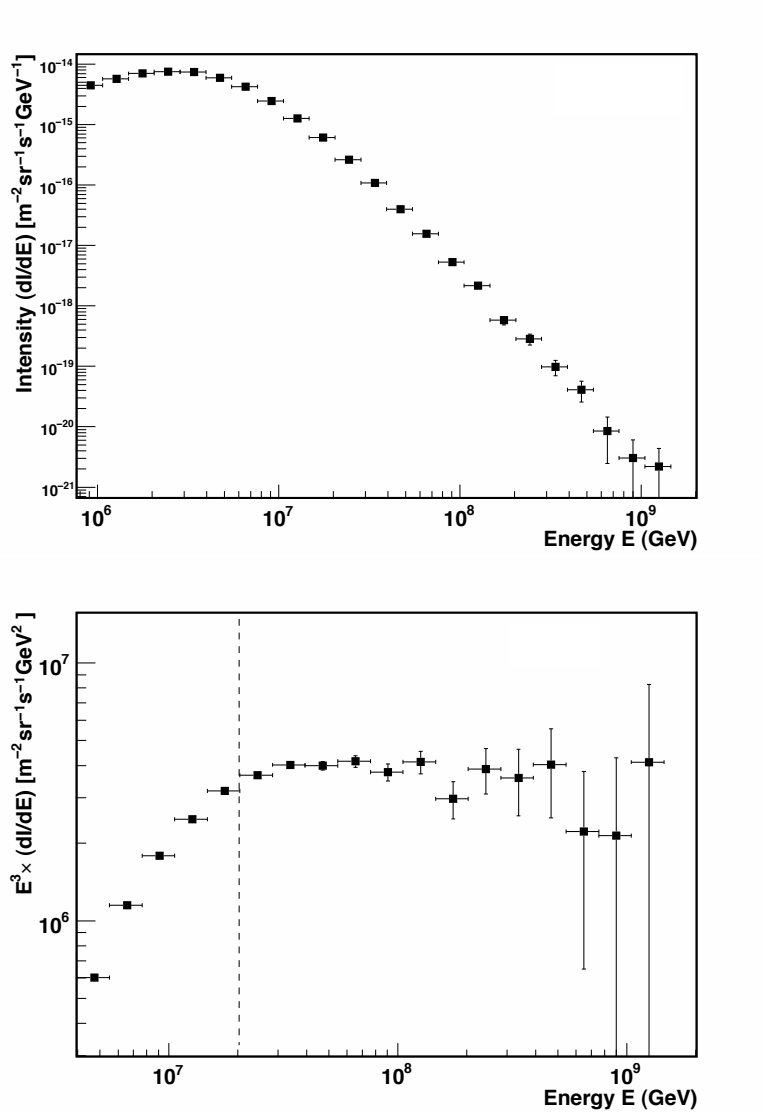

Figure 5.21: Top: Measured all-particle cosmic-ray energy spectrum. Bottom: The energy spectrum multiplied by E^3. The dashed line represents the energy above which the detection efficiency is 100%. Only statistical errors are shown in the plots.

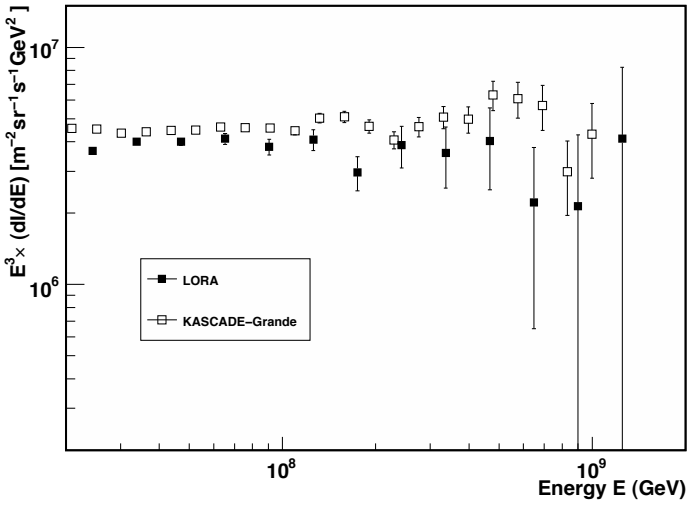

Figure 5.22: Measured all-particle cosmic-ray spectrum compared with the measurements of KASCADE-Grande [132]. Only statistical errors are shown in the plots.

Table 5.4: Data on the all-particle energy spectrum measured with LORA. The errors given are only statistical.

Energy (GeV)	Intensity ($m^{-2}sr^{-1}s^{-1}GeV^{-1}$)
2.41×10^7	$(2.63 \pm 0.05) \times 10^{-16}$
3.34×10^7	$(1.07 \pm 0.03) \times 10^{-16}$
4.64×10^7	$(4.02 \pm 0.15) \times 10^{-17}$
6.44×10^7	$(1.54 \pm 0.08) \times 10^{-17}$
8.94×10^7	$(5.34 \pm 0.40) \times 10^{-18}$
1.24×10^8	$(2.14 \pm 0.22) \times 10^{-18}$
1.72×10^8	$(5.82 \pm 0.96) \times 10^{-19}$
2.39×10^8	$(2.83 \pm 0.57) \times 10^{-19}$
3.32×10^8	$(9.79 \pm 2.83) \times 10^{-20}$
4.61×10^8	$(4.11 \pm 1.55) \times 10^{-20}$
6.40×10^8	$(8.47 \pm 5.99) \times 10^{-21}$
8.89×10^8	$(3.05 \pm 3.05) \times 10^{-21}$
1.23×10^9	$(2.20 \pm 2.20) \times 10^{-21}$

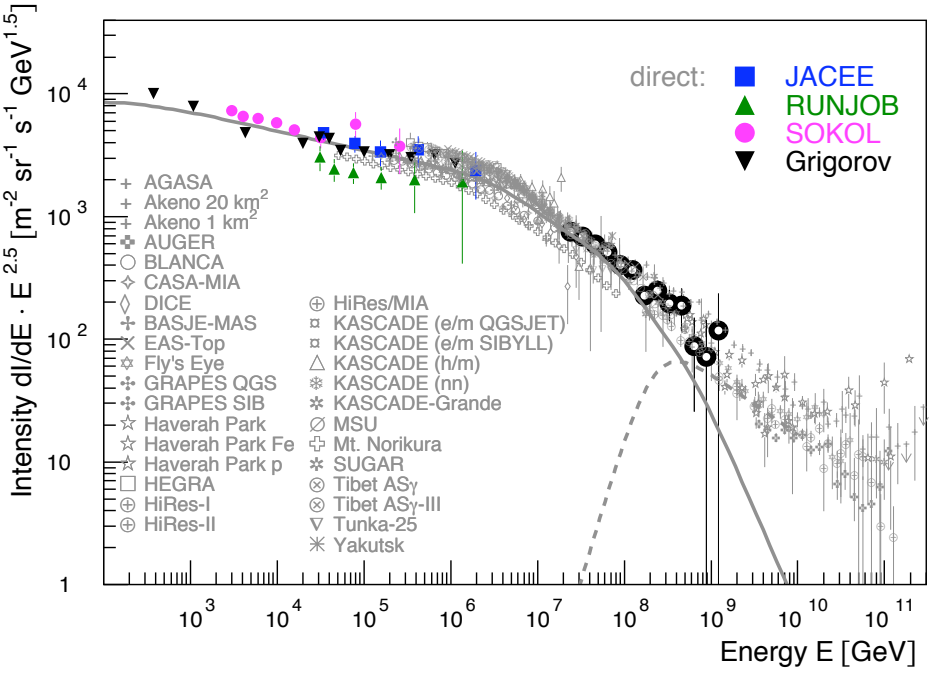

Figure 5.23: All-particle energy spectrum of cosmic rays, according to [117]. The LORA data are represented as big black circles. The solid line indicates the contribution of Galactic cosmic rays according to [113], and the dashed line indicates the corresponding contribution of extra-galactic particles.

result with the measurements of other experiments proves that our instruments, in particular the electronics and the detectors, are performing quite well. In addition, it also demonstrates that all the instrumental calibrations that we performed and the various data analysis steps followed are proper. Thus, we can use the LORA air shower array to set an absolute energy scale for the radio detection of air showers with LOFAR.

5.10 Conclusions

LORA is a small air shower array that has been built for cosmic-ray measurements with LOFAR. Its primary purpose is to trigger LOFAR with cosmic-ray events and to provide basic air shower properties such as the position of the shower axis, the arrival direction, and the energy of the primary particle. The full set-up of the LORA array was completed in June 2011 and during the same time, it had contributed to the first detection of cosmic rays with LOFAR [74].

By the time of writing this thesis, LORA has measured over 2 million air shower events. For the present analysis, we only use events that trigger a minimum of 5 detectors. We have determined several properties of the air showers including the arrival direction distributions and the averaged lateral density distribution. The averaged lateral distribution is calculated for showers with number of charged particles in the range of $\log_{10} N_{ch} \sim (5.8-7.3)$ which corresponds to the energy range of $\sim (5 \times 10^{15} - 2 \times 10^{17})$ eV. The Molière radii obtained by fitting the lateral distributions with the NKG functions are found to be $\sim (26 - 35)$ m. The values show a decrease with the number of particles up to $\log_{10} N_{ch} \sim 7.1$ and then, increase as the number of particles become larger. In terms of the reference angle, this turn over value of N_{ch} corresponds to $\log_{10} N_{ch}(21^\circ) \sim 7.0$.

We have also determined the atmospheric attenuation coefficient of air showers using the constant intensity method. For the calculation, we use 7 different zenith angle bins in the range of $(0^\circ - 34.9^\circ)$. The attenuation coefficients are measured to be $\sim (211 - 239)$ g cm^{-2} for showers with the number of charged $\log_{10} N_{ch}(21^\circ) \sim (6.5 - 7.2)$. The latter corresponds to an energy range of $\sim (2 \times 10^{16} - 10^{17})$ eV. The attenuation coefficient first increases with the number of particles up to $\log_{10} N_{ch}(21^\circ) \sim 7.0$ and then decreases. The turning points that we obtain in both the values of Molière radius and the attenuation coefficient are found to occur at approximately the same primary energy of $\sim 7.6 \times 10^{16}$ eV. The reason for the turn over is not clearly understood. One possible explanation might be a change in the composition of cosmic rays from lighter to heavier elements at these energies. Recently, by separating the electron-rich and electron-poor components of measured showers, the KASCADE-Grande experiment has found a fall-off of the heavy component, something like a "knee" at $\sim 8 \times 10^{16}$ eV [38]. Although not very significant, one effect of this is the presence of a "knee-like" structure in the all-particle energy spectrum at $\sim 8 \times 10^{16}$ eV. Detailed investigations on the presence of any such structure in our measured spectrum, and any correlation (if exists) with the turn over in the Molière radius and the attenuation coefficients are ongoing. We hope that our results would be better understood when more data becomes available in the future.

In this thesis, we have presented the first LORA measurement of the all-particle energy spectrum in the range of $\sim (2 \times 10^{16} - 1.5 \times 10^{18})$ eV. Our measured spectrum is found to be in very good agreement with the measurements of other cosmic-ray experiments. This good agreement in the energy spectrum, along with several other properties of air showers that we have measured, have demonstrated that LORA is performing well as expected and it can be used to set an absolute energy scale for the detection of radio emission from air showers with LOFAR.

The air shower informations determined by LORA are currently used as inputs for the reconstruction of air shower properties with LOFAR. The detectable LOFAR event rate of $\sim 10^{-3}$ Hz determined by LORA is used to optimize a radio only trigger for LOFAR. In future, LOFAR is soon expected to become enable to perform a stand-alone radio detection from air showers without any support from LORA.

Appendix 5.A: LORA data acquisition software

The DAQ software for LORA has been developed in C/C++ language for Linux based operating systems. The software (particularly the online monitoring tool) uses several features of the ROOT package [121].

Once an observation run has started, the main DAQ running on the master computer start up the DAQ on the station computers. Each station then handles the DAQ independently. All the input parameters including those required by the DAQ on the station computers are set on the master computer. When the (four) signals in an electronic unit (in a station) satisfy some minimum local trigger condition, the digitizers send the signals to the station computer. The station computer then sends the signals to the master computer for processing.

In our present networking set up, the master computer act as the server and the station computers as its clients. The master waits for signals from the clients. Once a signal is received from any of the stations, it then waits for some (user defined) time to collect signals from all the remaining stations. Presently, we set this waiting time to 100 ms. The first step in the signal processing is the identification of the type of the data signal. We have four types of data: event data, one second data, control parameters data and noise data (see Appendix 5.B for details). The master dumps the data immediately if it is not an event data and waits for the next signals. For event data, the time stamps are checked and select only those within a coincidence time window of 400 ns for further processing. If the event satisfy some minimum trigger condition (based on the number of detectors or stations set by the user) to accept as a cosmic-ray event, a first-level online analysis is performed and reconstruct the air shower parameters such as the position of the shower axis on the ground, the arrival direction and the energy of the primary. The reconstructed shower parameters are allowed to pass through some loose quality cuts to check the quality of the event. For good event, the data is recorded and if the event is bright enough to be detectable by the LOFAR antennas, a trigger message is sent to the LOFAR network. The processing of an event in the master computer takes ~ 30 ms. So, the overall processing time for an event including the event waiting time is $\sim (100 + 30) = 130$ ms. The processing time should be as minimum as possible since LOFAR also has to dump the corresponding radio signal for the same air shower event before they get overwritten in the memory ring buffer (transient buffer board, TBB). Presently, LOFAR can temporarily hold its data in the memory for a maximum of 1.3 s.

Once the event data is dumped in the master computer, the system memory is flushed and wait for the next signal. Figure 5.24 shows the complete flowchart of the DAQ running on the LORA master computer.

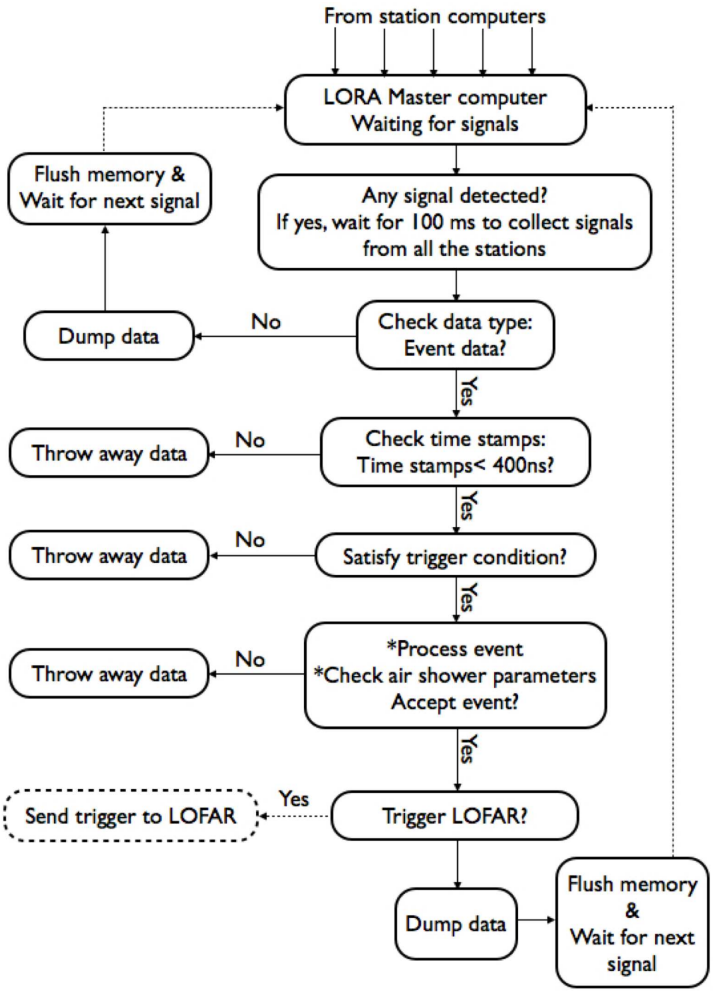

Figure 5.24: Flow chart of the DAQ running on the LORA master computer.

Appendix 5.B: Data structure

The LORA data is stored in the ROOT format [121] and consist of four kinds of data as mentioned in Appendix 5.A. The first are the event data which are generated whenever an air shower event is detected. These data contain the event time stamp for each station and the signal trace in ADC counts for each detector. The second kind of data stores the so-called one second messages send by the digitizers. These data are generated every second and contains information about the number of times the analog signal went over the threshold in the last second for each of the four channels. They also contain important timing informations which can be used for calculating an event time stamp with nanosecond accuracy. The third kind of data contains control parameters applied during the operation. These data are stored every interval of time fixed by the observer at the start of the run (presently set at one hour). The fourth kind of data contains information about the noise level in each channel averaged over the last one hour.

Appendix 5.C: Detector gain

In the following figures, the temporal gain variations of all the 20 detectors during the operation starting from June 2011 to January 2012 are shown. In the figures, the detectors are designated as "DetN", where "N" denotes the detector number. The gain variations are calculated with respect to the averaged gain obtained for the whole run. Except for "Det3" and "Det13", all the detectors show good stability with variations within $\pm 10\%$ for more than $\sim 93\%$ of the total operation time. "Det3" shows variation within $\pm 10\%$ for $\sim 70\%$ of the total operation and "Det13" shows for $\sim 85\%$ of the time.

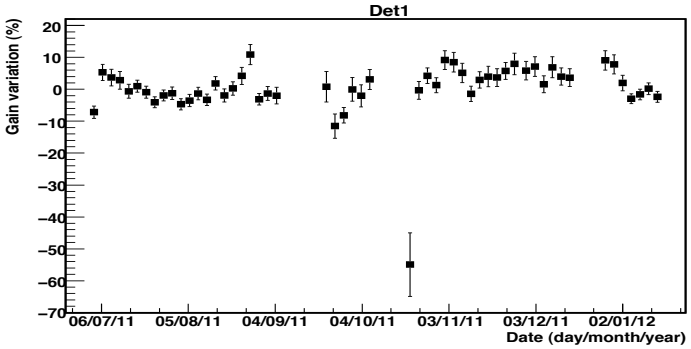
Det1
Gain variation (%)
20
10
0
−10
−20
−30
−40
−50
−60
−70
06/07/11
05/08/11
04/09/11
04/10/11
03/11/11
03/12/11
02/01/12
Date (day/month/year)

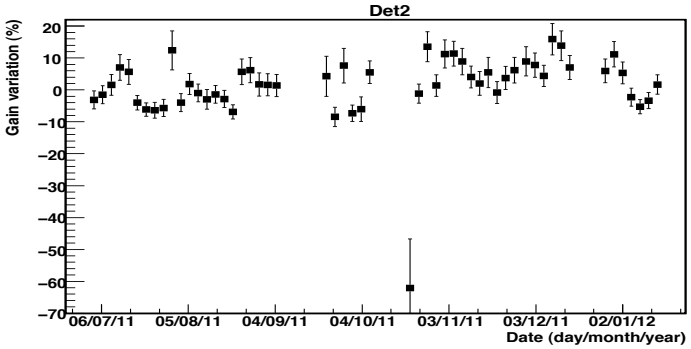
Det2
Gain variation (%)
20
10
0
−10
−20
−30
−40
−50
−60
−70
06/07/11
05/08/11
04/09/11
04/10/11
03/11/11
03/12/11
02/01/12
Date (day/month/year)

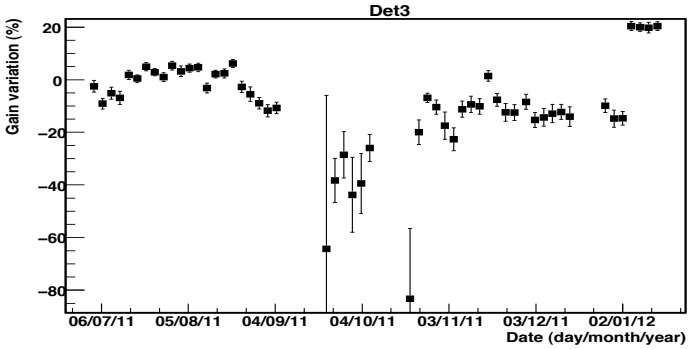
Det3
Gain variation (%)
20
0
−20
−40
−60
−80
06/07/11
05/08/11
04/09/11
04/10/11
03/11/11
03/12/11
02/01/12
Date (day/month/year)

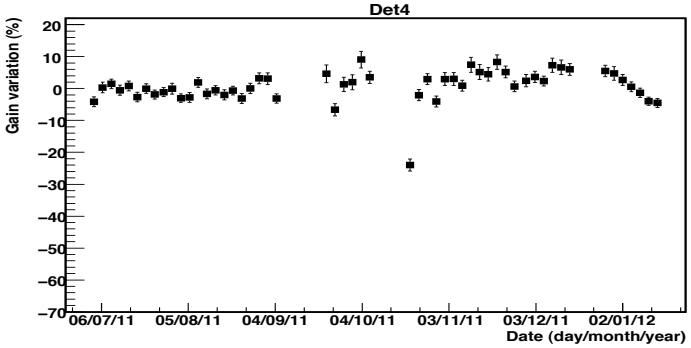
Det4
Gain variation (%)
20
10
0
−10
−20
−30
−40
−50
−60
−70
06/07/11
05/08/11
04/09/11
04/10/11
03/11/11
03/12/11
02/01/12
Date (day/month/year)

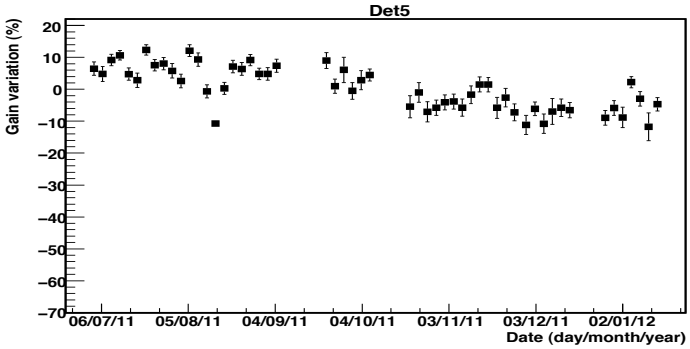
Det5
Gain variation (%)
20
10
0
−10
−20
−30
−40
−50
−60
−70
06/07/11
05/08/11
04/09/11
04/10/11
03/11/11
03/12/11
02/01/12
Date (day/month/year)

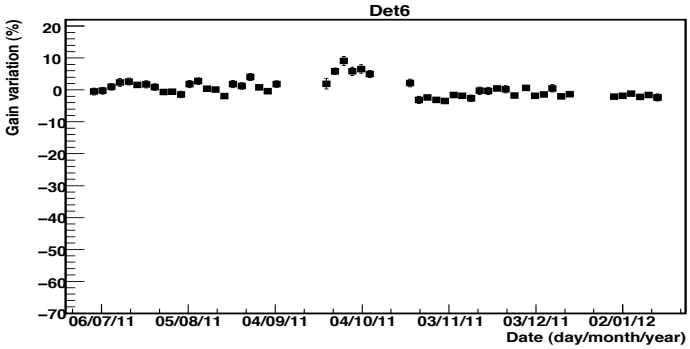
Det6
Gain variation (%)
20
10
0
−10
−20
−30
−40
−50
−60
−70
06/07/11
05/08/11
04/09/11
04/10/11
03/11/11
03/12/11
02/01/12
Date (day/month/year)

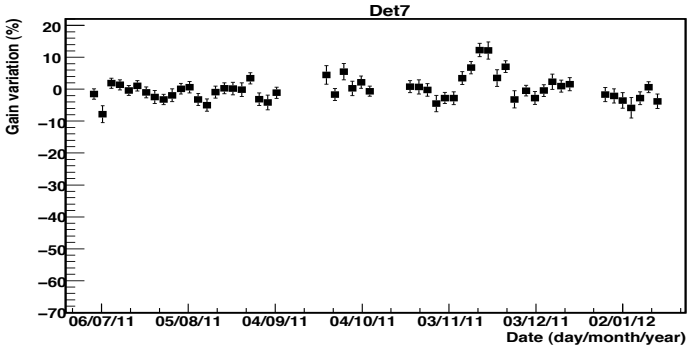
Det7
Gain variation (%)
20
10
0
−10
−20
−30
−40
−50
−60
−70
06/07/11
05/08/11
04/09/11
04/10/11
03/11/11
03/12/11
02/01/12
Date (day/month/year)

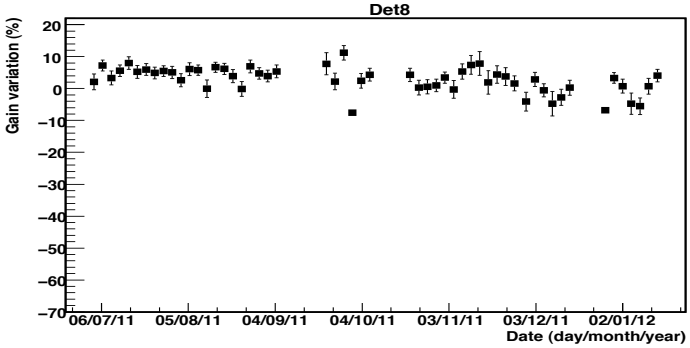
Det8
Gain variation (%)
20
10
0
−10
−20
−30
−40
−50
−60
−70
06/07/11
05/08/11
04/09/11
04/10/11
03/11/11
03/12/11
02/01/12
Date (day/month/year)

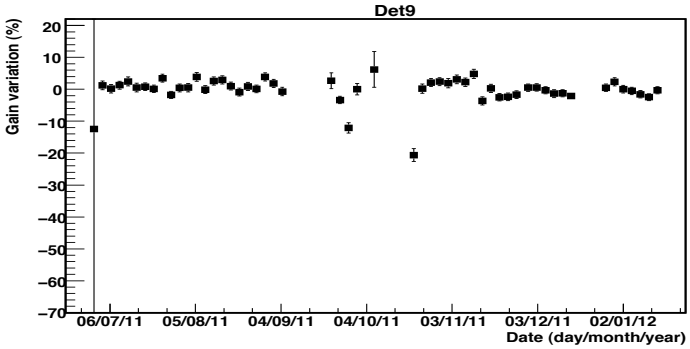
Det9
Gain variation (%)
20
10
0
−10
−20
−30
−40
−50
−60
−70
06/07/11
05/08/11
04/09/11
04/10/11
03/11/11
03/12/11
02/01/12
Date (day/month/year)

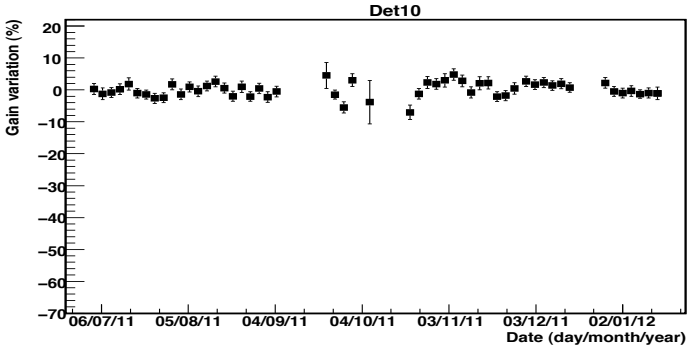
Det10
Gain variation (%)
20
10
0
−10
−20
−30
−40
−50
−60
−70
06/07/11
05/08/11
04/09/11
04/10/11
03/11/11
03/12/11
02/01/12
Date (day/month/year)

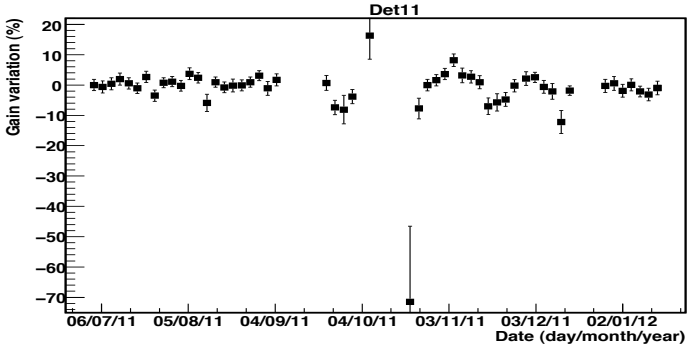
Det11
Gain variation (%)
20
10
0
−10
−20
−30
−40
−50
−60
−70
06/07/11
05/08/11
04/09/11
04/10/11
03/11/11
03/12/11
02/01/12
Date (day/month/year)

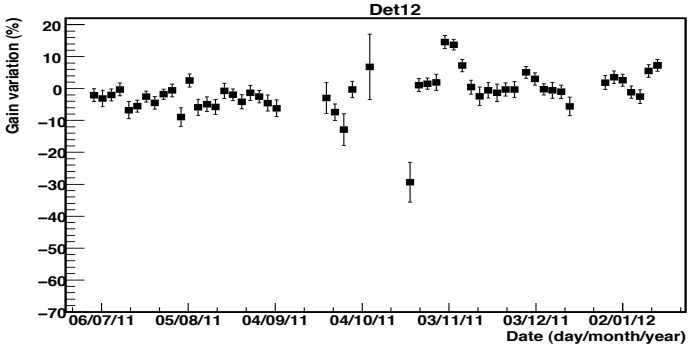
Det12
Gain variation (%)
20
10
0
−10
−20
−30
−40
−50
−60
−70
06/07/11
05/08/11
04/09/11
04/10/11
03/11/11
03/12/11
02/01/12
Date (day/month/year)

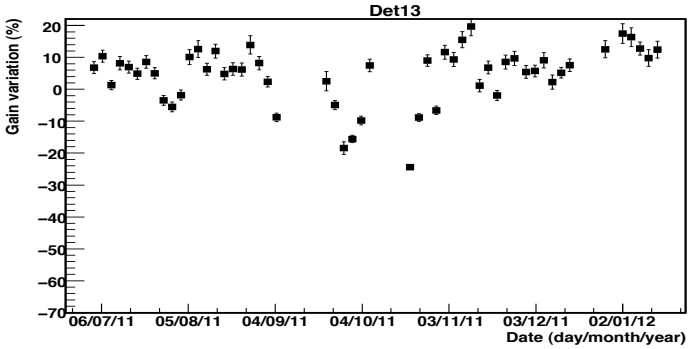
Det13
Gain variation (%)
20
10
0
−10
−20
−30
−40
−50
−60
−70
06/07/11
05/08/11
04/09/11
04/10/11
03/11/11
03/12/11
02/01/12
Date (day/month/year)

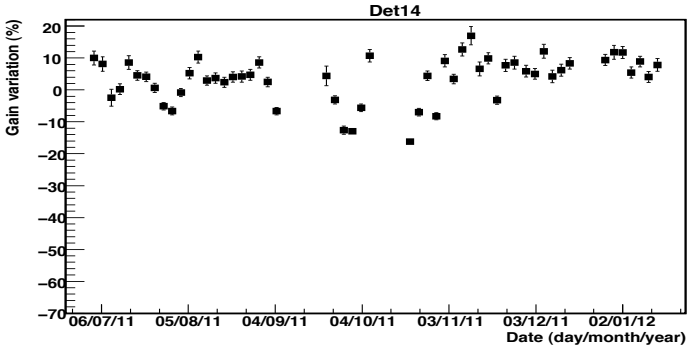
Det14
Gain variation (%)
20
10
0
−10
−20
−30
−40
−50
−60
−70
06/07/11
05/08/11
04/09/11
04/10/11
03/11/11
03/12/11
02/01/12
Date (day/month/year)

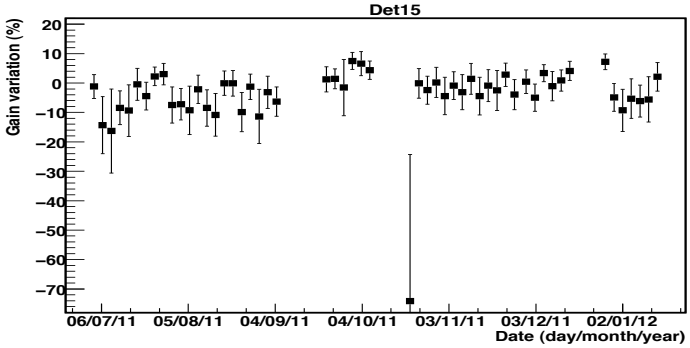
Det15
Gain variation (%)
20
10
0
−10
−20
−30
−40
−50
−60
−70
06/07/11
05/08/11
04/09/11
04/10/11
03/11/11
03/12/11
02/01/12
Date (day/month/year)

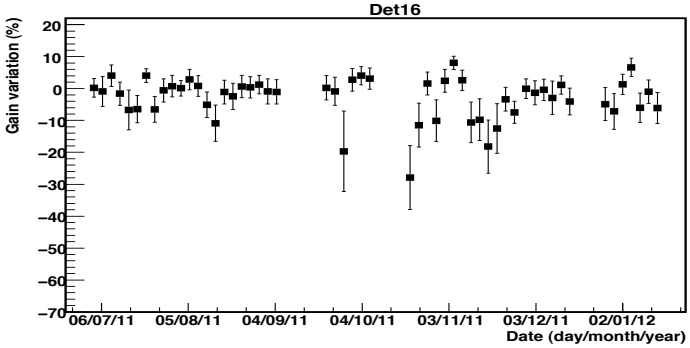
Det16
Gain variation (%)
20
10
0
−10
−20
−30
−40
−50
−60
−70
06/07/11
05/08/11
04/09/11
04/10/11
03/11/11
03/12/11
02/01/12
Date (day/month/year)

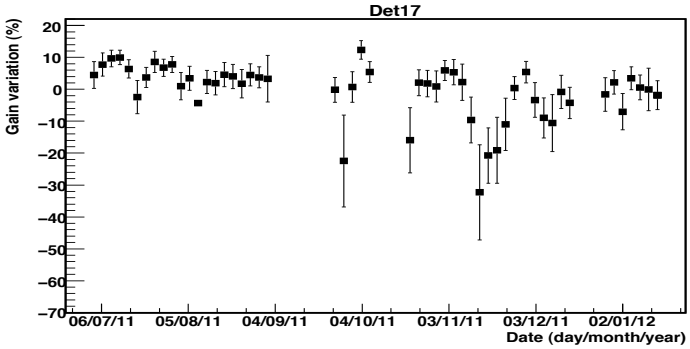
Det17
Gain variation (%)
20
10
0
−10
−20
−30
−40
−50
−60
−70
06/07/11
05/08/11
04/09/11
04/10/11
03/11/11
03/12/11
02/01/12
Date (day/month/year)

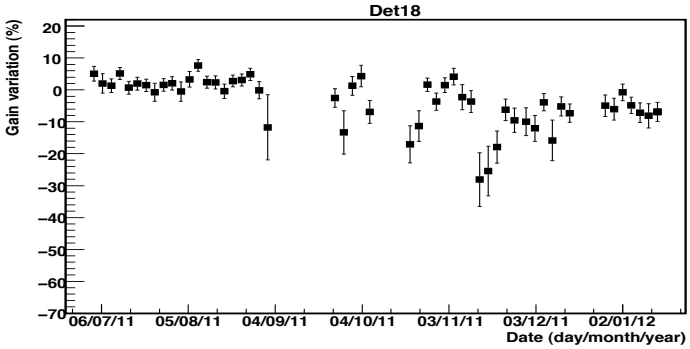
Det18
Gain variation (%)
20
10
0
−10
−20
−30
−40
−50
−60
−70
06/07/11
05/08/11
04/09/11
04/10/11
03/11/11
03/12/11
02/01/12
Date (day/month/year)

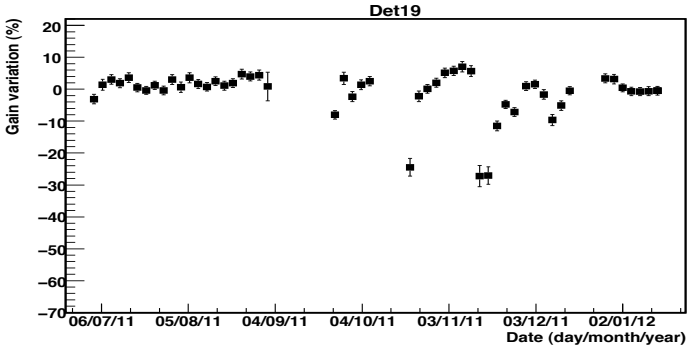
Det19
Gain variation (%)
20
10
0
−10
−20
−30
−40
−50
−60
−70
06/07/11
05/08/11
04/09/11
04/10/11
03/11/11
03/12/11
02/01/12
Date (day/month/year)

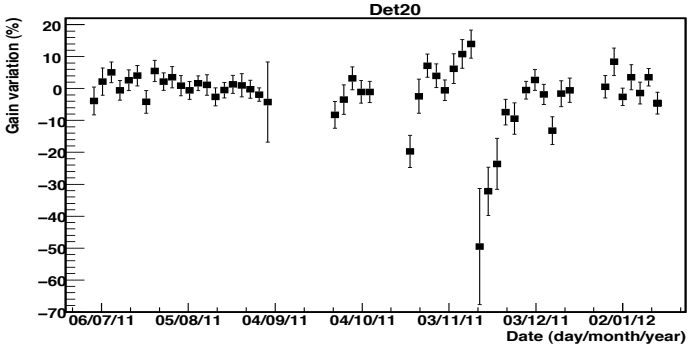
Det20
Gain variation (%)
20
10
0
−10
−20
−30
−40
−50
−60
−70
06/07/11
05/08/11
04/09/11
04/10/11
03/11/11
03/12/11
02/01/12
Date (day/month/year)

Summary and conclusions

In the first part of this thesis, the cosmic-ray propagation in the Galaxy is discussed with main emphasis given on the nearby sources. The study assumes that supernova remnants are the main sources of cosmic rays in the Galaxy. In particular, the effects of the presence of nearby supernova remnants on the observed cosmic-ray spectra are discussed in detail both under the assumption of burst-like point sources where cosmic rays of all energies are assumed to escape at one time from the remnant and also, under an energy dependent escape model where cosmic rays of different energies are assumed to escape at different stages during the evolution of the remnant. A significant portion of the work presented in this thesis is driven by the new results recently provided by the new generation cosmic-ray and gamma-ray experiments which are difficult to explain under the standard models of cosmic-ray production and their propagation in the Galaxy.

In Chapter 1, based on the burst-like point source approximation, it is shown that the nearby supernova remnants produce noticeable effects on the primary cosmic-ray spectra above ~ 100 GeV/n and almost no effect on the secondary spectra. The subsequent effects on the secondary-to-primary ratios imply that the observed ratios seem to give a reliable information of the cosmic-ray propagation parameters only below $\sim$ 100 GeV/n. Even then, the small Galactic region (which is of the order of the vertical halo height) scanned by the cosmic rays reaching the Earth allow them to carry information only for a small fraction of the whole Galaxy.

In Chapter 2, it is also shown that a simple model based on the considerations of diffusive shock acceleration theory can explain both the observed break in the electron spectrum at $\sim$ 1 TeV and the hardening of the secondary-to-primary ratios above $\sim$ 100 GeV/n. The model assumes that cosmic rays after acceleration by supernova remnant shock waves, escape downstream of the shock and remain confined within the remnant until they get released into the interstellar medium. During the confinement, electrons suffer from radiative losses while the nuclear components suffer from spallation leading to secondary production inside the remnants. This is different from the standard assumption that secondaries are produced only by the spallation of the primaries in the interstellar medium. Assuming the same magnetic field strengths inside the remnants as in the Galaxy, it is found that a confinement time of $\sim 1.2 \times 10^5$ yr can explain the observed break in the electron spectrum and at the same time, explain the observed hardening in the boron-to-carbon ratio above ~ 100 GeV/n if the matter density inside the remnants is ~ 2 cm^{-3}.

In a detailed phenomenological study given in Chapter 3, the validity of the widely adopted point source approximation for nearby cosmic-ray sources is investigated. Assuming burst-like (energy independent) liberation of particles from the sources, it is shown that the point source approximation does not always represent a good approximation for young

nearby sources. For typical source distances of $\sim (100 - 300)$ pc, it is found that the approximation breaks down at lower energies (below a few TeVs) for sources younger than $\lesssim 10^5$ yr. Some remnants such as Vela fall in this category. However, when applied to the supernova remnants within 1 kpc, it is interesting to find that the approximation still holds good for their total combined cosmic-ray spectrum at the Earth although some of the individual remnants show dependence on the source size. The study further shows that the results obtained under the point source approximation are significantly different from those calculated under the energy dependent escape model. The latter is favored by diffusive shock acceleration models inside supernova remnants. These results seem to suggest that if supernova remnants are the main sources of cosmic rays in the Galaxy, then the commonly adopted point source approximation with an energy *independent* escape scenario appears flawed for cosmic-ray studies from the nearby sources. The effect of this on the overall cosmic-ray spectrum is more significant in the case of electrons than the protons because of the high level of background generated by distant sources in the case of protons.

In Chapter 4, it is proposed that the nearby supernova remnants might be responsible for the cosmic-ray spectral changes at TeV energies recently reported by the ATIC, CREAM, and TRACER balloon experiments. Using a rigidity dependent escape of cosmic rays from the remnants, it explains the observations that the hardening of the helium spectrum occurs at relatively lower energies/nucleon with respect to the protons. It also shows that the spectral hardening should not persist beyond $\sim (20 - 30)$ TeV/n which is in good agreement with the new measurements of protons and helium. Future high energy measurements of heavier cosmic-ray species and the detection of any spectral turnover at ~ 10 TeV/n can provide an additional evidence in support of this model. In addition, future measurements of secondary cosmic-ray spectra and of the Galactic diffuse gamma-ray emission at TeV energies would be important.

The second part of this thesis discusses about the cosmic-ray measurements with LORA. Cosmic rays which impinge onto the Earth, during their propagation through the Galaxy, can be measured either using space-based or ground-based experiments. The LORA detector array is a ground-based experiment that measures cosmic rays in the energy range of $\sim (10^{16} - 10^{18})$ eV. This is the energy region where the transition from Galactic to extragalactic cosmic rays is expected to occur. The cosmic-ray measurements with LORA are presented in Chapter 5. LORA has been built as a part of the LOFAR "cosmic ray" key-science project. Its full set-up was completed in June 2011 and by the time of writing this thesis, it has collected around 162 days of clean data. In Chapter 5, the first science results from LORA are presented along with the details of the experimental set-up and its performance. The main results include measurements of charged particle lateral distribution, measurements of atmospheric attenuation of air showers and the all-particle energy spectrum. In our observables, Molière radius and attenuation length, we see some indications for a possible change of composition at energies around $\sim 10^{17}$ eV which may be due to the end of the Galactic component of cosmic rays. Such a behavior would be expected according to astrophysical models at around this energy. Investigation for any such indication in the measured all-particle spectrum is ongoing. The all-particle spectrum we have

measured is found to be in very good agreement with the measurements of other cosmic-ray experiments. This demonstrates that LORA can now be used to set an absolute energy scale for the radio detection from air showers with LOFAR.

The main objective of building LORA, which is to trigger LOFAR with air shower events, has already been implemented and it has already contributed to the first detection of cosmic rays with LOFAR in June 2011. Currently, LORA supports the reconstruction of air shower parameters with LOFAR by providing basic air shower information such as the energy of the primary particle, arrival direction, position of the shower axis, and the lateral distribution of the charged particles. Efforts are ongoing to optimize the radio trigger algorithm of LOFAR, and in the near future, it is expected to perform independent cosmic-ray measurements without any support from LORA.

Nederlandse samenvatting

In het eerste deel van dit proefschrift wordt de propagatie van kosmische straling binnen ons melkwegstelsel behandeld, waarbij de nadruk ligt bij nabije bronnen. Hierbij is aangenomen dat de voornaamste bron van kosmische straling binnen ons melkwegstelsel bestaat uit de overblijfselen van supernovae. In het bijzonder worden de effecten van nabije supernovarestanten op de waargenomen spectra van kosmische straling behandeld. Daarbij is gekeken naar een tweetal scenarios. In het eerste scenario wordt het supernovarestant als puntbron behandeld en komt alle kosmische straling in een keer vrij. In het tweede scenario wordt een energie-afhankelijk ontsnappingsmodel gebruikt waarbij is aangenomen dat kosmische straling van verschillende energie tijdens de verschillende evolutionaire stadia van de supernova vrijkomt.

Een belangrijk deel van dit werk is gemotiveerd door de meest recente resultaten van experimenten met kosmische- en gammastraling die moeilijk in overeenstemming te brengen zijn met het huidige model voor de productie van kosmische straling en hun propagatie binnen ons melkwegstelsel.

In hoofdstuk 1, waar supernovarestanten als puntbron worden beschouwd, blijkt dat nabije supernovarestanten een merkbaar effect hebben op de primaire spectra van kosmische straling boven de ~ 100 GeV per nucleon, maar nauwelijks een effect lijken te hebben op de secundaire spectra. Hieruit volgt dat de verhouding van de secundaire en primaire kosmische straling die wordt waargenomen een betrouwbare indicatie geeft van de propagatie parameters voor energieën lager dan ~ 100 GeV per nucleon. Er dient wel te moeten worden opgemerkt dat de gevonden resultaten slechts betrekking hebben op het lokale deel van de melkweg dat bekeken is, nl. ter grootte van de hoogte van de galactische halo.

In hoofdstuk 2 wordt een eenvoudig model behandeld dat gebaseerd is op versnellingen in diffuse schokken. Hieruit blijkt dat de knik in het elektronspectrum rond ~ 1 TeV en de sterkere afname in de verhouding tussen de secundaire en primaire kosmische straling boven ~ 100 GeV per nucleon goed kunnen worden beschreven door dit model. Hierbij is aangenomen dat de kosmische straling door schokgolven versneld en teruggeworpen wordt binnen het supernovarestant voordat deze uiteindelijk vrijkomt in het interstellaire medium. Tijdens hun opsluiting binnen het restant van de supernova raken elektronen energie kwijt door stralingsverliezen en zorgt de splijting van atoomkernen van de primaire kosmische straling voor de productie van de secundaire kosmische stralingscomponent binnen het supernovarestant. Dit wijkt af van de aanname dat de productie van de secundaire component van kosmische straling alleen in het interstellaire medium plaatsvindt. Indien wordt aangenomen dat het magnetisch veld binnen het restant van de supernova en dat van de melkweg dezelfde sterkte hebben, dan blijkt dat een opsluitingstijd van $\sim 1.2 \times 10^5$ jaar zowel de knik in het elektronspectrum alsook de verhouding van boor en koolstof boven energieën

van ~ 100 GeV per nucleon kan verklaren voor materiedichtheden van ~ 2 cm^{-3} binnen de restanten van supernovae.

Hoofdstuk 3 behandelt een gedetailleerde fenomenologische studie waarbij gekeken wordt naar de geldigheid van de veelgebruikte aanname dat nabije bronnen van kosmische straling beschreven kunnen worden als puntbronnen. Indien wordt aangenomen dat kosmische straling vrijkomt in uitbarstingen van de bron, dan blijkt dat deze puntbron aanname niet altijd een goede benadering is voor nabije bronnen van kosmische straling. Voor bronnen op een typische afstand van 100 tot 300 pc blijkt deze puntbron benadering niet houdbaar bij lage energieën (minder dan enkele TeV) voor bronnen jonger dan 10^5 jaar, zoals het restant van de Vela supernova. Voor supernovarestanten binnen 1 kpc lijkt deze benadering wel geldig indien wordt gekeken naar het totale spectrum van kosmische straling zoals wordt waargenomen op aarde, al blijken enkele bronnen wel een afhankelijkheid te hebben met grootte van het supernovarestant. De resultaten zoals gevonden met de puntbron benadering blijken significant af te wijken van de berekeningen met een energie-afhankelijk model. Deze laatste passen beter bij modellen van diffuse schok versnellingen binnen de restanten van supernovae. Hieruit volgt dat, indien supernovae de voornaamste bron van kosmische straling zijn binnen ons melkwegstelsel, de veelgebruikte puntbron aanname, waarbij er geen energie-afhankelijkheid is in de wijze waarop de kosmische straling vrijkomt, tekortschiet in de beschrijving van het spectrum van de kosmische straling voor nabije bronnen. Het effect hiervan op het totale spectrum van kosmische straling is sterker voor elektronen dan voor protonen vanwege de hogere achtergrond van protonen vanwege hun productie door verderweg gelegen bronnen.

In hoofdstuk 4 wordt voorgesteld dat nabije supernovae verantwoordelijk kunnen zijn voor veranderingen in het spectrum van kosmische straling bij energieën in de orde van TeV zoals recentelijk is gevonden door de ATIC, CREAM en TRACER experimenten. Indien gebruik gemaakt wordt van een model waarbij de ontsnapping van de kosmische straling uit het supernovarestant afhankelijk is van de rigiditeit (energie / lading) dan verklaart dit de versterkte afname in het helium spectrum bij relatief lage energie per nucleon vergeleken met dat in het proton spectrum. Bovendien zou deze versterkte afname niet mogen plaatsvinden bij energieën boven de $20 - 30$ TeV per nucleon, iets wat in goede overeenkomst is met recente metingen aan helium en proton. Toekomstige metingen aan zwaardere componenten van de kosmische straling en de spectrale overgang rond 10 TeV per nucleon kunnen dit verder ondersteunen. Daarbij zijn toekomstige metingen aan spectra van secundaire kosmische straling en gammastraling binnen ons melkwegstelsel rond energieën van TeV belangrijk.

In het tweede deel van dit proefschrift worden de metingen aan kosmische straling met behulp van de LORA detector behandeld. De LORA detectoren bevinden zich op het aardoppervlak en zijn gevoelig voor kosmische straling met energieën variërend van 10^{16} tot 10^{18} eV. In dit energiegebied wordt de overgang verwacht van galactische naar extragalactische kosmische straling. LORA is ontworpen als ondersteuning voor de radiodetectie van kosmische straling met LOFAR en was gereed in juni 2011.

In hoofdstuk 5 zijn de eerste wetenschappelijke resultaten van LORA gepresenteerd

alsook de technische set-up en prestaties. De voornaamste resultaten bestaan uit metingen van de laterale verdeling van de geladen component, de afname van de deeltjes cascade in de aardatmosfeer, en het energiespectrum van alle componenten van de kosmische straling. Metingen aan de Molière radius en de verzwakking van de deeltjes cascade in de atmosfeer lijken een aanwijzing te geven dat de samenstelling van kosmische straling rond energieën van $\sim 10^{17}$ eV verandert, wat kan worden verklaard doordat bij deze energieën het einde van de galactische component van de kosmische straling wordt bereikt. Dit effect wordt ook verwacht volgens verschillende astrofysische modellen. Verder onderzoek aan dit effect in het totale spectrum van alle componenten in de kosmische straling is momenteel nog gaande.Het gemeten totale spectrum van alle componenten van de kosmische straling blijkt in goede overeenkomst te zijn met de spectra die gemeten zijn door andere experimenten. Dit laat zien dat LORA gebruikt kan worden voor de bepaling van de absolute energie van kosmische straling ten behoeve van de radio-detectie door LOFAR.

Het hoofddoel van LORA is het ondersteunen van LOFAR bij het waarnemen van kosmische straling. Dit heeft in juni 2011 geresulteerd in de eerste waarnemingen van kosmische straling door LOFAR. Dit gebeurt momenteel door LOFAR te voorzien van verschillende paramaters van de gereconstrueerde deeltjescascade, zoals de energie van de primaire kosmische straling, de richting van de cascade, de locatie van het centrum van de cascade, en de ladingsverdeling binnen de cascade. Momenteel wordt gewerkt aan de ontwikkeling van een radio trigger algoritme zodat LOFAR in de nabije toekomst, onafhankelijk van LORA, metingen zal kunnen doen aan kosmische straling.

References

[1] Abbasi, R., et al., 2011, arxiv:1105.2326

[2] Abdo, A. A., et al. 2008, Phys. Rev. Lett., 101, 221101

[3] Abdo, A. A., et al. 2009, Phys. Rev. Lett., 102, 181101

[4] Abdo, A. A., et al. 2009, Phys. Rev. Lett., 103, 251101

[5] Abdo A. A. et al. 2009, ApJ, 706, L1

[6] Abdo A. A. et al. 2009, ApJ, 703, 1249

[7] Abdo, A. A., et al. 2010, ApJ, 710, 133

[8] Abdo, A. A. et al. 2010, ApJ, 712, 459

[9] Abdo, A. A. et al. 2010, ApJ, 718, 348

[10] Abdo, A. A. et al. 2010, Sci, 327, 1103

[11] Abramowitz, M. & Stegun, I. A. 1964, Handbook of Mathematical Functions (Dover, New York)

[12] Ackermann, M. et al. 2010, Phys. Rev. D 82, 092003

[13] Ackermann, M. et al. 2010, Phys. Rev. D 82, 092004

[14] Ackermann, M. et al. 2011, arXiv:1109.0521

[15] Adriani, O., et al. 2009, Nature, 458, 607

[16] Adriani, O., et al. 2011, Phys. Rev. Lett. 106, 201101

[17] Adriani, O., et al. 2011, Science, 332, 69

[18] Aguilar, M., et al. 2002, Physics Reports, 366, 331

[19] Aharonian, F.A., & Atoyan, A. 1996, A&A, 309, 917

[20] Aharonian,F. A., et al. 2006, ApJ, 636, 777

[21] Aharonian, F. A., et al. 2007, A&A, 467, 1075

[22] Aharonian, F. A., et al. 2008, A&A, 477, 353

[23] Aharonian, F. A., et al. 2008, A&A, 481, 401

[24] Aharonian, F. A., et al. 2008, Phys. Rev. Lett., 101, 261104

[25] Aharonian, F. A., et al. 2008, A&A, 490, 685

[26] Aharonian, F. A., et al. 2009, A&A, 508, 561

[27] Ahn, H. S., et al. 2008, APh, 30, 133

[28] Ahn, H. S. et al. 2009, ApJ, 707, 593

[29] Ahn, H. S. et al. 2010, ApJL, 714, L89

[30] Albert, J., et al. 2007, A&A, 474, 937

[31] Alcaraz, J., et al. 2000, Physics Letters B 490, 27

[32] Alkhofer, O. C., 1975, Introduction to Cosmic Radiation, Verlag Carl Thiemig

[33] Amenomori, M., et al., 2005, ApJ, 626, L29

[34] Amenomori, M., et al., 2006, Science, 314, 439

[35] Antoni, T., et al., 2001, APh, 14, 245

[36] Antoni, T., et al., 2003, Nucl. Instrum. Meth. A, 513, 490

[37] Antoni, T., et al., 2003, APh, 19, 703

[38] Apel, W. D., et al., 2011, PRL, 107, 171104

[39] Atoyan, A. M., Aharonian, F. A., & Völk, H. J. 1995, Phys. Rev. D, 52, 3265

[40] Ave, M. et al. 2008, ApJ, 678, 262

[41] Ave, M., Boyle, P. J., Höppner, C., Marshall, J., & Müller, D., 2009, ApJ, 697, 106

[42] Bamba A., Yamazaki R., Ueno M., Koyama K., 2003, ApJ, 589, 827

[43] Bamba, A., Yamazaki, R., Yoshida, T., Terazawa, T., & Koyama, K. 2006, Adv. Space Res., 37, 1439

[44] Beck, R. 2001, Space Science Reviews, 99, 243

[45] Bell, A. R., 1978, MNRAS, 182, 147

[46] Bell, A. R., 2004, MNRAS, 353, 550

[47] Berezhko E. G., 1996, APh, 5, 367

[48] Berezhko, E. G., Ksenofontov, L. T., Ptuskin, V. S., Zirakashvili, V. N., & Völk, H. J, 2003, A&A, 410, 189

[49] Berezhko, E. G., & Völk H. J., 2000, ApJ, 540, 923

[50] Berezhko, E. G., Yelshin V.K. & Ksenofontov L.T. 1996, J. Exp. Theor. Phys., 82, 1

[51] Berezinskii, V. S., Bulanov, S. V., Dogiel, V. A., Ginzburg, V. L., & Ptuskin, V. S., 1990, Astrophysics of Cosmic Rays (Amsterdam: North Holland)

[52] Biermann, P. L., Becker, J. K., Dreyer, J., Meli, A., Seo, E., & Stanev, T. 2010, ApJ, 725, 184

[53] Blair, W. P., Sankrit, R., & Raymond, J. C. 2005, AJ, 129, 2268

[54] Blair, W. P., Sankrit, R., Raymond, J. C., & Long, K. S. 1999, AJ, 118, 942

[55] Blandford, R., & Eichler, D., 1987, Physics Reports, 154, 1

[56] Blasi, P., 2009, PRL, 103, 051104

[57] Blasi, P., & Amato, E., arXiv:1105.4521

[58] Bloemen, J.B.G.M, Dogiel, V. A, V.L. Dorman, V. L., & V.S. Ptuskin, 1993, A&A, 267, 372

[59] Blümer, J., Engel, R., & Hörandel, J, 2009, Prog. Part. Nucl. Phys. 63, 293

[60] Braun, R., Goss, W. M., & Lyne, A. G. 1989, ApJ, 340, 355

[61] Bronfman, L. et al. 1988, ApJ, 324, 248

[62] Büsching, I., Kopp, A., Pohl, M., Schlickeiser, R., Perrot, C., & Grenier, I. 2005, ApJ, 619, 314

[63] Byun, D.-Y., Koo, B.-C., Tatematsu, K., & Sunada, K. 2006, ApJ, 637, 283

[64] Caprioli, D., Amato, E. & Blasi, P., 2010, APh, 33, 160

[65] Caprioli, D., Blasi, P., & Amato, E. 2009, MNRAS, 396, 2065

[66] Caraveo, P. A., Bignami, G. F., Mignami, R. P., & Taff, L. G. 1996, ApJ, 461, L91

[67] Caraveo, P. A., De Luca, A., Mignani, R. P., & Bignami, G. F. 2001, ApJ, 561, 930

[68] Casanova, S., et al. 2010, PASJ, 62, 1127

[69] Case, G., & Bhattacharya, D. 1996, A&AS, 120, 437

[70] Cesarsky, C.J., 1980, ARAA, 18, 289

[71] Chang, J., et al. 2008, Nature, 456, 362

[72] Chi, X., & Wolfendale, A. W., 1991, J. Phys. G, 17, 987

[73] Cohen, M., 1995, ApJ, 444, 874

[74] Corstanje, A., et al., 2011, arxiv:1109.5805

[75] Cowsik, R, & Lee, M. A. 1979, ApJ, 228, 297

[76] Cowsik, R., & Wilson, L. W., 1973, 13^{th} ICRC, Denver, 1, 500

[77] Cowsik, R., & Wilson, L. W., 1975, 14^{th} ICRC, Munich, 1, 74

[78] Delahaye, T., Lavalle, J., Lineros, R., Donato, F., Fornengo, N. 2010, A&A, 524, 51

[79] Di Bernardo, G., Evoli, C., Gaggero, D., Grasso, D., Maccione, L., Mazziotta, M. N., 2011, APh, 34, 528

[80] Di Sciascio, G., & Roberto, I., 2011, arxiv:1112.0666

[81] Dickey, J. M., & Lockman, F. J. 1990, Annu. Rev. Astron. Astrophys. 28, 215

[82] Drury, L. O'C. 2011, MNRAS, 415, 1807

[83] Drury, L. O'C., & Aharonian, F. A., 2008, APh, 29, 420

[84] Egger, R. J., & Aschenbach, B. 1995, A&A, 294, L25

[85] Engelmann, J. J. et al, 1990, A&A, 233, 96

[86] Erlykin, A. D., & Wolfendale, A. W. 2000, A&A, 356, L63

[87] Erlykin, A. D., & Wolfendale, A. W. 2001, J. Phys. G: Nucl. Part. Phys. 27 959

[88] Erlykin, A. D., & Wolfendale, A. W. 2006, APh, 25, 183

[89] Erlykin, A. D., & Wolfendale, A. W., 2011, 32^{nd} ICRC, Beijing

[90] Falcke, H., & Gorham, P., 2003, APh, 19, 477

[91] Falcke, H., et al., 2005, Nature, 435, 313

[92] Faherty, J., Walter, F. M., & Anderson, J. 2007, Ap&SS, 308, 225

[93] Fermi, E., 1949, Phys. Rev., 75, 1169

[94] Gabici, S., Aharonian, F. A., & Casanova, S., 2009, MNRAS, 396, 1629

[95] Gaisser, T. K. 1990, Cosmic Rays and Particle Physics. Cambridge Univ. Press, Cambridge

[96] Gallant, Y. A., 2011, Mem. S.A.It., 82, 714

[97] Garcia-Munoz, M., Mason, G. M., & Simpson, J. A., 1977, ApJ, 217, 859

[98] Ginzburg, V. L., & Ptuskin, V. S., 1976, Rev. Mod. Phys., 48, 161

[99] Ginzburg, V. L., & Syrovatskii, S. I. 1964, The Origin of Cosmic Rays (Oxford: Pergamon)

[100] Glasstetter, R., et al., 2005, 29tth ICRC, Pune, 6, 293

[101] Gleeson, L. J., & Axford, W. I. 1968, ApJ, 154, 1011

[102] Grasso, D., et al. 2009, APh, 32, 140

[103] Gratton, L. 1972, ApSS, 16, 81

[104] Green, D. A., 2009, BASI, 37, 45

[105] Greisen, K., 1960, Ann. rev. Nucl. Sci., 10, 63

[106] Grenier I. A., 2000, A&A, 364, L93

[107] Gordon, M. A., & Burton, W. B. 1976, ApJ, 208, 346

[108] Haino S. et al., 2004, Phys. Lett. B, 594, 35

[109] Hayakawa, S. 1969, Cosmic Ray Physics (New York: Wiley)

[110] Hess, V. F., 1912, Phys. Z. 13, 1084

[111] Huege, T., & Falcke, H., 2005, APh, 24, 116

[112] Huege, T., et al., 2008, APh, 30, 96

[113] Hörandel, J. R., 2003, APh, 19, 193

[114] Hörandel, J. R., 2004, APh, 21, 241

[115] Hörandel, J. R., Modern Physics Letters A, 2007, 22, 1533

[116] Hörandel, J. R., 2008, Rev. Mod. Astron. 20, 203

[117] Hörandel, J. R., 2008, Advances in Space Research 41, 442

[118] Hörandel, J. R., 2009, Nucl. Phys. Proc. Suppl., 2009, 196, 289

[119] Hörandel, J. R., 2009, arxiv:0910.2144

[120] Horneffer, A., 2006, PhD thesis, KASCADE

[121] http://root.cern.ch

[122] http://www.hisparc.nl

[123] http://www.lofar.org

[124] Jelley, J. V., et al., 1965, Nature, 205, 327

[125] Jokipii, J. R., 1976, ApJ, 208, 900

[126] Jian-Wen X., Xi-Zhen Z., & Jin-Lin H., 2005, Chin. J. Astron. Astrophys., 5, 165

[127] Kachelriess, M., Ostapchenko, S. & Tomas, R., 2010, arxiv: 1004.1118

[128] Kamata, K., & Nishimura, J., 1958, Prog. Theoret. Phys. Suppl., 6, 93

[129] Kardashev, N. S., 1962, Soviet Astronomy, 6, 317

[130] Katsuda, S., Tsunemi, H., & Mori, K., 2008, ApJ, 678, L35

[131] Kawanaka, N., Ioka, K., Ohira, Y., & Kashiyama, K. 2011, ApJ, 729, 93

[132] Kickelbick, D., 2008, PhD thesis, KASCADE

[133] Knödlseder, J., & Jean, P., 2009, arxiv:0912.4163

[134] Kobayashi, T., Komori Y., Yoshida K., & Nishimura J., 2004, ApJ, 601, 340

[135] Lazendic, J. S., & Slane, P. O., 2006, ApJ, 647, 350

[136] Leahy, D. A., & Aschenbach, B., 1995, A&A, 293, 853

[137] Leahy, D. A., & Aschenbach B., 1996, A&A, 315, 260

[138] Leahy, D. A., & Tian, W. W., 2007, A&A, 461, 1013

[139] Lerche, I., & Schlickeiser, R., 1982, A&A, 107, 148.

[140] Lingenfelter, R. E., 1969, Nature, 224, 1182

[141] Lukasiak, A., Ferrando, P., McDonald F. B., & Webber, W. R., 1994, ApJ, 423, 426

[142] Malkov, M. A., & Drury, L. O'C., 2001, Rep. Prog. Phys., 64, 429

[143] Mathis, J. S., Mezger, P. G., Panagia, N., 1983, A&A, 128, 212

[144] Mao, C. Y., & Shen, C. S., 1972, Chinese J. Phys., 10, 16

[145] Miceli, M., Bocchino, F., & Reale, F., 2008, ApJ, 676, 1064

[146] Minkowski, R., 1958, Rev. Mod. Phys., 30, 1048

[147] Nagano, M., et al. 1984, J. Phys. G: Nucl. Phys., 10, 1295

[148] Nagano, M., & Watson, A. A, 2000, Rev. Mod. Phys., 72, 689

[149] Obermeier, A., et al. 2011, ApJ, 742, 14

[150] Obermeier, A., 2011, PhD Thesis, TRACER

[151] Ohira, Y., & Ioka, K., 2011, ApJ, 729, L13

[152] Ohira, Y., Murase, K., & Yamazaki, R., 2010, A&A, 513, A17

[153] Ohira, Y., Murase, K., & Yamazaki, R., 2011, MNRAS, 410, 1577

[154] Over, S., et al., 2007, 30^{th} ICRC, Merida, Mexico

[155] Panov, A. D. et al. 2007, 30^{th} ICRC, Merida, Mexico, OG.1.1

[156] Panov, A. D. et al. 2007, Bull. Russ. Acad. Sci., Vol. 71, No. 4, pp. 494

[157] Parizot, E., Marcowith, A., Ballet, J., & Gallant, Y. A., 2006, A&A, 453, 387

[158] Plucinsky, P. P., et al. 1996, ApJ, 463, 224

[159] Pohl, M., & Esposito, J. A., 1998, ApJ, 507, 327

[160] Porter, T. A., Moskalenko, I. V., Strong, A. W., Orlando, E., & Bouchet, L., 2008, ApJ, 682, 400

[161] Ptuskin, V. S., Jones, F. C., Seo, E. S., & Sina, R., 2005, 29^{th} ICRC, Pune, OG.1.3

[162] Ptuskin, V. S., Jones, F. C., Seo, E. S., & Sina, R., 2006, AdSpR, 37, 1909

[163] Ptuskin, V. S., & Zirakashvili, V. N., 2005, A&A, 429, 755

[164] Reynolds, S. P., & Keohane, J. W., 1999, ApJ, 525, 368

[165] Scholten, O., et al., 2008, APh, 29, 94

[166] Seo, E. S., & Ptuskin, V. S., 1994, ApJ, 431, 705

[167] Shen, C. S., 1970, ApJ, 162, L181

[168] Shibata, T., Ishikawa, T., & S. Sekiguchi, S., 2011, ApJ, 727, 38

[169] Stephens, S. A., & Streitmatter, R. E., 1998, ApJ, 505, 266

[170] Strom, R. G., 1994, A&A, 288, L1

[171] Strong, A. W., 2011, arXiv:1101.1381

[172] Strong, A. W., & Moskalenko, I. V., 1998, ApJ, 509 212

[173] Strong, A. W., & Moskalenko, I. V., 2001, 27^{th} ICRC, Hamburg, Germany, 1942

[174] Strong, A. W. & Moskalenko, I. V., 2009, $31^{\rm th}$ ICRC, LODZ

[175] Strong, A. W., et al. 2010, ApJL, 722, L58

[176] Stupar, M., Filipović, M. D., Parker, Q. A., White, G. L., Pannuti, T. G., & Jones, P. A., 2007, Ap&SS, 307, 423

[177] Sturner, S. J., Skibo, J. G., Dermer, C. D., Mattox, J. R., 1997, ApJ, 490, 619

[178] Swordy, S. P., Müller, D., Meyer, P., L'Heureux, J., & Grunsfeld, J. M., 1990, ApJ, 349, 625

[179] Taillet, R., & Maurin, D., 2003, A&A, 402, 971

[180] Taillet, R., Salati, P., Maurin, D., Vangioni-Flam, E., & Cassé, M., 2004, ApJ, 609, 173

[181] Tatematsu, K., Fukui, Y., Landecker, T. L., & Roger, R. S., 1990, A&A, 237, 189

[182] Tibaldo, L., 2010, AIP Conference Proceedings, 1223, 89

[183] Thoudam, S., 2006, MNRAS, 370, 263

[184] Thoudam, S., 2007, MNRAS, 378, 48

[185] Thoudam, S., 2007, MNRAS Letters, 380, L1

[186] Thoudam, S., 2008, MNRAS, 388, 335

[187] Thoudam, S., & Hörandel, J. R., 2011, MNRAS, 414, 1432

[188] Thoudam, S., & Hörandel, J. R., 2012, MNRAS, 419, 624

[189] Trotta, R., Jóhannesson, G., Moskalenko, I. V., Porter, T.A., Ruiz de Austri, R., & Strong, A. W., 2011, ApJ, 729, 106

[190] Uchiyama, Y., Aharonian, F. A., Tanaka, T., Takahashi, T., Maeda, Y., 2007, Nature, 449, 576

[191] Vladimirov, A. E, Jóhannesson, G., Moskalenko, I. V. & Porter, T. A., 2011, arxiv:1108.1023

[192] Völk, H. J., Berezhko, E. G., & Ksenofontov, L. T., 2005, A&A, 433, 229

[193] Wandel, A., Eichler, D., Letaw, J. R., Silberberg, R., & Tsao, C. H., 1987, ApJ, 316, 676

[194] Webber, W. R., Kish, J. C., Rockstroh, J. M., Cassagnou, Y., Legrain, R., Soutoul, A., Testard, O., & Tull, C., 1998, ApJ, 508, 940

[195] Webber, W. R., Lee, M. A., & Gupta, M., 1992, ApJ, 390, 96

[196] Webber, W. R., & Soutoul, A., 1998, ApJ, 506, 335

[197] Wefel, J. P., 1991, NATO ASIC Proc., 337, 29

[198] Yoon, Y. S. et al., 2011, ApJ, 728, 122

[199] Yuan, Q., Zhang, B., &Bi, X. -J, 2011, Phys. Rev. D 84, 043002

[200] Zei, R. et al., 2007, 30^{th} ICRC, Merida, OG.1.1

Acknowledgements

I would like to express my sincere gratitude to all the people who made me possible to complete this thesis.

First of all, my deepest thanks to Prof. Dr. Jörg Hörandel for taking me in his group and sharing his broad knowledge of Astrophysics and Astroparticle Physics. His supervision and guidance has helped me throughout my PhD research. His valuable suggestions and advice have helped me sharpened many scientific skills including writing "good" scientific papers. His advice on not to over-interpret experimental data is something which I will always remember. His friendliness and the level of independence given to me during my PhD made me feel more like his colleague than his student. I could not have imagined having a better supervisor than him.

I would also like to thank Prof. Dr. Heino Falcke for his kind support and continuous encouragement on my work. I also thank him for sharing his broad knowledge of radio Astronomy and Astrophysics. Moreover, I thank both Heino and Jörg for their encouragement to work on cosmic-ray propagation studies in parallel to the LOFAR project activities.

My sincere thanks also goes to Prof. Dr. Paul Groot who gave me a very warm welcome when I joined his department in 2009. During my PhD, he always used to give me moral support by constantly praising me for my works. I would also like to thank all my colleagues at the Radboud University Nijmegen for all their kind help and support, and for all the good times we had together in the department. Without their help, the completion of the LORA experiment could have taken much longer.

Many thanks to all my old colleagues at the Bhabha Atomic Research Centre, Mumbai, where I started my first scientific career. Thanks to Dr. Ramesh Koul for his kindness and encouragement to carry out an independent research on cosmic-ray studies along with the departmental projects. Also, thanks to Dr. Abhas Mitra for the inspiration and the moral support he gave me during my stay in Mumbai.

Special thanks to my parents and all my family members in India for all the guidance and support they gave me throughout my life. Also, many thanks to my wife Jaya for her patience and for tolerating me without any complain during the completion of this thesis. And last but not the least, a very special thanks to my kid Aarush who had missed some good times with me and could not play multiplayer games when wanted, especially during the writing of the thesis.

Thank you all !!

List of publications

Refereed journals:

(1) Cosmic-ray measurements at very high energies with LORA
Thoudam, S. *et al., 2012, Astroparticle Physics, to be submitted*

(2) The LOFAR Radboud air shower Array: LORA
Thoudam, S. *et al., 2012, Nuclear Instruments and Methods A, to be submitted*

(3) Cosmic-ray spectral hardening at TeV energies: A possible effect due to the nearby supernova remnants
Thoudam, S. & *Hörandel, J. R., 2012, ApJ, in preparation*

(4) Nearby supernova remnants and the cosmic-ray spectral hardening at high energies
Thoudam, S. & *Hörandel, J. R., 2012, MNRAS, 421, 1209*

(5) On the point-source approximation of nearby cosmic-ray sources
Thoudam, S. & *Hörandel, J. R., 2012, MNRAS, 419, 624*

(6) A possible correlation between the high-energy electron spectrum and the cosmic-ray secondary-to-primary ratios
Thoudam, S. & *Hörandel, J. R., 2011, MNRAS, 414, 1432*

(7) An air shower array for LOFAR: LORA
Thoudam, S. *et al. 2011, Astrophys. Space Sci. Trans. 7, 195*

(8) Cosmic-ray and neutrino measurements with LOFAR
Horneffer, A. et al. 2010, Nuclear Instruments and Methods A, 617, 482

(9) Search for TeV γ-rays from H1426+428 during 2004-2007 with the TACTIC telescope
Yadav, K. K. et al. 2009, Journal of Physics G, 36, 085201

(10) On the contribution of nearby sources to the observed cosmic-ray nuclei
Thoudam, S., *2008, MNRAS, 388, 335*

(11) Very high energy gamma-ray observations of Mrk501 using the TACTIC imaging gamma-ray telescope during 2005-06

Godambe, S. et al. 2008, Journal of Physics G, 35, 065202

(12) The TACTIC atmospheric Cherenkov Imaging telescope
Koul, R. et al. 2007, Nuclear Instruments and Methods A, 578, 548

(13) Revisiting the effect of nearby supernova remnants on local Cosmic-rays
***Thoudam, S.,** 2007, MNRAS Letters, 380, L1*

(14) Effect of nearby supernova remnants on local Cosmic-rays
***Thoudam, S.,** 2007, MNRAS, 378, 48*

(15) Very High Energy γ-ray and Near Infrared observations of 1ES2344+514 during 2004-05
Godambe, S. et al. 2007, Journal of Physics G, 34, 1683

(16) Observations of TeV γ-rays from Mrk421 during Dec. 2005 to May 2006 with the TACTIC telescope
Yadav, K. K., et al. 2007, Astroparticle Physics, 27, 447

(17) Cosmic-ray proton spectrum below 100 TeV in the local region
***Thoudam, S.,** 2006, MNRAS, 370, 263*

(18) High energy diffuse gamma-ray emission of the Galactic disk and Galactic Cosmic-ray spectra
***Thoudam, S.,** 2006, Astroparticle Physics, 25, 328*

(19) A generalized ray-tracing procedure for an atmospheric Cherenkov imaging telescope and optical characteristics of the TACTIC light collector
Tickoo, A. K. et al., 2005, Nuclear Instruments and Methods A, 539, 177

Conference proceedings:

(1) LOFAR: Detecting Cosmic-rays with a Radio Telescope
Corstanje, A. et al. 2011, 32nd International Cosmic Ray Conference, Beijing, 916

(2) Towards the all-particle energy spectrum of cosmic-rays measured with LORA - an air shower array for LOFAR
Hörandel, J. R. et al. 2011, 32nd International Cosmic Ray Conference, Beijing, 1017

(3) Improved flux limits for particles with energies in excess of 10^{22} eV and the status of the NuMoon@LOFAR observations
Scholten, O. et al. 2011, 32nd International Cosmic Ray Conference, Beijing, 86

(4) NuMoon: Status of Ultra-High Energy Cosmic-ray detection with LOFAR and improved limits with the WSRT
ter veen, S. et al. 2011, 32nd International Cosmic Ray Conference, Beijing, 1042

(5) Air Shower Measurements with LOFAR
Horneffer, A., 2009, 31st International Cosmic Ray Conference, Lodz, 369

(6) Recent TeV observations of Mrk 501 with the TACTIC gamma-ray telescope
Godambe, S. et al. 2007, 30th International Cosmic Ray Conference, Merida, 170

(7) Threshold energy estimate of the proposed MACE gamma-ray telescope at Hanle
Sapru, M. L. et al. 2005, 29th International Cosmic Ray Conference, Pune, 5, 263

(8) VHE Observations of H1426+428 using TACTIC imaging telescope:2004
***Thoudam, S.** et al. 2005, 29th International Cosmic Ray Conference, Pune, 4, 363*

(9) TeV gamma-ray Observations of the Blazar Markarian 421 from January to April 2004 with TACTIC Imaging Element
Rannot, R. C. et al. 2005, 29th International Cosmic Ray Conference, Pune, 4, 355

(10) Very High Energy Gamma-ray and Near Infrared observations of 1ES2344+514 with TACTIC and MIRO Telescopes
Godambe, S. et al. 2005, 29th International Cosmic Ray Conference, Pune, 4, 347

(11) ANN based energy estimation procedure and energy spectrum of the Crab Nebula as measured by the TACTIC gamma-ray telescope
Dhar, V. K. et al. 2005, 29th International Cosmic Ray Conference, Pune, 4, 179

(12) Diffuse gamma-ray emission of the galactic disk and Galactic Cosmic-ray spectra
***Thoudam, S.,** 2005, 29th International Cosmic Ray Conference, Pune, 4, 35*

Posters presented at conferences:

An air shower array for LOFAR
(3-6) August 2010, 22nd European Cosmic Ray Symposium, Turku, Finland

A possible correlation between the high energy electron spectrum and the cosmic-ray secondary-to-primary ratios
(19-21) May 2010, 65th Dutch Astronomy Conference, Nijmegen, the Netherlands

Status of the air shower array for LOFAR

(19-21) May 2010, 65th Dutch Astronomy Conference, Nijmegen, the Netherlands

Energy thresholds and trigger rates estimate for the high altitude MACE telescope
(18-20) February 2009, 27th meeting of the Astronomical Society of India, Bangalore

Fluxes of cosmic-ray nuclei near the sources
(23-24) November 2007, National Symposium on Gamma-Ray Astronomy, Bangalore, India

Simulation results for the MACE experiment
(23-24) November 2007, National Symposium on Gamma-Ray Astronomy, Bangalore, India

The effect of nearby supernova remnants on the local Cosmic-rays
(7-9) February 2007, 25th meeting of the Astronomical Society of India, Hyderabad

Trigger rate simulation study for the MACE telescope
(7-9) February 2007, 25th meeting of the Astronomical Society of India, Hyderabad

VHE Observations of H1426+428 using TACTIC imaging telescope:2004
(3-10) August 2005, 29th International Cosmic Ray Conference, Pune, India

Diffuse gamma-ray emission of the galactic disk and the Galactic cosmic-ray spectra
(3-10) August 2005, 29th International Cosmic Ray Conference, Pune, India

Improved data analysis program for the TACTIC Imaging element
(17-20) February 2004, 13th National Space Science Symposium, Kottayam, India

Talks presented at conferences:

Cosmic-ray measurements with LORA: LOFAR Radboud air Shower Array (Invited)
(14-15) September 2011, LOFAR workshop: First Science with LOFAR, Dalfsen, the Netherlands

LORA: LOFAR Radboud air shower Array (Invited)
(18-20) May 2011, Nederlandse Astronomen Conferentie, Texel, the Netherlands

Detection of radio emission from air showers with LOFAR
(4-8) October 2010, NOVA fall school, Dwingeloo, the Netherlands

A possible correlation between the cosmic-ray electron spectrum and the secondary-to-primary ratios
(3-6) August 2010, 22nd European Cosmic Ray Symposium, Turku, Finland

Propagation of cosmic-rays in the Galaxy (Invited)
19^{th} March 2010, 13^{th} Symposium on Astroparticle Physics in the Netherlands, Nijmegen

Simulation studies for the MACE cherenkov telescope (Invited)
(23-24) November 2007, National Symposium on Gamma-Ray Astronomy, Bangalore, India

Curriculum vitae

Satyendra Thoudam was born on 1st March 1976 in Manipur, India. His father is a retired college professor and his mother is a school teacher. Inspired by his father, a physicist, he developed a strong interest in physics and mathematics during his High School.

He completed his 'Bachelor of Science' from Modern College, Manipur, India in 1998 with physics as the main subject. In 2000, he completed his 'Master of Science' in Physics from the M. S. University, Baroda, India with specialization in Nuclear and Particles physics.

In 2001, he was selected for the prestigious Training School of the Bhabha Atomic Research Centre (BARC), Mumbai (a one year training program for the recruitment of Research Scientists at various research institutes in India). He was one among the ten students in physics selected from all over India for the training.

From 2002 to March 2009, he worked as a Research Scientist at the Astrophysical Sciences Division, BARC, Mumbai. Then, he came to the Netherlands to pursue a PhD in Astroparticle Physics. He started his PhD in April 2009 at the Department of Astrophysics, Radboud University Nijmegen under the supervision of Prof. Dr. Jörg R. Hörandel.

During his stay in Mumbai, he worked on gamma-ray astronomy with the TACTIC and the MACE Cherenkov telescopes. His main contributions were in the data analysis for TACTIC and in the development of the simulation software for MACE. During the same time, he also started theoretical works on the propagation of cosmic-rays and the production of high-energy diffuse emissions in the Galaxy.

After coming to Nijmegen, he joined the LOFAR cosmic-ray group. There, as part of his PhD, he worked for the development of the LORA experiment, a particle detector array built for the LOFAR cosmic-ray studies. He took an important part in the roll-out of the experiment and developed the softwares required for the data acquisition and the data analysis of the experiment. In parallel to the experimental work, he continued his studies on cosmic-ray propagation under the guidance of his thesis advisor. His work on cosmic-ray propagation forms an important part of his PhD thesis.